Development of an Innovative Method for The Adaptation of Advanced Structural Bracing Systems into Heavy Timber Structures for Seismic Applications

by

Colin F. Gilbert

A thesis submitted to the Faculty of Graduate and Postdoctoral Affairs
in partial fulfillment of the requirements for the degree of

Master of Applied Science

in

Civil Engineering

Carleton University
Ottawa, Ontario

Development of an Innovative Method for The Adaptation of Advanced Structural Bracing Systems into Heavy Timber Structures for Seismic Applications

Colin F. Gilbert

Master of Applied Science
Civil and Environmental Engineering
Carleton University

2016

Abstract

This study investigates the adaptation of lateral load resisting systems that are typical of modern steel buildings for application to improve seismic performance and design of timber structures. Emphasis was placed on the adaptation of buckling restrained braces and friction damping devices through the development and application hybrid timber-steel design procedures. A hybrid braced heavy timber frame was designed, using capacity design principles to avoid damage in the primary timber structural components and connections. Innovative glued-in rod connections joined the steel and timber elements together in the frame. A pilot nonlinear dynamic analysis was performed to compare the seismic response of an innovative hybrid structure and steel-only building. The numerical modelling results showed that hybrid timber-steel structures can have equivalent seismic performance with respect to peak interstorey and residual drifts and maximum storey accelerations to steel-only buildings. An experimental study of the cyclic and monotonic strength and stiffness characteristics of glued-in rods, with and without pre-tensioning, validated three European fastener design methods and provided insight into elastic response characteristics. An experimental investigation in the wind simulation and seismic response of a hybrid braced frame prototype was conducted to evaluate global frame performance and glued-in rod fastener resilience. Overall, the findings suggest that the improvements in seismic performance may likely outweigh the presumed additional cost associated with the fabrication and construction of hybrid timber-steel buildings, providing a viable seismic design alternative to steel-only structures.

In dedication to my grandfather

Donald Cameron

Acknowledgments

The author would first like to extent his most heartfelt gratitude to Dr. Jeffrey Erochko for his academic support and friendship that made this research an interesting and enjoyable experience.

The author would like to acknowledge the technical guidance provided by Dr. Mohammad Mohammad from NRCan and FPInnovations and Kimberly Robinson of Star Seismic. For their generous donations, the author would like to acknowledge Williams Munoz Toro from Nordic Structures and Jonathan Clavet of Sika Canada.

For their unwavering support and advice, the author would like to thank his parents, Roy and Faye Gilbert, for without their guidance the experience would have been significantly more difficult.

The author would like to thank his grandfather, Donald Cameron, a man whose entertaining advice and support always provided a well needed break from the work required to complete this research.

For their assistance in the laboratory, the author would like to thank Ryan Gohlich, Joshua Woods, Manny Sardon, Xi "Dennis" Cheng, Hailey Quiquero, and Sean Miller. Without their help this research would not have been possible.

The author would like to thank Mr. Bruce Tate, a former teacher at Brentwood College School, whose captivating teaching style and intriguing life experiences provided the initial motivation to pursing studies in structural engineering.

Finally, the author would like to extend his heartfelt thanks to his family and friends: Graham Gilbert, Owen Gilbert, Ryan Gohlich, Talha Alhaj, Hussien Makke, Talal Khalaf, Amin Hosseini, Nicholas Patocki, Moe Zaber, Liza Watler, and Jesse Shannon. Their support and ongoing

interest provided the motivation to helped me complete this research.

Table of Contents

List of Tables

List of Figures

Nomenclature

a - unloaded edge distance

A_b - cross-sectional area of bolt

A_{bc} - cross-sectional area of brace core

A_{ef} - effective cross-sectional area of a rod

$L_{elastic}$ - elastic brace core area

A_g - gross cross-sectional area

A_n - tensile area of the steel rod; net cross-sectional area

A_r - cross-sectional area of a rod; distance between the plastic hinge in rod and end grain based

A_{sc} - cross-sectional area of brace core

A_w - cross-sectional area of wood

B - beam width

b - bolt characteristic specific coefficient

B_x - lateral sensitivity factor

C_e - exposure factor

C_g - gust factor

C_p - external pressure factor

C_{pr} - probabilistic compression resistance

C'_{pr} - post-bucking compression resistance

C_r - factored compression resistance

d, d_r - nominal rod diameter

d_b - beam depth

d_{equ} - equivalent embedment hole diameter

d_h - embedment hole diameter

d_m - mean rod diameters

d_{ts} - minimum thread diameter

e_{min} - minimum edge distance

E_r - elastic modulus of threaded steel rod

E_w - elastic modulus of wood

F_a - acceleration-based ground motion amplification factor

$f_{ax,k}$ - glued-in rod shear strength characteristic

$f_{ax,k}$ - DIN 1052 (2004) shear strength of glued-in rod connection

f_{bp} - positive bending strength

f_{bn} - negative bending strength

f_c - compression parallel to grain strength

f_{cp} - compression perpendicular to grain strength

$F_{f,dyn}$ - dynamic friction resistance

$f_{fat,d}$ - glued-in rod fatigue resistance

F_{Frame} - frame friction contribution

$f_{h,1}$ - embedment strength of the timber determined from DIN 1052 (2004)

f_k - glued-in rod pull out resistance

F_{lat} - lateral force contribution of the brace

F_{Nb} - normal pre-tensioned bolt force

$F_{f,static}$ - static friction resistance

f_t - tension parallel to grain strength

f_t - Higher mode effect force (whipping force)

f_v - longitudinal shear strength

F_v - velocity-based ground motion amplification factor

F_y - characteristic yield strength

$f_{y,k}$ - characteristic yield strength of steel glued-in rod fastener

F_u - characteristic ultimate strength

F_x - seismic force contribution at storey x

G_f - shear modulus

H - beam depth

h - building height

H_B - bolt head thickness

h_i - distance from the lower edge to i^{th} rod

H_N - nut thickness

h_s, h_{sx} - storey height

I_E - building importance factor

K - glued-in rod stiffness, torque coefficient

K_e - elastic stiffness

k - ratio of rod and wood material parameters

K_{brace} - brace stiffness

K_c - slenderness factor

k_{fat} - fatigue coefficient

$k_{fat,2000}$ - fatigue coefficient associated with 2000 loading cycles

k_s, k_r - geometric lateral resistance parameters

K_{Zcg} - member size factor

l_a,l_{ad} - embedment (or anchorage) length

L_b - beam length

L_{brace} - brace length

$L_{elastic}$ - elastic brace length

l_{geo} - geometric characteristic parameter

L_J - total joint or grip length

l_m - material length parameter

L_{rigid} - rigid connection zone length

L_s - unthreaded bolt shank length

m - bolt characteristic specific coefficient

M_y - yield moment resistance of the rod

M_v - higher mode factor

n - number of glued-in rod in grouped connection; optimal edge distances

n_b - number of pre-tensioned bolts

n_s - number of friction surfaces

N_t - notional loads

P_f - axial resistance of glued-in rod fastener

P_r - compressive resistance of timber

P_x - column axial force

$R_{90,d}$ - lateral resistance of glued-in rod fastener

$R_{ax,d}$ - axial resistance of glued-in rod fasteners (DIN 1052, 2004)

R_d - seismic force reduction factor for ductility

R_{mech} - factor associated with increase resistance due to mechanical behaviour

R_O - seismic force reduction factor for overstrength

R_{size} - size factor

R_{sh} - factor associated with strain hardening

R_y - probable yield stress factor of steel

R_{yield} - factor associated with material strength and stiffness properties

R_ϕ - factor associated with member strength variability (factored resistance)

S_E - acceleration scaling factor

S_E - elastic modulus scaling factor

S_F - force scaling factor

S_I - moment of inertia scaling factor

S_L - length dimensions scaling factor

S_M - moment scaling factor

S_{min} - minimum spacing

S_{Ma} - mass scaling factor

S_{MT} - median spectral acceleration

S_{NRT} - design spectral acceleration

S_T - time scaling factor

S_{Ta} - fundamental period scaling factor

S_V - velocity scaling factor

S_Z - section modulus scaling factor

SF - earthquake scaling factor

$S(T)$ - spectral acceleration

t - distance form the end grain to the location of the applied load; bond-line thickness

T - applied pre-tensioning torque

T_a - first mode fundamental period of a structure

t_{bl} - bond-line thickness

T_{ef} - effective member width

T_f - applied torque

T_g - glass transition temperature

T_{pr} - probabilistic tension resistance

T_r - factored tensile resistance

$T_{r,n}$ - factored net tensile resistance

$T_{r,g}$ - factored gross tensile resistance

T_s - torque resistance provided by bolt shank

T_w - torque resistance contribution of bearing surface and nut interaction

U_2 - p-delta lateral effect factor

V - base shear

V_{brace} - vertical component of brace force

V_d - design base shear

V_{ed} - elastic base shear

V_{lat} - distributed lateral shear force

V_x - seismically induced shear

W - effective brace core width; seismic weight

w_c - column width

β - factor associated with friction behaviour; angle between isotension curves

Δ_a - activation displacement

δ_{ave} - average storey displacement

δ_b - bolt elongation

Δ_{bm} - maximum drift displacement

Δ_{brace} - brace elongation

Δ_{Drift} - drift displacement

Δ_{MCE} - MCE drift displacement

δ_{max} - maximum storey displacement

δ_p - maximum plastic displacement

$\delta_{ultimate}$ - ultimate displacement

δ_y - displacement associated with the onset of yielding

Δ_x - anticipated storey drift

Γ - shear stiffness factor

$\gamma_{M,fat}$ - Eurocode fatigue factor for material safety

μ_d - dynamic friction coefficient

μ_{df} - mean dynamic friction coefficient

μ_s - static friction coefficient, thread surface friction coefficient

μ_w - bearing surface friction coefficient

ω - factor associated with BRB strain-hardening behaviour

ϕ - resistance modification factor of steel

ϕ_{Ar} - anchor rod resistance factor

ϕ_b - structural bolt resistance factor

ρ - timber density

τ_f - bond-line shear strength

θ_{beam} - brace angle

θ_x - stability coefficient

ϖ - glued-in rod connection stiffness ratio

Chapter 1: Introduction

Structural seismic performance is directly affected by building weight and the energy dissipation capability of well designed lateral force resisting systems (LFRS). The high strength-to-weight ratio of timber reduces seismic weight and provides a comparative advantage over equivalent steel or concrete structures. Current timber seismic force resisting systems (SFRS) contain carefully detailed connections that rely on fastener yielding and bearing failure modes for energy dissipation. Timber braced frames containing glue laminated (Glulam) bracing elements are examples of earthquake systems that rely on this connection behaviour to provide wood structures with adequate seismic performance. These LFRSs typically have lower force reduction factors (R-factors) than modern steel bracing systems, resulting in comparatively higher seismic design forces. The adaptation of advanced structural steel bracing systems into timber buildings would allow designers to take advantage of higher R- factors when designing the timber members to remain elastic under the anticipated seismic forces. This would allow the design to take advantage of the lower seismic weight associated with the high strength-to-weight ratio of timber (which is normally mitigated by the need to use lower R-factors). The application of capacity design procedures that concentrate nonlinear behaviour in the steel bracing systems, will justify the use of the lower ductility and overstrength factors associated with the steel bracing systems. The steel connections could therefore be designed using steel detailing guidelines, supplemented by hybrid timber-steel connection design recommendations to ensure efficient force transfer into the strong parallel-to-grain direction throughout the braced timber frame.

Advanced structural bracing systems have been developed for applications in steel seismic design to provide optimal energy dissipation. These systems utilize yielding mechanics, friction interfaces, and viscous materials to provide the structure with supplemental damping to

resist severe ground motions. The most common forms of these systems are buckling restrained braces (BRBs), friction damping devices, and viscous dampers. However, studies conducted by Christopoulos et al. (2008) and Erochko et al. (2013) combine self-centering and friction damping mechanisms into a single bracing system. These Self-Centering Energy-Dissipative (SCED) braces prevent residual drifts and experience no permanent damage during activation, resulting in the added benefit of long lasting seismic performance. These bracing systems are design to satisfy the inelastic demands of seismic events.

The structural fuse concept concentrates the damage, caused through nonlinear behaviour, in the well detailed bracing elements. When used in combination with a capacity design procedure, the design ensures the surrounding structural elements of the SFRS and gravity frame remain elastic under the anticipated earthquake hazard levels. This improves the longevity of a structure while simultaneously reducing post-disaster costs. The capacity design procedure utilizes the maximum probable nonlinear forces of the ductile yielding elements as a lower limit to design the remaining structural members of the seismic force resisting system. Seismic design forces are typically increases by a factor to overdesign the major structural elements to ensure the structural integrity of the system will not be compromised, preventing progressive collapse and preserving public safety through efficient design. More detailed capacity protection procedures design the structural components in stages with progressing force increments to allow for the detailing of secondary failure mechanisms that will provide additional energy dissipation during severe or long-duration ground motions, while protecting structural elements susceptible to brittle failure modes.

The efficient detailing of timber connections is vital to the adaptability of efficient lateral force resisting systems. Advanced fastener technology, such as self-tapping screws and glued-in rods, are becoming more prevalent in the field of timber engineering. Glued-in rod connections typically consist of threaded steel rods embedded into the end grain of large timber elements. These fasteners are capable of transferring high tension forces into the strong, parallel to grain, direction of the wood members. Research conducted by Malczyk (1993) investigated the early use of glued-in re-bar as a possible connection detail. The lack of a Canadian approved design procedure means designers must rely on the findings of dedicated European academic research

projects intended to develop design equations for glued-in rods. The ideal design of glued-in rod connections would ensure failure occurs within the steel rods, preventing brittle pull-out failure in the substrate interface of the fasteners. Even after extensive research, a governing design procedure has not been reached. However, the design methods presented in the GIRod Report (2002), LICONS Report (2003) and German Design Code DIN 1052 (2004) have been shown to provide reliable results (Bengtsson and Johansson 2002; Tlustochowicz et al. 2011). Additionally, the cyclic and pre-tensioned behaviour of these connections has yet to be investigated, which is critical if these connections are to be utilized for seismic applications.

This study presented in this paper, aims to develop a structural system that will adapt high R-factor bracing systems into heavy timber frames, to take full advantage of the high strength-to-weight ratio of timber and the force reduction capabilities of these advanced steel systems. This concept would reduce seismic design forces and optimize the earthquake design of heavy timber buildings. This objective was achieved through a nonlinear dynamic time-history analysis and two experimental research programs, that investigated the adaptation of advanced structural steel bracing systems into hybrid timber-steel buildings. The hybrid timber-steel design concept combines pre-fabricated steel sections and heavy timber members by utilizing advanced fastener technology to provide insight in the seismic performance of braced hybrid timber-steel frames. The nonlinear dynamic analysis of six storey hybrid timber-steel and steel-only structures containing buckling restrained braced frames (BRBFs) was conducted to evaluate the seismic performance and design properties of both building. This study also investigated whether the significant reduction in seismic weight of the hybrid structures affects drift and acceleration performance compared to the steel-only buildings. The first experimental program focused on the strength characteristics and cyclic behaviour of glued-in rods, as well as the effects of pre-tensioning, on the seismic performance of these fasteners. The second experimental study, based on the finding of the associated glued-in rod study, investigated the application of glued-in rods for the adaptation of BRBs and friction dampers, into an advanced hybrid timber-steel building, through the development and application of capacity design principles for such a system. The study subjected a half-scale hybrid braced heavy timber frame, utilizing intermediate steel connection details with glued-in rod fasteners to: wind simulations, a quasi-static cyclic loading procedure, and dynamic

earthquake record tests.

The findings of the three studies previously mentioned are presented in Chapters 4 through 6. However the contextual and theoretical information used in the design and testing of these concepts is presented in Chapters 2 and 3. Chapter 2 outlines various research concepts and studies that, when applied collectively, formed the basis for the proposed method of adapting advanced structural bracing systems into innovative hybrid timber-steel buildings. The results and limitations of previously conducted studies in the field of advanced braced heavy timber design will be presented. As well, results from the various investigations into the development of a reliable design procedure for glued-in rod fasteners are discussed and the major design methods are detailed in this chapter. Chapter 3 presents the analytical information regarding the seismic design of braced hybrid timber-steel frames containing BRBs and friction damping devices. The capacity design procedure and design methodology surrounding the detailing of these structural fuses is also presented here. Chapter 4 presents the results from the nonlinear dynamic analysis of the numerical modelling investigation into the seismic performance of both a hybrid timber-steel and steel-only structure. The design and testing of the single glued-in rod specimens used to investigate the effects of pre-tensioning on pull-out resistance, as well as the monotonic and cyclic resistance characteristics of these fasteners, are presented in Chapter 5. Chapter 6 discusses the fabrication and experimental testing of the half-scale hybrid timber-steel braced frame prototype. Lastly, Chapter 7 summarizes the finding of the experimental and numerical modelling programs previously mentioned, and discuss the shortcomings and future research necessary to further improve the adaptation of advanced seismic force resisting systems into heavy timber structures.

Chapter 2: Literature Review

2.1 Seismic Design

2.1.1 Background

Modern seismic design methodologies are founded on the performance-based design concept that classifies the strength and durability requirements of a structure to limit lateral displacements and accelerations. Based on the intended performance of lateral force resisting systems, this method define multiple structural performance objectives to satisfy different earthquake hazards while ensuring life safety. The continuous development of this design principal has improved the earthquake performance of structures in regions of high seismic risk. Current seismic design codes do not explicitly detail performance-based design procedures, with building performance being dictated at the Maximum Credible Earthquake (MCE) hazard level to ensure public safety. These modern seismic design procedures have proven their values in the review following recent earthquakes in regions of the world that apply these design philosophies. The 6.9 magnitude earthquake that struck Kobe, Japan in 1995, caused severe structural damage and collapse in structures design in accordance to obsolete building codes (Decker et al. 1995). However, the majority of buildings designed using modern seismic design practices experienced low levels of structural damage and a high rate of post disaster occupancy (Decker et al. 1995). This excludes buildings constructed in regions of soft soils, these structures experienced higher than normal levels of structural damage due to ground motion amplification (Decker et al. 1995). Interestingly, the majority of the buildings that experience collapse during this severe seismic event contained braced frames that failed in part due to inadequate connection capacity and insufficient

lateral stiffness (Popovski et al., 2003). Although tragic, this presents an important lesson in the significance of brace stiffness and connection capacity, that can be applied to the seismic design of braced heavy timber frames. Furthermore, engineering reports show that structures designed in accordance to modern seismic provisions, that were subjected to the more recent 2011 Tohoku earthquake, sustained low structural damage, with the majority of the destruction being reported in the non-structural building components (Motosaka and Mitsuji 2012). The application of modern seismic design provisions provide substantial protection against major structural damage and building collapse through effective structural design.

The National Building Code of Canada (NBCC, 2010) categorizes structures based on importance factors that accounts for human occupancy, post-disaster requirements, and building response with respect to seismic performance. These categories are designed to classify post-disaster performance through susceptibility to structural damage. The factors range from 1.5 for post-disaster structures to 0.8 for buildings of low importance. A structure of normal importance, importance factor of 1.0, designed in accordance with the seismic design provisions, is expected to sustain structural damage during the design hazard level earthquake without experiencing collapse (Mitchell et al. 2003). As a result, the structure may sustain significant residual drift due to inelastic action in the seismic force resisting system (SFRS). The NBCC (2010) specifies equivalent static and response spectrum analyses to anticipate peak seismic forces and displacements, that are used to design building in regions of seismic risk. Additionally, dynamic time history analysis is a supplementary structural analysis method used to further assess the seismic performance of structures that may contain advanced SFRS. The seismic previsions of the NBCC (2010) define the design spectrum at the MCE hazard level with a probability of exceedance of 2% in 50 years that corresponds to a return period of 2475 years. These Canadian response spectra are adapted from a uniform hazard level model that assumes 5% inherent damping for site specific ground accelerations (Filiatrault et al., 2013). To satisfy additional performance-based design considerations, further analysis can be done to include the design-basis earthquake (DBE) hazard level, probability of exceedance of 10% in 50 years, to establish seismic performance under lower seismic intensities. The MCE accelerations are divided into ranges defined by critical fundamental periods, T_a, that are used to compile the response spectrum within a geographic

region. These periods correlate to the fundamental period of a structure which is a factor of the lateral stiffness of the SFRS and the total building mass. In rare cases where the frequency content of a ground excitation matches the natural frequency of a structure, the building can experience amplified lateral displacements with the potential to exceed specified drift limits that can severely impact seismic performance and even cause buildings to collide in densely populated regions. Additionally, the response spectrum is prescribed for level C site class conditions and is subject to factorization depending on the soil composition and bedrock depth at the building location.

Ground amplification factor accounts for soil characteristics that increase ground motion intensity. This phenomenon can have a profound effect on building performance and sustaining structural damage during severe ground accelerations. In the recent Tohoku earthquake, clear structural damage was visible in mid-rise building constructed due to soil amplification, even though the structures were design to modern seismic standards (Motosaka and Mitsuji 2012). The Canadian seismic provisions account for ground motion amplification through the acceleration-based, F_a, and velocity-based, F_v, factors that vary depending on the design spectrum ordinates (NBCC 2010). These factors are increased with the reduction of ground motion amplitudes in regions containing elastic soil characteristics due to the amplified dynamic response these ground conditions create at the surface (Filiatrault et al., 2013). Additionally, geometric irregularities can amplify the lateral forces and subsequent inelastic demand imparted on the structure. Therefore designers must take into account induced torsional effects resulting from asymmetry in the structural layout. For symmetrical structures common practice dictates that an accidental eccentricity of 10% is used in the conservative design of all SFRS.

2.1.2 The Concepts of Ductility, Overstrength and Energy Dissipation

Modern design codes permit structural engineers to utilize nonlinear material characteristics to reduce seismic loads expected for the elastic design of seismic force resisting systems to optimize the structural design through localized inelastic behaviour (Bruneau et al., 1998). The force reduction concept reflects a SFRS's ability to dissipate seismic energy defined by the non-linear hysteretic behaviour of the well detailed structural fuses (Mitchell et al. 2003). These force

modification factors depend on the fundamental material characteristics of ductility and overstrength that define the plastic behaviour. According to the NBCC (2010) seismic provisions the ductility factor, R_d, ranges from 1.0 for brittle systems to 5.0 for highly ductile systems. As a result of the wide spread structural collapse during the 1985 Mexico earthquake, upper limits were placed on the ductility factors for steel and concrete systems (Mitchell et al. 2003). These limits provide practical guidelines when determining acceptable force reduction factors for modern SFRS. The overstrength factor, R_o, ranges from 1.0 to 1.7 for brittle and highly ductile systems respectively (NBCC 2010). According to the Canadian design guidelines, the ductility and overstrength factors associated with structural bracing systems fall within the ranges of 2.0 to 4.0 and 1.2 to 1.5 respectively.

Ductility is provided by specially detailed structural elements that are activated during sizeable seismic loading scenarios. The ductility concept is illustrated in idealized force-displacement graph in Figure 2.1. The elastic region, region I, of the force-deformation curve represents the linear stiffness of the structural element that is limited by its characteristic yield strength, F_y. Ductility occurs when the element exhibits plastic behaviour due to the applied force exceeding the characteristic yield strength represented in region II of Figure 2.1. This plastic action causes inelastic behaviour in the element is typically experienced in the form of localized damage. The magnitude of ductility can be calculated as the ratio of plastic and elastic deformations experienced by the element, equation (2.1).

$$Ductility = \frac{\delta_p}{\delta_y} \tag{2.1}$$

Steel has a particularly high ductility characteristic that can withstand repeated nonlinear cyclic loading with marginal strength degradation. This is representative of the wide range of high ductility factors presented in the NBCC (2010).

Another plastic behaviour responsible for providing energy dissipation to the structure is that material overstrength characteristic. Overstrength accounts for the reserve strength of the SFRS provided by multiple geometric and material characteristics factors as well as resistance factorization. The overstrength factor, R_o, allows for further reduction of seismically induced

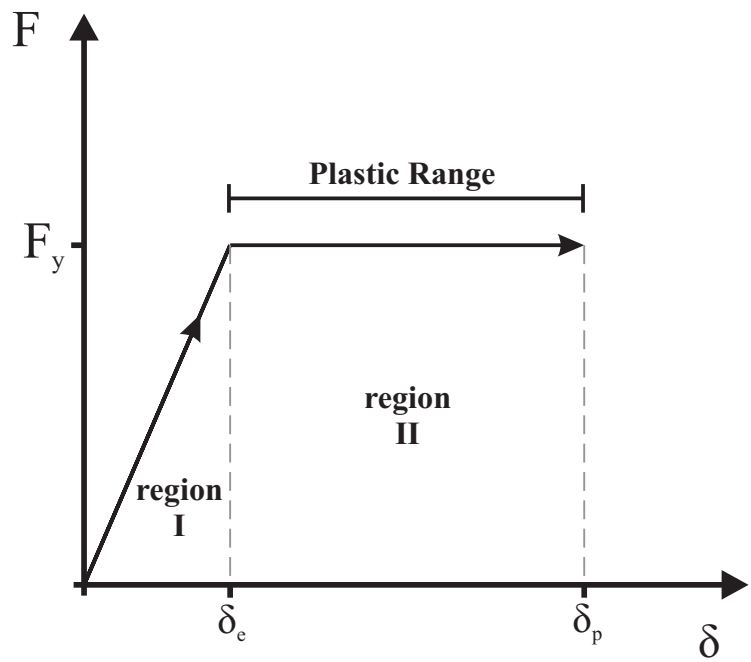

Figure 2.1: Concept of Ductility

lateral design forces, aiding in the economical seismic design of structures. Mitchell et al. (2003) proposed the following equation (2.2) that accounts for the factors contributing to overstrength.

$$R_o = R_{size} R_\phi R_{yield} R_{sh} R_{mech} \tag{2.2}$$

The size factors, R_{size}, signifies the increased resistance of SFRSs due to variability in actual member size (Mitchell et al. 2003). This accounts for the member size limitations engineers face because of standardization for manufacturing simplification. This limits designers to select member sizes when calculating the factored resistance of structural elements used in the LFRS. The CSA resistance factors, ϕ, associated with inconsistency in material strength, geometry and workmanship utilized in member strength calculations offer additional overstrength to the system (Kulak and Grondin 2010). This variability is accounted for in the seismic design procedure through the R_ϕ factors contributing to the over-strength factor. However, investigations into the unfactored resistance of SFRSs can been used to evaluate the near-collapse response of a structure to anticipate the worst case scenario in regards to unexpected loading events or severe seismic hazard (Mitchell et al. 2003). In reality, the materials used in the building construction have strength

characteristic higher than the assumed values used for the factored design procedure. R_{yield}, accounts for these increases in the material strength and stiffness properties not represented by the minimum specified properties outline the CSA design manuals. Nonlinear characteristics that increased the plastic resistance of a material loaded into the inelastic region is accounted for by factor R_{sh}. This strain-hardening strength phenomenon is known as the Bauschinger effect, which dictates the ultimate strength, F_u, and the initiation of premature yielding of an element during load reversal (Kassner et al., 2009). The material behaviour represented in Figure 2.2. R_{mech} represents additional resistance provided by the SFRS prior to the development of a collapse mechanisms. This is due to increased resistance provided by the formation of additional mechanical fuses and specific structural elements that are activated under extreme seismic loading during severe ground excitations. For example, the gusset plate connection in a braced frame can be designed to provide additional nonlinear behaviour if the intended design forces are exceeded within the brace. This supplemental damping, provided by a hierarchy of yielding, is known as the capacity design concept (Mitchell et al 2003). These factors make up the energy dissipation contributions of the structure provide by overstrength.

The ground motions during a seismic event inputs energy into a structure that must be dissipated by well detailed element throughout the SFRS. Energy dissipation is dependent on the material behaviours of ductility and overstrength, which can result from plastic deformations, crack propagation and tearing in the base material (Reid 1993). The energy dissipation due to nonlinear deformation is a product of the plastic resistance and the maximum ductility, which is represented as the area within the force-deformation graph. Under cyclic loading scenarios, the total energy dissipation is a summation of the individual hysteretic loops of each cycle, visible in Figure 2.3. This cumulative energy dissipation behaviour is the primary defence ductile structures have against the formation of severe structural damage and progressive collapse.

Structural steel has excellent energy dissipation capabilities due to its high tolerance of plastic deformations without the development of brittle failure. Additionally, structural grade steel does not experience large amounts of strength degradation in the higher cycles, which resulted in large sweeping hysteresis responses that represent maximized energy dissipation. The impact of

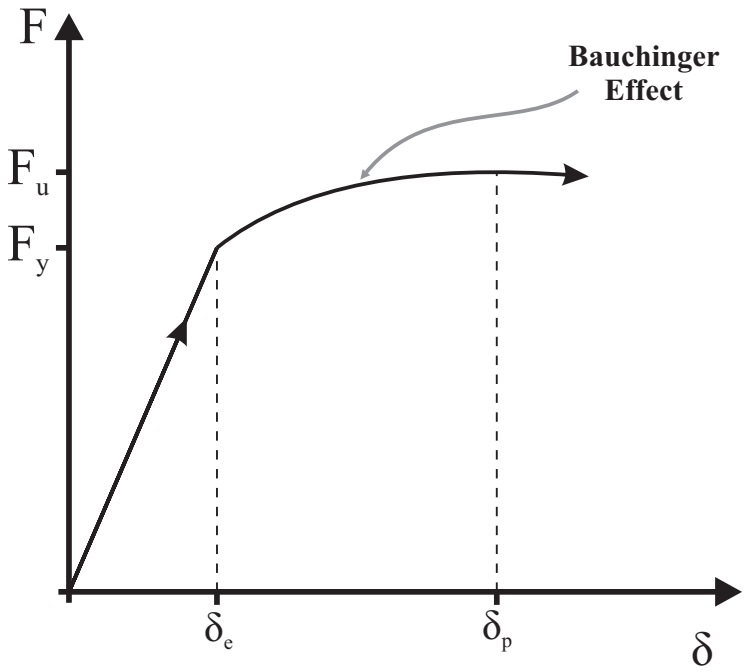

Figure 2.2: Bauschinger Effect

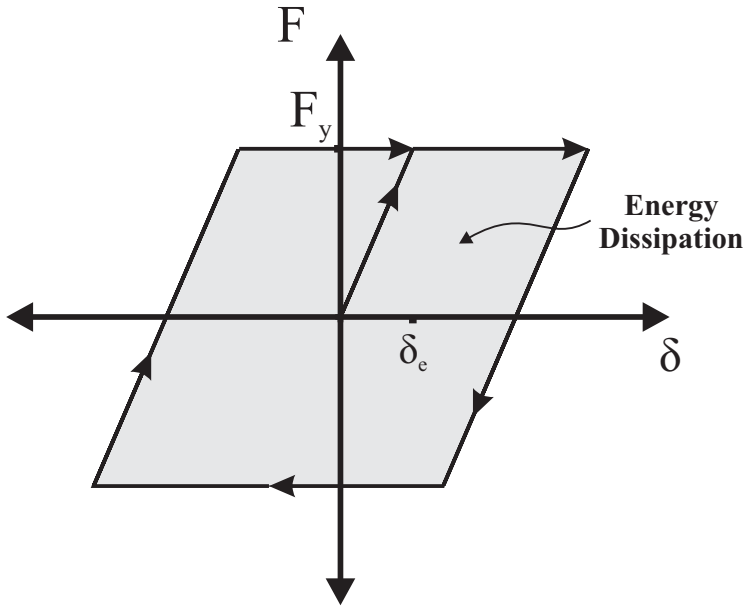

Figure 2.3: Idealized Energy Dissipation Response

energy dissipation in seismic design ensures well designed structures can withstand severe ground motions while meeting stringent code limitations for drift. Nonlinear axial deformations are utilized for energy dissipation in traditional and advanced structural bracing systems when subjected to tension loading (refer to Figure 2.4 a). In seismic design, the localized regions of plastic deformations caused by inelastic rotation is referred to a plastic hinge, which is the secondary energy dissipation mechanism of conventional bracing systems, shown in to Figure 2.4 b.

Seismic systems typical of wood structures, can be detailed to provide energy dissipation through inelastic connection behaviour known as fastener yielding and fatigue. This method of plastic behaviour typically has lower energy dissipation capabilities than braced or moment resisting frames. This results in the use of lower ductility and overstrength force reduction factors when designing timber structures against seismic hazards.

2.1.3 Building Performance and Seismic Provisions

Based on NBCC (2010) requirements, peak interstorey drifts are analysed to evaluate seismic performance. Structures that undergo excessive lateral displacements can experience total structural failure in the form of excessive residual drifts that lead to progressive collapse caused by P-Delta effects. It is because of the substantial risk to damage and loss of life that structures face during a seismic event that the NBCC (2010) imposes limits on the interstorey drifts at the MCE hazard level. These restrictions are based on the specified importance category of the building and aim to ensure that the structural integrity remains intact following a disaster by minimizing

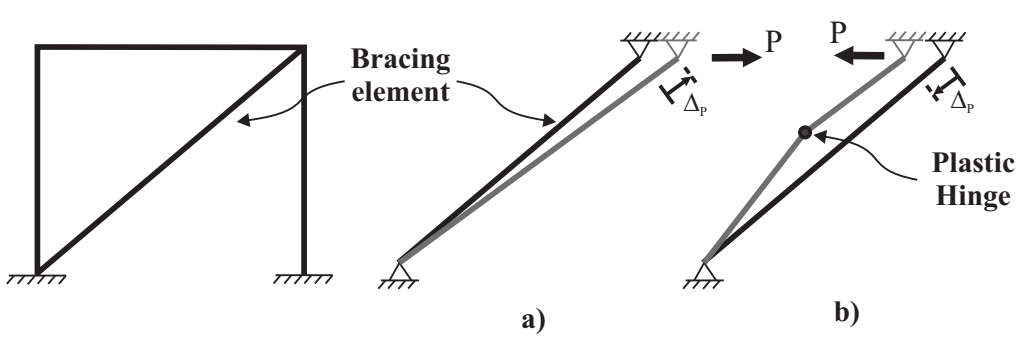

Figure 2.4: Conventional Brace Response
a) Tension Loading Behaviour b) Compression Loading Behaviour

damage in the structural components (Filiatrault et al., 2013). These limits also aid in structural stability to prevent the formation of collapse mechanisms due to excessive inelastic demands within the SFRS. The drift limits are dependent on the importance factor and storey height, h_s, of a structure and are categorized as $0.01h_s$ from post-disaster buildings, $0.02h_s$ for building of high importance, and $0.025h_s$ for the remaining importance categories (NBCC 2010). The magnitude of residual drift a structure sustains is directly influenced by the peak interstorey drifts and ductility demands imparted on the SFRS. In the context of performance-based design, residual drifts represent the amount of damage a structure has sustained in the form of permanent lateral displacement. However, the NBCC (2010) does not explicitly place limits on the residual drift a structure can experience. These permanent deformations impact structural integrity and serviceability that dictate the post-disaster occupancy of a building. Therefore, to improve building performance and serviceability considerations, further emphasis should be placed on performance-based design procedures to evaluate building performance at multiple seismic hazard levels.

The dynamic time history analysis investigation conducted by Erochko et al. (2011) proposed a method for determining residual drift demands as a function of peak interstorey and elastic drift contributions. The authors suggest that the residual drift can be calculated by subtracting the elastic drift demand of the SFRS from the peak interstorey drifts. The resulting drift accounts for the inelastic demand imparted in the structure during the ground motion. The elastic drift demand is determined from an elastic analysis of the SFRF, to predict the initial stiffness of the system. This proposed methodology aids in the advancement of performance-based design by providing designers with a means to predict the magnitude of structural damage a building will sustain during the varying magnitudes of seismic threats. This information could be used as part of the iterative seismic design process to efficiently limit residual drifts, resulting in higher building performance.

Storey accelerations are the final factor that governs the building performance of structures exposed to seismic risk. Similar to residual drifts, limits on acceptable storey accelerations are not presented in the seismic provisions of the NBCC (2010). However, designers are required to limit storey accelerations during seismic action, as well as comply with occupancy requirements

for acceptable levels of comfort. This ensures occupants do not experience nauseating lateral motions due to excessive structural swaying and abrupt changes in direction during designed-bases earthquakes and low to moderate wind events. Braced frames can be used as effective lateral force resisting systems (LFRSs) to ensure established interstorey drift limits are met and structures are protected against excessive residual drifts and storey accelerations.

2.1.4 Seismic Performance of Braced Frames

Concentrically braced frames (CBF) contain quasi-truss elements which resist lateral loads through the development of axial tension and compression in the bracing elements, which are then transferred into the surrounding structural members. Conventional braced frames provide lower levels of ductility and overstrength compared to advanced bracing systems, as demonstrated by the R_d and R_o factors specified in the National Building Code of Canada (NBCC 2010). These systems satisfy inelastic demand through the brace responses of tension yielding and compression buckling, as previously depicted in Figure 2.4. The plastic hinge induced buckling response provides limited resistance to seismic forces due to instability and the low flexural resistance of the steel bracing sections. These yielding mechanisms provide moderate energy dissipation which is limited by the compressive behaviour and flexural strength degradation (Sabelli et al., 2013). Unlike a moment resisting frame, all beam and column elements are designed to remain elastic during lateral loading to prevent the formation of collapse mechanisms under the gravity loads supported by the braced frame. The design of CBFs is typically governed by strength requirements rather than the NBCC (2010) limitations set for drift performance. This is attributed to high lateral stiffness and inelastic yielding behaviour that restricts the horizontal displacement of braced frames (Sabelli et al., 2013). These mechanisms ensure carefully detailed CBFs can resist severe ground motions while simultaneously satisfying the stringent displacement limits of the NBCC (2010). Due to the excellent interstorey drift response, the residual drifts and storey accelerations of braced frames have been shown to be lower than moment resisting frames (Gilbert et al., 2015). This results in less damage to non-structural components and limits violent movement of inanimate objects within the structure.

Braced frames have multiple geometric configurations that are utilized in the seismic design

of steel structures. Some sample configurations are illustrated in Figure 2.5 and consist of diagonal bracing, alternating diagonal bracing, Chevron bracing, cross or x-bracing, split x-bracing, and k-bracing. The selection of brace frame geometry depends not only on the structural layout of the building but also on the intended bracing system. However, not all frame geometries are acceptable for application in Canada. The Canadian steel design standard CSA S16-09 (2009) has imposed limitations on acceptable brace configurations for given systems. These restrictions are a result of the buckling behaviour of traditional bracing elements, which forbids the use of both diagonal and alternating diagonal frame geometries for conventionally braced frames. This is due to the development of irregular brace responses caused by severe lateral instability resulting in excessive interstorey and residual drifts in directions dependent on the compressive brace resistance (Filiatrault et al., 2013). However, advanced structural bracing systems, such as buckling restrained braces (BRBs), are exempt from this specification (CSA S16-09, 2009). In addition to the strength requirements, geometric specifications also dictate the design and selection of the bracing elements and frame geometry. Therefore, building height and occupancy requirements may further restrict the selections of suitable frame configurations.

2.1.5 Capacity Design Methodology

The capacity design concept is a structural hierarchy that dictates that inelastic action is localized in well detailed ductile structural components of the SFRS. These structural fuses have well established yielding behaviour that provides effective energy dissipation to ensure structural integrity during long duration ground motion. This hierarchy stretches along the lateral load transfer path where the forces in the system are amplified to the maximum inelastic strength of the yielding elements. The loads are increased at each phase of this design approach to enhance the use of ductility while simultaneously capacity protecting the successive members, preventing the development of unintended failure modes. This methodology is used to counteract the uncertainties of the design ground motions and amplification phenomenon associated with soil conditions and seismic hazards, that may leave the structure vulnerable to severe damage or collapse. Additionally, the capacity design procedure ensures seismic performance requirements are

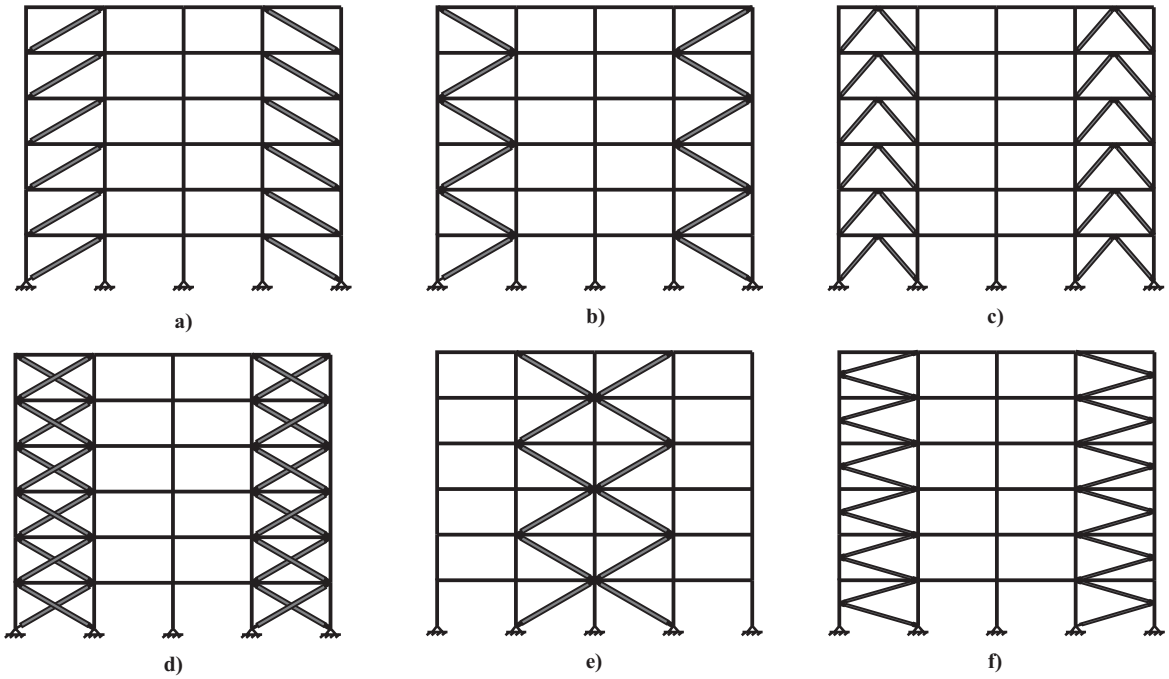

Figure 2.5: Brace Frame Configurations
a) Diagonal Bracing b) Alternating Diagonal Bracing c) Chevron Bracing d) X-Bracing e) Split X-Bracing f) K-Bracing (Adapted from Filiatrault et al. 2013)

met through strength progression and limiting localized inelastic deformations.

Upon selection of the seismic force resisting system that satisfies geometric, project and hazard based requirements, the capacity design procedure follows three remaining stages to design the failure mechanisms and elastic structural members. First, the ductile elements or primary structural fuses are designed to satisfy the inelastic demands of the MCE seismic hazard level. The intended localized plastic deformations and material properties must provide adequate energy dissipation during severe lateral loading to prevent collapse mechanisms form forming within the SFRS and gravity frames. Additionally, the cyclic behaviour of the structural fuse must be detailed to satisfy strength degradation limits. The probable inelastic resistance of the yielding elements are then determined based on the sections selected through the primary seismic design of the SFRS. These anticipated seismic forces are then factored by a previously determined magnitude and used to design the secondary failure mechanism and remained elastic structural elements. Second, secondary failure mechanisms can be selected and detailed to provide additional energy dissipation for cases of extreme seismic loading where the applied lateral loads exceed the

anticipated design forces. In the case of braced frames, bracing elements must have significant axial strength in order to satisfy specifications for tension and compression resistance. Therefore the secondary fuses must be designed for the corresponding probabilistic tension, T_{pr}, and compression, C_{pr}, forces developed in the bracing elements (NBCC 2010 & Filiatrault et al. 2013). These force requirements are dependent on the characteristics of the selected bracing elements and are outlined for steel bracing systems in the CSA S16-09 (2009) design manual. Connection zones are typically detailed as these secondary mechanisms, and provide energy dissipation through ductile behaviour in the connections including fastener fatigue. Additionally, for bracing systems that experience critical loading conditions and significant strength degradation, such as post-bucking resistance, a further reduction in compression force, $C\prime_{pr}$, must be accounted for in the connection design. This additional design requirement ensures connections are detailed to accommodate out-of-plane plastic hinging. This is typically accounted for through the design of a plastic hinge zone in the gusset plate which provides additional ductility and desired cyclic behaviour (Astaneh-Asl et al., 2006). Lastly, the capacity design concept is reinforced by designing the remaining structural elements of the lateral force resisting system to remain essentially elastic while resisting anticipated design forces through the application of force amplification factors. This force controlled design method ensures the SRFS can reach maximum performance through the fulfilment of inelastic demands while maintaining structural integrity as the major structural elements remain within the elastic range.

2.2 Steel Bracing Systems

The limited ductility associated with the buckling response of conventional steel bracing elements under compression loading is a motivating factor behind the development of advanced structural steel bracing systems (Tremblay et al., 2004). These systems have high lateral stiffnesses capable of resisting severe seismic action. The carefully designed and well detailed nonlinear fuse components offer enhanced inelastic action and exhibit consistent hysteretic performance which provides exceptional energy dissipation and ductility behaviour. Examples of these systems include buckling restrained braces (BRB), friction damping devices, and most recently

Self-Centering Energy-Dissipative (SCED) braces.

2.2.1 Buckling Restrained Braces

BRBs are a state-of-the-art earthquake force resisting systems used in modern steel structures to improve seismic performance and prevent severe structural damage. These structural bracing elements are designed and detailed to yield axially under tension and compression loading. These systems typically consist of an inner brace yielding steel plate core encased in a restraining mechanism. There are two main restraining mechanism designs that laterally support the steel core allowing it to undergo axial yielding in compression. The predominant mechanism is the concrete-filled tube design, which is comprised of a concrete or mortar infill enclosed in a hollow structural steel (HSS) section, as seen in Figure 2.6 (Tremblay et al., 2006). A low friction material is placed in the gap between the steel core and the concrete infill to prevent the concrete from bonding to the steel and to reduce surface friction. The steel HSS section prevents crushing and spalling of the concrete infill and allows the brace to withstand severe cyclic loading. An alternative to the concrete core design is the hollow steel tube restraining mechanism, shown in Figure 2.6. This all-steel system consists of steel shims, incrementally spaced along the length of the core between the brace core an external steel tube to provide additional lateral support. The inner core of both systems contains end plate details that extend out of the restraining mechanism which are heavily stiffened to prevent buckling and plastic hinging in the connection zone under severe compression loading.

Under cyclic loading, the axial resistance of BRBs is dictated by the material properties of the steel core and the confining characteristics of the restraining mechanism. Since the brace core is designed to initiate plastic behaviour at the seismic design forces, factored axial resistance for tension, T_r and compression, C_r, presented in equation (2.3), must equal the anticipated brace forces (CSA S16, 2009):

$$T_r = C_r = \phi A_{sc} F_y \tag{2.3}$$

where A_{sc} i the cross-sectional area of the steel core, F_y is the yield strength of the steel core and ϕ

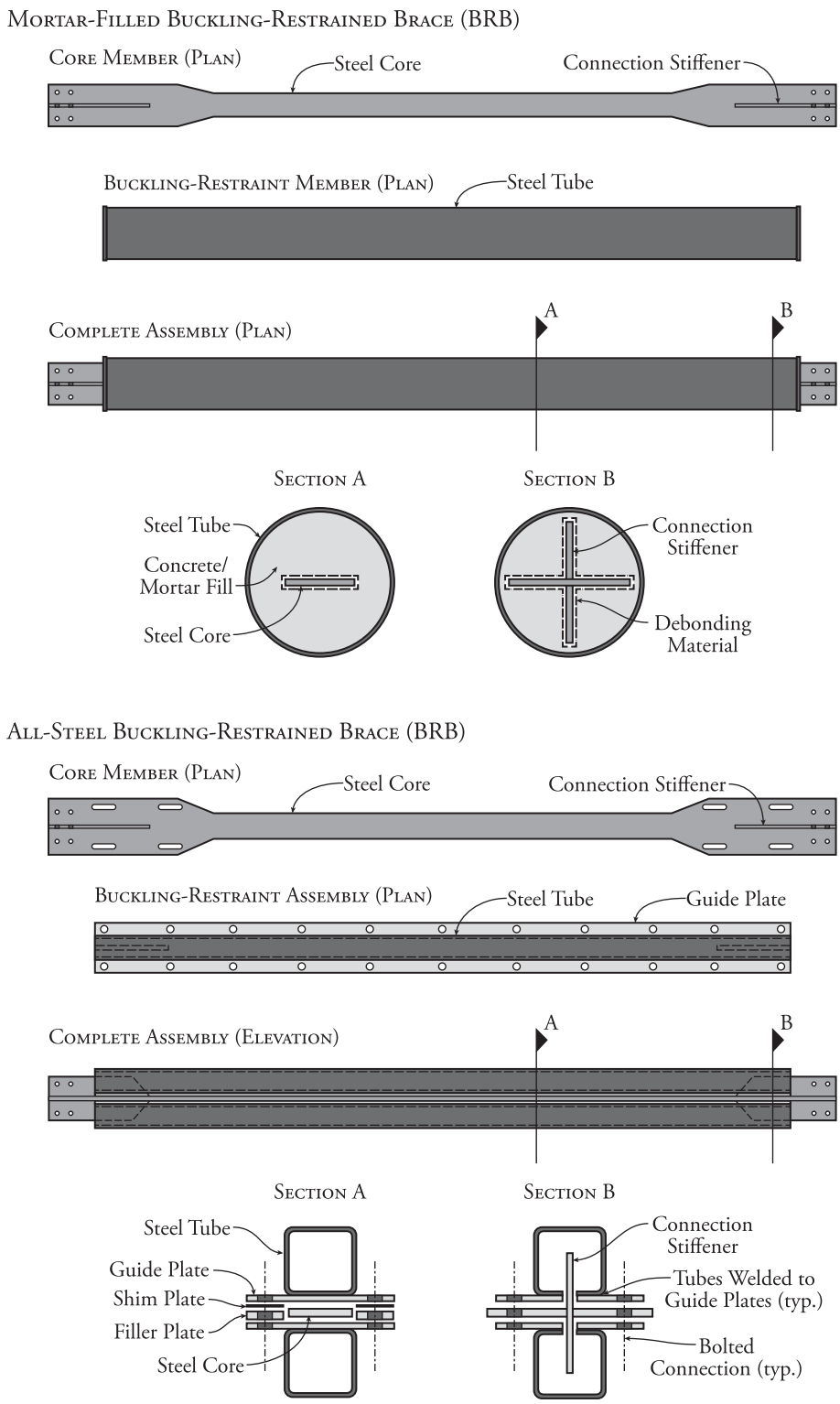

Figure 2.6: Buckling Restrained Brace Configurations (Erochko 2013)

is the resistance modification factor taken as 0.9, based on CSA S16-09 (2009) specifications. This design assumes axial yielding will govern the inelastic response of the BRBs under both loading directions. As the brace is loaded in tension the inner steel core yields axially to satisfy ductility demands. Typical of steel, strain-hardening characteristics increase the brace resistance within the plastic range to provide additional overstrength during severe seismic loading. Upon load reversal, the plastic deformations due to tensile yielding in the core is overcome as compressive forces develop in the brace. In the first stage of plastic action under compressive loading, the core experiences local buckling and axial yielding as the core begins to cripple within the restraining system. As excessive compressive loads are developed, the inner steel core continues to experience severe localized buckling that causes the steel core to rub against the restraining mechanism. This behaviour generates surface friction and provides additional axial resistance. Finally, with the beginning of another load cycle, tension forces straighten the core and axial yielding occurs at a lower force level than the previous cycle (Tremblay et al., 2004). This force progression is depicted in Figure 2.7.

The probabilistic tension and compression forces, T_{pr} and C_{pr}, must be determined due to the increase in brace resistance caused by inelastic action. These force calculations are part of the CSA S16-09 (2009) BRB design method and ensure designers can accurately anticipate the maximum brace forces.

$$T_{pr} = \omega A_{sc} R_y F_y \tag{2.4}$$

$$C_{pr} = \beta \omega A_{sc} R_y F_y \tag{2.5}$$

These force projections are used in the capacity design of the brace connections and remaining structural elements. The factor ω accounts for the strain-hardening behaviour that occurs in both tension and compression. Whereas the contribution of axial resistance provided by friction and local buckling under compression, accounted for in the factor β. R_y is a material strength factor that accounts for variability in the yield strength of the core material. This factor can be omitted from the equation if the yield stress, F_y, is determined from coupon testing (Filiatrault

et al. 2013). Because of the complex interaction between the core and restraining mechanism, buckling restrained braces are sensitive to fabrication methods and tolerances. Therefore, the performances of these systems are subject to material behaviour testing to quantify the strength, strain-hardening, and friction characteristics.

The cyclic response characteristics of buckling restrained brace frames (BRBFs) have been numerically and experimentally researched to analyse the seismic behaviour of these systems. BRBs have high ductility and energy dissipation capabilities due to the high inelastic action of the axial yielding system. The experimental work presented by Fahnestock et al. (2007), studying the seismic performance of a multi-storey mortar-filled BRBF, found peak and average maximum ductility demands of 26.0 and 19.9 respectively. The ductility response of the upper storeys were limited due to the high inelastic response of the first and second storey braces, which accounted for the majority of the energy dissipation during the test. This high plastic action in the bottom storeys is partially attributed to the concentrated gravity loads in these levels. The test frame experienced significant peak residual storey drifts of 1.3 and 2.7% at the DBE and MCE hazard levels respectively. Their study showed that the susceptibility of BRBs to permanent deformations that result in residual drifts is a drawback of these bracing systems. The DBE and MCE hazards resulted in overstrength factors of 1.35 and 1.51 during tension loading and 1.43 and 1.74 for compression. Additionally, in this study the highest β factor, determined from the ratios between the maximum tension and compression forces, was found to be 1.21. This factor is consistent with supporting research that has shown that the increase in compressive resistance can be as high as 35% greater than the tensile capacity of a BRB (Della Corte et al. 2011).

Even though the majority of the plastic action occurred within the brace core of a BRB, the strength and overall earthquake performance of BRBFs can be influenced by the additional structural components of the frame. Buckling failure in the gusset plates has been shown to impair the seismic performance of BRBFs preventing the braces from reaching their maximum ductility and energy dissipating capacities (Tsai and Hsiao 2008). Additionally, the high rotational demands within the gusset-to-brace connection imparts additional loading on the system that further impacts the performance (Tsai and Hsiao 2008). The use of true-pin connections has

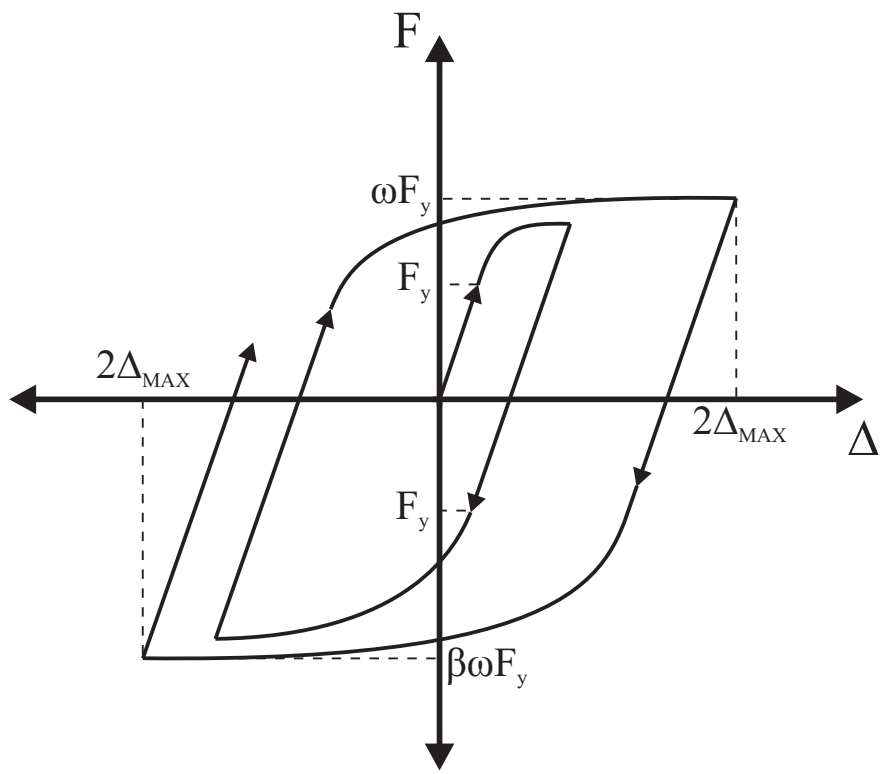

Figure 2.7: Idealized BRB Cyclic Load Progression

been suggested by Fahnestock et al. (2007) to prevent the localized buckling failure and plastic hinging in the connection regions.

BRBFs provide enhanced seismic behaviour compared to concentrically braced frame (CBF) systems containing conventional steel braces. The nonlinear dynamic analysis and seismic response comparison conducted by Tremblay et al. (2004) evaluated the behaviour of two 3-storey structures containing BRBFs and CBFs. The BRBF and CBF models were calibrated based on prototype test results to accurately capture the hysteretic response characteristics of the two systems. The storey drift in the first floor of the BRBF and CBF were similar; however, the CBF experience significantly higher frame forces due to the severe drop in post-buckling resistance associated with these systems. The BRBF experienced slightly higher lateral displacements overall when compared to the CBF, however, this behaviour can be reduced through the detailing of smaller core lengths (Tremblay et al 2004). Additionally, both frames had higher peak storey drifts in the first floor than anticipated, which could be accounted for when considering

displacement amplification due to P-delta effects.

In an attempt to provide supplementary self-centering behaviour and reduce residual drifts, Miller (2011) adapted shape memory alloy (SMA) rods into bucking restrained braces. Varying yielding core configurations were tested to determine the effect of core stiffness on self-centering capabilities of the modified BRB specimens. The finding showed that the specimen containing a stiff bracing core was not able to fully center upon load reversal during each cycle, due to the permanent deformations and overstrength characteristics within the BRB core. The second test specimen, designed with a weak core, exhibited close to optimal centering characteristics under cyclic loading. This insight into the seismic performance of BRBs containing self-centering mechanisms could improve the seismic performance of BRBs through the reduction of residual drifts.

2.2.2 Friction Damping Devices

Currently, a wide variety of friction devices have been researched for seismic bracing and moment resisting applications for use in modern steel structures (Duff 1999; Butterworth 2000; Latour et al. 2013 & Borzouie et al. 2015). Where conventional bracing systems rely on inelastic material behaviour, friction damping devices utilize surface friction to dissipate seismic energy and satisfy ductility demands. These advanced friction bracing devices can be adapted in a variety of brace configurations to efficiently resist severe ground motions. The surface friction is developed as two or more friction interfaces slide relative to each other under an applied normal force. The normal force is typically provided by high strength pre-tensioned bolts, and the sliding action is accommodated through the use of slotted bolt holes. Figure 2.8 presents a typical friction device detail. Since these supplemental damping devices do not rely on material yielding, they have the potential to provide reliable energy dissipation and optimal seismic performance even if exposed to multiple seismic events. In addition to being used as primary energy dissipation mechanisms in SFRS, friction devices have been detailed as secondary fuse elements in connection zones to provide supplementary damping during severe ground motions (Erochko 2013).

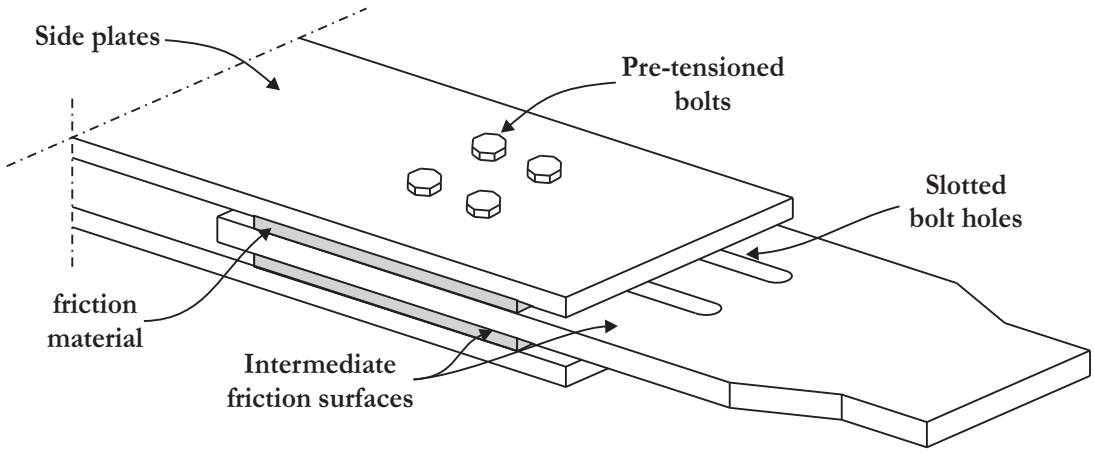

Figure 2.8: Detail of Friction Damping Devices

The friction force behaviour is dependent on the interface materials which can vary the static and dynamic friction responses of these devices. Three factors affect the contact area of friction devices that influence the system's overall performance. First, adhesion between the interface materials, influenced by the actual contact area and the governing shear strength of the base materials, can increase the static friction force (Christopoulos and Filiatrault 2006). This results from an increase in contact area as asperities lock against one another. However, this affect can be reduced through the application of high normal forces which distort deficiencies in the contact surfaces. Second, ploughing effect, caused by imperfections in the friction surfaces, can create asperities and gouging which increases surface roughness and contributes to stick-slip behaviour (Christopoulos and Filiatrault 2006). Last, the effects caused by foreign bodies, that limits friction through the reduction in contact area, is challenging to quantify. However, effects such as rolling friction, can occur as the particles isolate the friction surfaces and facilitate sliding (Christopoulos and Filiatrault 2006). The sliding velocity can directly influence the static and dynamic characteristics of the friction interface. At low velocities, the coefficient of friction is reduced due to the friction behaviour being defined by the shear resistance of a thin film that forms as a result of oxygenation of the friction surfaces (Christopoulos and Filiatrault 2006). However, as sliding velocity is increased, the friction behaviour is characterised by the interaction between the base materials of the friction interface and the formation of debris that increases the friction resistance of the assembly up to a maximum velocity (Christopoulos and Filiatrault

2006). As sliding velocity continues to increase, higher surface temperature causes softening of the asperities and localized melting in the softer friction surface. This behaviour reduces the shear strength of the interface the friction resistance of the assembly (Christopoulos and Filiatrault 2006). However, the distribution of dynamic resistance can be influenced by variations in the applied normal force, as the friction coefficient can decrease with increases in the applied normal force at high velocities (Christopoulos and Filiatrault 2006). Lastly, friction devices can be affected by time dependant characteristics, such as surface deterioration and corrosion, that can occur because of extended periods of time between loading and exposure to contaminants (Christopoulos and Filiatrault 2006).

Investigation into the cyclic response of multiple surface materials to quantify friction coefficients and evaluated damping characteristics was conducted by Latour et al. (2014). The authors determined that the friction material strongly influences the activation force and stability of the dynamic friction response. The steel-on-steel friction assembly had an unstable hysteretic response that exhibited a sharp increase in the dynamic friction force during the first ten cycles followed by a steady decline in active friction resistance during the subsequent 20 cycles. The brass-steel specimens had a more stable response with a predictably lower activation force when compared to the steel-steel assembly due to the significantly lower coefficient of static friction. The static friction coefficients, determined from the initial cyclic tests for the two systems, were approximately 0.17 and 0.1 for the steel-steel and brass-steel assemblies respectively. However, these coefficients increased significantly throughout the course of the subsequent cyclic tests. Generally, brass-to-steel interfaces are favoured over steel-to-steel friction assemblies due to the stability in the hysteretic behaviour (Duff 1999 & Latour et al. 2014).

For seismic applications utilizing friction braces, the slip force (or static friction force) of the system is equal to the anticipated seismic brace force. As the brace force increases past the initial resistance, the friction interface will activate and slippage occurs. After activation, the resistance in the brace is limited to the dynamic friction force of the system. The stability of the dynamic friction force is dependent on the friction properties of the interface materials. Friction behaviour, that is not influenced by moderate sliding velocities, ensures stability in the siding resistance (Christopoulos and Filiatrault 2006). The ideal cyclic response of the friction interface

as it has been described, is illustrated in Figure 2.9.

The theoretical static and dynamic friction forces are dependant on material surface characteristics and the friction device geometry. The following equations defined the static friction, F_{Static}, and dynamic friction, $F_{Dynamic}$, resistances of bolted friction devices:

$$F_{Static} = \mu_s n_b n_s F_N \tag{2.6}$$

$$F_{Dynamic} = \mu_d n_b n_s F_N \tag{2.7}$$

where, μ_s and μ_d are the static and dynamic friction coefficients, n_b is the number of pre-tensioned bolts contributing to the applied normal force, n_s is the number of contact friction surfaces, F_N is the individual normal force in each pre-tensioned bolt. With respect to seismic design applications, the static friction force of the device is calibrated to the anticipated seismic brace force determined through the applicable code specified analyses. This ensures the device provides the desired lateral resistance and subsequent inelastic action required to satisfy the ductility demands. Since friction devices do not rely on metallic yielding to satisfy inelastic demands, the stable and repetitive hysteretic behaviour of these systems provides excellent energy dissipation that requires no post-disaster maintenance. Additionally, researchers have investigated the seismic performance of friction devices coupled with self-centering mechanisms to provide efficient energy dissipation while simultaneously preventing the development of residual drift (Kim et al., 2004; Christopoulos et al., 2008 & Erochko 2013).

2.2.3 Self-Centering and Energy Dissipative Braces

Self-centering energy dissipative (SCED) brace systems developed by Christopoulos et al., (2008) and improved by Erochko (2013), are advanced structural braces that provide energy dissipation paired with self-restoring characteristics. SCED braces typically consist of an inner and outer structural steel section, energy dissipation device and pre-tensioned high strength tendons (Erochko, 2013). Energy dissipation is provided by metallic yielding elements, friction devices or supplemental dampers that activate as the two steel brace components move relative to one

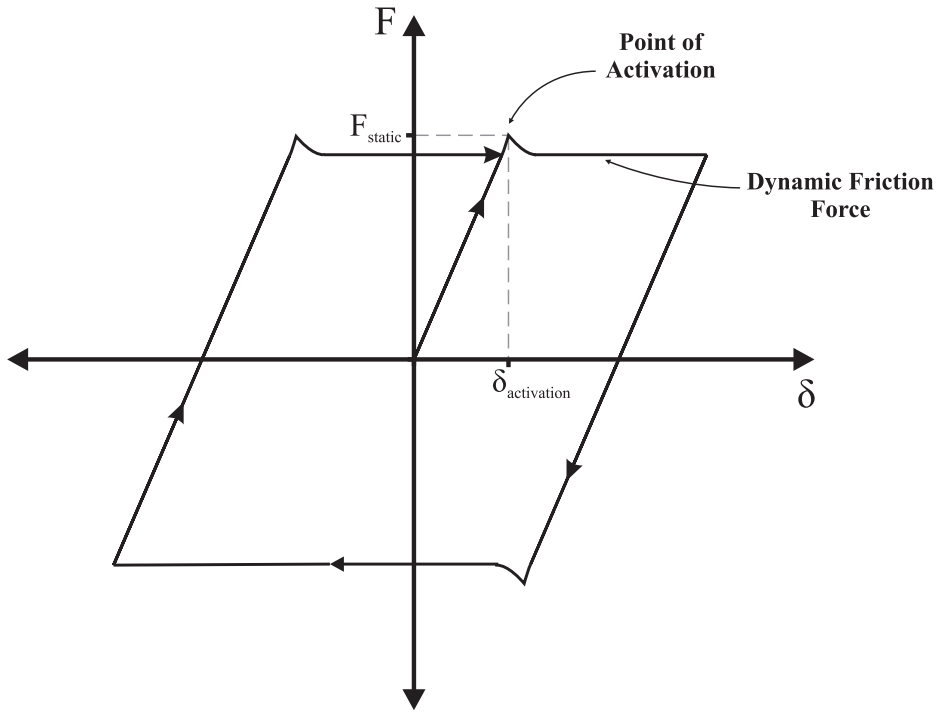

Figure 2.9: Cyclic Response of Friction Devices

another. The well detailed and easily calibrated self-centering behaviour ensures a structure passes through its center of mass during every half cycle of the hysteretic response during randomized seismic loading (Erochko 2013). This prevents residual drifts from developing which eliminates post-disaster repairs and maintenance to the seismic force resisting system and surrounding structural elements.

2.3 Seismic Design of Modern Timber Buildings

2.3.1 Strength Mechanics of Timber

The high strength-to-weight ratio and orthotropic material characteristics of wood are defined by the resilience of porous timber fibres and wood grain orientation. Tension and compression parallel-to-grain provides the greatest resistance, which allows timber sections to satisfy high axial force demands (CSA 086, 2009). Compression parallel to grain exhibits the most ductile failure through crushing of the wood fibres, making it a favourable failure mode when applying

capacity design principles to the seismic design of wood structures. The combination of these tension and compression resistance characteristics results in the high bending resistance of timber. Due to the cellular structure of wood, structural members can develop high bearing resistance, which is dependent on the compression perpendicular to grain strength, effective bearing area, the bearing size factor and the length of bearing factor (CSA O86, 2009). Furthermore, timber sections, such as bending members or laterally loaded columns, are susceptible to longitudinal shear failure mechanisms that must be considered in the design (Faherty and Williamson 1995). The weakest mechanical strength characteristic of timber is tension perpendicular to grain that leaves connection zones susceptible to splitting and brittle failure.

Duration of loading (DOL) effects can influence timber strength with an increase in factored resistance of 15% under short duration loading and a decrease of 35% for long term loads. The increase in short term strength is attributed to fibre resilience, which prevents rapid force transfer through the timber fibres (Faherty and Williamson 1995). The phenomenon can be utilized in the design of earthquake resistant heavy timber buildings to effectively limit timber member sizes in the SFRS. The decrease in long-term strength is attributed to creep effects that cause relaxation in the wood fibre.

Ambient moisture and moisture content are other factors capable of reducing the strength characteristics of wood. The moisture content of timber is dependent on the saturation water content that is characterized by the amount of water bonded within the cell walls. The time dependant process of bonded water variation induces dimensional changes in timber elements due to the environmental conditions and the mechano-sorptive characteristics of the wood (Kiwelu 2013). This shrinking and swelling can cause crack propagation due to the development of tension perpendicular to grain stresses in rigid connection zones where the wood is restrained. Structural engineers are required to employ careful considerations when detailing timber connections to account for moisture effects.

The orthotropic properties of timber pose challenges when designing seismic force resisting systems, due to the potential for brittle failure modes such as tension perpendicular-to-grain. Therefore, designers must place emphasis on transferring seismic force into strong resistance mechanisms, such as tension and compression parallel-to-grain, as well as flexural bending.

2.3.2 Current Seismic Force Resisting Systems

The high strength-to-weight ratio of wood provides structural engineers with the ability to design light, resilient timber buildings. This characteristic can provide a significant reduction in seismic forces for timber buildings compared to steel or concrete structures (Lam et al., 2015). However, due to brittle strength characteristics which result in limited ductility, current seismic force resisting systems in wood structures rely primarily on bearing failure in the wood, connection yielding, and fastener fatigue to provide energy dissipation (Andreolli et al., 2011). These failure modes have limited ductility and experience significant strength degradation impacting the seismic performance of timber structures subjected to long duration ground motions.

Currently, light frame wood buildings are designed with sheathed stud shear walls as the primary seismic force resisting system. These systems utilize a combinations of the flexural ductility of nailed connections and bearing failure in the surrounding embedment area of the sheathing to satisfy inelastic seismic demands (Andreolli et al., 2011). These connection details provide good energy dissipation under low cycle loading; however, fastener fatigue, nail withdrawal and timber bearing fatigue has the potential to limit the resistance of high-rise light frame structures subjected to extreme seismic action. Therefore, the Canadian Timber Design Manual (CSA O86 2009) outlines the specifications pertaining to fastener size, minimum embedment length, sheathing thickness, and fastener spacing to ensure the adequate lateral resistance and plastic behaviour of light frame shear walls. The current push to design mid and high-rise buildings out of heavy timber has motivated research and development in the field of innovative timber earthquake resisting systems capable of improving the seismic performance of these structures.

2.3.2.1 Timber Moment Resisting Frames

Research into the seismic performance of moment resisting and braced timber frames has growing in popularity in recent decades. These systems contain timber structural elements and utilize traditional and advanced timber fasteners to satisfy the inelastic demand of seismic loading to overcome the low ductility characteristics of timber. Currently, timber moment resisting frames containing dowel connections are typically found in single storey heavy timber structures.

These systems contain a circular steel dowel arrangement within the beam-column connections to resisted laterally induced bending moments. The connection develops moment resistance from the summation of the individual fastener resistances acting perpendicular to the center of rotation (Bouchair et al 2007). This action limits tension perpendicular to grain stress as the load orientation changes from fastener to fastener. The resistance of the dowel fasteners can be easily calculated using the lateral yielding resistance checks presented in CSA O86 (2009). The fasteners should be detailed to prevent embedment failure in the wood and allow for ductile steel yielding in the dowels to provide maximum energy dissipation. Research conducted by Bouchair et al (2007) investigated the moment capacity of reinforced and unreinforced circular dowel connections. Splitting failure was observed in the joint zone of the unreinforced moment connection as a result of localized shear forces. The authors observed a 75% increase in moment capacity in the reinforced connection over the unreinforced joints. Therefore, self-tapping screws and side panels can be used to provide perpendicular to grain reinforcement in the connection zone to increase moment capacity and further prevent the development of brittle failure modes prior to fastener yielding (Bouchair et al., 2007). The high cost, susceptibility to splitting, and limited post-disaster connection resistance restricts the application of these systems to low rise timber buildings with relatively low gravity loads (Jamil et al., 2012).

2.3.2.2 Braced Heavy Timber Frames

Braced frames are a design alternative to light frame wood shear walls that can be utilized in the seismic design of heavy timber buildings. Though there are limited examples of timber braced frames in Canadian industry, extensive research into the seismic performance of these systems has been conducted to evaluate system behaviour and connection ductility (Popovski 2000; Popovski et al., 2002; Popovski 2003 & Popovski and Karacabeyli 2008). The force transfer mechanics of concentrically braced frames make these systems attractive when designing in timber. The axial force transfer ensures the lateral loads can be resisted in the strong parallel to grain direction of the timber element, taking advantage of inherent strength characteristics. The complex seismic performance of braced timber frames involves the efficient detailing of connection components to dissipate seismic energy while providing adequate lateral stiffness and limiting

horizontal displacements (Popovski 2000). Because the performance of these systems relies heavily on the hysteretic response of ductile fasteners, excessive lateral deflections are possible under extreme loading scenarios that inflict considerable plastic deformations in the brace connections. The low ductility and overstrength factors are presented in the NBCC (2010), characterize the limited seismic performance of braced frames in heavy timber. The ductility factors assigned are 2.0 to 1.5 for moderately ductile and limited ductility systems, while an overstrength factor of 1.5 is assigned to both system types. The ductility factors vary depending on the inelastic behaviour of the fasteners used to design the brace connections (Popovski and Karacabeyli 2008).

Timber rivets and structural bolts have been researched by Popovski (2000) as connection details in braced timber frames. This study assessed the monotonic and quasi-static cyclic behaviour of these fasteners to evaluate energy dissipation capabilities. The bolted connections consisted of a glulam bracing elements with side steel plates that loads the 9.5, 12.7 and 19 mm diameter structural bolts in double shear. The timber rivet connections contained groups of 65 mm rivets fixed to the braces through external steel plates providing single shear loading. Both connection types exhibited good energy dissipation under cyclic loading even though pinching behaviour was observed in the hysteretic responses of both configurations, as shown in Figure 2.10. The bolted connections experienced pinching in the lower cycles due to crushing in the timber surrounding the fasteners. The pinching action later developed into inelastic bending in the fasteners, providing increased energy dissipation in the later cycles. The monotonic and cyclic ductility characteristics of the bolted connections were limited, reaching a maximum ductility of 3.09 and 2.91 for the monotonic and cyclic tests respectively. Furthermore, the load bearing capacity of the bolted connections was governed by the brittle failure modes of row shear and timber splitting. The opposite connection behaviour was observed in the timber rivet connection. Pinching in the earlier cycles was attributed to yielding of the steel rivets which provided higher initial energy dissipation than the bolted connections. However, as the testing progressed plastic behaviour, due to embedment failure in the riveted connection, began to dominate the hysteretic response. The rivet connection showed favourable ductility performance ranging from 10.7 to 16 cyclic tests and 15.4 to 18 for the monotonically loaded specimens. Ultimately, the connection capacity was governed by fastener withdrawal from the wood due to excessive lateral

displacements. The high inelastic response, due to earlier onset of fastener yielding and delayed timber failure makes, the timber rivet connections preferable over bolted connections for timber bracing applications (Popovski et al. 2002). This response is especially attractive in less severe seismic loading conditions because the timber members will experience minimal structural damage protecting structural stability.

These connections have been implemented in additional shake table frame tests to evaluate the seismic response of braced timber frames containing the same bolted and timber riveted connections. Multiple full-scale single storey braced timber frame shake table tests were conducted by Popovski et al. (2003) to further investigate the dynamic performance of the bolted and riveted brace connections. The test setup consisted of diagonal glulam bracing elements attached to a laterally unstable steel frame supporting 4500 kg of inertial mass, shown in Figure 2.11. Each brace configuration contained either a single row of bolted fasteners of 9.5, 12.7 or 19 mm in diameter, or a grouped connection of 65 mm long timber rivets at each end of the brace specimen. The shake table applied a single horizontal ground acceleration time history at three amplitudes of low, moderate, and high, that contained a dominant frequency similar to the fundamental frequency of the test setup. All tests experienced maximum storey acceleration at the top of the test frame lower than the applied peak ground acceleration (PGA). This is largely a result of the inelastic response of brace connections and the localized embedment failure in the wood (Popovski et al., 2003). The greatest difference between storey acceleration and PGA was observed in the reinforced 9.5 mm bolted connections, where the connections containing 19 mm bolts exhibited the lowest amount of acceleration control. However, under high amplitude testing large reductions in storey acceleration were observed in connections that experienced substantial amounts of localized crushing in the wood due to the isolating effects produced by the damage (Popovski et al. 2003). With regards to inelastic response, the top and bottom connections experienced different plastic deformations during testing. This behaviour means the combined total ductility of timber brace connections cannot be reached during a seismic event, which contributes to the low R_d and R_o factors of braced timber frames. The hysteretic responses of all connections exhibited pitched behaviour similar to the quasi-static test results of the single bracing elements previously

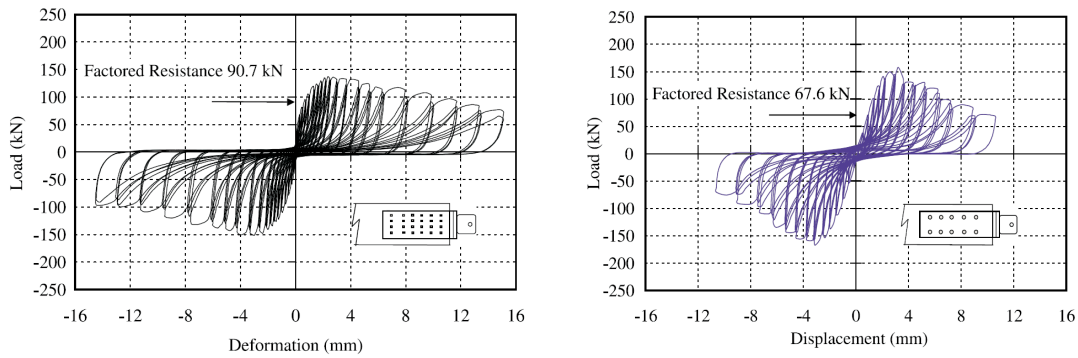

Figure 2.10: Pinching Behaviour of Braced Timber Connections
a) Timber Rivet Brace Connection b) Bolted Brace Connection
(from Popovski et al. 2002)

discussed. The initial stiffness of the timber rivet connection were almost identical to the 9.5 and 12.7 mm bolted connections. However, the riveted connections displayed the highest levels of energy dissipation with a ductility of approximately 2 to 3 times that of the bolted connections. Strength decreases of 12%, 13% and 38% were observed for the rivet, 12.7 mm and 19 mm bolted connections, respectively. The reductions in strength may be attributed to connection relaxation and excessive damage caused by impact loading due to abrupt displacement changes. The 9.5 mm diameter bolted connections experienced an increase in maximum load resistance of 13%. Visible connection failure was observed in the braces containing riveted connections as well as the 9.5 and 12.7 mm bolted connections. The authors concluded that these specimens contained the only connections that reached their maximum load bearing capacity during testing. Overall, the timber rivets and small diameter bolted connections exhibited excellent energy dissipation and high plastic deformation tolerances. Therefore, these connection types offered the best seismic performance for braced timber frame applications.

This research has provided structural engineers with the ability to safely design and implement braced timber frames. Even though the implementation of these systems is limited in North America, the UBC Earth Science Building contains an example of braced timber frames in industry. The system was designed with heavy timber glulam braces as a component of the overall lateral force resisting system within the structure. These timber braces also rely on yielding of

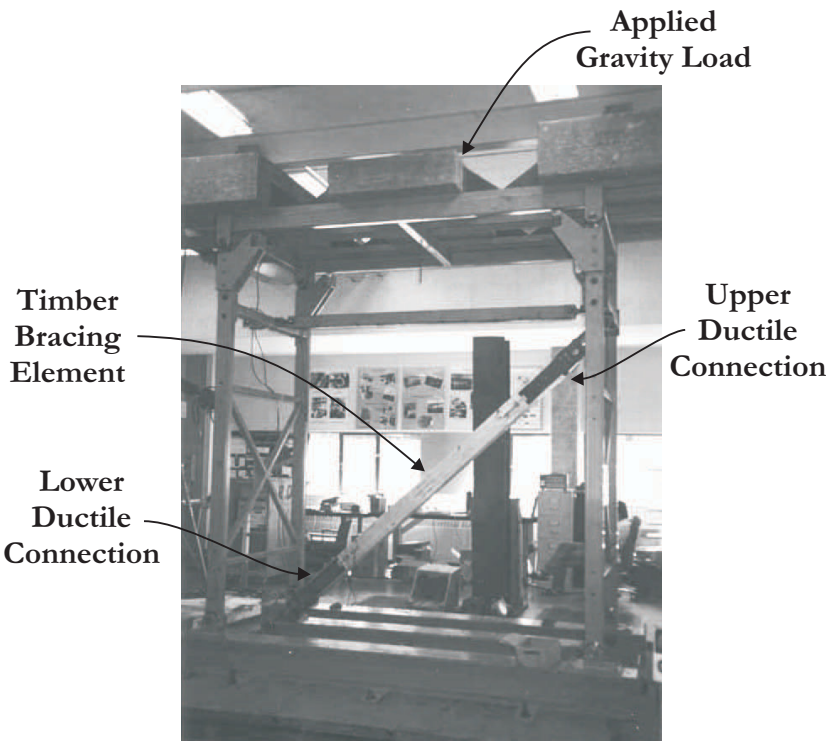

Figure 2.11: Shake Table Single-storey Braced Timber Frame Assembly (from Popovski et al. 2003)

the ductile steel dowels to dissipate seismic energy, and the glulam bracing elements are intended to remain elastic under the anticipated seismic forces. However, the low modification factors associated with braced heavy timber frames, compared to advanced steel bracing systems, limit the reduction of seismically induced forces. This prevents designers for utilizing the inherent benefits of wood, resulting in larger connections and higher building cost. This poses the question of whether it is economical to design heavy timber structures in regions of high seismic activity. These constraints could be resolved with the adaptation of advanced steel bracing systems into heavy timber building, which will be presented in this thesis.

2.4 Hybrid Timber-Steel Design

Hybrid timber design has grown in popularity as research into the adapting advanced seismic systems presents promising results for the construction of economical tall heavy timber buildings. The combined use of structural steel and heavy timber allows designers to reduce seismic design forces through the application of high ductility and overstrength factors, while utilizing the inherent benefits of wood. These hybrid structures can provide efficient solutions to the complicated problems related to the design of heavy timber structures to seismically outperform comparable advanced steel buildings (Bhat et al., 2014). A possible method for steel SFRSs is to use intermediate steel connections which replace the damage prone beam-column interface of the timber elements, shown in Figure 2.12. These ascetically pleasing joints are detailed to provide easy connection capabilities between the steel and timber sections. The ability to prefabricate these assemblies ensures workmanship while allowing for reductions in on-site construction lead time and required labour (Andreolli et al. 2011). Additionally, the use of minimally intrusive fasteners, such as glued-in rods or self-tapping screws, allows for efficient connections with enhanced fire performance and aesthetic appeal that showcases the timber elements. These connections can also be used in the design of timber structures containing concrete shear walls, anchoring the timber gravity frame to the concrete cores. In that case, the concrete system is designed to resist all imparted lateral loads while the timber frame and diaphragms accommodate lateral force transfer and support the gravity loads. Cross-laminated timber (CLT) panels are heavy timber

panel systems with high strength and in-plane stiffnesses ideal for efficient lateral force transfer (Ashtari, S. 2012). These advanced low weight prefabricated panels provide structural engineers with the opportunity to design effective diaphragms that could significantly reduce the seismic weight of timber buildings compared to structure containing concrete floor slabs or composite steel decking.

Based on capacity design principles, hybrid timber-steel connection components can be designed to resist the inelastic action and probabilistic yield forces, to ensure structural stability and satisfy global seismic performance requirements (Andreolli et al., 2011). Depending on the seismic force resisting system, the secondary failure mechanism should be selected to optimize system performance under severe seismic loading and provide additional capacity protection to the timber elements. For scenarios where the hybrid design concept is implemented to adapt advanced structural bracing systems, the gusset plate can be detailed as the addition energy dissipative mechanism to provide supplementary inelastic action. Additionally, the fasteners utilized in the timber to steel connection should be detailed to prevent brittle failure modes from developing. This requires the design engineer to consider tension perpendicular to grain loading, brittle fastener pull-out, and moisture induced failures, that may impact connection performance.

2.4.1 Advanced Hybrid Seismic-Resistant Systems

A number of studies have been conducted on the seismic performance of hybrid timber-steel moment resisting connections (Andreolli et al., 2011; Nakatani et al., 2012; Gecys and Daniunas 2013; Bhat et al., 2014; Komatsu et al., 2014 & Gecys et al., 2015). In these studies, the joints were detailed to accommodate inelastic action through flexural steel yielding or ductile connection failure. The bending capacity and internal force distribution of moment resisting hybrid joints can be analysed using strain compatibility to accurately design the fasteners and bearing interaction zones (Andreolli et al 2011). However, this method does not usually account for the variations in stiffness across connection components which could alter the load distribution.

Andreolli et al. (2011) researched the adaptation of reduced beam sections into heavy timber moment resisting frames. The authors used glued-in rod fasteners to transfer high bending

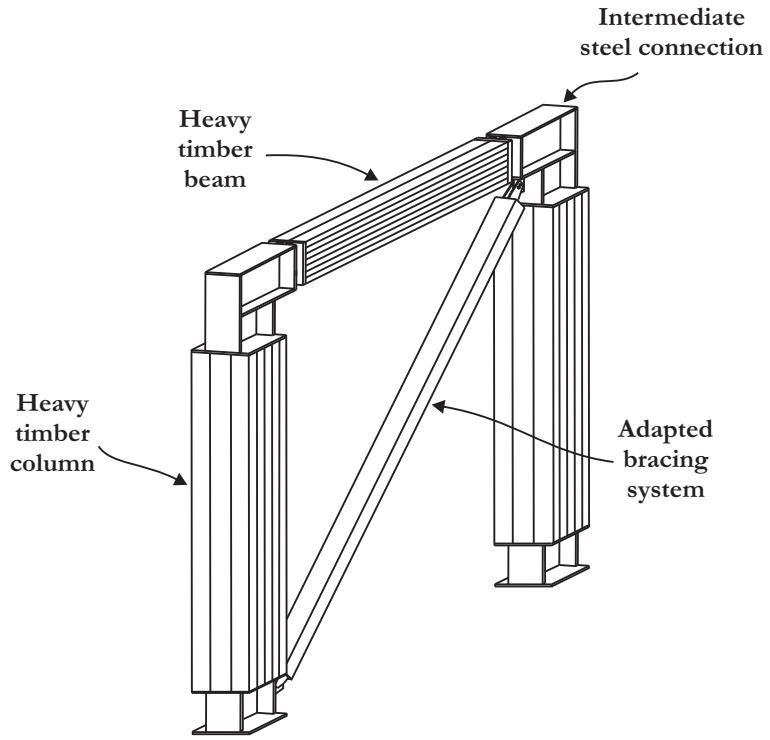

Figure 2.12: Hybrid Timber Frame Concept

induced axial forces and bonded-in perforated steel plate shear connections to provide continuous shear resistance through the hybrid steel-timber connection. End plates welded to the reduced beam sections were designed as the inelastic mechanism to dissipate earthquake input energy through flexural yielding while avoiding brittle failure modes in the fasteners and timber. These hybrid connections have good seismic performance that integrate well detailed moment resistant steel sections that also provide ascetic appeal.

Bhat et al. (2014) investigated the seismic performance of moment resistant rectangular HSS and wide flange w-section steel beams partially embedded into mass CLT panels and laterally supported by the lag bolt mechanical fasteners. The steel sections were designed as ductile coupling beams using the strong-column weak-beam design method to join the panels across wall openings. The lateral loads are transferred into the steel through bearing as the vertical timber panels rock in plane. The HSS sections provided high ductility with less strength degradation than the w-sections. Additionally, the HSS sections experienced high deformation capacity due to bearing against the CLT panels that caused plastic hinges to occur on both sides of the steel

section (Bhat et al., 2014). Overall, both systems exhibited acceptable energy dissipation capabilities, however some damage occurred in the timber panels due to localized bearing failure and fastener pull-out.

Komatsu et al. (2014) investigated the use of steel-on-steel replaceable friction devices as an energy dissipater in heavy timber moment resisting frames. The friction devices were placed at the timber beam-column interfaces and column base. These connections were tested in a two and a half storey test set-up that consisted of a single column frame containing four cantilevered beams, shown in Figure 2.13. The friction devices utilize vertically slotted bolt holes to accommodate the rotation and vertical displacement demands in the connection region. The connections were fastened to the timber sections using lagscrewbolts, which are speciality fasteners researched in Japan (Komatsu et al. 2014). These fasteners are made of large diameter lag screws that contain an internal thread designed to accommodate small diameter structural bolts. The lag screws were embedded 300 mm and 360 mm into the timber columns and beams respectively after which the steel components were joined to the wood using the structural bolts. The friction devices showed reputable energy dissipation during the lower scale loading protocols. However, during the later stages of the testing program the friction interfaces suffered abrasion damage due to the number of high cycle tests previously conducted on the system. This had a severe impact on the energy dissipation capabilities of the friction devices. Furthermore, the most severe loading protocol did cause shear failure to occur in the first storey timber panel zone. Overall, the application of friction moment resisting system provided good energy dissipation with the added benefit of replaceable friction interfaces improving post-disaster maintenance and occupancy.

As previously mentioned, the majority of braced timber frame studies have been conducted using timber bracing elements containing ductile connections. Research into the seismic performance of the hybrid timber-steel braced frames is limited. This presents a promising research opportunity into the seismic performance of advanced steel bracing systems adapted into heavy timber structures. So far, an experimental study into the behaviour of slotted friction connections has been conducted (Tjahyadi 2002). This investigation concentrated on understanding the

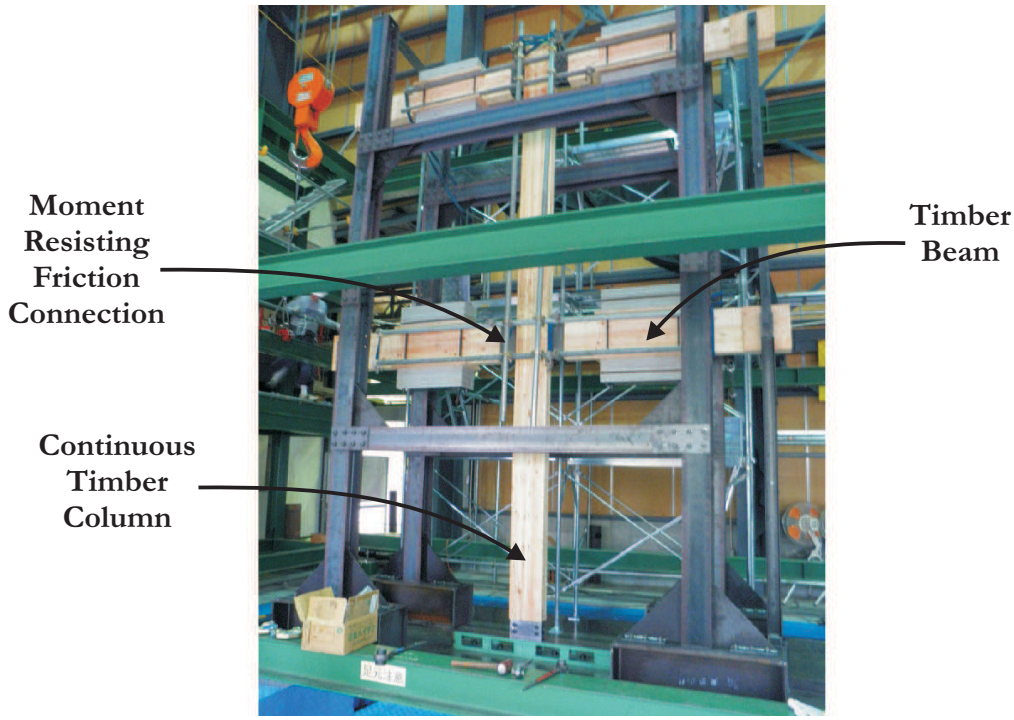

Figure 2.13: Friction Moment Resisting Hybrid Timber Frame (Modified from Komatsu et al., 2014)

application of well detailed slotted friction connections in braced heavy timber frames.

The study into the seismic performance of friction connections for braced timber frame applications was conducted by Tjahyadi (2002). The system consisted of two bolted steel-on-brass friction devices connected to a heavy timber bracing element, as shown in Figure 2.14. Slotted steel plates, located on either side of the brace, were confined between brass shims and outer steel side plates. Structural timber bolts were used to transfer the high axial forces into the timber bracing elements. The steel-on-brass interface provides energy dissipation through dynamic friction behaviour activated during cyclic loading. As the inner slotted steel plate moves relative to the outer brass shims a friction force is developed with an amplitude dependent on the applied normal force provided by the pre-tensioned steel bolts. The slip force and rectilinear coulomb's friction behaviour of these connections is predictable and easily controlled, making these systems relatively easy to design and calibrate to various force and displacement demands (Duff 1999). Additionally, a gap was left between the bracing element and beam-column joint

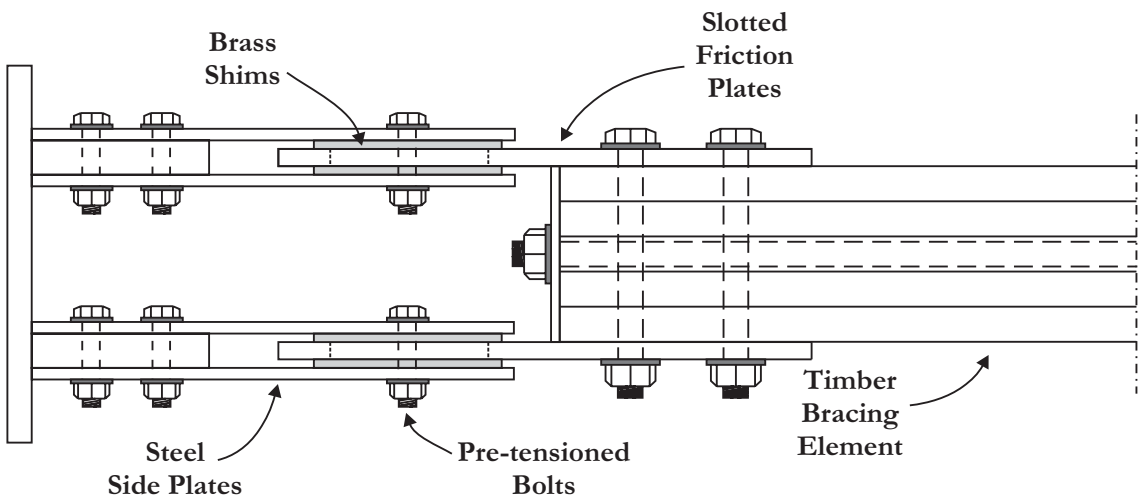

Figure 2.14: Timber Bracing Friction Connection
(Adapted from Tjahyadi et al., 2002)

to accommodate the displacement requirements of the slotted friction device. The test results showed that the friction resistance provided good energy dissipation under cyclic loading. The theoretical friction slip force was approximately 12% greater than the experimental activation force and the reasoning for this discrepancy was unclear. However, it was attributed to an over-estimation in the coefficient of friction of the steel-bass interface, the presence of debris between the friction surfaces, or a difference in the theoretical and applied normal forces. Small levels of pinching were observed in the hysteretic behaviour of the friction device due to slippage between the wood to steel connections. Based on the cyclic response, energy dissipation capabilities and lack of damage to the timber bracing elements, the author concluded that the friction devices offered excellent bracing characteristics for application in braced heavy timber frames.

2.5 Glued-in Rod Fasteners

Glued-in rod fasteners are threaded-steel or carbon fibre composite rods that are embedded into timber sections using structural grade adhesives. The minimally intrusive embedment characteristics of these fasteners provide high axial resistances and added fire protection. The main applications of glued-in rods are as axially loaded connectors between wood-to-steel and wood-to-wood structural components and to provide reinforcement perpendicular to grain in regions

of high perpendicular-to-grain stresses (Aicher, S. et al. 2008; Bengtsson, C. et al. 2002). The application of this fastener technology is limited in North America due to the absence of an approved design method in the Canadian Wood Design Manual CSA O86 (2009). However, these fasteners are currently used in the structural design of timber buildings in New Zealand, the UK, Switzerland, Germany, and Sweden (Stepinac, M. et al. 2013; Tlustochowicz et al. 2013). These fasteners have been extensively researched as a highly efficient and minimally intrusive solution to connection and retrofit design challenges. Glued-in rods optimally serve as tension parallel to grain force transfer mechanisms when designing timber connections susceptible to high axial forces. The rods transfer high tensile forces in the timber through cohesion and mechanical interlock at the rod-adhesive and timber-adhesive interfaces. The uniaxial force transfer capabilities of these fasteners prevent force development in the weak perpendicular-to-grain direction that would otherwise leave the connection vulnerable to brittle failure. There are a number of design methods, presented in past literature, which have been derived from theoretical and/or empirical studies (Stepinac et al., 2013). Large scale research projects have been conducted in recent years in an attempt to develop an accurate pull-out resistance design procedure (Bengtsson and Johansson, 2002; Connolly and Mettem, 2003). Furthermore, the complex strength characteristics of glued-in rod connections are susceptible to environmental conditions, duration of load, and fatigue effects which necessitates additional force modification factors to account for these phenomena.

2.5.1 Geometric and Mechanical Characteristics

There is much debate surrounding the geometric and mechanical characteristic that govern the pull-out resistance of glued-in rod fasteners. Extensive work has been done to evaluate the effects these characteristics have of fastener strength through the comparison of various design methodologies (Stepinac et al., 2013; Rossignon et al., 2008). According to these studies there are many geometric and mechanical characteristics that can effect the pull-out resistance of glued-in rod fasteners. However, the exact parameters that dictate connection resistance vary from study to study (Rossignon et al. 2008). The influential geometric parameters that have been previously identified are:

- Embedment length
- Rod diameter
- Embedment hole diameter
- Bond-line thickness
- Rod spacing and edge distance
- Effective area of timber
- Rod cross-sectional area
- Slenderness ratio
- Timber-adhesive interface
- Steel-adhesive interface

The mechanical properties of interest are:

- Adhesive rheological characteristic
- Adhesive grade and base compounds
- Material strength properties
- Adhesive-timber fracture energy
- Substrate interaction properties
- Adhesive shear modulus
- Wood moisture content

The strength and durability effects of the geometric and mechanical properties that impact the pull-out resistance of glued-in rod fasteners are discussed in further detail within the sections that follow.

2.5.2 Rod Types

A wide range of rod types with varying surface characteristics have been investigated to identify rod interact properties that effect the resistance of these glued-in rod connections. Rod types considered have included: fibre-reinforced polymers (FRP), threaded and smooth steel rods, and steel re-bar. Findings have concluded that the rod materials and interface characteristics do

not have a significant impact on the pull-out resistance (Serrano 2001b). However, smooth steel rods embedded with PRF adhesives should be avoided due to poor adhesion between these substrates (Serrano 2001b). Provided that ideal adhesion occurs between the adhesive and rod, the tensile capacity of the rod is the only rod specific characteristic that can govern the connection capacity. Threaded steel rods are the most versatile option of rod type when designing GIRod connections. These fasteners provide designers with the ability to detail simple yet reliable timber-timber and timber-steel connections. However, there is minimal difference between the pull-out resistances of threaded steel and FRP rods when embedded with epoxy resins (Serrano 2001b). The smooth exterior surfaces of FRP rods means surface preparation is required to improve adhesion of the bonding agent. The entire embedment length requires light sanding and cleaning with an alcohol based agent that forms a rough surface to which the adhesive can bond (Serrano 2001b). This minimally destructive procedure does not affect the cross-sectional area and therefore the tensile capacity of the rod is not affected. Additionally, FRP rods provide additional resistance to corrosion in acidic or humid environments compared to steel bars (Tannert et al. 2014).

2.5.3 Adhesive Characteristics

Structural adhesives are an important component responsible for facilitating axial force transfer in glued-in rod connections. Kemmsies (1999) conducted a study testing 12 different adhesive types to establish the most resilient adhesives for applications in glued-in rod connections. There are three main adhesive groups that have been investigated experimentally for the application of glued-in rod fasteners. These include phenolresorcinal formaldehyde (PRF), also referred to as phenolic resorcinol, two-component polyurethane (PUR) bonding agents and epoxies resins (EPR)(Bengtsson and Johansson 2002; Broughton and Hutchinson 2001; Stepinac et al., 2013). Although extensive experimental investigations have been conducted on a variety of adhesive types, 2-component PURs and EPRs are the most common adhesive types (Steiger et al 2015 and Rossignon and Espion 2008). Select grades of these adhesives have optimal strength and durability characteristics that provide high connection performance. It is important to note that bonding agents should not be selected simply by the designations PUR or EPR, because adhesive rheology

and performance characteristics can vary substantially within each category. For example, EPRs currently produced may range from ductile to very brittle depending on the chemical compounds used in the adhesive components (Feligioni et al 2003). The brittleness of the adhesive has a significant impact on the load bearing capacity of the timber-adhesive interface. A numerical finite element analysis, conducted by Serrano et al. (2001a), determined that doubling the fracture energy, which is a representation of adhesive ductility, of the adhesive layer resulted in an approximate 20% increase in pull-out resistance. Fracture energy is defined as the energy required to rupture the timber-adhesive interface represented by the area underneath the stress-displacement diagram seen in Figure 2.15 (Gustafsson 1987; Jensen et al., 2001). The energy developed in the post-fracture stage of loading is due to surface friction and mechanical interlock of the damaged timber-adhesive interface. Therefore, the tangent of the post-peak force-deformation response is used to calculate the effective fracture energy (Serrano 2001b). This method presented by Serrano (2001b) suggested the effective fracture area can be calculated by drawing a linear descending line at a tangent to the post-peak behaviour of the plastic stress-strain response to approximately 1 mm of displacement, refer to Figure 2.16. The approximate displacement of 1 mm represented the average deformation within the timber-adhesive interface required to induce shear rupture failure. Additionally, Feligioni et al. (2003) discovered that there is minimal strength correlation between brittle and ductile epoxies, with connections containing ductile EPRs having approximately twice the pull-out resistance of the brittle EPRs connections. Furthermore, the authors found that the ductile EPR exhibited a strong relationship between strength and an increase in glue-line thickness. However, the pull-out resistance of the brittle epoxy exhibited a more significant variation with increases in rod diameter. This is a clear indication of the sensitivity glued-in rod connections have to variations in geometric and mechanical properties and the complexities engineers face when designing these connections.

The findings from the GIROD Report (Bengtsson and Johansson, 2002) concluded that the following three adhesive types had increasing pull-out resistances in the subsequent order: PRFs, PURs, and EPRs. Epoxy resins are capable of a strong adhesion with both the steel and wood

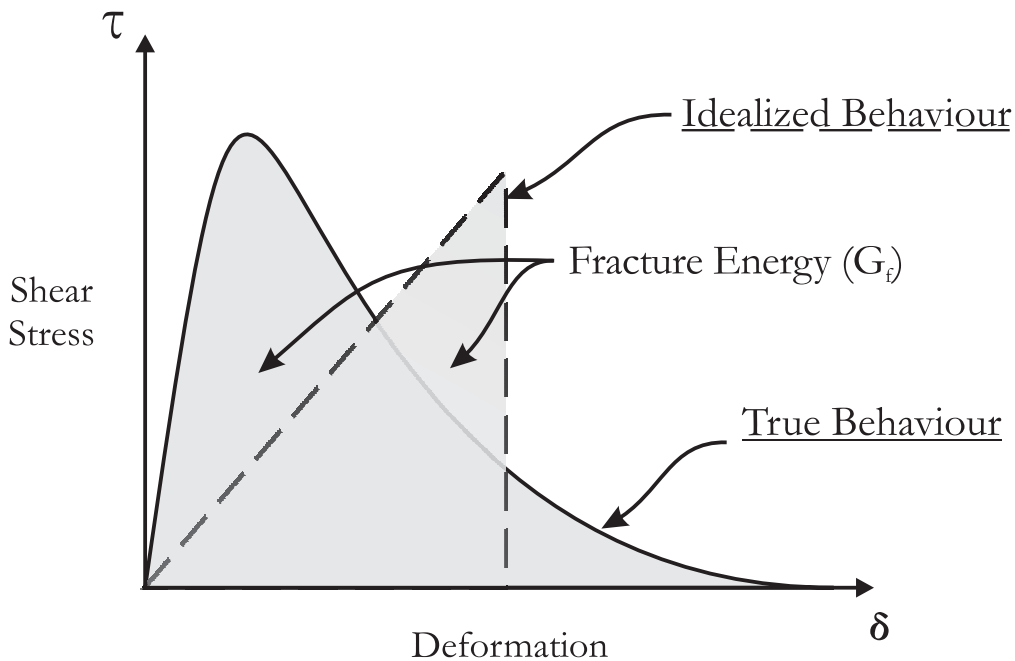

Figure 2.15: Glued-in rod Connection Fracture Energy adapted from Serrano 2001b

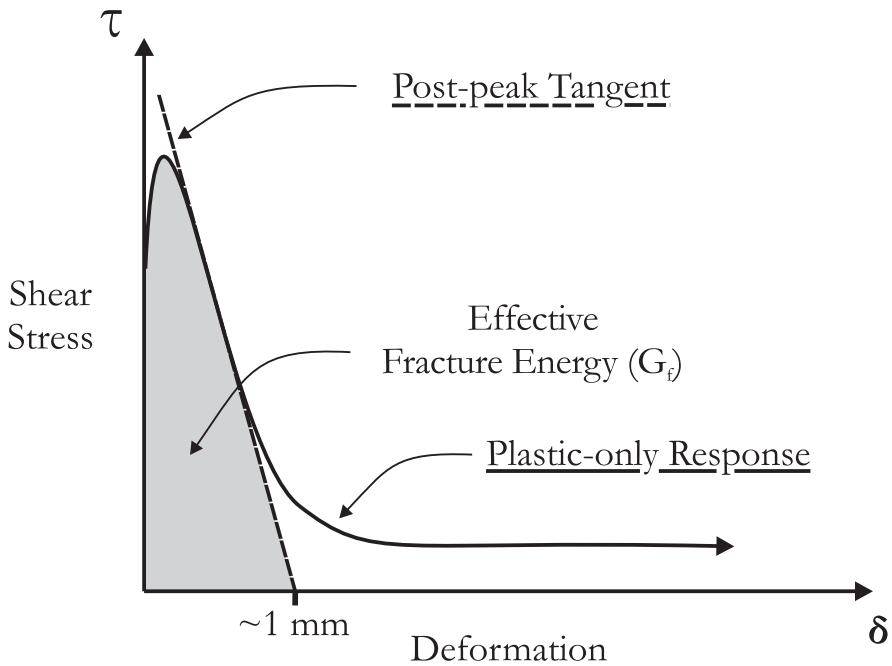

Figure 2.16: Post-Rupture Effective Fracture Energy Diagram (Serrano, 2001b)

elements, which typically means the wood is the weakest link in connections with short embedment lengths. The project also found that PRF adhesives performed poorly because the bonding agent cannot develop the required adhesion with steel rods. Therefore, it is suggested that the use of these bonding agents be limited to applications utilizing threaded steel rods (Gustafsson, 2002). In these cases the force is transferred through mechanical interlock, similar to the force transfer the threaded rod would exhibit on a nut. The PRF adhesive fills the void space between the threads and provides a bearing area onto which the force can be transferred as shown in Figure 2.17.

Adhesive viscosity is a governing factor on the development of air bubbles within the bonding agent and void space between threads. For this reason it is important that the adhesive have a low viscosity and substantial working time to ensure that the bonding agent has excellent gap filling characteristics that allow for the air bubbles to be removed prior to setting of the adhesive. Another draw back to PUR adhesives is the formation of CO_2 when exposed to moisture that is present in the air and within the timber. This foaming action can affect the structural integrity of the PUR-timber bond-line. Therefore, it is important to remove the majority of the air bubbles from the adhesive and ensure the timber is at a reasonable moisture content level prior to installation (Serrano 2001b). Additionally, the bonding agents should undergo minimal shrinkage during the curing process, to ensure a strong bond between the surrounding elements and preventing the formation of gaps between the substrates. De-lamination impacts the force transfer mechanics between the rod and timber because it is entirely facilitated by the adhesive. PRF adhesives have a tendency to shrink during curing which promotes de-lamination to occur at the rod-adhesive interaction zone (Serrano 2001 b).

Climate control and environmental conditions are factors that need to be considered during the installation and life span of GIRod connections. This includes temperature, moisture and other factors that may retard the curing process or effect connection strength. Adhesives sensitive to variations in climate conditions should be avoided, due to the potential for strength degradation and shrinkage that may form cracks in the substrate. Water absorption has been found to

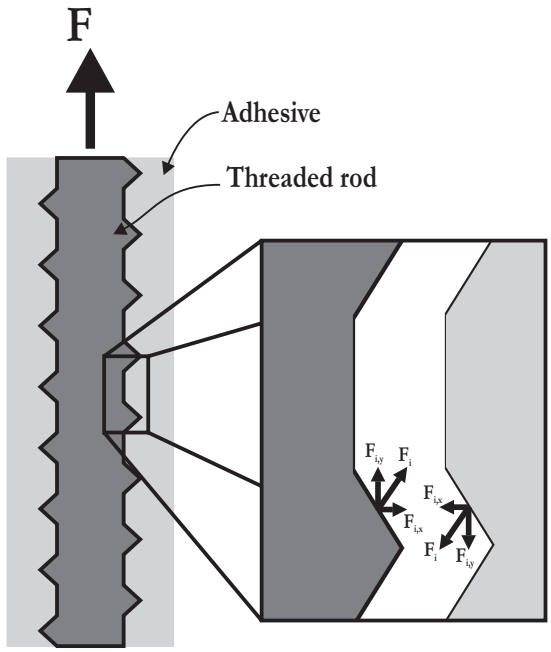

Figure 2.17: Mechanical Force Transfer in PRF Adhesives

cause adhesion breakdown, degradation in the glass transition temperature and mechanical properties of some EPR adhesives (Tlustochowicz 2011 and Hergenrother et al. 2005). Additionally, exposure to extreme temperatures can promote deterioration of the adhesive structural matrix responsible for essential mechanical characteristics (Liu et al. 2004). However, modern adhesives are less susceptible to climate conditions as more resilient bonding agents are continuously being developed. Temperature resilience is an important characteristic for fire considerations and it is imperative that adhesives exposed to extreme heat be robust to avoid strength deterioration.

2.5.4 Embedment Techniques

Centering of the glued-in rods within the embedment hole is vital to the connection compatibility and can also potentially impact on strength and durability. The centering techniques used may vary depending on the drill bit and adhesive application method selected for the embedment of fasteners. Rod centering will allow for the structural members to be easily fastened to the timber sections improving construction conditions. Furthermore, centering of the rod within the anchorage hole ensures the stress distribution along the embedment length is more

uniform due to even adhesive distribution, maximizing pull-out resistance (Serrano 2001b). Last, proper alignment will prevent prying and avoid induced moments and tension perpendicular to grain forces from developing. Various methods have been adapted for the purpose of centering GIRods. The tip of the embedded end of the rod can be turned down using a lathe to form a bead or nub. This bead is then inserted into a pre-drilled countersunk hole at the base on the anchorage length (Broughton and Hutchinson 2001). This provides an efficient technique for centering the blind end on the rod in the base of the hole. Use of a bushing, fabricated from styrofoam, scrap wood, or plastic and glued around the embedded end of the rod is another viable option (Faghani 2013). The bushings must be equal in thickness to the desired bond line and spaced evenly around the outside diameter of the rod to ensure gaps large enough to allow the adhesive to flow throughout the embedment hole. Similar to fabricated bushings, Rossignon and Espion (2008) placed internally threaded metal ring at each embedment boundary to center the glued-in rod fasteners. The upper portion of the rod can be centered relative ease because of the accessibility. The bushings and metal rings are also viable options for centering the exposed end of the rod. Additionally, end caps or centering washers can be placed in the top of the hole to guide and center the rod during installation and curing. Prior to installation, a countersunk hole is drilled in the top of the embedment hole to accommodate the centering washer. This system has the added benefit of reducing peak shear stresses that develop at the upper embedment boundary during tensile loading (Broughton and Hutchinson 2001).

There are a variety of techniques used to embed glued-in rod fasteners into timber sections regardless of grain orientation. The most basic method involves filling the embedment hole half way with the adhesive then inserting the rod into the hole (Tlustochowicz et al., 2011; Steiger et al., 2015). Once the tip on the rod has reached the adhesive a clockwise turning motion is used in combination with mild downward pressure to force the rod down through the substrate. The turning motion allows the adhesive to evenly work around the rods exterior surface or into the threads to prevent air bubbles from forming in the void space (Broughton and Hutchinson 2001). Depending on the embedment length, an extension tube can be placed on the end of the adhesive cartridge to ensure the bonding agent reaches the bottom of the hole and prevent the development of suspended air pockets. This method is shown in Figure 2.18 a). There are

two other methods that use an injection techniques which require additional holes to be drilled perpendicular to the embedment hole (Steiger et al., 2015). These techniques allow for enhanced quality control with regards to the elimination of unwanted air bubbles and improve centering of the rods (Widmann et al., 2007; Tlustochowicz et al., 2011; Steiger et al., 2015). The first method, seen in Figure 2.18 b, uses a single perpendicular injection hole. This additional hole is located close to the end of the anchorage depth, which is used for the pressurized injection of the adhesive (Widmann et al., 2007). The rod is first inserted, centered and fixed into the embedment hole, after which the bonding agent is injected into the anchorage hole through the injection port until a consistent follow of adhesive pours out the top (Rossignon and Espion 2008). It is important to ensure that the rod remains fixed in position during the injection process because the pressurized adhesive can shift the rod causing unwanted inclinations in the fasteners. The alternate injection method used for glued-in rods, shown in Figure 2.18 c), requires that two additional holes be drilled perpendicular to the embedment length. The first hole is located at the lower end on the hole base similar to the previous method. The second perpendicular hole is tapped at the desired distance from the end grain to achieve the intended embedment depth and to accommodate an end cap. The rod is then embedded, centered and fixed into the hole and the cap is snuggly fitted into the hole at the end grain (Tlustochowicz et al., 2011). The cap prevents adhesive from leaking out the top of the embedment hole and ensures the rod remains centered at the top (Rossignon and Espion 2008; Steiger et al., 2015). The pressurized bonding agent is injected into one of the two injection holes and the flow continues until a consistent stream of adhesive exits the effluent hole free of air bubbles (Steiger et al., 2015). After the injection process is completed, the perpendicular holes can be caped to ensure the bond line remains pressurized and undisturbed during the curing process. The pressurization will limit boundary condition effects that can impact the bond line strength (Serrano 2001). These three methods can also be used to embed rods both parallel and perpendicular to the longitudinal grain direction.

Embedment quality parameters are important to provide manufactures and designers with the acceptable criteria required for the design and construction of connections and reinforcement applications utilizing glued-in rod fasteners. These guidelines are particularly important when

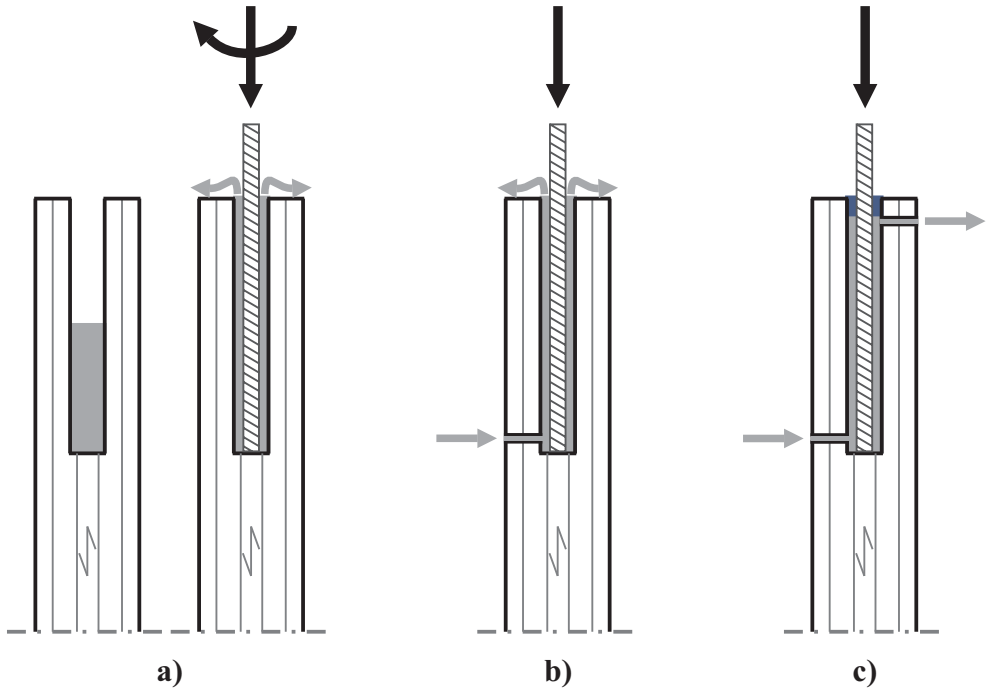

Figure 2.18: Embedment Techniques for Glued-in Rod Fasteners
(Adapted from Steiger et al., 2015)

these fasteners are intergraded into lateral force resisting systems that rely heavily on exceptional connection performance to resist intense dynamic force demands. Installation deficiencies, presented in Figure 2.19, include: the presence of trapped air bubbles with in the adhesive layer, which introduce discrepancies in the bond-line that can impact strength (a). Off-center but vertical embedment in the rod (b), due to uneven distribution of adhesive reduces the shear stress transfer area. Installation leading to rod inclination relative to the end grain (c), also known as skewing, magnifying tension perpendicular to grain stresses in the end grain responsible for splitting failure. Partial embedment of the rod limits the anchorage length of the connection, resulting in lower pull-out resistances (d). Unwanted inclination in the hole caused by deficiencies in the timber or issues with drilling (e) can lead to premature failure in the glued-in rod connection and affect connection alignment (Gardelle et al. 2006). Discrepancies in rod to grain orientation can result in variations in connection stiffness due to the combined elastic modulus of the adhesive and the stiffness characteristics of the wood (Serrano, 2001b). Additionally, the unwanted inclination can result in multi-stress scenarios where the timber is loaded in both longitudinal shear

and tension perpendicular to grain. Considering that strength characteristic of timber are directional dependant, if these two resistances vary significantly the connection capacity is affected considerably resulting in a splitting failure mode in the timber (Serrano 2001b).

Alternatively, a study conducted by Barillas (2015) investigated the impact of fabrication errors on the pull-out resistance of glued-in rod connections containing thin bond lines. This investigation excluded the impact air bubbles, caught in suspension within the adhesive bond-line, had on connection performance. The author concluded that the errors and defects associated with improper embedment of glued in rods had minimal impact on the pull-out resistance of specimens with small bond line thicknesses. However, studies have suggested that these fabrication errors could lead to premature connection failure that would limit fastener performance (Gardelle et al. 2006, Tlustochowicz et al 2011). Although, the study conducted by Barillas (2015) presents interesting results, further experimental investigation is required to determine the influence fabrication errors have on the pull-out resistance of glued-in rod connections with varying geometric and mechanical characteristics.

2.5.5 Failure Mechanisms

There are four areas of a glued-in rod connections in which failure can occur. These include the emdedded rod, structural adhesive, timber section, and timber-adhesive interface. The rod, timber and adhesive are all vulnerable to a single failure mechanism. The load bearing capacity of the rod and timber is governed by tensile resistance, where that adhesive is susceptible to shear failure. However, the timber-adhesive interface can experience multiple failure modes that depend on the relative strength characteristics of the substrates. These failure modes that govern the strength of glued-in rod fasteners are shown in Figure 2.20. For ideal connection performance, the governing failure mode should be tension yielding in the glued-in rod, since this mode provides the most ductility, shown in Figure 2.20 a). For capacity design considerations this failure mechanism offers a secondary ductile failure mode, preventing brittle failure in the adhesive and timber. Tension perpendicular to grain failure in timber at the end of the rod is common for rods embedded perpendicular to grain (Gardelle et al. 2006 and Widmann et al.,

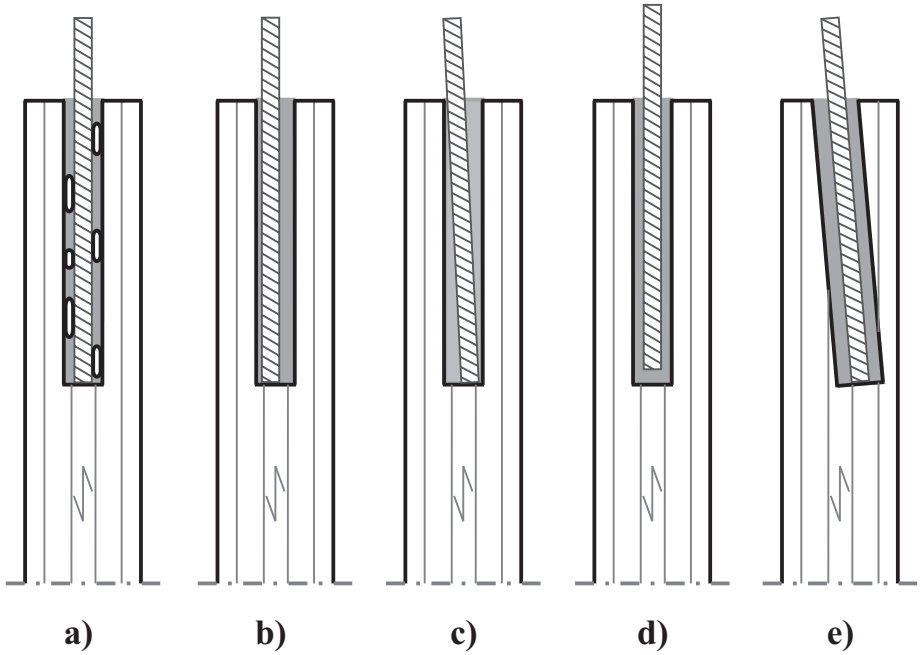

Figure 2.19: Embedment Issues for Glued-in Rod Fasteners
(Adapted from Steiger et al., 2015)

2007). However, it is not typically seen in rods loaded parallel to grain due to the high tensile capacity of the gross timber section (Gardelle et al. 2006). If strong, durable adhesives that posses adhesion characteristic compatible with both steel and timber are selected, the timber section will typically form the weakest link, resulting in this brittle failure mode (shown in Figure 2.20 b). The remaining failure modes result from failure in the rod-adhesive interface or timber-adhesive interaction zone.

Failure between the rod and adhesive (shown in Figure 2.20 d) can result from adhesive rupture, de-bonding, or a combination of the two failure mechanisms. This failure mechanism is most common for PRF adhesives largely due to their low adhesion with steel rods and shrinkage characteristics present during the curing stage (Serrano 2001b). For applications using structural grade adhesives shear failure in the adhesive bond line is rare, particularly in epoxies, due to the high tensile and shear strengths of the bonding agents.

Failure in the timber-adhesive interface is the most frequently occurring failure mechanism that dictates the tensile load capacity of glued-in rod connections. Adhesive plug failure at this interface can result from imperfect bonding between the timber and adhesive. There are two

mechanical explanations for cohesive failure within this region. First, the radial tension stresses at the exposed end of the hole can cause splitting which limits the pull-out resistance (Gardelle et al. 2006). The second is that the variation in the geometric embedment parameters, known as scaling effect, restricts the shear resistance of the timber-adhesive interface (Gardelle et al. 2006). Visual clues of failure in the timber-adhesive bond-line are present upon failure. Timber splinters can be seen adhered to the adhesive layer following rupture; however, the amount of residual timber fibres is dependent on the adhesive used and the failure plane that dictates the strength within this interaction zone (Serrano 2001b). A prepresentation of this failure mechanism is presented in Figure 2.20 c). This failure mode is characteristic of both PUR and EPR adhesives. Failure in specimens using PUR bonding agents occurs close to the wood within the adhesive layer with minimal wood fibers visible along the failure plane (Serrano 2001b). This is in part due to the chemical reactions that occur when PFRs come in contact with moisture during the curing process. However, the failure in EPR specimens occurs in the timber in close proximity to the adhesive layer, with large sections of wood fibres visible in the Epoxy (Serrano 2001b). EPR adhesives can also cause failure to occur completely in the timber section which is referred to as wood plug pull-out failure, presented in Figure 2.20 e). Wood plug pull-out occurs when the adhesive has a higher shear strength than the surrounding timber, and the plug is a result of a rupture occurring in the timber surrounding the timber-adhesive interface. This mode of failure is highly brittle and offers little visual cues prior to breaking. The strength of the connection in this mode is dependent on the mechanical properties of the wood, instead of the complex characteristics between the timber and adhesive.

Splitting is another failure mode that occurs within the timber section that is initiated at the top of the embedment hole surrounding the adhesive (Rossignon and Espino 2008). The cracks propagate outward towards the edges of the timber element and continue down the embedment length, as shown in Figure 2.20 f). Glued-in rods are especially susceptible to splitting in the wood surrounding the fasteners if the connection is improperly detailed. Splitting may be caused by insufficient edge and spacing distances, imperfections in the timber parallel to the embedment length and shrinkage caused by variations in moisture content. Splitting may also result from the development of adhesive radial tension stresses, that are transferred transversely

into the wood, and peak shear stresses that can develop at the exposed embedment boundary (Rossignon and Espion 2008 and Steiger et al. 2015). Additionally, the development of abnormal transverse shear and tension perpendicular to grain forces in the connection, due to rod misalignment and inconsistency in the adhesive substrate, increases the probability of timber splitting failures (Gardelle et al. 2006). Spacing and edge distance requirements, discussed in more detail later, required to prevent splitting also protect the connection against tensile failure in the timber as well as group tear-out. (Blass et al. 1999 and Gardelle et all 2006).

Group tear-out failure is only relevant in connections containing multiple glued-in rod fasteners. However, these connections are still susceptible to the single rod failures previously discussed. The group tear-out is a combination of longitudinal shear failure and tension rupture in the timber around a group of glued-in rods. Depending on the failure plane, this mode could also incorporate failure in the timber-adhesive interface. Figure 2.21 depicts a example of this failure mechanism.

2.5.6 Loading and Boundary Condition Effects

The boundary conditions used to load a specimen vary the pull-out resistance of the glued-in rod fastener. These loading conditions listed in order of pull-out resistance from greatest the least are pull-pull, pull-distributed, and pull-compression. The only exception to this boundary condition effect is in specimens with short embedment lengths. Under these circumstances the three setups have identical pull-out resistances because the stress distribution along the embedment is more uniform (Serrano 2001a). As the embedment length increases, the boundary conditions cause variations in shear stress distribution along the timber-adhesive interface affecting resistance behaviour.

The pull-pull boundary condition refers to a specimen with rods embedded parallel to grain at both ends of the timber that are simultaneously loaded in tension, as shown in Figure 2.22 a). The linear elastic finite model for the pull-pull loading scenario assumptions alternate displacement boundary conditions, meaning the two ends of the rod experience different displacements under loading. All of the displacement at the exposed end of the embedment hole,

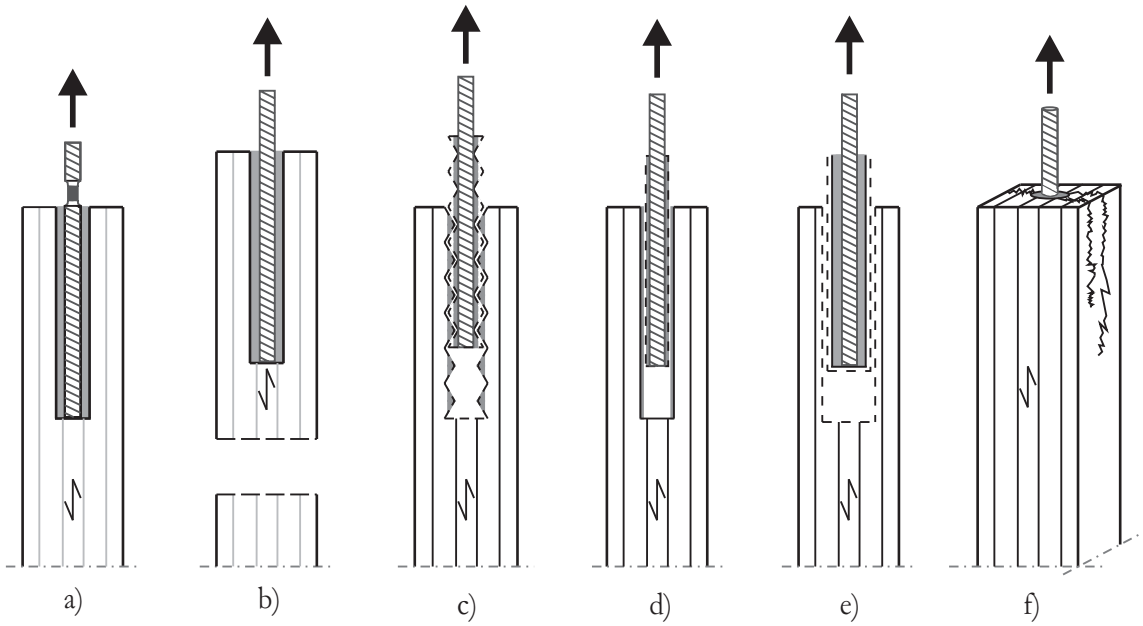

Figure 2.20: GIRods Failure Mechanisms
(Adapted from Steiger et al., 2015)

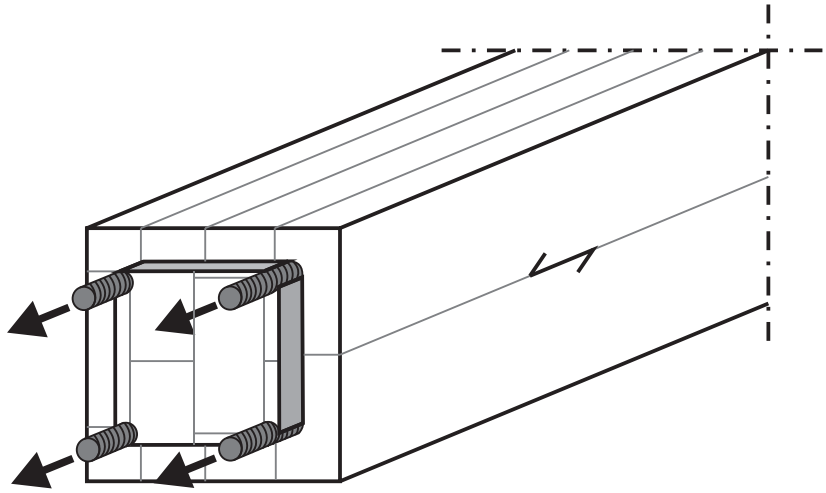

Figure 2.21: Group Tear-out Failure
(Adapted from Steiger et al., 2015)

$x = 0$, is accommodated by the rod, where all of the displacement at the embedded end, $x = l$, is experienced in the wood, as shown to Figure 2.23 a) (Jensen et al 2001). These displacement boundary conditions provide a shear stress distribution along the embedment length with stress peaks occurring at the embedment boundaries, as shown in Figure 2.24. Due to these shear stress distribution, specimens tested under pull-pull loading conditions exhibit an increase in the pull-out resistance of approximately 10-20% when compared to a specimen with pull-compression boundary conditions (Serrano 2001a).

The pull-distributed setup has a the glued-in rod connection at one end with a distributed connection that utilizes a common timber fastener, such as bolts, screws, nails, etc., at the opposite boundary of the specimen, as shown in Figure 2.22 b). The stress distribution based on non-linear fracture mechanics is slightly less uniform and pull-out resistance is noticeably weaker for specimens continuing pull-distributed boundary conditions than that of a pull-pull configuration (Gustafsson et al 2001). However, according to linear elastic fracture mechanics, as Gustafsson et al. (2001) theoretically derived, the loading criterion for pull-distributed and pull-pull is identical.

Under pull-compression boundary condition, as seen in Figure 2.22 c), the surface into which the rod is embedded is loaded in end grain bearing or compression parallel to grain. The linear elastic finite modelling displacement arguments for this boundary condition assume equal and opposite displacement behaviour during loading occurs at the exposed end, $x = 0$, in both the rod and wood components. Where there is zero displacement interaction at the embedded end of the hole at $x = l$, refer to Figure 2.23 b) (Jensen et al. 2001). The bearing stress applied around the embedment hole, in combination with the assumed displacement boundary conditions, result in a distinctly asymmetrical shear stress distribution along the anchorage length, resulting in stress concentrations at the end grain embedment boundary, $x = 0$, as shown in Figure 2.24. These stress distribution characteristics are a function of such end grin boundary constraints as embedment hole diameter and bearing plate size, that dictate the magnitude of peak stress at the embedment boundary (Broughton and Hutchinson, 2000). As stress concentrations in the end grain increase glued-in rod fasteners exhibits a greater reduction in pull-out resistance (Bengtsson et al., 2002). A numerical analysis investigation on the effect of bearing surface size on pull-out

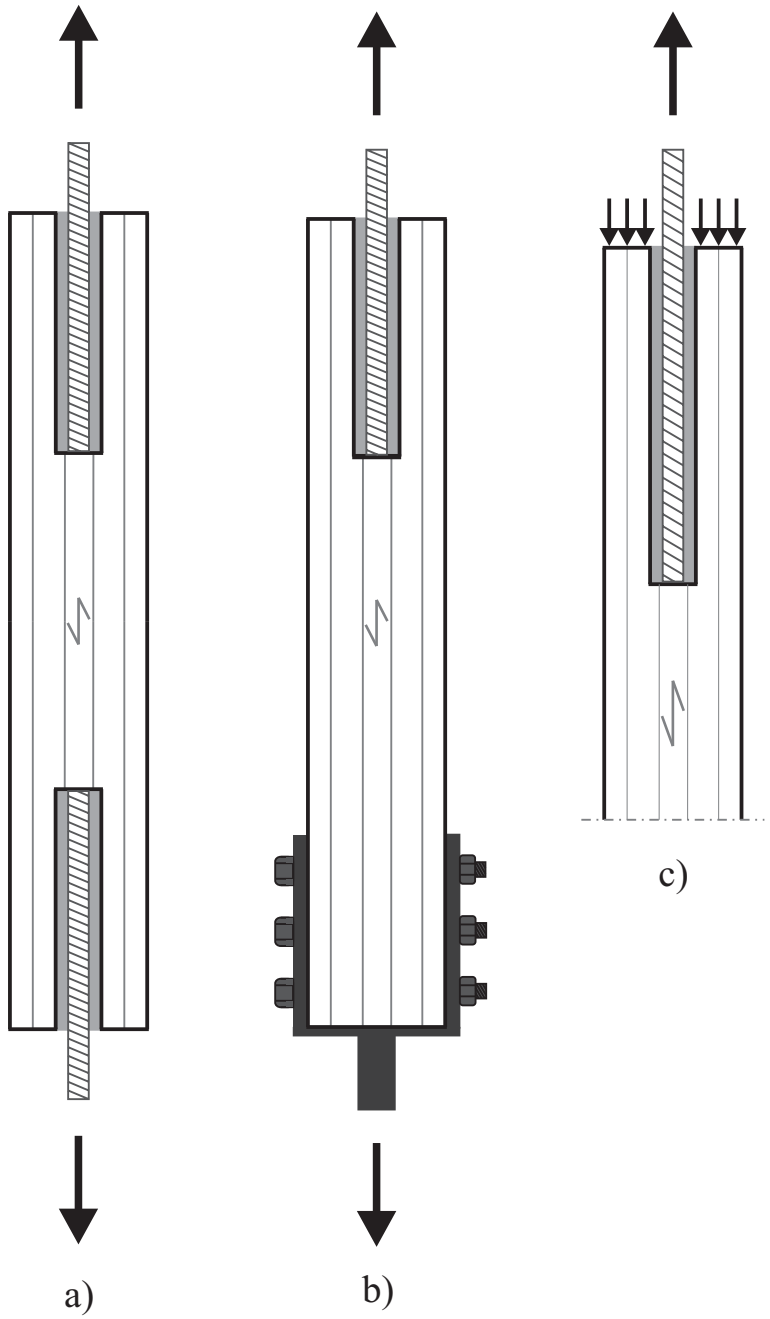

Figure 2.22: Boundary Conditions of GIRod Fasteners

resistance conducted by Serrano (2001a) showed a drop of 10% in the load bearing capacity in specimens constrained by small bearing areas.

2.5.7 Strength Characteristics Parallel to Grain

Extensive research has been conducted over the past 30 years to evaluate the strength characteristics of glued-in rod fasteners, yet there is no normalized design standard for these connections (Stepinac et al., 2013). This can be attributed to the numerous proposed strength calculations presented in the literature and the large number of geometric and mechanical factors that affect the load bearing capacity of these glued-in rods. For example, the embedment hole diameter is the factor that regulates the bond-line thickness for a set rod diameter. Research conducted by Broughton et al. (2001), Townsend (1990), and Deng (1997) found that increasing the bond-line thickness between 0.5 to 5 mm results in higher pull-out resistances. According to the LICONS Report (2003) the 1 mm bond-line shows an approximate 6% capacity increase over connections containing a 0.5 mm bond-line thickness. Furthermore, the results presented by Feligioni et al. (2003) indicate that the predominant failure mechanism changes from the typical timber-adhesive interface to the rod-adhesive interface in specimens using a ductile epoxy in combination with thick bond-lines. Lastly, the stress distributions vary along the timber-adhesive and rod-adhesive interfaces which adds a degree of complexity to the connection interaction. As previously mentioned, the stress distribution along the timber-adhesive interface is not uniform, with peaks occurring at the embedment boundary that depend on the loading scenario. Figure 2.24 shows an idealized stress distribution along the timber-adhesive interaction zone for both pull-pull and pull-compression boundary conditions. The maximum stress occurs at the exposed end of the rod-adhesive interface with negligible stress at the other embedment boundary. The timber-substrate interface area determines the stress distribution magnitude and profile of the shear stress transfer along the embedment length.

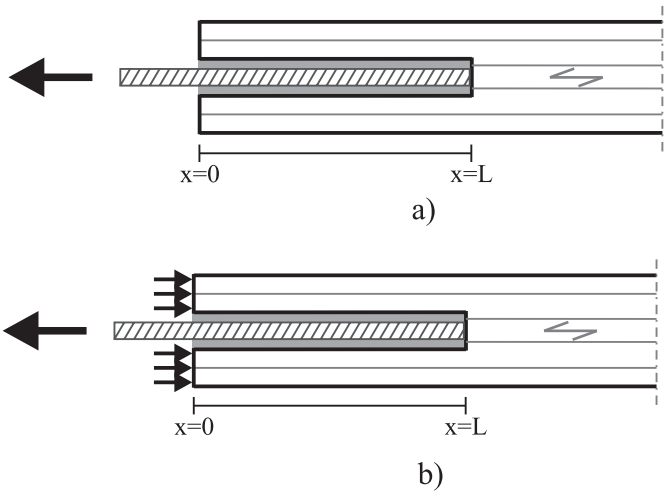

Figure 2.23: Detailed Specimen Embedment Models for GIRod Connections

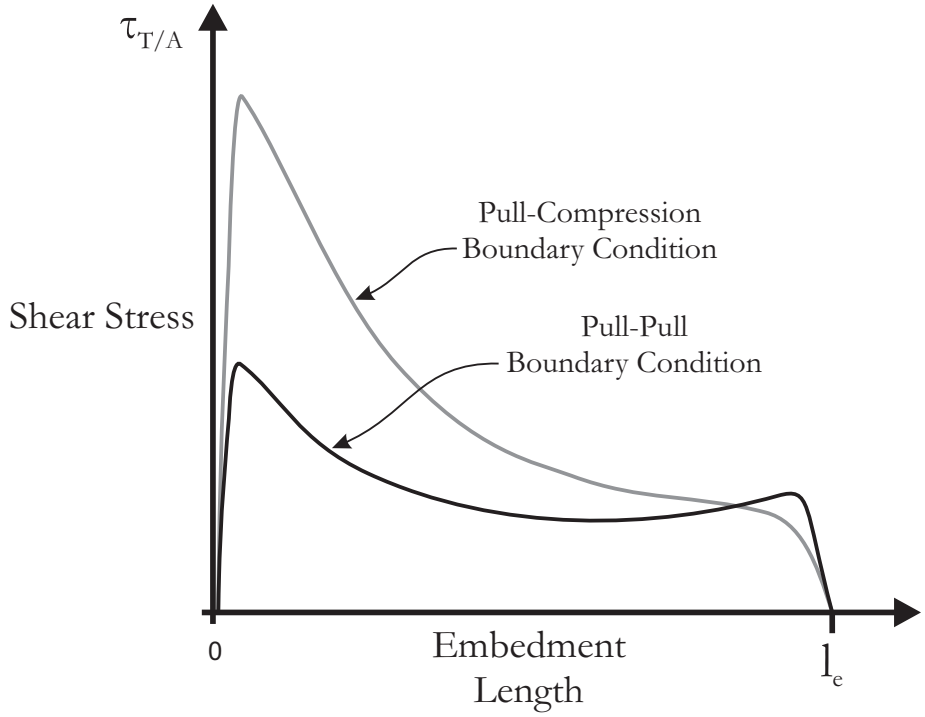

Figure 2.24: Embedment Length Shear Stress Distribution
(Adapted from Broughton and Hutchinson, 2000)

2.5.8 Axial Load Resistance

There are three main theoretical approaches that have been used in past literature to predict the pull-out behaviour and load bearing capacity of glued-in rod fasteners. These models are the traditional elasto-plastic strength analysis, linear elastic fracture mechanics, and nonlinear fracture mechanics (Tlustochowicz et al., 2011; Camino, 2015). The idealized elasto-plastic model is used to predict the stress and strain distribution along the bond-line. Failure characteristics are then applied to the stress analysis to predict the load bearing capacity and stiffness of the connection. The linear elastic fracture mechanics model analyses the energy release characteristics of the joint. The main variation to the previous traditional elasto-plastic model is the assumption that a pre-existing crack is present in the bond-line interaction zone. The resulting theoretical model requires the calculation of joint failure based on the energy release rate due to crack propagation of the bond-line (Steiger et al., 2015). The method defines failure when the strain energy within the bond-line equals the critical energy release rate of the joint (Steiger et al., 2015). The critical energy release rate is defined as the energy rate required to accommodate crack propagation in the substrate interaction zone (Steiger et al., 2015). Lastly, the unifying theory of nonlinear fracture mechanics, also known as the generalized Volkersen theory, uses a combination of the elasto-plastic model and linear elastic fracture mechanics to derive the strength and stiffness characteristics of the bonded-in rod connection (Steiger et al., 2015). The elastic perfectly plastic model assumes the fracture energy to be zero for the elastic range and infinity within the ideal plasticity behaviour. The latter assumption of infinite fracture energy must be replaced with a finite fracture energy model within the plastic region to accurately capture the rupture failure experienced in the bond-line during failure. This adapted model limits strength while introducing nonlinear softening behaviour into the bond-line and forms the basis of nonlinear fracture mechanics (Steiger et al., 2015). The assigned nonlinear behaviour can be modelled using finite element software to accurately predict the stress-strain behaviour of the bond-line and subsequent interaction zone characteristics of these connections.

The parallel to grain pull-out strength equations presented in the GIROD report (2002) are based on the generalized Volkersen theory. The theoretical derivation of the equation assumes

that the adhesive substrate acts entirely in shear, while the timber section and steel rod deform purely in tension (Gardelle and Morlier 2007). This model is theoretically sound for glued-in rod fasteners containing brittle bonding agents with thin bond-lines (Gardelle and Morlier 2007). The assumptions exemplified in the methodology ensure a subtle underestimation in the pull-out resistance regardless of the joint characteristics. This design method is widely regarded as the most reliable of the proposed methods and gives "exact" predictions of the pull-out resistance of glued-in rod connections containing thin bond lines for various adhesive rheology under pull-compression loading (Bengtsson and Johansson 2002). This equation is therefore valid for both pull-pull and pull-distributed loading scenarios due to the increase in resistance provided by these boundary conditions. The parallel to grain resistance calculation presented in the GIROD Report (2002) for pull-compression loading conditions has a asymptotic trend that limits the theoretical connection resistance for connections with large embedment lengths. This glued-in rod fasteners pull-out resistance calculation presented in equation (2.8) is defined in terms of normalized mean shear stress:

$$\frac{P_f}{\pi d_h l_a} = \tau_f \frac{\tanh \varpi}{\varpi} \tag{2.8}$$

where, P_f is the axial resistance, the embedment hole diameter is defiend by d_h , l_a in the embedment (or anchorage) length, and ϖ is the stiffness ratio of the connection defined by equations (2.9):

$$\varpi = \sqrt{\frac{l_{geo}}{l_m}} \tag{2.9}$$

where, l_{geo} is the geometric characteristic parameter and l_m is the material length parameter. The geometric characterization parameter is determined from equation (2.10):

$$l_{geo} = \frac{\pi d_h l_a^2}{2} \left(\frac{1}{A_r} + \frac{\frac{E_r}{E_w}}{A_w} \right) \tag{2.10}$$

where A_r and A_w are the cross-sectional areas of the rod and wood section, respectively, and the elastic modulus of the rod and wood are defined as E_r and E_w, respectively. Last, l_m is expressed

in terms of the elastic modulus of the rod, and the shear modulus, G_f, and shear strength of the bond-line, τ_f, using equation (2.11)).

$$l_m = \frac{E_r G_f}{\tau_f^2} \tag{2.11}$$

Therefore, by solving equation (2.8) for P_f, the pull-out resistance of the glued-in rod connection can be determined from the following equation:

$$P_f = \pi d_h l_a \tau_f \frac{\tanh \varpi}{\varpi} \tag{2.12}$$

For reasons related to mechanical and practical application, Rossignon and Espion (2008) suggest maximum anchorage length guidelines presented in equation (2.13):

$$l_{a,max} = \min \begin{cases} 25 d_r \\ 500 \text{ mm} \end{cases} \tag{2.13}$$

where, d_r is the rod diameter in mm. However this guideline can be exceeded if designers require additional anchorage length the ensure rod yielding governs the connection resistance.

Additionally, Gustafsson et al. (2001) derived the fastener resistance in terms of normalized mean shear stress for specimens loaded under pull-pull and pull-distributed boundary conditions.

Pull-pull (PP) boundary condition resistance:

$$\frac{P_{f,PP}}{\pi d_h l_a} = \tau_f \frac{\sinh(\varpi)(1+k)}{\varpi(\cosh(\varpi)+k)} \tag{2.14}$$

where, k is the ratio of the material parameters of the rod and wood defined by the following equation:

$$k = \frac{E_r A_r}{E_w A_w} \tag{2.15}$$

Pull-Distributed (PD) boundary condition resistance:

$$\frac{P_{f,PD}}{\pi d_h l_a} = \tau_f \frac{1+k}{\frac{\varpi}{\tanh \varpi} + k} \tag{2.16}$$

The stiffness of glued-in rod fasteners can be calculated by the following boundary condition dependant equations adapted from Jensen (2001). This theoretical derivation could be utilized in the numerical modelling of glued-in rod connections for structural applications such as seismic force resisting systems.

Pull-Compression (PC) Stiffness:

$$K_{PC} = \pi d_h l_a \Gamma \frac{\tanh \varpi}{\varpi} \tag{2.17}$$

Pull-Pull Stiffness:

$$K_{PP} = \pi d_h l_a \Gamma \frac{\sinh(\varpi)(1+k)}{\varpi(\cosh(\varpi)+k)} \tag{2.18}$$

Pull-Distributed Stiffness:

$$K_{PD} = \pi d_h l_a \Gamma \frac{1+k}{\frac{\varpi}{\tanh \varpi} + k} \tag{2.19}$$

where Γ is the shear stiffness factor determined from the following equation:

$$\Gamma = \frac{\tau_f^2}{2G_f} \tag{2.20}$$

A more conservative and normalized design method has been adapted as a proposed design procedure for the Eurocode for timber structures (Connolly and Mettem (2003)). This method determines strength characteristics assuming pull-compression loading in connections containing PRF adhesives and a predetermined shear strength characteristic, $f_{ax,k}$. Additionally, a generalized stiffness ratio of the connection based on PRF adhesives, ω, is presented. According to the LICONS report (2003), the axial resistance calculation should be calculated as:

$$F_{ax,Rk} = \min \begin{cases} f_{y,k} A_{ef} \\ \pi d_{equ} l_a f_{ax,k} \frac{\tanh \omega}{\omega} \end{cases} \tag{2.21}$$

where, $f_{y,k}$ is the characteristic yield strength of the steel, A_{ef} is the effective cross-sectional area of the rod, the shear strength of the connection, $f_{ax,k}$, is assumed to be 5.5 N/mm^2, d_{equ} is the equivalent diameter of the embedment hole, and the stiffness parameter ω is determined from equation (2.22).

$$\omega = \frac{0.016 * (l_a)}{\sqrt{d_{equ}}} \tag{2.22}$$

Similar to the Eurocode proposal, the German Design Code DIN 1052 (2004) defines the governing resistance of glued-in rods in terms of the minimum tensile strength of the steel rod or the pull-out resistance of the embedded fastener using the following equation:

$$R_{ax,d} = \pi d l_{ad} f_{k1,d} \tag{2.23}$$

where,

$$f_{k1,d} = \begin{cases} 4.0 & \text{if } l_{ad} \leq 250\text{mm} \\ 5.25 - 0.005 l_{ad} & \text{if } 250 > l_{ad} \leq 500\text{mm} \\ 3.5 - 0.0015 l_{ad} & \text{if } 500 > l_{ad} \leq 1000\text{mm} \end{cases} \tag{2.24}$$

In this design method $f_{k1,d}$ is the adhesion strength characteristic defined by the three embedment length ranges presented. d is the nominal rod diameter of the fastener. The embedment length of the steel rod is denoted as l_{ad}. The code criteria has established minimum embedment length requirements dependent on the rod diameter, presented below.

$$l_{ad,min} = \max \begin{cases} 0.5 d^2 \\ 10 d \end{cases} \tag{2.25}$$

Additionally, there are various other design equations that have been developed by researchers based on theoretical and empirical finds in an attempt to characterize the pull-out resistance of glued-in rods. The methods developed by Riberholt (1988), Steiger (2007) and Yeboah et al. (2013) are just some of the few that are commonly cited in research.

2.5.9 Fatigue Loading Resistance

The effect of high cycle fatigue loading is important for the design of glued-in rod fasteners exposed to dynamic loading, vibrations or long term randomized cyclic loading below the ultimate capacity of the connection such as wind loading or vehicle induced vibrations. In these loading scenarios, failure in the connection can occur at a lower force level than the static pull-out resistance presented in Section 2.5.8 due to deterioration in the rod, timber, adhesive and adhesive interfaces that govern connection resistance. The GIRod Report (2002) has presented a design method for the fatigue resistance of glued-in rod fasteners based on empirical results for two specimen configurations containing PRF, PUR and EPR adhesive types. The testing procedure subjected the test specimens to a high number of low force level cycles to establish the failure modes and fatigue resistance of the test specimens. Furthermore, the conclusions reached in terms of connection performance after 10^6 loading cycles have been extrapolated from the test results obtained from the lower loading cycles. The results showed that the specimens containing PRF experienced failure in the adhesive due to the poor high cycle rheology characteristics of the adhesive. However, the PUR and EPR connections experienced failure in the rod, timber and timber-adhesive interface. As a result of the findings an empirical equation for the fatigue strength, $f_{fat,d}$, was derived based on Eurocode 5 fatigue design principles:

$$f_{fat,d} = \frac{k_{fat} f_k}{\gamma_{M,fat}} \tag{2.26}$$

where, k_{fat} in the fatigue coefficient obtained graphically from Figure 2.25 by linear extrapolation dependant on the number of load cycles or from Table 2.1 for the maximum loading condition, $k_{fat,\infty}$. f_k in the static pull out resistance of the connection determined in equation (2.12). Lastly, $\gamma_{M,fat}$ is the Eurocode fatigue factor for material safety which is dependant on the

damage tolerance of a structure. This factor can be assigned a value of 1.0 for structures classified as damage tolerant or selected from Table 2.2 for structures intolerant to damage (Bengtsson and Johansson 2002).

2.5.10 Lateral Loading Resistance

Varying the angle between the load and the grain direction alters the failure mode demonstrated in the timber surrounded the rod (Serrano 2001b). Rods embedded perpendicular to grain induce tension perpendicular to grain stress in the timber just past the embedment plane. The theoretical investigation presented in the GIROD report (2002) and defined in equation (2.27) offers a method for determining the lateral resistance of glued-in rod connections embedded parallel to grain. This method is heavily dependent on geometric connection characteristic. Figure 2.26 represents the layout of the parameters relevant the lateral resistance calculation for multiple fastener connections.

$$R_{90,d} = 0.5k_s k_r (6.5 + (\frac{18a^2}{H^2})(t_{ef}H)^0.8 \tag{2.27}$$

where, H and B are the beam depth and width, respectively. a is the distance between the last row of fasteners at the unloaded connection edge and the beam depth, $H - a_3$, in mm, d is the nominal rod diameter, n is the number of rods in the connection, and T_{ef} is the effective member width determined from the expression:

$$T_{ef} = \min \begin{cases} B \\ 6d \end{cases} \tag{2.28}$$

Additionally,

$$k_s = \max \begin{cases} 1 \\ 0.7 + \frac{1.4a_r}{H} \end{cases} \tag{2.29}$$

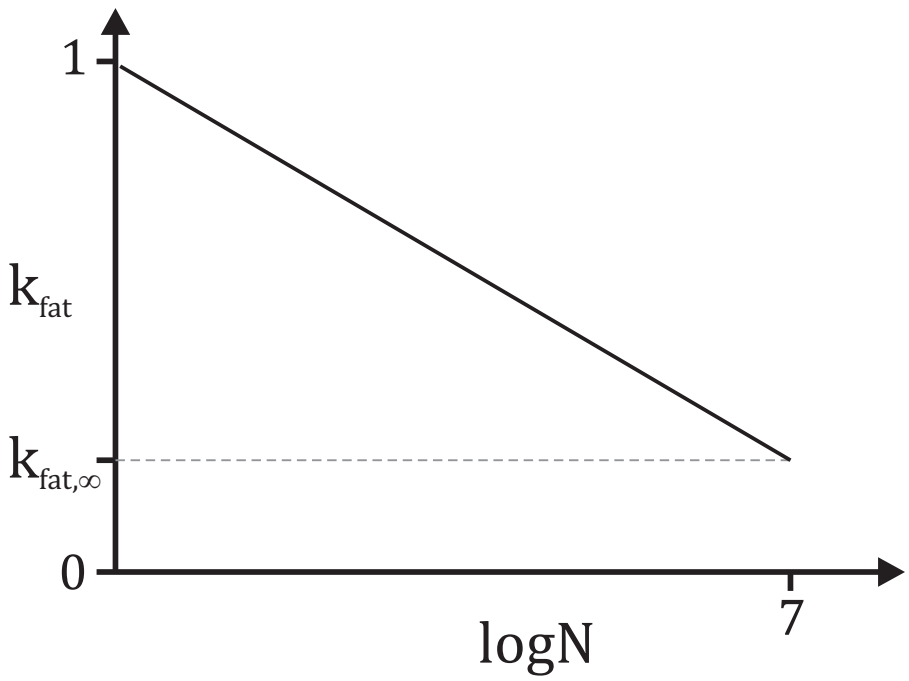

Figure 2.25: k_{fat} factor values related to number of load cycles
(Adapted from Bengtsson and Johansson, 2002)

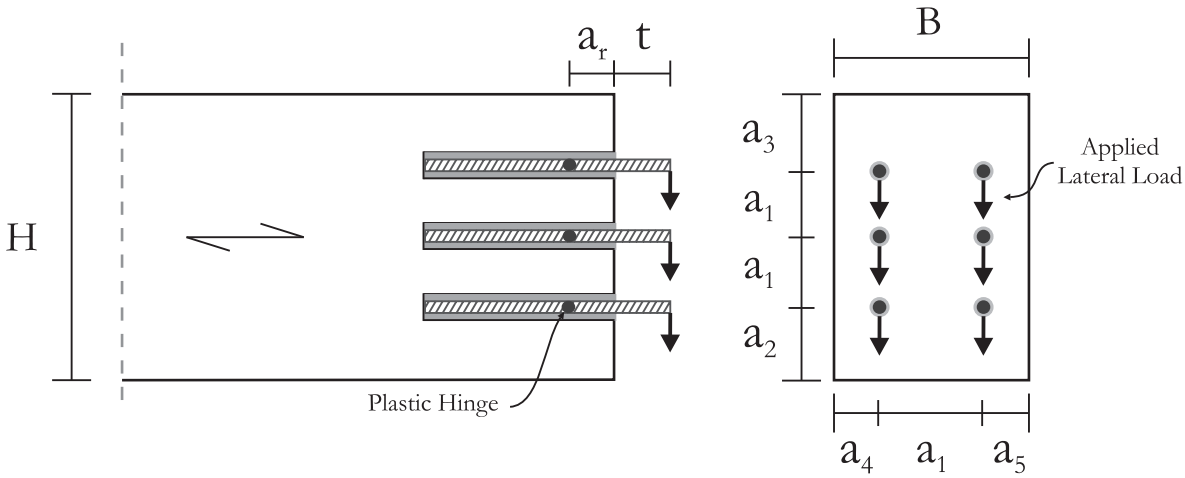

Figure 2.26: Connection Detail for Lateral Resistance
(Adapted from Bengtsson and Johansson, 2002)

Table 2.1: Ultimate Fatigue Modification Factors (Bengtsson et al. (2002))

Failure Mode	$k_{fat,\infty}$ coefficient
Failure in Timber Section	
Compression Failure	0.6
Tension Failure	0.3
Cyclic Failure (Tension-Compression)	0.3
Localized Failure in Timber	
Shear Plug Failure	0.2
Failure in the Adhesive	
Adhesive Failure	0.2
Failure in the Rod	
Steel Rod Failure (Lateral Loading)	0.25
Steel Rod Failure (Lateral Loading)	0.15

Table 2.2: $\gamma_{M,fat}$ Factors for Damage Intolerant Structures (Bengtsson et al. (2002))

Level of Inspection	$\gamma_{M,fat}$ coefficient	
	Fail Safe Joints	Non-Fail Safe Joints
Periodic Inspection, good access	1.5	2.0
Periodic Inspection, poor access	2.0	2.5
No Inspection or Maintenance	2.5	3.0

$$k_r = \frac{n}{\sum_{i=1}^{n}(\frac{h_1}{h_i})^2} \tag{2.30}$$

where, h_i is the distance from the lower edge to i^{th} rod, and a_r is distance between the plastic hinge in the rod and the end grain based on distance form the end grain to the point of loading (Bengtsson and Johansson, 2002). For scenarios where double bending is induced in the glued-in rods, the plastic hinge location is determined from the following equations:

$$a_r = -t + \sqrt{t^2 + 4(\frac{M_y}{f_{h,1}d})} \tag{2.31}$$

$$M_y = 0.26 f_u d_m^{2.7} \tag{2.32}$$

where, t is the distance form the end grain to the location of the applied load, M_y is the yield moment resistance of the rod according the the German design code DIN 1052 (2004), $f_{h,1}$ is the embedment strength of the timber determined from DIN 1052 (2004), and d_m is the average of the outer and inner rod diameters. This method does not consider the lateral load resistance of glued-in rod fasteners subjected to single action bending in the rods (Bengtsson and Johansson, 2002).

2.5.11 Spacing Requirements

Spacing requirements are a critical factor to the prevention of splitting failure caused by tension perpendicular to grain stresses in the timber members (Serrano 2001a). In the early tests conducted to determine the pull-out resistance of glued-in rod fasteners, an edge distance of $4d_r$ was used for single rod specimens (where d_r is the rod diameter) (Steiger 2007). However, more recent studies have reduced this requirement significantly as a result of the findings. Multiple research programs have been conducted to establish the minimum edge distance and spacing requirements as a factor of the rod diameter d_r (Riberholt 1988, Blass and Laskewitz 1999 and Steiger et al. 2007). The study conducted by Riberholt (1988) proposed a minimum requirement for the edge distance of $2d_r$. In addition to these findings, an investigation by Steiger et al. (2007)

was conducted to determine the effects of varying edge distances had on strength degradation in timber specimens containing glued-in rods. The authors concluded that edge distances of $2.3d_r$ and greater prevented premature splitting failure and severe losses in pull-out resistance for connections containing rods with diameters ranging from 12 to 20 mm. Additionally, the findings supported the use of this suggested spacing for connections with smaller rod diameters because the transfer of tensile stresses from the steel, through the adhesive, to the wood was optimized in specimens containing these geometric characteristics. Blass and Laskewitz (1999) conducted investigations into the effects of varying edge and spacing distances in specimens containing multiple rods with multiple connection configurations. The test was intended to determine minimum edge distance. The test specimens contained edge distances and connection spacings ranging from $1.5d_r$ to $5d_r$ and $2.5d_r$ to $6.5d_r$ respectively. The authors concluded that the load carrying capacity was reduced in specimens with edge distances less than $2.5d_r$. The second test conducted in the study by Blass and Laskewitz (1999) was intended to determine the minimum spacing requirements for glued-in rod connections containing multiple fasteners. The multiple rod specimens that had a connection spacing ranging from $2d_r$ to $3.75d_r$ experienced splitting failures as expected. However, the theoretical investigation that followed the experimental study determined that the minimum spacing requirement should be twice the edge distance requirement previously determined. Resulting in the proposed design limit for spacing of $5d_r$. Their research was conducted as part of the GIROD program (2002) which has validated and accepted these edge distance and connection spacing guidelines.

Additionally, numerical modelling and experimental research conducted by Gardelle et al. (2006) developed a method for calculating optimal edge distances, n, to prevent axial tension failure in timber sections containing glued-in rod connections. The calculations are presented as follows:

$$n = \min \begin{cases} n_b \\ n_t = 2.5d_r \end{cases} \tag{2.33}$$

Where,

$$n_b = \frac{l_a}{2} \tan \beta \tag{2.34}$$

where, l_a is the anchorage length, d_r is the rod diameter, and β is the angle between isotension curves in the timber and embedded rod based on the grade specific characteristics (Gardelle et al. 2007). This model for calculating n_b is developed from stress tensor theory for the crack propagation of reinforced concrete and ignores the effect section size has on splitting (Gardelle et al. 2007). Therefore, further experimental research is require to validate this calculation. A more conservative approach could use the maximum value of the two distance calculations to determine the governing edge distance, refer to equation (2.35).

$$n = \max \begin{cases} n_b \\ n_t = 2.5 d_r \end{cases} \tag{2.35}$$

Based on the findings presented by Gardelle et al. (2007), the spacing requirement of $2.5d_r$ determined by Blass (1999) will typically govern this check due to strength requirements that prevent the premature brittle splitting failure mode previously discussed.

2.5.12 Duration of Loading and Climate Effects

Load duration modification factors account for variations in timber strength dependant on the duration of the expected loading scenario. During long term loading, timber experiences a decrease in resistance regardless of load angle to grain, due to fibre relaxation known as creep (CSA O86 2010). The long term resistance of glued-in rod connections is believed to be dependant on multiple factors. The adhesive characteristics of the bond material can fail in creep-rupture anywhere between a few minutes to approximately 10000 hours (Bengtsson et al. 2002). In addition to creep, fastener fatigue has a noticeable impact on the strength capacity of glued-in rod connections, with shear stress dropping as much as 70% depending on the grade and type of structural adhesive used for embedment (Bengtsson et al. 2002). These two issues could pose difficulties when designing tension connections that require pre-tensioning of the glued-in rod fasteners to

prevent gaps forming between the structural elements or pounding during cyclic loading. Furthermore, this could be a problem for connections that will experience low cyclic forces during the life span of the structure resulting in fatigue failure.

The development of standardized empirical force reduction factors for load duration and service conditions for glued-in rod connections is still outstanding. Aicher and Dill-Langer (2001) investigated the effects of load duration on glued-in rod fasteners with varying adhesive types. The authors reported that the type of adhesive used had a direct impact on the long term strength performance of the connections. PRF and PUR adhesives experienced strength degradation as a result of long term loading effects, while the strength of EPR adhesive was not effected. The GIROD Project(2002) findings determined short term strength reductions of 15% in moist climates for both the PUR and PRF bonding agents. Furthermore, 13% and 23% reductions in resistance occurred in the warm climate for the PUR and PRF adhesive respectively. However, EPR adhesive connections experienced a drop in resistance similar to that of the timber. This suggests that the load duration characteristics of the timber will govern the long term performance of glued-in rod connections containing epoxies. Therefore, the pull-out resistance calculations can be used to determine the long term resistance of glued-in rod connections provided load duration and environmental factors are accounted for through force modification factor (Deng 1997). A summary of the duration of loading modification factors from the GIROD Report (2002) is presented in Table 2.3. These factors can be used to estimate the factored pull-out resistance of glued-in rod connections exposed to various climate conditions. Additionally, investigation into the long term behaviour of glued-in rod fasteners in Canadian lumber species is vital to the development of a Canadian approved design standard.

2.5.13 Fire Resistance

Adhesives, such as epoxy resins, typically degrade when exposed to temperatures that exceed the glass transition temperature, T_g, of the adhesive. Traditionally, fire retardant epoxies contain halogen additives which improve the thermal stability of the epoxy compounds by suppressing the production of volatile thermal decomposition products (Camino et al. 2005). Fire

Table 2.3: Load Duration Modification Factors Modified from Bengtsson et al. (2002)

Adhesive or Wood Type	Climate Conditions	Load Duration Modification Factor	
		Short Term 1 week (168 hr)	Medium Term 6 months (4380 hr)
PRF & PUR	Sheltered Outdoor	0.7	0.6
	Const. 85% RH	0.6	0.54
EPR	Sheltered Outdoor & Const. 85% RH	0.77	0.68
Solid Wood (Madison Curve)	Service Class 1	0.76	0.67
Solid Wood and Glulam (Eurocode 5)	Service Class 1 & 2	0.9	0.8

performance characteristics define the onset degradation temperature as the point at which deterioration in the adhesive structural matrix occurs under thermal loading conditions (Reghunadhan Nair et al., 2001). The glass transition temperature of adhesives dictates the point of severe strength degradation through the breakdown of this structural matrix, promoting a change-in-state (Liu et al. 2004). The addition of inorganic nano-composites aids in the fire retardancy of epoxy resins through the elimination of corrosive and toxic chemicals, increasing the onset degradation and glass transition temperatures, and promotion optimal charring characteristics that improves strength performance (Camino et al. 2005). These additives enhance mechanical properties in the resins through the fortification of the adhesive structural matrix (Liu et al. 2004). Fire retardant characteristics can alternatively be improved through the early onset of charring, which acts as an insulator to protect the virgin material under the burnt surface. Chemicals used to increase char yield, such as phosphorus used in EPRs, decrease the glass transition temperature and onset degradation temperatures which will affect connection strength performance (Hergenrother et al. 2005 and Jeng et al. 2002). However, some adhesives containing additives used to improve charring characteristics experience improvements in strength performance under fire loading conditions (Harrison, 1986).

A glued-in rod fire performance study conducted by Buchanan and Barber (1996) showed

single glued-in rod specimens experience minimal strength degradation when exposed the temperatures ranging for 40-45 °c. However, strength degradation ranging from 0-80% was observed within the temperature range of 45-70 °c, and between 70-90 °c the load resistance plateaued at 20% of the maximum resistance until failure. An additional study conducted by Harris (2004) observed strength degradations in the range of 20-90 kN for incremental temperature loading of 20-100 °c. Additives, used to improve adhesive fire characterises, that do not reduce the tensile and shear strength of the bonding agent are ideal for glued-in rod connections susceptible to heat exposure during structural fires. For adhesives with excellent fire performance, strength deterioration is minimal as long as the exposure temperature remains below the glass transition temperature of the adhesive (Lartigau et al. 2012). Furthermore, fire performance is an important attribute that requires a specific design considerations in order to accurately select the appropriate adhesive for these fastener applications.

Chapter 3: Hybrid Braced Frame Design and Methodology

The adaptation of advanced structural steel bracing systems into heavy timber buildings has yet to be investigated in the field of seismic design research. This research program explored the use of friction damping devices and buckling restrained braces (BRBs) in hybrid timber-steel braced frames. The overall goal of ensuring elastic behaviour in timber elements during severe seismic loading was also achieved through the application of capacity design principles. This methodology safeguards the timber elements against structural damage by preventing the development of brittle failure mechanisms. This was done primarily through the design and testing of a hybrid timber-steel brace frame prototype that utilized modern glued-in rod fastener technology. This system consisted of an intermediate steel brace connection, utilizing glued-in rod fasteners, to accommodate advanced structural steel bracing systems into hybrid timber-steel building. The hybrid timber-steel braced frame also allowed for the testing of the wood to steel glued-in rod connections under realistic loads and displacements. This hybrid timber-steel system was accomplished through the development and application of capacity and hybrid timber design methodologies. These design procedures were developed to use steel as the main energy dissipating elements while keeping the wood elements completely elastic, avoiding damage. Furthermore, the innovative hybrid timber-steel design meant that additional intensive finite element modelling of the orthotropic timber members was essential to establish the seismic performance and structural integrity of the hybrid systems.

For the experimental investigation, a friction damping brace was detailed as the primary structural fuse element used to satisfy the ductility associated with the seismic demand for the

experimental hybrid braced frame prototype tests. This system provided a more severe hysteretic response that could be calibrated to satisfy the force and deformation demands of the BRBs. Since these systems do not rely on metallic yielding to provide energy dissipation, multiple repetitive loading procedures could be applied to the hybrid timber-steel braced frame without having to replace the bracing element. Through the application of capacity design concepts, the gusset plate (used to connect the brace to the intermediate steel connection) was detailed as a secondary failure mechanism to provide additional energy dissipation through ductile failure in the bolted connection. The glued-in rod fasteners were designed to remained elastic during the wind simulation tests, quasi-static cyclic brace loading protocol investigation, and dynamic multi-hazard seismic loading scenarios. The application of pre-tensioning in the glued-in rod connections was evaluated to analyse the affect this applied force had on connection stiffness and ultimate capacity. The well-known behaviour of the steel details of the intermediate hybrid brace connection was the main benefit of this system. This would make it appealing to practising structural engineers and increase the likelihood that these steel bracing systems could be adapted into emerging advanced seismic timber design practices.

3.1 Preliminary Design

The preliminary design phase consisted of the overall structural design of a prototype hybrid timber building to determine a realistic braced frame geometry and probable seismic design forces. This information would be used for the design of the experimental frame and friction damping device. The six-storey prototype braced frame had four 6.5 meter bays and a storey height of 3.7 meters, with buckling restrained braces detailed in the two outer bays. After the frame geometry was finalized, the preliminary member sizes of the frame were determined using the equivalent static design method. The member sizes were refined using the iterative response spectrum seismic analysis and design procedure outlined in the NBCC (2010). Since all timber elements in the frame remain elastic, the braced frame was designed assuming that it would behave similarly a steel structure. This justified the use of ductility , R_d, and overstrength, R_o, factors of buckling restrained braces in the response spectrum analysis of the heavy timber

building. These factors of 4.0 and 1.2, respectively, were taken from the CSA S16 (2009) steel design manual for steel buckling restrained brace frames. This iterative design process resulted in the preliminary storey shear forces and subsequent braced forces that were used to design the steel yielding cores of the BRBs. The mechanical characteristics of the bracing system were determined based on experimental testing done by others (Tremblay et al., 2004) and used in the design to provide adequate seismic capacity. Appendix B provides a detailed discussion of the iterative seismic design process, outlining the detailed design of the buckling restrained braces and describing the overall structural design of the six storey timber building. The individual members of the experimental hybrid braced frame prototype were designed using the applicable Canadian wood design standard CSA O86 (2009) and steel design standard CSA S16-09 (2009).

Based on the loads and preliminary member geometries resulting from the prototype building frame design, a variety of timber fastener alternatives were evaluated to determine the most effective and economically viable design method for connecting the timber and steel elements together in the hybrid frame. These fasteners were required to transfer high member axial forces into the strong parallel to grain direction of the wood, while ensuring the structural integrity of the surrounding timber elements was not compromised. The primary criterion used to finalize the fastener selection was connection efficiency, in terms of force transfer, capacity, and overall size. Consideration was also given to ease of construction, fire performance, and aesthetic appeal. The connection alternatives that were considered were structural bolts, timber rivets, lag screws, self-tapping screws, and glued-in rod fasteners. In all alternatives the fastener spacing requirements governed the design and detailing of the connection zones. All but one alternatives, utilized an intermediate steel brace connection to replace the damage prone beam-column interface. This steel section was detailed to include a gusset plate connection that would indirectly fasten the bracing elements to the timber sections. The bolted connection detail was the only alternative that was designed with a large knife plate slotted into the column, that would accommodate the gusset plate connection for the bracing elements. That design prevented the need to fabricate intermediate steel brace connections. The beam connection was detailed with a smaller knife plate and hanger that would be bolted to the column knife plate to form a continuous shear

connection. Due to the relatively low lateral force transfer properties of the mechanical fasteners (structural bolts, timber rivets, and lag screws), these designs required an excessive number of fasteners to elastically transfer the high axial capacity design forces. This resulted in uneconomical fastener designs and in the early rejection of the bolt, rivet and lag screw connection alternatives. The self-tapping screw alternative used fully threaded 305 mm long fasteners with a diameter of 10 mm. These fasteners provided an efficient connection design with regards to capacity. However, the required 45 degree screw inclination, which was required to develop optimal force transfer, posed significant installation challenges on the interior column faces due to the limited space provided by the intermediate brace connection. Lastly, the investigation into the use of glued-in rod fasteners resulted in a combination of efficient force transfer and high axial capacity which reduced the size of the connection zone compared to the other alternatives. Furthermore, the minimally intrusive embedment characteristics provided additional fire protection and resulted in an overall appealing aesthetic design. After evaluating the design alternatives, it was determined that the hybrid braced frame glued-in rod connections were the most economical in terms of connection size and ease of construction. This alternative satisfied all of the design requirements, providing a connection with high axial resistance and efficient force transfer.

3.2 Hybrid Braced Frame Prototype Design

3.2.1 Methodology

The primary objective of the experimental braced frame tests was to develop and design a hybrid timber-steel system using current Canadian design standards and construction techniques. This would allow structural engineers to design advanced high-performance, high-ductility braced frames in heavy timber.

Since the first storey of the lateral force resisting system experiences the highest seismic loads, the hybrid braced frame prototype was designed to represent the first storey hybrid timber-steel connection. This provided stringent force demands that were used to evaluate the adaptation of advance structural bracing systems into heavy timber frames. As previously mentioned, the preliminary design of the six storey hybrid structure utilized buckling restrained braces as the

primary lateral load resisting system, therefore, the probabilistic tension and compression forces and amplified capacity design forces for the first storey BRB were used to design the hybrid braced frame test specimen components. A friction damping device was selected as the optimal bracing element because it offers an acute static and dynamic friction response that can satisfy the probable forces and displacement demands of the BRBs used in the building design. The device could be calibrated to various force levels while having the added benefit of a consistent response capable of resisting multiple loading scenarios. Therefore, this advanced system was selected to simultaneously test the capability of the hybrid frame and glued-in rod connections to use advanced structural bracing systems while experiencing realistic force, displacement and rotation demands.

The adaptation of advanced bracing systems into heavy timber required the combined performance of various structural components. The hybrid braced frame design contained the following components that are detailed in Figures 3.1 and 3.2.

- Bracing Element
- Intermediate Brace Connection
- Gusset Plate
- Beam Shear Connection
- Glulam Timber Members

A half-scale partial frame design was selected to accommodate laboratory space and equipment restrictions that still allowed for the analysis of two beam and column connections simultaneously. The frame was tested parallel to the floor for ease of assembly and instrumentation. This provided additional safety in the event that a sudden failure was to occur in a component of the test setup. Additionally, the application of the tension and compression column force contributions from the upper storeys was not considered for this study, that resulted in conservative tension force development in the column connections.

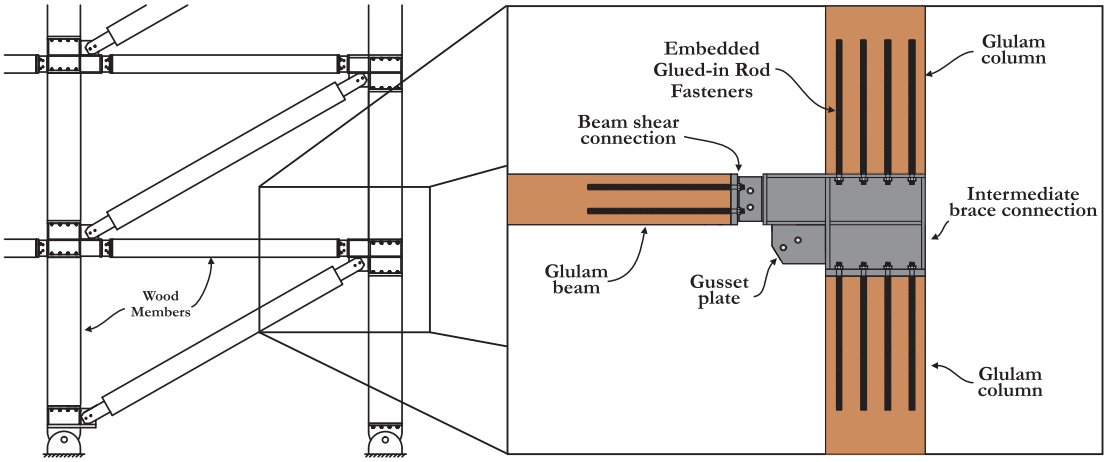

Figure 3.1: Hybrid Braced Frame Detail (Adapted from Gilbert et al. 2015)

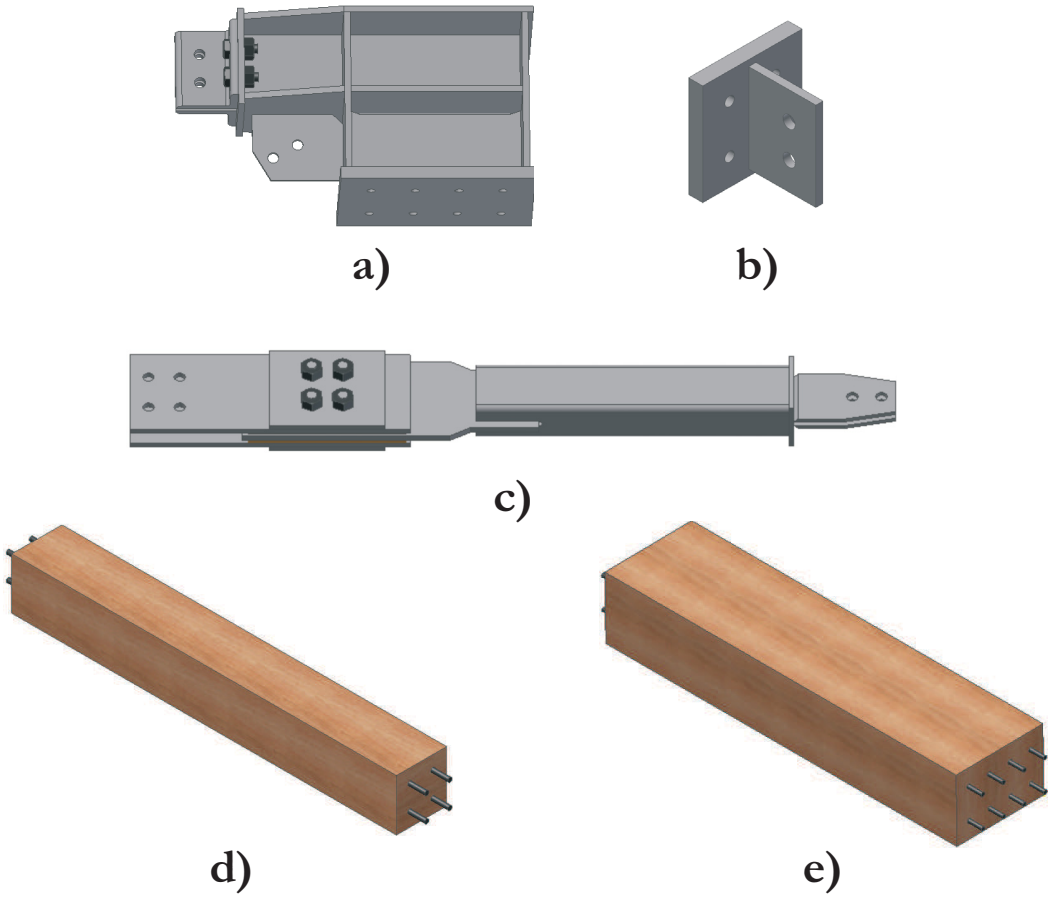

Figure 3.2: Experimental Hybrid Braced Frame Components
a) Intermediate Brace Connection b) Beam Shear Connection c) Friction Damping Device
d) Timber Beam with Glued-in Rod Connections
e) Timber Column with Glued-in Rod Connections

3.2.2 Full Scale Design Forces

The application of capacity design methodology ensures the integrity of the lateral load resisting system by systematically increasing the seismic forces as they are transfer throughout the seismic force resisting system. This procedure was applied, in combination with a hybrid timber-steel design methodology, to ensure that the ductility demand of the Maximum Credible Earthquake (MCE) hazard level earthquake was satisfied in its entirety by the inelastic behaviour of the bracing element. The capacity design forces derived from the full-scale hybrid braced frame prototype design are presented in Table 3.1. The brace core geometry was designed in order to establish the probabilistic tension and compression design forces of the BRB. Therefore, the area of the yielding brace core was determined by the anticipated seismic brace forces from the response spectrum analysis and equation (3.1) (CSA S16, 2009):

$$T_r = C_r = \phi A_{sc} F_{ysc} \tag{3.1}$$

where, T_r and C_r are the tension and compression resistance, respectively, of the steel core, A_{sc} in the cross-sectional is the brace core, and F_{ysc} is the yield strength of the steel. The yield strength of the steel core was assumed to be 370 MPa determined in the BRB investigation conducted by Tremblay et al. (2004). The probabilistic tension and compression brace forces presented were then determined from the following equations (3.2) and (3.3), respectively (CSA S16, 2009):

$$T_{pr} = \omega A_{sc} R_y F_{ysc} \tag{3.2}$$

$$C_{pr} = \beta \omega A_{sc} R_y F_{ysc} \tag{3.3}$$

where, the strain-hardening factor, ω, and compression behaviour factor, β, of 1.2 and 1.1 were taken from Tremblay et al. (2004) for the force calculations. The probably yield strength factor, R_y, was taken as 1.0 because the assumed yield strength of the steel core was determined from material behavioural testing conducted by Tremblay et al. (2004). Through the application of the capacity design procedure, a force multiplication (overstrength) factor of 1.1, taken from the

CSA S16 (2009) capacity design procedure, was applied to the probabilistic forces used for the design of the gusset plate. This element was to be detailed as the secondary fuse element to provide additional energy dissipation if the brace forces exceed the probabilistic forces previously determined. Lastly, the brace and beam connection and timber fastener forces were further increased by additional minimum amplified factors of 1.1 primarily due to limited research surrounding the elastic and cyclic performance of the glued-in rod fasteners. These connection must remain elastic during the extensive testing program in order to validate the use of the high force reduction factors assumed in the seismic design procedure. Therefore, the forces were systematically increased throughout the structural hierarchy to provide conservative design forces. Practical applications of capacity design procedures in heavy timber structures can forgo the additional force amplification past the initial increase of the probable braces forces to produce a more efficient design capable of satisfying the NBCC (2010) seismic design requirements. It is important to note that the shear forces and bending moments presented for the beam design were from the governing gravity load case which differed from the anticipated gravity loads of the seismic loading combination. These and the anticipated seismic brace forces were calculated by an extensive frame analysis discussed in detail in appendix B.

3.2.3 Frame Force Scaling

The testing was performed on a half-scaled hybrid braced frame test specimen adapted from the three dimensional structure design. The scaling procedure used a frame geometry scaling factor, S_L, of $\frac{1}{2}$. As a result, the storey height and bay width were scaled to 1850 mm and 3250 mm, respectively. The elastic modulus scaling factor, S_E, was set to 1.0, because material properties are not affected by scaling. This resulted in a force scaling of 1/4 justified in equation (3.4).

$$S_F = S_E S_L^2 = 0.25 \tag{3.4}$$

The acceleration scaling factor, S_A, of 1.0 was consistent with the factors relevant to scaling the seismic forces and fundamental period derived in Table 3.2. The resulting time scaling factor,

Table 3.1: Full-Scale Capacity Design Forces

Frame Component	Tension (kN)	Compression (kN)	Shear (kN)	Moment (kN·m)
Brace Core	380	450	0	0
Probable Brace Force	648	712	0	0
Gusset Plate	712	784	0	0
Hybrid Connection	921	1252	681	0
Timber Beam	681	619	75	115
Timber Columns	921	1252	0	0
Beam Connection	681	619	75	0
Beam Fasteners	749	681	0	0
Column Fasteners	1013	1377	0	0

S_T, required time-scale compression of first-storey displacement responses when applied to the braced frame prototype during the dynamic earthquake response tests. Additionally, the scaling factor of the fundamental period, S_{Ta} was required to determine the scaled building period for the wind loading protocol discussed in Chapter 6. The remaining geometric and dynamic factors associated with the scaling of the hybrid frame and earthquake loading response records are presented in Table 3.2.

The initial brace forces were factored by $\frac{1}{4}$ and the buckling restrained brace cores were designed to resist these scaled forces. Then, the probable tension and compression forces were determined using equations (3.2) and (3.3). The remaining capacity design forces were determined by applying an overstrength factor of 1.1 at each stage of the design hierarchy. The scaled forces relevant to the hybrid braced frame prototype design are presented in Table 3.3.

The structural analysis and deflected shape of the braced frame prototype is presented in Figure 3.3. The anticipated brace displacement and connection rotation at two times the allowable storey drift of 2.5% for structures of normal importance are derived below (NBCC 2010). The elongation of the brace, Δ_{brace}, was determined from equation (3.5), and the beam connection rotation, θ_{beam} was determined from equation (3.6) for small displacements.

Table 3.2: Scaling Factors for the Experimental Prototype (Adapted from Erochko, 2013)

Quantity	Description	Scaling Factor
Geometric Properties		
Length	S_L	0.500
Elastic Modulus	S_E	1.000
Force	$S_F = S_E S_L^2$	0.250
Moment	$S_M = S_F S_L$	0.125
Area	$S_A = S_L^2$	0.250
Section Modulus	$S_Z = S_L^3$	0.125
Moment of Inertia	$S_I = S_L^4$	0.063
Dynamic Properties		
Acceleration	S_A	1.000
Mass	$S_{Ma} = S_F/S_A$	0.250
Time	$S_T = \sqrt{(S_M S_L)/S_F}$	0.250
Fundamental Period	$S_{Ta} = \sqrt{S_M/(S_F/S_D)}$	0.250
Velocity	$S_V = S_L/S_T$	0.500

Table 3.3: Half-Scale Capacity Design Forces

Frame Component	Tension (kN)	Compression (kN)	Shear (kN)	Moment (kN·m)
Bracing Core	95	113	0	0
Probable Brace Force	167	183	0	0
Gusset Plate	183	202	0	0
Hybrid Connection	405	480	170	0
Beam Connection	184	175	19	0
Beam Fasteners	202	193	0	0
Column Fasteners	446	528	0	0
Timber Beam	222	212	19	14
Timber Columns	491	581	0	0

$$\Delta_{brace} = \Delta_{Drift} cos(\theta_{brace,i}) = 92.5cos(29.65) = 80.4 \text{ mm} \tag{3.5}$$

$$\theta_{beam} \approx \frac{\Delta_{Drift}}{h_s} = 92.5/1850 = 0.05 \text{ rad} = 2.9 \text{ degrees} \tag{3.6}$$

where, $\theta_{brace,i}$ is the initial brace angle determined from the frame geometry, and h_s is the storey hight.

The half-scale frame geometric properties of the timber members and brace core are presented in Table 3.4. Additionally, the subsequent scaled target geometric properties are also presented. The final timber section sizes were governed by the spacing requirements of the glued-in rod connections and the standardized cross section dimensions available from the manufacturer.

3.2.4 Design Codes and Material Properties

The design of the various structural components of the hybrid braced frame prototype required the application of two Canadian design standards, a German Design Code and two European design methods, as well as a variety of methods from the literature. The design codes and guidelines required are the following:

- CSA O86-09 Wood Design Manual (2009)
- CSA S16-09 Handbook of Steel Construction (2009)
- German Design Code DIN 1052 (2004)
- GIRod Project Design Procedure (2002)
- LICONS Report Design Procedure (2003)

The steel components were designed in accordance with the CSA S16-09 (2009) design standard using common structural design and construction techniques. The intermediate steel sections were fabricated from grade CSA G40.21-300W (CSA S16, 2009) steel plate with yield and ultimate strengths of 300 MPa and 400 MPa, respectively. Furthermore, the hollow structural

Table 3.4: Half-Scale Capacity Design Section Properties

Geometric Property	Full-scale Measurement	Target Measurement	Actual Measurement
Frame Geometry			
Beam Span (mm)	6500	3250	1750
Column Height (mm)	3700	1850	1850
Glulam Member Geometry			
d_{Beam} (mm)	418	209	228
b_{Beam} (mm)	265	133	222
S_{Beam} (mm^3)	7.7210^6	9.6810^5	1.9210^6
d_{Column} (mm)	342	171	457
b_{Column} (mm)	315	158	327
S_{Column} (mm^3)	6.14710^6	7.7010^5	11.3810^6
Brace Geometry			
Length (mm)	7479	3740	N/A
Brace core (mm × mm)	25×56	12.5×28	15×24
Core Area (mm^2)	1400	350	360

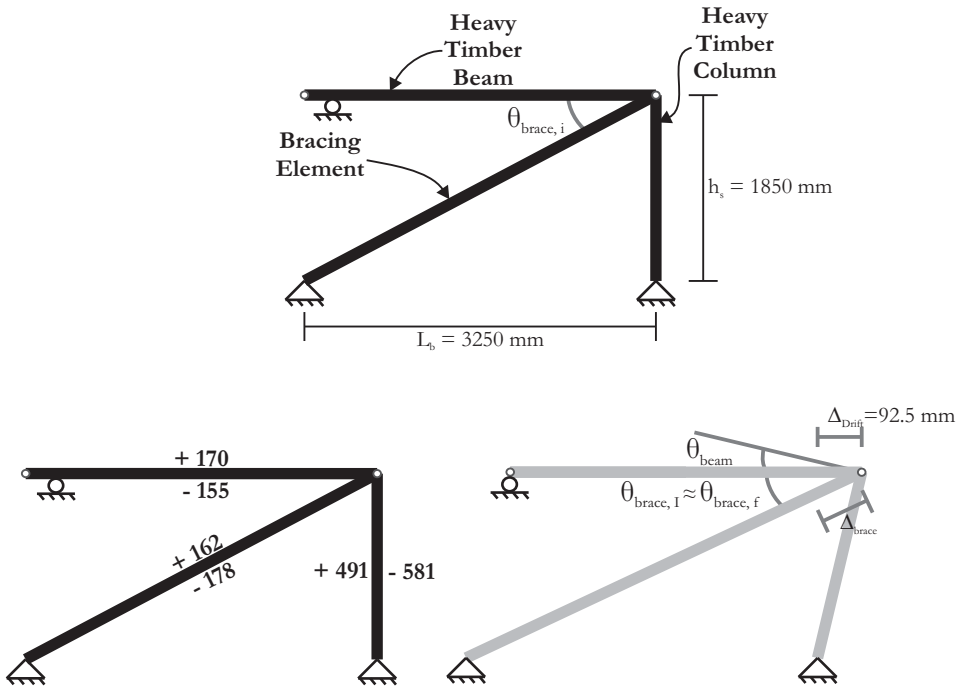

Figure 3.3: Analysis of Experimental Frame a) Frame Forces b) Frame Displacements

section used in the friction damping device design, was fabricated from the standard CSA G40.21-350W (CSA S16, 2009) steel. This steel has a yield strength of 350 MPa and an ultimate strength of 450 MPa. The tabulated values of both steel types were assumed based on code specified material properties in the design because coupon tests were not performed to verify these properties.

A two-component epoxy resin characterised as a high-strength, low volatile organic compound was selected for the design and fabrication of the glued-in rod fasteners. As previously discussed, PUR and PRF adhesives provide lower strength performance than EPRs due to such shortcomings as poor adhesion and adhesive expansion. Therefore, the two-component epoxy, commercially designated as Sika AnchorFix©-3001 and provided by Sika Canada Inc. (2014), was selected as the ideal adhesive to anchor the thread rods into the timber sections. This adhesive has an extended working time which makes it suitable for laboratory and construction applications. The robust characteristics of this epoxy allows for structural grade adhesion under dry, wet, or submerged conditions making it attractive for construction applications exposed to various environmental conditions (Sika Canada Inc., 2014). This adhesive has a 5.9% elongation at

breakage providing the relative epoxy classification of non-brittle (Sika Canada Inc., 2014). The manufacturer material data sheets did not contain shear strength and fracture energy information which limited the material specific characteristics available for the connection design. However, the mechanical properties from the product data sheet of the adhesive are presented in Table 3.5 for a relative humidity of 50% and ambient temperature of 20°c (Sika Canada Inc., 2014).

The B7 threaded steel rods used for the glued-in rod fasteners provided high axial strength characteristics that was utilized in the fastener design. The material property relevant to the connection design were the tensile strengths, Young's modulus and thread pitch presented in Table 3.6. The other material properties were not required for the detailed design of the threaded rods because these fasteners were subjected to pure axial loading due to the load transfer mechanics of the braced frame.

The original timber elements of the hybrid system were designed using the Douglas Fir material properties specified in CSA O86 (2009). However, due to the lack of availability the hybrid braced frame prototype was designed and fabricated using a spruce-pine-fir glulam product, commercially designated as Nordic Lam, that consists predominately of northern black spruce. The glulam was comprised of 50.8 mm x 25.4 mm (1 x 2 inch) laminations finger jointed in succession to ensure homogeneous section properties. The material properties of this heavy timber type is listed in Table 3.7 (Nordic Engineered Wood, 2013).

3.2.5 Friction Damper Design

A friction damping device was selected as the ideal bracing system because the friction behaviour, slotted hole detail and pre-tensioned bolt design allowed for the slip load to be easily calibrated to satisfy load and displacement demands of the buckling restrained brace, shown in Figure 3.4. In addition to testing of the glued-in rod connections at these force demands the seismic performance of the friction brace was used to evaluate and characterize the friction behaviour of the stainless-steel on brass assembly. Furthermore, since the friction interfaces experiences minimal surface damage, many tests can be conducted on the same test frame assembly

Table 3.5: Adhesive Properties (Sika Canada Inc., 2014)

Property	Strength (MPa)	Modulus (GPa)
Compression		
1 Day	59	-
7 Days	85	5
Tension		
1 Day	18	5.7
7 Days	23.5	5.5
Flexure		
1 Day	45	-

Table 3.6: B7 Threaded Steel Rod Properties

Property	Specified Value	Unit of Measure
Tension Strength, f_u	860	MPa
Yield Strength, f_y	725	MPa
Elastic Modulus	200000	MPa
Thread Pitch	10	mm

Table 3.7: Nordic Glulam Material Properties (Nordic Engineered Wood, 2013)

Property	Specified Value	Unit of Measure
Compression Parallel to Grain, f_c	33.0	MPa
Compression Perpendicular to Grain, f_{cp}	7.5	MPa
Tension Parallel to Grain, f_t	20.4	MPa
Positive Bending, f_{bp}	30.7	MPa
Negative Bending, f_{bn}	30.7	MPa
Shear, f_v	2.2	MPa
Elastic Modulus, E	13100	GPa
Density, ρ	560	$\frac{\text{kg}}{\text{m}^3}$

without the need to replace or recalibrate the bracing system. The friction device was detailed to activate at the probabilistic compression resistance of the BRB from the prototype building (appropriately scaled) in order to capture the most severe loading scenario of the original systems, shown in Figure 3.4. These probabilistic tension and compression forces were calculated using equations (3.2) and (3.3) to be 166.5 kN and 183.2 kN respectively. Therefore, the probabilistic forces used in the design of the gusset plate for tension and compression were 183.2 kN and 201.5 kN, respectively. These forces were determined as the lower bound design forces for the friction damping device. Meaning the components of the friction brace were designed against a force level greater than that of the gusset plate to ensure that all components of the damper would remain elastic if the secondary failure mechanism was to be tested. The friction damping device was designed conservatively to provided sufficient axial stiffness and resistance in order to prevent high cycle fatigue and excessive braced deformations from impacting the seismic performance evaluation of the glued-in rod connections and hybrid timber-steel braced frame prototype. An overall detail of the friction damping device is presented in Figure 3.5.

3.2.6 Friction Device Component Design

The friction set-up consists of a stainless-steel on brass interface detail to provide a reliable friction behaviour capable of enduring repeated testing. The stainless-steel was selected because it has corrosive resistance properties that are not affected when placed in contact with brass, unlike low-carbon alloy steels (BSI, 1979; Di Sarno & Elnashai, 2005). Corrosion resistance is essential for the long term performance and durability of these devices because it ensures the friction characteristics do not change over time, providing reliable and consistent energy dissipation. A brass plates was placed on each stainless-steel surface to form the second component of the friction interface. The inner steel plate and stainless plates that were welded to it were detailed with oversized slotted bolt holes to accommodate the anticipated brace elongation, Δ_{brace}, at two times the MCE drift displacement, $2.0\Delta_{MCE}$, and the brace rotation demands of the various loading protocols. The slotted holes were designed to ensure these rotation demands could be satisfied by the friction device because the gusset plate and brace anchor connection were specified as slip

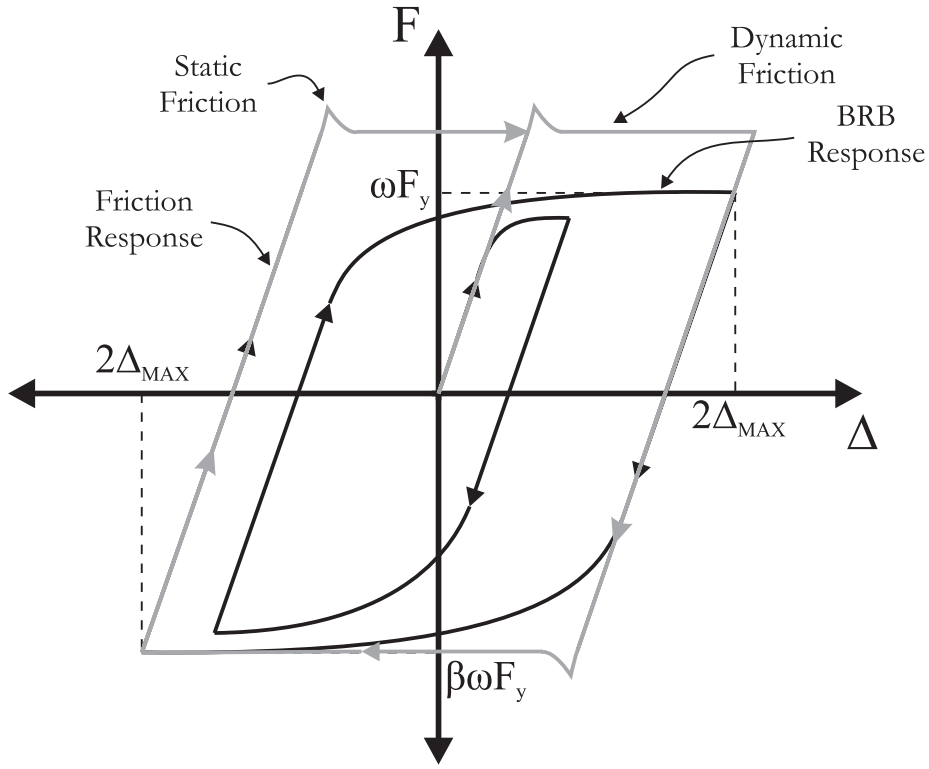

Figure 3.4: BRB and Friction Response Comparison

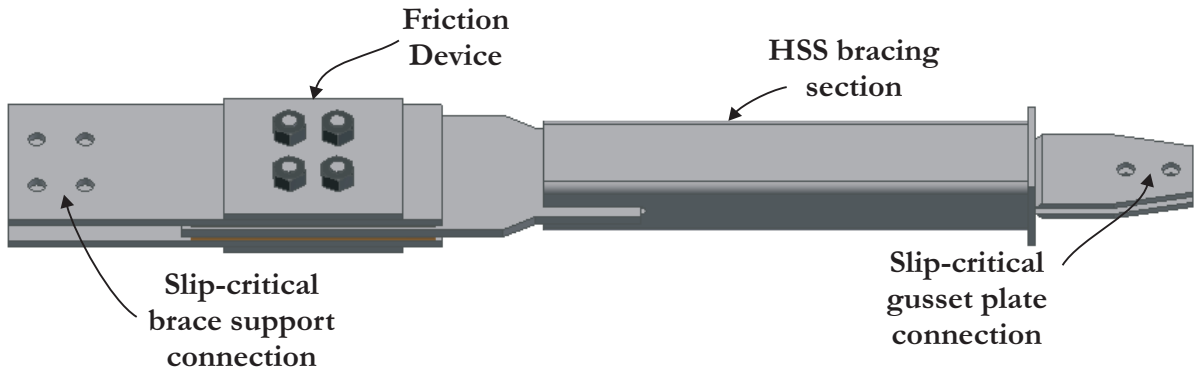

Figure 3.5: Friction Brace Detail

critical connections, required to ensure the proper behaviour of the friction device. Additionally, steel side plates and washer plates were used to confine the friction components and aid in the transfer to the normal force evenly across the interface. Lastly, four 25.4 mm (1 inch) A 325 structural bolts were used to constrain the fuse components while simultaneously providing the normal bolt force vital to develop the required friction force. Figure 3.6 shows the various friction interface components designed for the friction brace assembly.

The limited previous literature on stainless-steel and brass friction devices meant the force resistance of the friction interface was estimated using the static and dynamic friction coefficients of 0.31 and 0.21 presented in Grigorian (1994) for a steel on brass system. The coefficient of static and dynamic friction of the interface would be determined as part of the brace calibration process discussed in Chapter 6. The initial slip and dynamic friction resistance were calculated using equations (3.7) and (3.8) provided by Tjahyadi, (2002):

$$F_{f,static} = n_{fs} n_b \mu_s F_{Nb} \tag{3.7}$$

$$F_{f,dynamic} = n_{fs} n_b \mu_d F_{Nb} \tag{3.8}$$

where, n_{fs} is the number of friction interfaces providing resistance. n_b is the number of pre-tensioned bolts contributing to the applied normal force. μ_s and μ_d are the static and dynamic

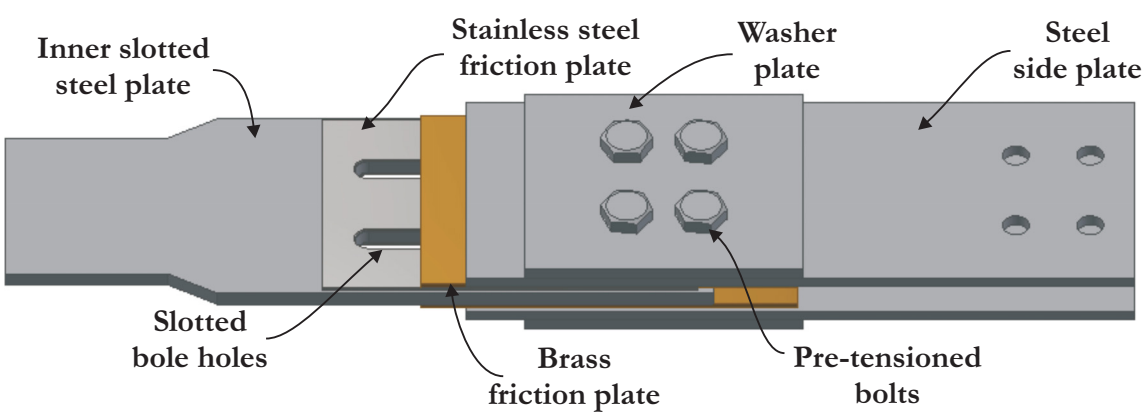

Figure 3.6: Friction Interface Detail

friction coefficients, respectively, and the normal force provided by each bolt is represented in the variable F_{Nb}. To determine the number of bolts required to provide the required brace force at the pre-tensioning force level of 70 % of the bolt tension resistance outline in CSA S16 (2009), the friction force equation (3.7) was rearranged in terms of the number of bolts as shown in equation (3.9).

$$n_b = \frac{F_f}{n_{fs}\mu F_{Nb}} \tag{3.9}$$

This equation was analysed for the one inch A325 and A490 bolts. The finding showed that the 3- 25.4 mm (1") A325 bolts were required, while 2- 25.4 mm (1") A490 bolts would just satisfy the demand. Therefore, in order to simplify the bolt layout and provide a uniform normal force stress distribution, 4-25.4 mm (1") A325 bolts were selected for the friction interface. Providing additional friction capacity also provided the ability to lock the brace by fully tightening all four bolts, increasing the brace resistance past the actuator capacity, in an attempt to yield the gusset plate or evaluate the variation in glued-in rod connection stiffness at different levels of pre-tensioning. Furthermore, once the number of bolts was established, the friction equation was then re-arranged to determine the required normal force in each of the four pre-tensioned bolts to satisfy the brace force. This was accomplished by using equation (3.10) for either friction coefficient.

$$F_{Nb} = \frac{F_f}{n_{fs} n_b \mu} \tag{3.10}$$

Therefore, a minimum normal bolt forces of 84 kN and 120 kN was estimated to be required in each bolt for the static and dynamic resistance to equal the required brace force. The brass plates were checked against bearing failure under the applied normal forces and were well within the allowable resistance. Furthermore, the resistance of the bolted connection in the brass plates and side plates (see Figure 3.6) was check against bearing, row shear, and group tear-out to ensure each plate could withstand the friction force generated, that would be equal to half the capacity protected brace force. This was especially important because exact 25.4 mm (1") holes were to be milled into the brass plate to provide complete bearing contact with the four A325

bolts of the friction interface. This tight hole sizing would ensure that slippage between the brass plates and steel side plates would not occur during calibration and testing.

The inner steel plate of the friction device was detailed with slotted bolt holes to accommodate the displacement demands of the brace expected during the testing program, shown in Figure 3.6. Therefore, the slotted holes were required to have a minimum slot length of 81.4 mm between the pre-tensioned bolt and the end of the slotted hole to accommodate the maximum drift demand on the test frame. However, the final design detailed a slot length of 107 mm from each bolt to the corresponding end of the slotted holes, providing additional displacement capacity if required. The slot lengths in combination with a 75 mm bolt spacing resulted in a total slotted bolt hole length of 288 mm. The resistance of the inner plate was checked for both factored gross and net tension against the capacity protected brace force. Furthermore, the flexural and local buckling resistance of the plate would be critical to the performance of the friction device. Even at low levels of out-of-plane brace buckling the friction resistance could see increases past the intended brace force due to an increase in the normal force applied to the friction interface as the plate deforms. Alternatively, failure could have also result from complete compressive bucking of the inner plate, rendering the device ineffective. Therefore, the inner plate needed to resist the relatively high compression force without experiencing any out-of-plane buckling. For that reason, the compressive resistance was checked using an unsupported length of 280 mm to simulate the worse case scenario of compression loading when the device was fully extend, as shown in Figure 3.7. The buckling capacity of 628 kN was within the required resistance which ensured that out-of-plane behaviour would not effect the device performance. Additionally, the moment resistance of the plate was checked against the moment induced by a combination of the self-weight and a 5 % accidental out-of-plane eccentricity in the brace force.

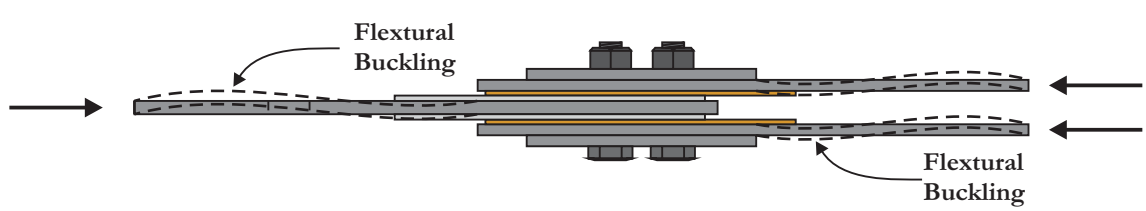

Figure 3.7: Plate Buckling Failure Detail

Similarly to the inner plate, the geometry of the two steel side plates was checked for the buckling capacity against the scaled brace forces. This factored buckling resistance was determined to be 660 kN per side plate, meaning this conservative design provided a combined over-strength factor of 6.5. However, due to induced flexural behaviour under dynamic loading caused by frame eccentricities due to misalignment, stiffeners were added in the early stages of the testing phase, discussed in more detail in Chapter 6. These stiffeners prevented the development of plastic hinges in the friction device due to out-of-plane buckling amplified by the high velocity randomized seismic loading. Furthermore, the gross and net section resistances of the plates were checked against the applied tension forces. The moment resistance of the side plates was also checked against the previously discussed conservative assumption of self-weight and fraction of the brace force. A conservative design assumption was made such that the plates were analysed individually, ignoring the possible increase in moment capacity if the two plates were assumed to act together. This resulted in a moment capacity for the un-stiffened side plates of 7.3 kN·m which satisfied the minimum moment resistance requirement of the assumed force equal to 6.7 kN·m. In addition to the standard tension, bearing, and fastener resistance checks, the connection between the side plates and brace support column was designed to be slip-critical using clause 13.12.2.1 of CSA S16 (2009).

The main axial brace element of the friction brace was designed using a 152 x 102 x 13 HSS section that was fabricated with two slotted holes that allowed the inner steel plate to be welded to the HSS at the center of the section depth. The 150 mm holes were detailed to provide adequate length for the 8 mm weld on the top and bottom of either side of the inner plate. Shear lag resistance of the welded connection was evaluated to ensure the section could resist uneven stress distribution in the brace if required. An end plate was welded to the opposite end of the HSS section to accommodate the brace to gusset plate connection. The two side plates, that formed the brace contribution of the gusset connection, were spaced 7 mm apart to accommodate the gusset plate. The 45 degree partial penetration grove weld was designed to develop the full governing tensile capacity of the side plate.

3.2.7 Gusset Plate Design

The bolted connection at the gusset plate was detailed to act as a secondary failure mechanism. This provided additional protection to the intermediate brace connection, glued-in rod fasteners and timber members, while providing the structure with additional energy dissipation if required. The failure mode for this connection was detailed to be row shear at a capacity tension design force of 185 kN using clause 13.11 of CSA S16 (2009). Because of stringent code requirement, the minimum edge distance and spacing for the 2- 25.4 mm (1 inch) A325 bolts had to be satisfied in the design. The final design resulted in a 6.4 mm ($\frac{1}{4}$ inch) thick gusset plate with an edge distance of 35 mm and a bolt spacing of 70 mm, providing a factored row shear resistance of 225 kN. A final detail of the gusset plate design is shown in Figure 3.8.

3.2.8 Glued-in Rod Design

The glued-in rod fastener design needed to consider the pull-out resistance of the timber-adhesive interface, the ultimate tensile capacity of the rod and the gross tensile capacity of the timber element past the embedment boundary of the fastener. Due to the absence of a Canadian approved design method, the pull-out resistance of these fasteners was designed using three different European design procedures. The strength characteristics used in the glued-in rod fastener design were experimentally derived from specimens containing Europe adhesives and timber species. Therefore, the strength characteristics would be experimentally validated as part of the single rod test program discussed in Chapter 5, to determine if these parameters applied to the Canadian adhesive and timber species selected. The pull-out resistances were determined from the GIRod Report design method (2002), the LICONS Report EUROCODE 5 Annex C design proposal (2003) and the approved German design method presented in DIN 1052 (2004), all previously detailed in Chapter 2.

A two-component structural epoxy was used for the design and fabrication of the glued-in rod connections. Based on the empirical findings, this adhesive type had the highest pull-out resistance and most reliable long term and high cycle fatigue characteristics. These properties

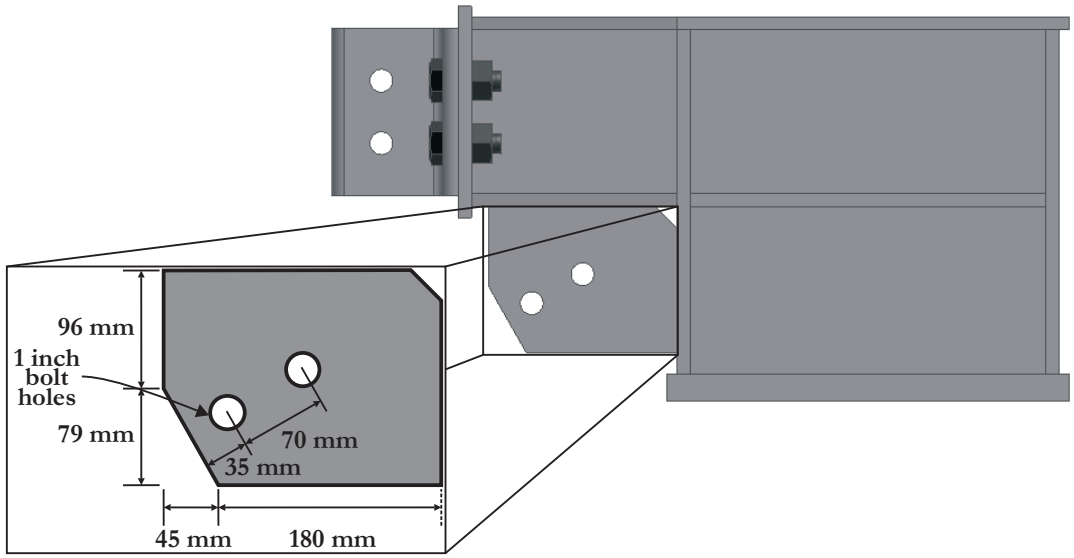

Figure 3.8: Gusset Plate Detail

made it the optimal bonding agent for connections subjected to the randomized axial loads typical of braced lateral force resisting systems. Furthermore, the extended working time of the adhesive simplified the installation process allowing for higher quality control. Fully threaded 19 mm ($\frac{3}{4}$ inch) B7 steel rods were utilized in the connection design to provide an excellent bonding surface for the adhesive. Additionally, these rods provided the optimal fastening characteristics to connect the steel section to the timber elements. The B7 rods were chosen over A307 rods because of their higher tensile capacity. Because the rods would not experience yielding during the testing program, any strength or stiffness degradation in the timber-adhesive interface within the elastic range of the glued-in rod fasteners will be captured. This behaviour analysis would help to define the cyclic response characteristics of glued-in rods. The ideal glued-in rod design would detail failure in the rod due to tension yielding prior to fastener withdrawal. This ductile failure mode would provide additional energy dissipation and axial force limitation if the axial forces within the braced frame exceeded the capacity design forces.

3.2.8.1 Capacity Design Forces

The horizontal component of the capacity design forces used to design the gusset plate were multiplied by an overstrength factor of 1.1 to provide the necessary capacity force protection to

design the glued-in rod connections. This provided tension and compression forces of 202 kN and 193 kN, respectively. This ensured that the forces developed in the glued-in rods would remain within the elastic range, preventing brittle failure from occurring under the anticipated seismic forces. Furthermore, the glued-in rod connections in the timber column were designed to resist the capacity protected column forces from the seismic analysis of the six storey structure. The axial column forces that are to be used in the design of the intermediate brace connection were also increased by a factor of 1.1. This provided tension and compression design forces of 446 kN and 528 kN, respectively, to ensure elastic behaviour throughout the various testing procedures.

3.2.8.2 Rod Tensile Capacity

Prior to determining the pull-out resistance of the glued-in rod fasteners, the tensile capacity of the threaded steel rods had to be confirmed. The factored ultimate rod resistance was calculated using the design methods presented in CSA S16-09 (2009) for either anchor rods or high strength bolts defined by equations (3.11) and (3.12):

$$F_{u,rod} = \phi_{Ar} A_n f_u \tag{3.11}$$

$$F_{u,Bolt} = 0.75\phi_b A_b f_u = 0.75(0.8)(284.5)(860) = 146 \text{ kN} \tag{3.12}$$

where, ϕ_{Ar} and ϕ_b are the anchor rod and structural bolt resistance factors, A_n in the tensile area of the steel rod, A_b is the cross-sectional area of the fastener, and f_u is the ultimate resistance of the steel. The selection of the appropriate resistance calculation depended on the grade and material characteristics of the rods selected for the connection. Based on the high strength characteristics of the B7 rod type, the latter equation was used to determine the tension resistance of 146 kN for each of the 19 mm ($\frac{3}{4}$ inch) rods.

3.2.8.3 Spacing and Edge Distance Requirements

To avoid splitting failure in timber surrounding the connection zone, the minimum edge distance, e_{min}, and minimum spacing, S_{min}, criteria from the GIRod Report (2002) was used to

detail the final connection design, calculated using equations (3.13) and (3.14):

$$e_{min} = 2.5d_r = 2.5(19) = 48 \text{ mm} \tag{3.13}$$

$$S_{min} = 5d_r = 5(19) = 95 \text{ mm} \tag{3.14}$$

where, d_r is the diameter of threaded steel rod. Therefore, the connection design, utilizing 19 mm ($\frac{3}{4}$ inch) threaded steel rods, required a minimum edge distance and spacing of 48 mm and 95 mm, respectively.

3.2.8.4 GIRod Project Design Procedure

Prior to the full connection design and detailing, a preliminary analysis of the glued-in rod pull-out resistance was conducted using the GIRod Report (2002) design method, previously described in Chapter 2. The primary objective of this analysis was to establish the embedment length, l_a, corresponding to the maximum efficient resistance using the minimum spacing and edge distance requirements. The glued-in rod fasteners were designed with a bond-line thickness of 2 mm, resulting in an embedment hole diameter, d_h, of 23 mm associated with the application of 19 mm ($\frac{3}{4}$ inch) rods. Lastly, the shear strength of the timber-adhesive interface was assumed to be 10.5 MPa, taken from the results presented in the GIRod Report (2002). Based on the preliminary analysis it was established that the pull-out resistance plateaued at approximately 115 kN for an embedment length of 450 mm. This suggests that the pull-out resistance of the fasteners would not surpass the tensile capacity of the 19 mm ($\frac{3}{4}$ inch) B7 rods. Figure 3.9 shows the pull-out resistance verses embedment length comparison showing this plateau characteristic that defines the maximum effective fastener resistance. The 450 mm length was within the optimal embedment length guidelines, presented in equation (3.15), suggested by Rossignon and Espion (2008).

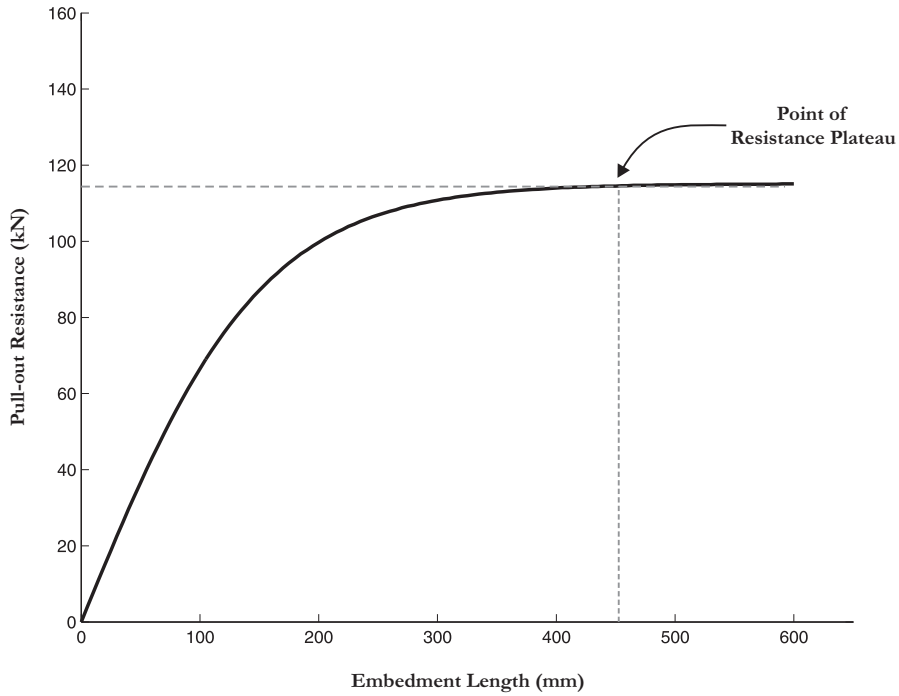

Figure 3.9: Preliminary GIRod Report Design Method Strength Prediction

$$l_{a,max} = \min \begin{cases} 25d_r = 25(19) = 475 \text{ mm (Governs)} \\ 500 \text{ mm} \end{cases} \tag{3.15}$$

However, the embedment length was increased to 600 mm in an attempt to provide additional fastener overstrength, observed in previous literature (Rossignon & Espion, 2008), to induce the ductile failure mode of tension yielding in the rod, as suggested by Rossignon and Espion (2008). Additionally, due to the lack of information surrounding the high cycle fatigue characteristics of glued-in rod connections utilizing this adhesive type, it was determined that an increase in embedment length would be beneficial to safeguarding the connections against wind loading and high frequency vibrations.

Following the preliminary analysis the GIRod report design procedure was used to calculate the individual rod pull-out resistance of the detailed glued-in rod connection design for an embedment length of 600 mm (Bengtsson and Johansson, 2002). The method was the most detailed of the three design procedures (GIRod Repot (2002), LICONS Report (2003), DIN 1052

(2004)) and accounts for various geometric and mechanical joint characteristics including the effective area of the timber and adhesive type (Bengtsson and Johansson, 2002). Prior to determining the axial resistance, the minimum embedment length requirements from the DIN 1052 Design code (2004) where checked using equation (3.16).

$$l_{a,min} = \begin{cases} 0.5d_r^2 = 0.5(19)^2 = 181 \text{ mm (Governs)} \\ 10d_r = 10(19) = 190 \text{ mm} \end{cases} \tag{3.16}$$

The pull-out resistance form the GIRod report (2002) is presented in equation (3.17).

$$P_f = \pi d_h l_a \tau_f \frac{\tanh \varpi}{\varpi} \tag{3.17}$$

In order to determine the stiffness ratio, ϖ, the geometric and material property length parameters l_{geo} and l_m need to be established. The parameter l_m would be determined from the empirical results of small scale single rod tests using equation (3.18) (Serrano, 2001b).

$$l_m = \frac{E_r G_f}{\tau_f^2} \tag{3.18}$$

However, in the attempt to establish if the design method of the GIRod Report (2002) was applicable to Canadian materials, a material property length parameter of 3600 mm was selected, based on the presented findings of the GIRod report, for glued-in rod fasteners containing epoxy adhesives (Bengtsson and Johansson, 2002).

The geometric length parameters were calculated through an iterative process using equations (3.19) and (3.19) for the beam and column connections, respectively.

$$l_{geo,beam} = \frac{\pi d_r l_a^2}{2}\left(\frac{1}{A_r} + \frac{\frac{E_r}{E_w}}{A_{w,beam}}\right) = \frac{\pi(19)(600)^2}{2}\left(\frac{1}{283.5} + \frac{\frac{200000}{13100}}{14117}\right) = 49515 \text{ mm} \tag{3.19}$$

$$l_{geo,column} = \frac{\pi d_r l_a^2}{2}\left(\frac{1}{A_r} + \frac{\frac{E_r}{E_w}}{A_{w,column}}\right) = \frac{\pi(19)(600)^2}{2}\left(\frac{1}{283.5} + \frac{\frac{200000}{13100}}{16617}\right) = 47767 \text{ mm} \quad (3.20)$$

This process required the connection spacing and edge distance be established in order to calculate the effective area of the wood, A_w, surrounding a glued-in rod calculated using equation (3.21):

$$A_{w,beam} = a^2 - A_r = (60 + 60)^2 - 283.5 = 14117 \text{ mm}^2 \quad (3.21)$$

$$A_{w,column} = a^2 - A_r = (65 + 65)^2 - 283.5 = 16617 \text{ mm}^2 \quad (3.22)$$

where $a/2$ is the minimum distance between the center of the embedded rod and the edge of the timber section designated as a_2 and a_3 in Figure 3.10.

In the first iteration the minimum spacing and edge distance requirements were used to determine the effective area and subsequent lower boundary of the pull-out resistance. The final connection detail specified an edge distance of 60 mm for the beam connection and 65 mm for the column connection. Resulting in an effective areas of 14117 mm^2 and 16617mm^2 for the beam and column connections, respectively. Where, the area of the $\frac{3}{4}$ inch rods, A_r, was 283.5 mm^2, The modulus of elasticity for the wood, E_w, and rod, E_r, were taken as 13100 MPa (Nordic Engineered Wood, 2013) and 200000 MPa (CSA S16-09, 2009), respectively. Therefore, the geometric parameters, l_{geo}, of 49515 mm and 47767 mm were calculated for the final beam and column glued-in rod designs with an embedment length of 600 mm.

Stiffness ratios of 3.71 and 3.64 were determined for the final beam and column connection designs for the associated geometric and material property parameters, as shown in equations (3.23) and (3.24).

$$\varpi_{beam} = \sqrt{\frac{l_{geo,beam}}{l_m}} = \sqrt{\frac{59939}{3600}} = 3.71 \quad (3.23)$$

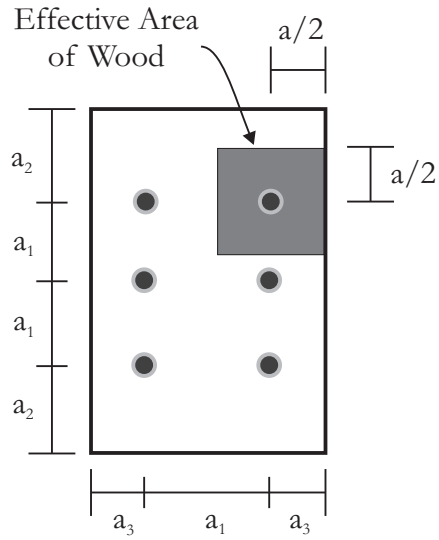

Figure 3.10: Effective Area of the Wood

$$\varpi_{beam} = \sqrt{\frac{l_{geo,column}}{l_m}} = \sqrt{\frac{47767}{3600}} = 3.64 \tag{3.24}$$

The establishment of the related variables for geometric and material properties allowed for the pull-out resistance to be calculated for a single glued-in rod fastener utilized in the final connection design. The strength capacities were determined to be 123 kN and 125 kN for the beam and column connections, derived from equations (3.25) and (3.26):

$$P_{f,beam} = \pi d_{equ} l_a \tau_f \frac{\tanh \varpi_{beam}}{\varpi_{beam}} = \pi(23)(600)(10.5)\frac{\tanh(3.71)}{3.71} = 123 \text{ kN} \tag{3.25}$$

$$P_{f,column} = \pi d_{equ} l_a \tau_f \frac{\tanh \varpi_{column}}{\varpi_{column}} = \pi(23)(600)(10.5)\frac{\tanh(3.64)}{3.64} = 125 \text{ kN} \tag{3.26}$$

where, d_{equ} is the equivalent hole diameter determined from expression (3.27).

$$d_{equ} = \min \begin{cases} d_r + t_{bl} = 19 + 4 = 23 \text{ mm (Governs)} \\ 1.25 d_r = 1.25(19) \approx 24 \text{ mm} \end{cases} \tag{3.27}$$

In the expression t_{bl} is the bond-line thickness of the connection and d_r is the rod diameter. For the given connection dimensions the effective hole diameter was calculates as 23 mm.

3.2.8.5 LICONS Report Proposed EUROCODE 5 Design Procedure

The proposed EUROCODE 5 design procedure from the LICONS Report (2003) was established from the detailed GIRod Report design method. However, this conservative method is based on the assumption that the weakest adhesive type, PRF, would be used in the fabrication of the glued-in rod connections. This assumption provided an underestimation in the connection capacity of fasteners design with PUR and EPR bonding agents that provided these connection types with additional overstrength. Additionally, the method also outlined the tensile capacity calculation of the steel rods used in the fastener design. However, the tensile capacity of the glued-in rods designed for the hybrid braced frame was calculated using CSA S16 (2009) discussed above in section 3.2.8.2. Therefore, the axial capacity of the glued-in rod fasteners was determined using the latter equation in expression (3.28):

$$F_{ax,Rk} = \min \begin{cases} f_{y,k} A_{ef} \\ \pi d_{equ} l_a f_{ax,k} \frac{\tanh \omega}{\omega} \end{cases} \tag{3.28}$$

where, the proposed shear strength, $f_{ax,k}$, of 5.5 MPa is assumed for the timber-adhesive interface.

After establishing the equivalent hole diameter, from equation (3.27) previously discussed, the stiffness parameter, ω, could be calculated using equation (3.29).

$$\omega = \frac{0.016 * (l_a)}{\sqrt{d_{equ}}} = \frac{0.016 * (600)}{\sqrt{23}} = 2.00 \tag{3.29}$$

This resulted in a stiffness parameter of 2.00 for the previously determined embedment length of 600 mm.

The resulting nominal pull-out resistance, $F_{ax,R}$, for the given fastener geometry was calculates to be 115 kN, derived in equation (3.30):

$$F_{ax,R} = \pi d_{equ} l_a f_{ax,k} \frac{\tanh \omega}{\omega} = \pi(23)(600)(5.5)\frac{\tanh(2.00)}{2.00} = 115 \text{ kN} \tag{3.30}$$

The resistance determined from the method was not directly dependant on the geometric parameters of the connection and therefore both the beam and column connection were calculated to have the same capacity.

3.2.8.6 German Design Procedure DIN 1052

The German design method was the last procedure used to estimate the pull-out resistance of the glued-in rod fasteners. This simplified design method relied on three different embedment length ranges to determine the adhesion strength characteristic, $f_{k1,d}$, presented in expression (3.31).

$$f_{k1,d} = \begin{cases} 4.0 & \text{if } l_{ad} \leq 250\text{mm} \\ 5.25 - 0.005 l_{ad} & \text{if } 250 > l_{ad} \leq 500\text{mm} \\ 3.5 - 0.0015 l_{ad} & \text{if } 500 > l_{ad} \leq 1000\text{mm} \end{cases} \tag{3.31}$$

For the embedment length of 600 mm this fastener characteristic was defined by the latter equation, resulting in a adhesion strength of 2.6 MPa calculated in equation (3.32):

$$f_{k1,d} = 3.5 - 0.0015 l_{ad} = 3.5 - 0.0015(600) = 2.6 \text{ MPa} \tag{3.32}$$

According to the DIN 1052 design method the axial resistance, $R_{ax,d}$, of the glued-in rod fasteners for the given geometric and material properties is equal to 113 kN. This resistance was determined from equation (3.33) for both the beam and column connections.

$$R_{ax,d} = \pi d l_{ad} f_{k1,d} = \pi(19)(600)(2.6) = 113 \text{ kN} \tag{3.33}$$

3.2.8.7 Duration of Load Considerations

The resistance calculations presented for the three different design methods were developed for short duration loading and therefore apply to seismic design considerations. As a result, load duration factors, such as 1.15 from the Canadian Wood Design Manual, CSA O86 (2009) for short term loading, were not required for the design of the glued-in rod connections. However, there was a lack of research pertaining to the load duration effects on glued-in rod fasteners constructed from Canadian materials. Because of uncertainty and variability in the assumptions made with regards to timber-adhesive interface characteristics, these short duration resistances were compared to the findings of the associated single rod experimental investigation in Chapter 5 to validate the short term fastener resistance calculations.

3.2.8.8 High Cycle Fatigue Considerations

The wind loading consideration for the lateral load resisting systems required that the glued-in rod connections be designed against high cycle fatigue failure. The GIRod report (2002) suggests a fatigue resistance modification factor to account for the connection fatigue strength, $f_{fat,d}$, of glued-in rod connections loaded under high cyclic conditions determined by equation (3.34):

$$f_{fat,d} = \frac{k_{fat} f_k}{\gamma_{M,fat}} \tag{3.34}$$

where f_k is the nominal static resistance of the glued-in rod fasteners determined in sections 3.2.8.4, 3.2.8.5 and 3.2.8.6. Additionally, k_{fat} is the cycle fatigue factor and $\gamma_{M,fat}$ is the fatigue partial factor.

The factor, k_{fat}, is dependant on the number of high frequency loading cycles and the intended failure mode of the connection design, determined graphically from Figure 3.11. The ultimate limits of the fatigue factor are presented in Table 3.8 depending on the anticipated failure mode. The designed failure mode of shear pull tear-out provides an ultimate fatigue factor of 0.2. Therefore, based on the logarithmic cycle-factor relationship of Figure 3.11 the fatigue factor for the 2000 wind cycles, part of the frame loading protocol, was determined to be 0.47 using

equations (3.35) and (3.36).

$$m = \frac{\log(\frac{k_{fat,n}}{k_{fat,o}})}{\log(\frac{x_n}{x_o})} = \frac{\log(\frac{0.2}{1})}{\log(\frac{10^7}{1})} = -0.1 \tag{3.35}$$

$$k_{fat,2000} = \frac{k_{fat,1}}{x_o^m} x_n^m = \frac{1}{1^{-0.1}} 2000^{-0.1} = 0.47 \tag{3.36}$$

The fatigue partial factor $\gamma_{M,fat}$ is dependant on limit states design considerations of the glued-in rod connections. For serviceability limit states (SLS) a fatigue partial factor of 1.0 was assigned for fatigue resistance considerations. However, The factors shown in Table 3.9 are specific to connections design for ultimate limit states (ULS) and are dependent on connection inspection considerations. The potential for pre-tensioning relaxation as well as the uncertainty in the long term performance and splitting susceptibility of grouped glued-in rod connections provides a basis for periodic inspections to be performed on glued-in rod fasteners utilized in such vital structural frameworks as the seismic force resisting system. This consideration stipulates that the partial fatigue factor be defined by connections accessibility. The embeddment characteristics of glued-in rod connections limits visual inspection accessibility of the timber-adhesive interface suggesting these connections can be classified under poor access conditions. Therefore, the fatigue partial factor of 2.5 was selected based on these considerations.

The individual glued-in rod and combined connection fatigue resistances were evaluated to ensure the structural integrity of the hybrid braced frame when subjected to 2000 wind loading cycles during the ASCE 7-05 (2005) wind simulation testing procedure. The factored fatigue resistances for the three design methods were determined for both SLS and ULS. The GIRod Project (2002) design method factored fatigue resistance for SLS design considerations were calculated as 57.8 kN and 58.8 kN for a single glued-in rod utilized in the beam and column, respectively (refer to equation (3.37)).

$$f_{fat,2000} = \frac{k_{fat,2000} f_k}{\gamma_{M,fatSLS}} = \frac{0.47(123)}{1.0} = 57.8 \text{ kN} \tag{3.37}$$

Table 3.8: Ultimate Fatigue Modification Factors (Bengtsson et al. (2002))

Failure Mode	$k_{fat,\infty}$ coefficient
Failure in Timber Section	
Compression Failure	0.6
Tension Failure	0.3
Cyclic Failure (Tension-Compression)	0.3
Localized Failure in Timber	
Shear Plug Failure	0.2
Failure in the Adhesive	
Adhesive Failure	0.2
Failure in the Rod	
Steel Rod Failure (Lateral Loading)	0.25
Steel Rod Failure (Lateral Loading)	0.15

Table 3.9: $\gamma_{M,fat}$ Factors for Damage Intolerant Structures (Bengtsson et al. (2002))

Level of Inspection	$\gamma_{M,fat}$ coefficient	
	Fail Safe Joints	Non-Fail Safe Joints
Periodic Inspection, good access	1.5	2.0
Periodic Inspection, poor access	2.0	2.5
No Inspection or Maintenance	2.5	3.0

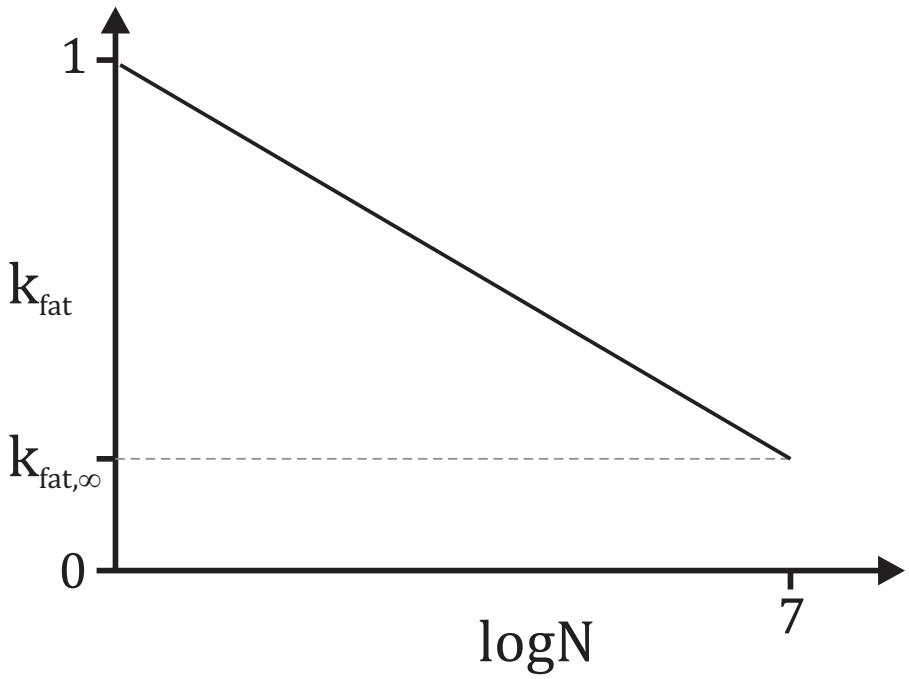

Figure 3.11: k_{fat} factor values related to number of load cycles (Adapted from Bengtsson and Johansson, 2002)

This resulted in in total beam and column connection capacities of 231.2 kN and 407.4 kN, respectively. The factored single rod fatigue resistances specific to SLS design for the LICONS Report (2003) and DIN 1052 (2004) were calculates as 54.1 kN and 53.1 kN, respectively. Therefore, the beam connection capacities of the two design methods were determined to be 216.4 kN and 212.4 kN. The column connections provided factored SLS fatigue resistance of 432.8 kN and 424.8 kN. The ULS single rod design resistances were determined from the fatigue partial factor for the periodic inspiration of poorly accessible connections. The single fastener resistance of the beam and column connections were calculated as 23.1 kN and 23.5 kN from the GIRod Report method using equation (3.38).

$$f_{fat,2000} = \frac{k_{fat,2000} f_k}{\gamma_{M,fatULS}} = \frac{0.47(123)}{2.5} = 23.1 \text{ kN} \tag{3.38}$$

Providing significantly lower full connection capacities than the SLS fatigue strengths of 92.4 kN and 188 kN, respectively. The factored single rod wind loading resistances of 21.6 kN

and 21.2 kN were determined for the LICONS Report (2003) and DIN 1052 (2004) design procedures respectively. These resulted in connection capacities of 86.4 kN and 84.8 kN for the beam connection and 172.8 kN and 169.6 kN for the column connection.

The high cycle fatigue resistance calculation procedures were developed from small scale moderate loading cycle testing program that required assuming behaviour characteristics of glued-in rods subjected to high number of loading cycles (Bengtsson and Johansson, 2002). The hybrid braced frame investigation would evaluate the validity of the design assumptions made and determine the accuracy of the fatigue strength design method.

3.2.8.9 Pre-tensioning Considerations

The application of pre-tensioning in the glued-in rods aims to limit gap formation and prevent impact loading on the timber sections during randomized seismic loading scenarios. Therefore, pre-tensioned glued-in rod connection conditions were considered in the design and testing of the hybrid braced frame prototype to determine in gap formation between the steel and timber sections would impact seismic performance. The connections were also designed for a pre-tensioned resistance equal to 70% of the glued-in rod governing resistance in accordance with the maximum pre-tensioning force criteria of the steel design standard (CSA S16, 2009). Therefore, the failure criteria dictates that connection failure occurs once the combined force in the rods has exceeded 70% of the tensile capacity of the connection. At this stage of loading, a gap should form between the timber element and the steel section. Theoretically, this gap formation can cause pounding or impact loading on the timber members if the load is suddenly reversed, which could effect connection strength and timber resilience. This force transfer behaviour is shown in Figure 3.12. The resulting pre-tensioned single rod axial capacities for the GIRod Report for the beam and column connection are 86.1 kN and 87.5 kN. Where the pre-tensioned resistance of the LICONS and DIN 1052 design methods are 79.1 kN and 80.5 kN respectively.

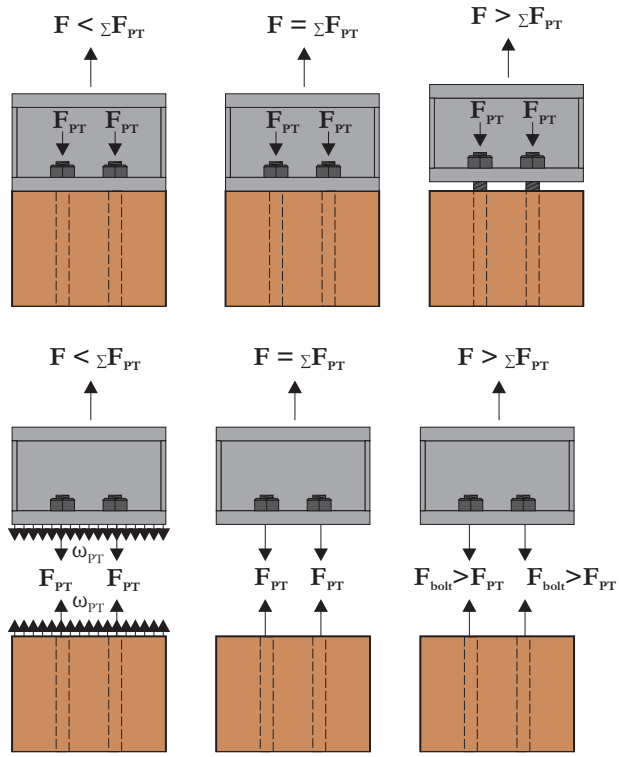

Figure 3.12: Pre-Tension Force Transfer Mechanism

3.2.8.10 Final GIRod Connection Details

The final design and detailing of the beam and column connections was completed after the governing axial capacity of glued-in rods was established for an embedment length of 600 mm. The preliminary beam connection design containing two glued-in rod fasteners was satisfactory from an ultimate limit states perspective. However, given the stringent connection performance requirements it was deemed insufficient because each rod was require to resist a force of approximately 100 kN, which had the potential to induce plastic behaviour in the connections. Initially, consideration was given to a connection detail containing three glued-in rods. However, this layout would have induced prying action in the base plates of the beam connections due to connection eccentricity. As a result, a more symmetric connection detail was required. In an attempt to ensure elastic behaviour and satisfying beam geometric constraints, four glued-in rods were selected for the final connection design. This design would provide nominal axial pull-out resistances based the GIRod Report, LICONS Report, and DIN 1052 design procedures of 492

kN, 460 kN and 452 kN, respectively. Furthermore, the total factored pre-tensioned resistance of the beam connection for the three design procedures was determined to be 344 kN, 322 kN and 316 kN, respectively. Figure 3.13 shows the final beam connection detail including the spacing and edge distance dimensions selected to satisfy the minimum criteria. In the direction of the beam depth, the spacing and edge distances were detailed to be 108 mm and 60 mm, respectively. However, due to the reduction in the member width the spacing was reduced to be 102 mm and the edge distance of 60 mm remained in this direction.

The final column connection was detailed with eight glued-in rod fasteners to resist the high axial forces while ensuring elastic behaviour within the timber-adhesive interface. The total pull-out resistance of the connection design determined from the GIRod Report, LICONS Report, and DIN 1052 design procedures were 1000 kN, 920 kN and 904 kN, respectively. Where the pre-tensioned axial resistances of the three methods were determined to be 700 kN, 644 kN, and 633 kN, respectively. This would provide a strong and symmetrical connection capable of withstanding the anticipated capacity design forces. Additional, given the long embedment length and overall nominal connection resistance the connection should be able to withstand high cycle fatigue failure during the wind loading tests. The connection dimensions in the vertical direction consisted of spacing and edge distances of 109 mm and 65 mm, respectively. The horizontal direction was detailed with spacing and edge distances of 157 mm and 85 mm. Figure 3.14 shows the final column connection detail.

Additionally, the final beam and column geometry presented was governed be the spacing and edge distance requirements previously discussed. This resulted in a beam section size of $228x222$ mm and a column section size of $457x327$ mm. Lastly, the governing axial resistance calculations provided over-strength factors of 2.5 and 1.75 for the non pre-tensioned and pre-tensioned details of both the beam and column connections. This design philosophy intended to allow both the primary and secondary failure mechanisms to fully develop to satisfy excessive inelastic demand prior to connection failure.

The strength property parameters for the design of glued-in rod fasteners were gathered from small scale tests. It is difficult of gather strength and fracture characteristics from large scale

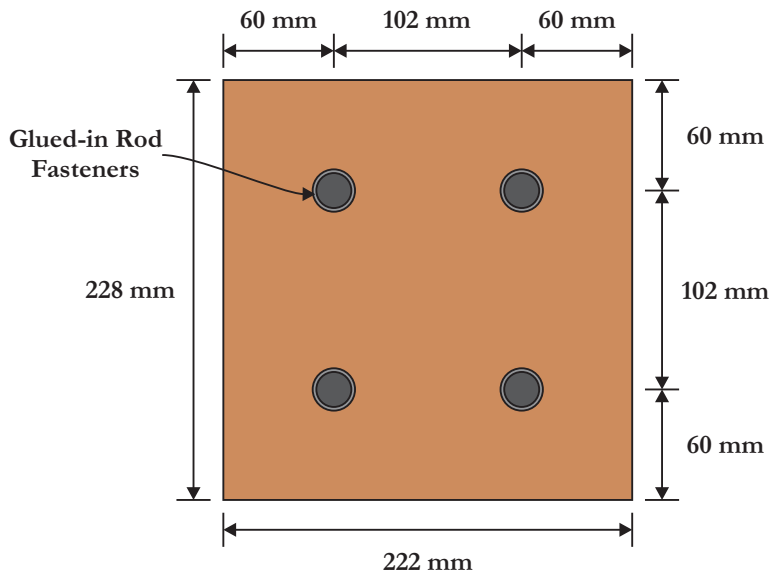

Figure 3.13: Final Detail of the Glued-in Rod Beam Connection

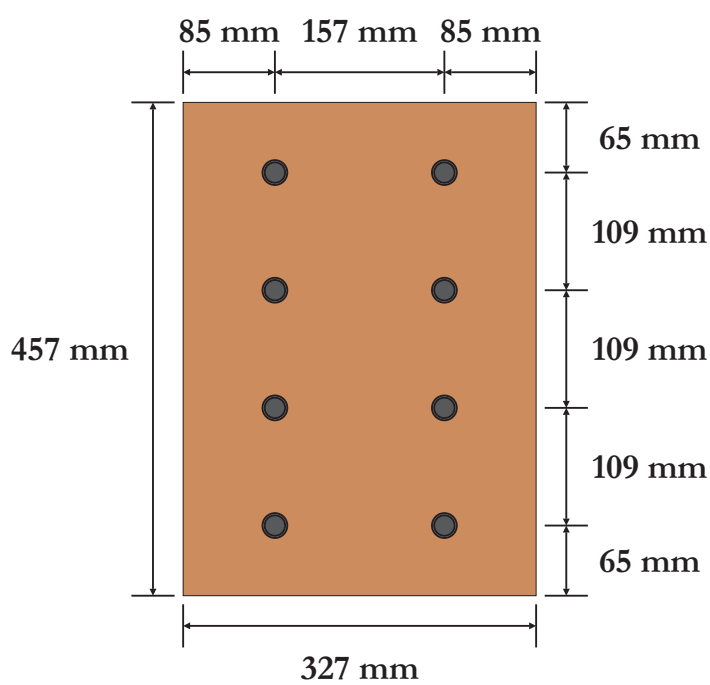

Figure 3.14: Final Detail of the Glued-in Rod Column Connection

tests that are representative of that entire embeddment range applicable to the fasteners (Serrano 2001). As a result, testing of specimens intended for structural application was necessary to validate and calibrate the design calculations. Based on this consideration, an associated study on the monotonic and cyclic strength characteristics of single rod specimens containing the same fastener detail was conducted. The findings of this experimental investigation are discussed in Chapter 5.

3.2.9 Intermediate Steel Connection Components

The intermediate brace connection design was dependant on the final sizes of the timber beam and columns. The steel section was designed to line up flush to the edges of the timber members to provide a more ascetic appearance. Furthermore, through the application of capacity design principles the intermediate brace connection was designed and detailed in accordance with the requirements of the Canadian design standards for steel construction (CSA S16-09). The connection type was selected to replace the damage prone beam column interface of conventional heavy timber frames, where failures associated with fastener behaviour and tension perpendicular-to-grain forces can compromise the structural integrity of the connection zone. Figure 3.15 shows the intermediate brace connection detail complete with the capacity design forces considered for the section design. The compression resistance of the pre-fabricated section was designed using the standard resistance calculations. However, additional bearing resistance checks required for plate girders fabricated from steel plate were used to ensure the structural integrity of the web, flanges and stiffeners. The shear resistance at the beam-column location above gusset plate was analysed against the vertical force component, V_{brace}, of the anticipated capacity design forces, to ensure shear failure would not occur in this region of the connection.

Special consideration was given to prying action in the base plates fastened to the glued-in connections, shown in Figure 3.16. A thin bearing plate design could experience deforms at high force levels causing force amplification in the glued-in rod fasteners that could exceed the capacity design forces. To avoid this behaviour, the prying checks presented in CSA S16 (2009) were used to determined adequate base plate thicknesses. Additionally, this design would ensure even force

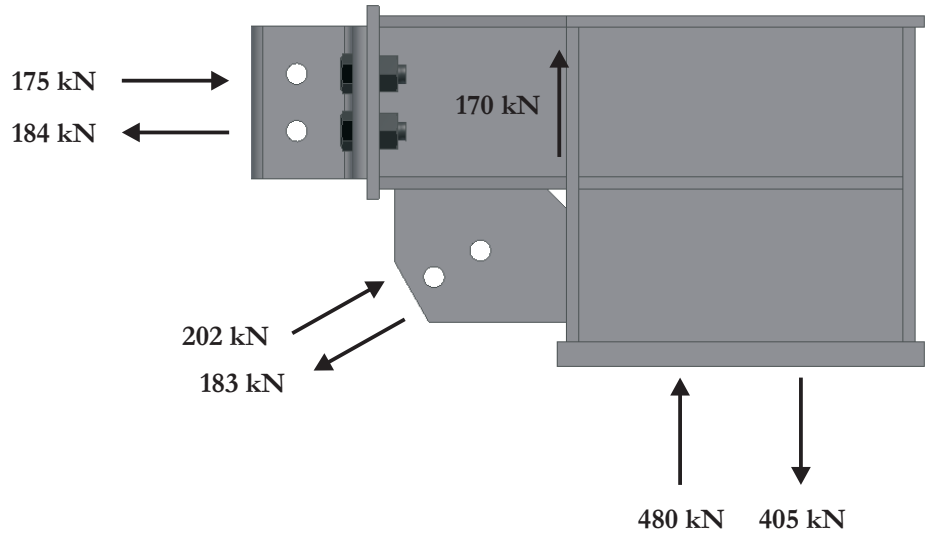

Figure 3.15: Intermediate Brace Connection Design Force Detail

distribution to the fasteners which would provide a more accurate analysis of the connection stiffness and cyclic behaviour of the glued-in rods. The susceptibility of the plates to prying is dictated by the plate thickness and geometric layout of the fasteners. For the prying analysis the plates were analysed as t-stub sections, providing the worse case loading scenario resulting in a conservative plate design.

To avoid the limiting characteristics of welded side plates the double angle connection detail was selected for the beam pin connection. In addition to ease of construction, this detail also provided access to the pin connection interfaces to allow for inspection during testing that did not require moving the beam section out of alignment.

The beam connection was designed to efficiently transfer the seismic and gravity loads

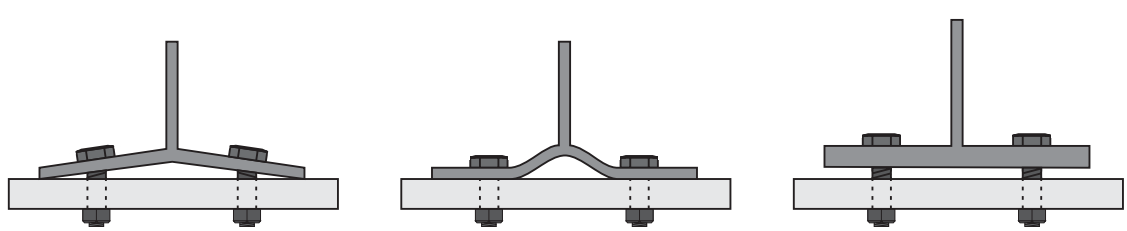

Figure 3.16: Prying Action
a) Single Curvature Bending b) Double Curvature Bending
c) No Prying Due To Adequate Plate Thickness

awhile accommodating frame rotations and moisture effects. In the frame analysis the bolted shear connection was assumed to be a pinned connection capable of providing the rotation demands required to transfer the seismic forces in pure tension and compression. In reality the connection would impart additional forces to the glued-in rod fasteners due to rotational friction between the connection interfaces. Because of the small magnitude of these forces, the effect was not considered in the fastener and connection designs. However, according to the seismic provisions of CSA S16 (2009), the bolts must be pre-tensioned to prevent connection slip. Therefore, attention was given to the connection behaviour during the hybrid braced frame tests to evaluate the accuracy of the pinned connection assumption made in the structural analysis.

The steel beam connection component was originally designed to resist the high capacity design forces while considering environmental effects. As a result, the holes in the base plate used for the glued-in rod connection were detailed as slotted bolt holes, as shown in Figure 3.13 a). This design would accommodate geometry changes due to variations in moisture content in the timber over the life span of the structure. The spacing of the slotted holes was governed by the location of the glued-in rod fasteners. However, the requirements outlined in the steel design standard, CSA S16-09 (2009), were also satisfied with this configuration. This design is intended for practical applications, however, the effect of pre-tensioned and the development of friction forces between the steel and the wood could restrain the movement. The slotted bolt hole design meant a bearing hanger detail was required for the continuous transfer the gravity loads to the columns. The length of this hanger was designed using the timber bearing resistance calculations presented in CSA O86 (2009). The design confirmed that a bearing plate detail of 222x25 mm would satisfy the timber section requirements. However, to facilitate fabrication the bearing length was increased from 25 mm to 100 mm. The side stiffeners were welded to the hanger bearing plate and slotted base plate to provide a continuous steel section. Additionally, the base plate thickness of 32 mm (1-$\frac{1}{4}$ inches) was selected based on the most conservative prying requirement.

The controlled laboratory environment and test arrangement parallel to the floor meant the slotted bolt holes and bearing hanger details could be removed from the intermediate beam connection to simplify the design and reduce fabrication costs. However, the bearing resistance

perpendicular to the holes of the glued-in rod connection for this alternate design was checked to ensure the connections could support the member self-weight and loads associated with construction and installation. Figure 3.17 shows the initial beam connection detail intended for the hybrid timber-steel building and the connection design used in the hybrid braced frame prototype.

3.3 Design of Timber Members

The strength capacity of the half scaled preliminary timber elements was checked against the scaled capacity design forces. The geometry of these sections was increased in the later stages of the capacity design procedure as a result of the spacing and edge distances required by the GIRod Report design guidelines for the glued-in rod connections. However, the strength of the increased sections was calculated again using the new material properties shown in Table 3.7 to ensure the capacity design forces did not exceed the factored member resistances. The load duration factor of 1.15 was assigned to all resistance calculations relevant to the anticipated seismic forces. Where the resistance check pertained to the governing gravity load case for the beam design, a factor of 1.0 was used. Tension and compression strengths are the primary force resistances that govern the seismic performance of the hybrid braced heavy timber frame. These member strengths were checked using equations (3.39), (3.40) and (3.41) taken from clauses 6.5.11 and 6.5.8.4.2 CSA O86 (2009).

$$T_{r,n} = \phi F_{tn} A_n \tag{3.39}$$

$$T_{r,g} = \phi F_{tg} A_g \tag{3.40}$$

$$P_r = \phi F_c A K_{Zcg} K_c \tag{3.41}$$

The bearing resistance parallel-to-grain of the timber sections had to be determined to ensure the sections could resist the end grain surface bearing resulting from the base plates of the

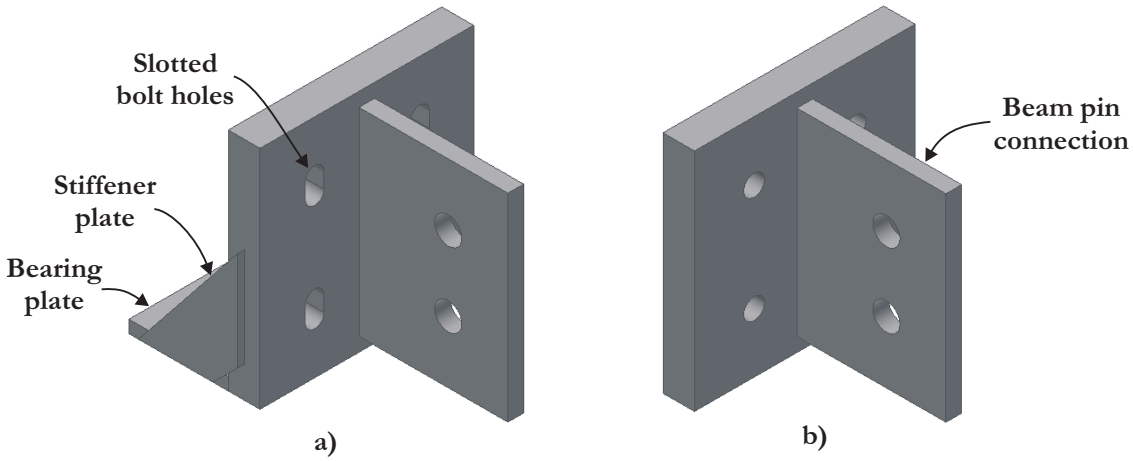

Figure 3.17: Beam Connection Details
a) Complete Connection Design b) Hybrid Frame Prototype Design

intermediate steel connection as they are loaded in compression. Although, there is not a defined equation for this strength characteristic, equations (3.41) was used with the added assumption that the slenderness factor, K_c, was equal to 1.0. The theoretical gravity loads imparted on the beam element induces shear forces and bending moments that were checked against the member resistance. The shear resistance was checked using clause 6.5.7.2.1 of CSA O86 (2009) and the moment capacity for local buckling and lateral torsional buckling was checked using clause 6.5.6.5 of CSA O86 (2009). In all cases, the increased member sizes provided more than adequate resistance to ensure elastic behaviour would occur throughout the testing program.

3.3.1 Shrinkage and Moisture Considerations

Environmental conditions can induce changes in the moisture content of structural timber elements that can affect member strength and dimensions. The changes in section geometry can cause splitting in the timber connections. This behaviour can govern the strength capacity of timber joints exposed to fluctuations in ambient moisture content over the life span of the structure. The original design of the beam connections were detailed to accommodate moisture effects as previously discussed through the application of slotted bolt holes. The glued-in rod connections in the timber columns are more difficult to detail for these moisture effects. The spacing and edge distance used must be large enough that the perpendicular the gain stresses do

not induce splitting in the timber. Slotted bolt hole column connection details could not be used in the braced frame applications because any movement in the beam-column connection or eccentricity in the frame could develop shear forces in the column connection zone. This force development could result in slippage between the intermediate steel connection and the timber column that would impact the seismic performance of the lateral force resisting system. The lack of research in this area requires designers to relay on experience rather than specific guidelines when detailing these connection types.

3.4 Fire Performance

The fire performance of timber buildings, in particular timber connections, often limits the allowable building height for heavy timber structures (Frangi and Fontana, 2010). The exposed surfaces of timber connections limit the connection capacity and performance when exposed to fire. However, the embedment characteristics of glued-in rod fasteners and self-tapping screws within large heavy timber members, acts as a barrier against fire exposure, protecting against damage and improve connection fire performance (Milke, 2002). The surrounding timber will char after prolonged exposure to the flames, protection the virgin timber material and slowing heat transfer to the fasteners. Minimal consideration was given to the fire performance of the hybrid braced frame or glued-in rod connections. However, adhesives with improved fire performance can be used in glued-in rod connections at risk of fire damage. As long as the shear strength and fracture energy of the bonding agent satisfies the design guideline requirements. Additionally, the steel sections are vulnerable to strength and stiffness degradation when exposed to fire that could impact the performance of the hybrid system. Heat transfer from the steel connections into the threaded rods and surrounding epoxy could reduce the structural fire performance of the connection. However, this heat transfer can be limited through that application of intumescent paints that char when exposed to extreme heat to protect the underlying steel section and slow heat transfer.

3.5 Final Hybrid Frame Design Details

The final design and detailing of the hybrid braced frame prototype assembly is presented in Figure 3.18. These sections were designed in accordance with the Canadian and European design methods previously mentioned with special consideration given to current construction and fabrication methods used in industry. The seismic and wind performance of this innovative system will be discussed in detail in Chapter 6. Additionally, an experimental investigation into the strength and stiffness characteristics of the glued-in rod fasteners designed in section 3.2.8 will be presented in Chapter 5 to validate the design procedures and resistance calculations.

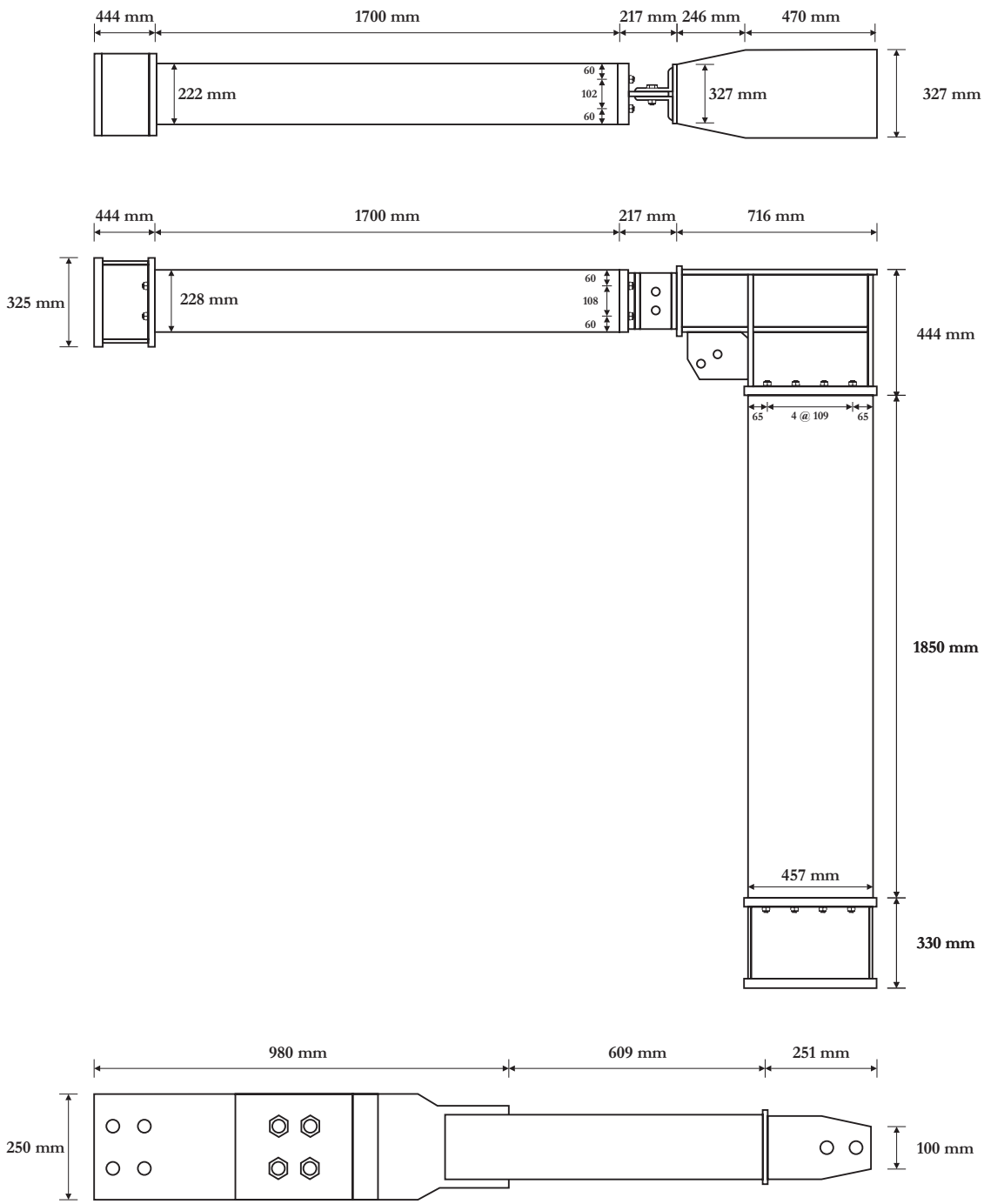

Figure 3.18: Final Hybrid Braced Frame Prototype Design

Chapter 4: Numerical Modelling

4.1 Objectives

Advanced computer modelling is used to evaluate the performance of innovative and complex seismic force resisting systems, such as those in this study. After the development and application of innovative hybrid and capacity design concepts, a numerical modelling investigation was chosen for a seismic evaluation, to confirm the design assumptions and expected building performance of the response spectrum analysis. The nonlinear dynamic analysis was performed at the maximum-considered earthquake and design basis earthquake hazard levels using the seismic analysis software OpenSees (McKenna et al., 2000).

This chapter presents the techniques and methodology used in the evaluation of the seismic response comparison of geometrically similar hybrid timber-steel and steel-only structures containing buckling-restrained braced frames (BRBFs). This numerical modelling investigation had three primary goals. First, to conduct a seismic performance comparison of both structures that would evaluate whether capacity protected hybrid timber-steel buildings provide a viable seismic design alternative to steel-only structures. Since the buckling-restrained braces (BRBs) were designed as the ductile structural fuse, the second goal was to assess the seismic force demands on the structural components of the adopted models, to ensure all inelastic demands were satisfied by the BRBs. Lastly, a set of earthquake response records from the hybrid timber-steel structure were selected from the nonlinear time history analysis results for a dynamic force evaluation of the hybrid braced frame prototype, discussed in Chapter 6. This experimental validation would confirm the use of buckling-restrained brace force reduction factors in the seismic design of the hybrid timber-steel systems.

4.2 Prototype Building Designs

For this investigation, two complete six storey structures were analysed and designed according to Canadian design standards. The two structures contained a buckling-restrained braced frame (BRBF) in the outer grids spanning the north-south direction, and a moment-resisting frame (MRF) in the east-west direction, as shown in Figure 4.1. The primary focused of this study was on the seismic performance evaluation of the BRBF. The assessment of the MRF was conducted as part of an associated study conducted by Gohlich (2015). Both the hybrid timber-steel and steel-only structures were designed using the NBCC (2010) response spectrum analysis method, accounting for structural irregularities, notional loads, accidental torsion and P-delta amplification. The symmetrical building layout minimized torsional effects which allowed for the separate analysis of the BRBFs and MRFs according to NBCC (2010) response spectrum analysis specifications, prevented the MRFs from affecting the seismic analysis of the BRBFs. The design spectrum for Victoria BC was determined assuming site class C. Based on the seismic provisions of the NBCC (2010), both structures had a drift limit of 2.5% that had to be satisfied by the BRBFs. The steel building was designed using BRBF capacity design techniques typical of modern steel-only structure. The wood building was designed using hybrid steel-timber BRBF system, consisting of predominately heavy timber members that are fastened to intermediate steel connections. Identical building geometry was selected for both structures to facilitate seismic response comparison. Therefore, both structures were designed with a storey height of 3700 mm and bay width of 6500 mm.

A concrete composite deck floor slab system was utilized on the design of the steel structure on all levels, while 131-5s cross-laminated timber (CLT) panels provided a one-way slab floor system in the hybrid structure. The CLT panels were sized using the Nordic Inc. selection tables (Nordic Engineered Wood, 2013a) and strength calculations were completed following the CLT Handbook (FPInnovations, 2010). The mass timber panels resulted in a significant reduction in storey dead loads and seismic weight of the hybrid timber-steel structure compared to the steel-only building. As a result, the design base shear of the hybrid structure was approximately 61%

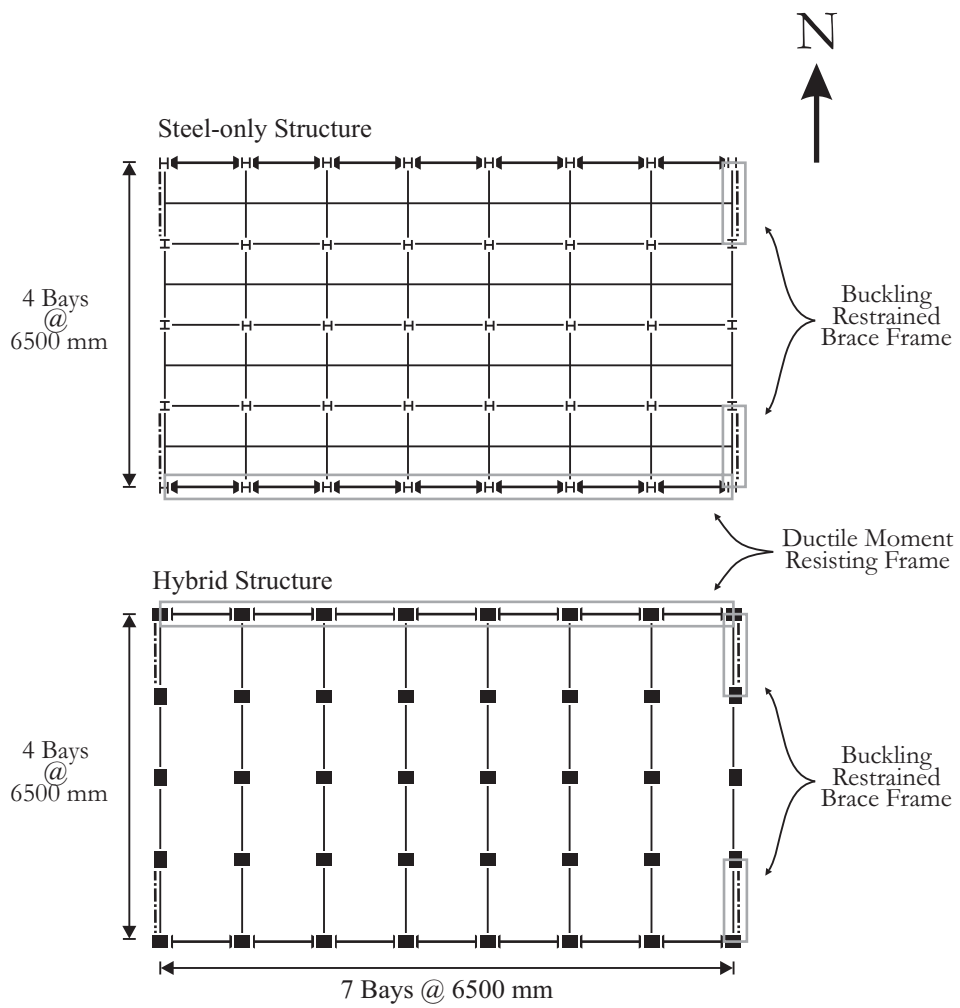

Figure 4.1: Plan View of Building Layouts

of the design base shear for the steel-only building. A comparison of the seismic weight and design base shear for the two structures are presented in Table 4.1. A complete discussion into the seismic design of the two buildings is presented in Appendix B.

The BRBFs diagonal bracing frame geometry was selected to minimize foundation forces and optimize the lateral force transfer through the frames. A generalized layout of the structural elements for both the hybrid timber-steel and steel-only BRBFs is shown in Figure 4.2. Since the BRBFs were designed as the seismic force resisting system in both the hybrid and steel-only structures, the BRB R_d and R_o factors were assigned to both buildings. Using these factors in the seismic design of both structure assumed that all of the plastic behaviour would occur in the ductile BRBs. The R_d and R_o factors 4.0 and 1.2 were taken from the NBCC (2010) for ductile buckling restrained braced frames. The core areas and yield strength of the BRBFs for the hybrid and timber structures are provided in Table 4.2. The surrounding structural elements were capacity designed to protect the brittle glulam members and prevent failure in the steel sections. For the capacity design of the BRBFs, an overcapacity of 10% was assigned to the probable tensile and compressive brace forces, as dictated by CSA S16-09 (2009).

The design of the steel-only system followed modern steel design practices currently used in industry. By using pre-fabricated sections and typical connection details, the steel building design provided a model comparable to current steel structures containing BRBFs. Therefore, the steel-only structure was expected to withstand the majority, if not all, of the MCE records while satisfying the NBCC (2010) seismic performance criteria for interstorey drifts.

Table 4.1: Summary of Seismic Properties

Building Type	Seismic Weight (kN)	Design Base Shear (kN)
Hybrid Timber-Steel	18933	1130
Steel-only	31276	1866

Table 4.2: Summary of Seismic Properties

	Hybrid Timber-Steel		Steel-Only	
Storey	BRB Core Area (mm^2)	Yield Strength (kN)	BRB Core Area (mm^2)	Yield Strength (kN)
Roof	510	169.8	796	266.4
5	720	239.8	1111	369.6
4	795	264.7	1306	436.2
3	920	306.4	1487	499.5
2	1040	346.3	1682	564.4
1	1140	379.6	2042	679.3

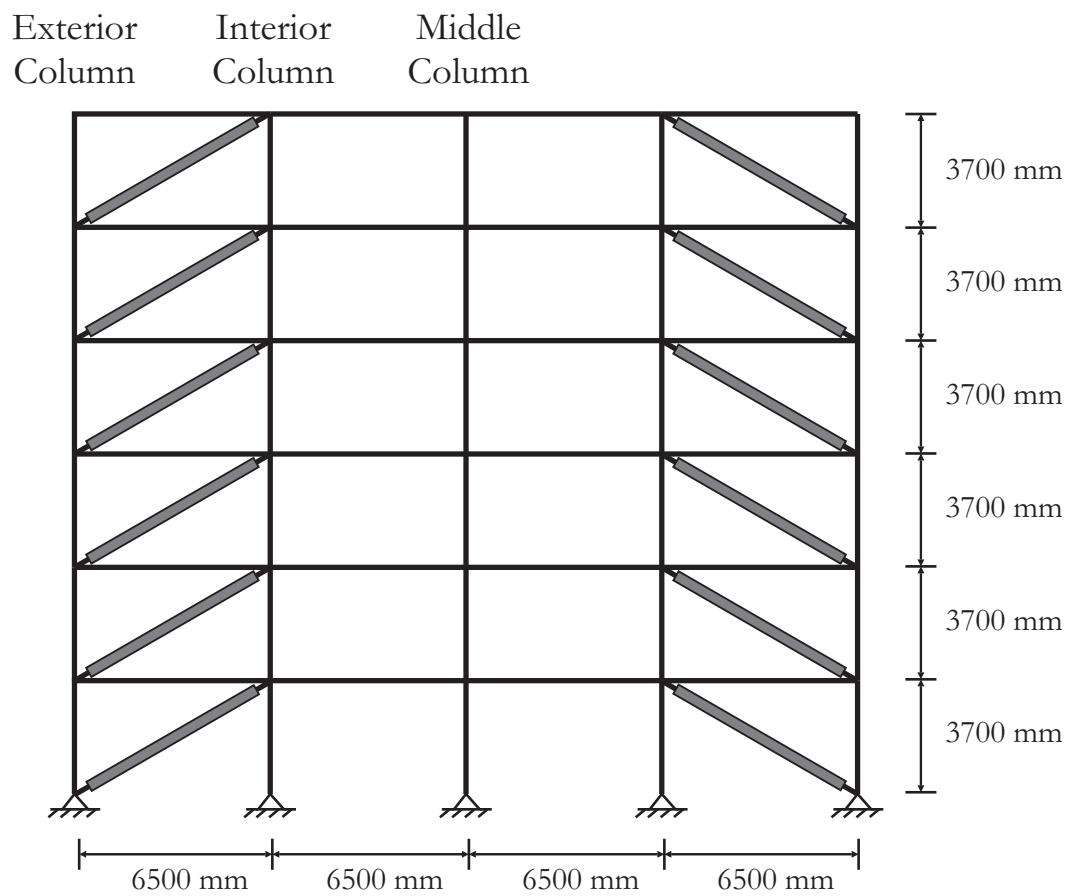

Figure 4.2: Elevation view of Building Layouts

However, when subjected to long duration ground motions, heavy timber connections are prone to bearing failure, fastener yielding and splitting perpendicular to the grain direction. The hybrid BRBF system methodology was designed to provide an alternative ductile yielding mechanism to fastener failures in the wood building. Therefore, the timber members in the hybrid system could be easily capacity designed to localize all damage and energy dissipation to the BRBs, as previously discussed in Chapter 3. For the hybrid timber-steel BRB frame design, the damage prone beam-column-brace connection zone was replaced by a steel joint assembly. This design used glued-in rod connections at the connection interfaces that were used to fastener the intermediate steel connections to the wood elements. These connections are typically comprised of a single or group of threaded steel rods, embedded into the end-grain of heavy timber members using structural grade adhesives. Glued-in rods predominantly resist axial loads, transferred along the embedment length of the fasteners. This enables the transfer of forces into the strong, parallel to grain direction of the glued laminated (glulam) beams and columns. The glued-in rod connection, steel assembly, and wood members were all capacity designed, based on the probable brace forces, to remain elastic during an earthquake. The glued-in rod connections were designed using the worst-case of the GIROD Project and the LICONS Report Eurocode 5 design proposal, with an additional check completed using the method outlined in the German Design Code (Bengtsson et al. 2002; Connolly et al. 2003 & NABau 2004). Intermediate brace connections of the hybrid timber-steel frame were sized to the final member dimensions governed by the glued-in rod design. This braced frame connection is also applicable to other types of bracing systems in addition to the BRB, including friction braces, viscous dampers, and self-centering braces.

4.3 Brace Model Calibration

Buckling-restrained braces (BRBs) were modelled using spring elements. The uniaxial Giuffre-Menegotto-Pinto material in OpenSees was used to represent the steel brace core because it accounts for kinetic and isotropic strain hardening properties of steel. Prior to establishing the post yield charcteristics of the steel yielding core, the initial series stiffness of the BRB was calculated based the geometry of the inner steel yielding core. The geometry and lengths of the

BRB and rigid gusset plate connection zones were determined based on brace geometry equations and industry modelling information provided by Star Seismic (Personal communication, April 08, 2015), shown in Figure 4.3. The brace length, L_{brace}, was determined from the braced frame geometry using Equation 4.1:

$$L_{brace} = \frac{L_b}{\cos\theta_b} \tag{4.1}$$

where, L_b is the beam length measured from the center of the columns, and θ_b is the braced angle. The rigid connection length, L_{rigid}, was determined to establish the effective brace length required to estimate the elastic stiffness of the BRBs. The rigid connection zone length was calculated using Equation 4.2 (Personal communication, April 08, 2015).

$$L_{rigid} = \text{Max}\begin{cases} W\tan(\theta_b) + \dfrac{w_c}{\cos\theta_b} + \dfrac{50.8}{\cos\theta_b} \\ \dfrac{W}{\tan\theta_b} + \dfrac{d_b}{\sin\theta_b} + \dfrac{50.8}{\sin\theta_b} \end{cases} \tag{4.2}$$

where, w_c is the column width, d_b is the beam depth, and the effective width, W, was calculated from Equation 4.3 based on the brace core area A_{bc} (Personal communication, April 08, 2015).

$$W = 10.16A_{bc} + 76.2 \tag{4.3}$$

After the general brace length and rigid connection zone details were established, the elastic brace length, $L_{elastic}$, and core area, $A_{elastic}$, were calculated using equations 4.4 and 4.5 (Personal communication, April 08, 2015).

$$L_{elastic} = 289.9\ln(A_{bc}) + 1294.0 \tag{4.4}$$

$$A_{elastic} = 3.2A_{bc} + 38.1 \tag{4.5}$$

Finally, once the frame and brace geometry was established the elastic brace stiffness, K_{brace}, was calculated by equation 4.6 (Personal communication, April 08, 2015).

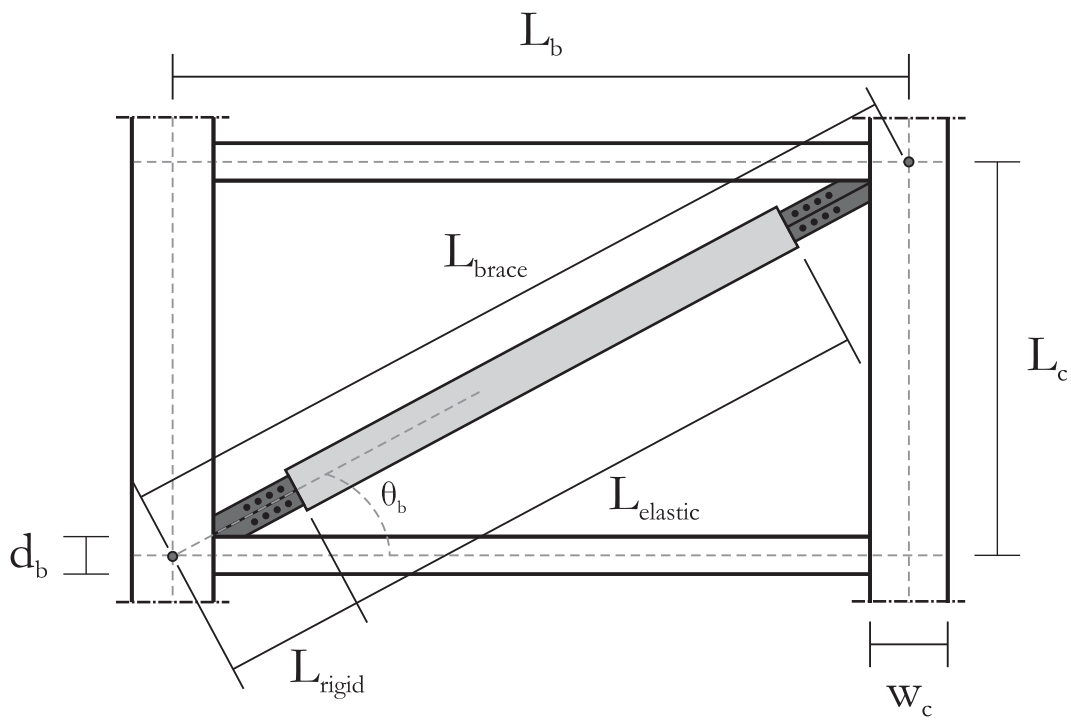

Figure 4.3: Elevation view of Building Layouts

$$K_{brace} = \frac{E}{\frac{L_b - L_{elastic} - L_{rigid}}{A_{bc}} + \frac{L_{elastic}}{A_{elastic}}} \tag{4.6}$$

The initial brace stiffnesses determined from the brace core areas previously presented for both the hybrid timber-steel and steel-only structures are provided in Table 4.3.

After calculating the initial brace stiffness, the strain-hardening and isotropic hardening material parameters of the uniaxial Giuffre-Menegotto-Pinto material were calibrated to the experimental results of Tremblay et al., (2004), to model the BRBs. Increased strength in the compressive direction, due to friction effects within the brace, was not considered. A brace frame model was developed to calibrate the nonlinear parameters of the BRB material. The frame was subjected to a displacement controlled cyclic push-over analysis with deformation cycle intervals equal to the displacements of the loading protocol used by Tremblay et al., (2004). This iterative trial and error method was used to match the uniaxial material response to the BRB brace behaviour from Tremblay et al. (2004). The post-yield stiffness (post-yield tangent) of the

Table 4.3: Summary of Initial Brace Stiffnesses

Storey	Elastic Brace Stiffness (kN/mm)	
	Hybrid Timber-Steel	Steel-Only
Roof	19.29	30.19
5	28.35	44.65
4	31.40	54.01
3	36.51	61.80
2	43.44	69.84
1	47.78	82.94

model was set to 0.2%, which appears to have accurately represented the BRB core post-yield characteristics. In the first iteration, the nonlinear parameters were set at the default values of the supporting technical documents for McKenna et al. (2000). Prior to starting the subsequent iterations, the material parameters were adjusted to compensate for the variation in the model response compared to the test results. A comparison of the nonlinear BRB material response and the experimental results is shown in Figure 4.4, and the initial and final uniaxial Giuffre-Menegotto-Pinto material parameters are presented in Table 4.4.

4.4 Modelling Assumptions and Characteristics

Full-scale 2-D frame models were constructed to evaluate the seismic performance of the hybrid timber-steel and steel-only BRBFs when subjected to earthquakes at the MCE and DBE hazard levels. A rendition of the two-dimensional frame models is presented in Figure 4.5. Leaning gravity columns were assigned half the building weight and gravity loads, not directly tributary to the studied frames, to account for inertial forces and P-delta effects. The gravity loads tributary to the frames were lumped at the appropriate column nodes on each storey. The concrete composite deck and CLT floor slab system of the steel-only and hybrid structure, respectively, were modelled as rigid diaphragms by constraining horizontal displacement of the frame nodes

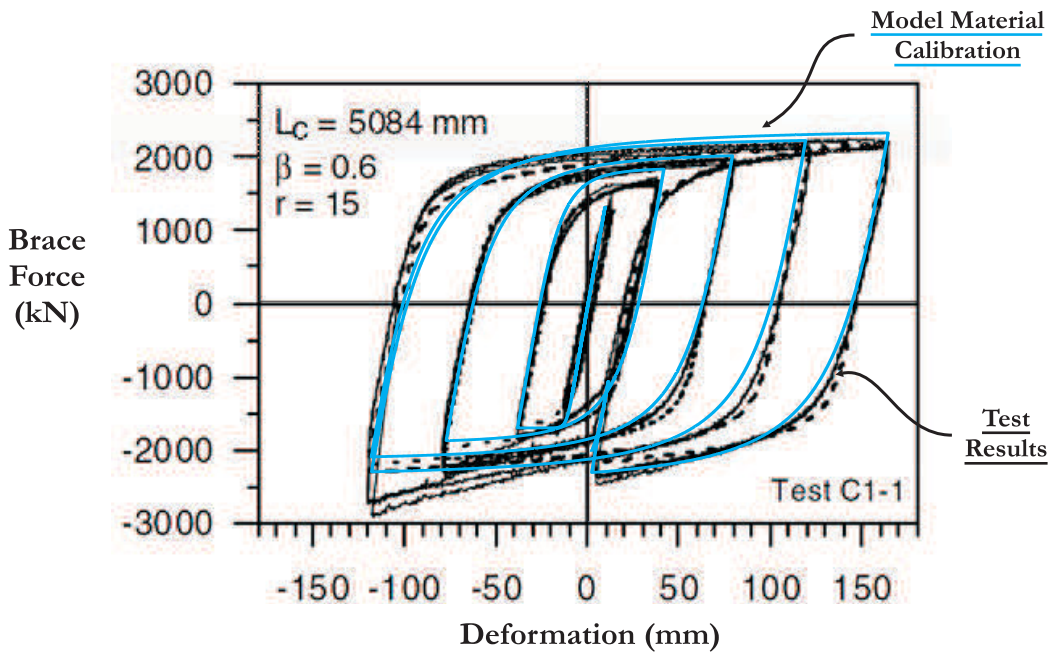

Figure 4.4: OpenSees Material Response Calibration Test Comparison

Table 4.4: Summary of Brace Material Parameters

Material Parameter	Initial Iteration	Final Iteration
R0	15	20
CR1	0.925	0.925
CR2	0.15	0.15
a1	0.0	0.075
a2	1.0	1.0
a3	0.0	0.075
a4	1.0	1.0

at each storey to the leaning column node at that storey. This modelling assumption, typical of steel structures, was validated for the CLT system by the numerical modelling investigation conducted by Ashtari (2009). The study showed that the high in-plane stiffness of CLT panels allowed these floor slab systems to act as rigid diaphragm behaviour. Additionally, the author determined that high lateral stiffness of the seismic force resisting system can influence the rigidity of CLT diaphragms and in some cases causing these systems to act as semi-rigid. However, this semi-rigid diaphragm behaviour was not considered in the hybrid BRBF modelling investigation.

As previously discussed, the beam and column elements of the frames were capacity designed to remain elastic. For this reason, the beam and column elements of both BRBFs were model using elastic beam-column elements. The appropriate strength and stiffness characteristics were assigned to the timber and steel sections based on the member design properties. Rigid offsets were modelled at the connection zones of the elastic beam-column elements to represent the intermediate brace connection and rigid panel zones of the hybrid and steel-only frames, respectively. The rigid joint dimensions of the hybrid BRBF were determined from the geometry the intermediate brace connections, while offsets of half the beam and column depths were assigned to the column and beam elements of the steel-only frame, respectively. All BRBs were modelled using two-node-link axial spring elements. The material models of the BRBs were defined by the previously determined initial brace stiffness, yield resistance, and nonlinear response parameters. Pin fixities were modelled at the beam shear connections using zerolength elements connected to two superimposed nodes that were constrained together in the vertical and horizontal directions. The base reactions were also modelled as pin supports.

4.5 Earthquake Acceleration Time-history Analysis

Nonlinear dynamic time-history analysis of each building was performed using OpenSees seismic analysis software (McKenna et al. 2000). Large displacement analysis was considered to account for P-Delta effects through the application of P-Delta geometric transformations on all columns. Typical for steel structures, 3% Rayleigh damping was assumed for modes 1 and 6 which provided conservative assumption for the wood structure (Welch et al., 2014). The dynamic

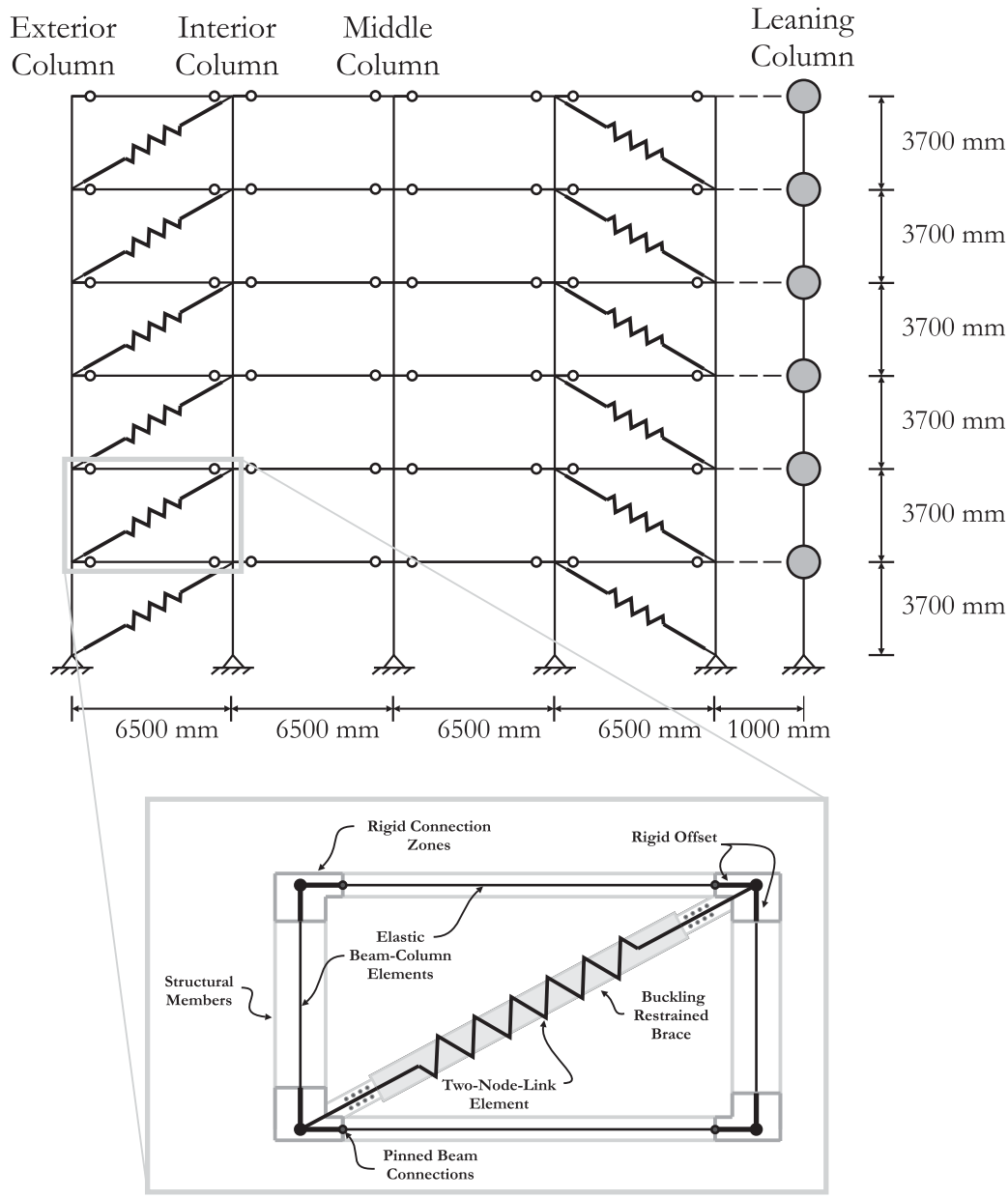

Figure 4.5: OpenSees Two-Dimensional Frame

ground motion time-histories of the full set of FEMA P695 (2009) far-field ground accelerations were applied to the frame at the support nodes. This far-field earthquake record set consists of two-directional horizontal ground accelerations recorded 10 km or more from the point of fault rupture (FEMA P695 2009). The records were previously normalized to the mean peak ground velocity (PGV) of the record set, meaning the PGVs of the individual ground motions were scaled to match the mean PGV of the entire record suite. This procedure eliminated dispersion of the ground motion characteristics associated with site conditions, magnitude effects and epicentral distance (Michaud and Léger, 2014). A summary of the velocity normalized far-field earthquake records is presented in Table 4.5 (FEMA P695, 2009).

4.5.1 Scaling of Ground Motions

The earthquake record scaling procedure presented in the FEMA P695 documentation, calibrated the ground accelerations based on the median spectral value, instead of calibrating the individual spectral intensities, to evaluate building performance (FEMA P695, 2009). The suite of 44 records were scaled using equation (4.7) (FEMA P695, 2009):

$$SF = \frac{S_{MT}}{S_{NRT}} \tag{4.7}$$

where, S_{MT} is the median spectral acceleration at the building first mode period for each 2D frame and S_{NRT} is the NBCC (2010) design spectral acceleration for Victoria, BC at the corresponding fundamental periods (FEMA P695 2009). This method matches the median spectral acceleration of the Opensees models to the spectral accelerations associated with the seismic hazard of the building site location. Since the NBCC (2010) spectral accelerations are defined for the MCE design level, these scaled records represent the seismic hazard level associated with the MCE. The records were then further scaled by a factor of 2/3 to attain an additional set of ground motions that approximated the seismic hazard level associated with the DBE. A summary of the first and second mode periods and the corresponding ground motion scaling factored for the hybrid and steel-only structures are presented in Table 4.6.

Table 4.5: Summary of ATC Far Field Ground Motions (FEMA P695, 2009)

Excitation ID #	Year	Station	Fault Type	Magnitude	$PGA_{Normalized}$ (g)
ATC F01	1994	Northridge	Thrust	6.7	0.34
ATC F02	1994	Northridge	Thrust	6.7	0.40
ATC F03	1999	Duzce, Turkey	Strike-slip	7.1	0.52
ATC F04	1999	Hector Mine	Strike-slip	7.1	0.37
ATC F05	1979	Imperial Valley	Strike-slip	6.5	0.46
ATC F06	1979	Imperial Valley	Strike-slip	6.5	0.39
ATC F07	1995	Kobe, Japan	Strike-slip	6.9	0.53
ATC F08	1995	Kobe, Japan	Strike-slip	6.9	0.26
ATC F09	1999	Kocaeli, Turkey	Strike-slip	7.5	0.25
ATC F10	1999	Kocaeli, Turkey	Strike-slip	7.5	0.30
ATC F11	1992	Landers	Strike-slip	7.3	0.24
ATC F12	1992	Landers	Strike-slip	7.3	0.48
ATC F13	1989	Loma Prieta	Strike-slip	6.9	0.58
ATC F14	1989	Loma Prieta	Strike-slip	6.9	0.49
ATC F15	1990	Manjil, Iran	Strike-slip	7.4	0.40
ATC F16	1987	Superstition Hills	Strike-slip	6.5	0.31
ATC F17	1987	Superstition Hills	Strike-slip	6.5	0.53
ATC F18	1992	Cape Mendocino	Thrust	7.0	0.45
ATC F19	1999	Chi-Chi, Taiwan	Thrust	7.6	0.18
ATC F20	1999	Chi-Chi, Taiwan	Thrust	7.6	0.49
ATC F21	1971	San Fernando	Thrust	6.6	0.44
ATC F22	1976	Friuli, Italy	Thrust	6.5	0.50

Table 4.6: Summary of Ground Motion Scaling Factors

Building Type	Periods		Scaling Factor	
	First Mode	Second Mode	MCE	DBE
	T_1	T_2	SF_{MCE}	SF_{DBE}
Hybrid Structure	1.51	0.54	1.21	0.81
Steel-only Structure	1.59	0.56	1.25	0.83

The decrease in seismic weight and lateral stiffness of the hybrid building compared to the steel-only building resulted in the two BRBF designs having similar periods. These similar first mode periods had an effect on the earthquake scale factors of each frame. Furthermore, the first mode periods were similar to the fundamental periods of 1.58 s and 1.70 s for the hybrid and steel-only ETABs models, respectively, that were used to design the buildings (discussed in Appendix B). This validated the accuracy of the system component assumptions and material characteristics used to model the two-dimensional frame.

4.6 Modelling Results and Discussion

Two-dimensional nonlinear dynamic analysis was conducted using the suite of 44 MCE level records and 44 DBE level records to compare the seismic performance of the six-storey hybrid and the six-storey steel-only BRBFs. Both the hybrid timber-steel and steel-only frames experienced collapse during the MCE level 1979 Imperial Valley earthquake. Therefore, the frame responses for this record were removed from the data analysis of the mean and standard deviation response parameters to avoid skewing the results. All response results were presented in the mean and the mean plus one standard deviation to account for variations in earthquake intensity.

4.6.1 Base Shear and Foundation Forces

The base shear of the two structures are compared in Table 4.7. It is important to note that the seismic weight of the hybrid structure was approximately 60% of the steel-only structure. This resulted in a reduction in total base shear of 40% in the hybrid BRBF, relative to the steel-only structure. This directly influences lateral load magnitudes which decreases member size demands and reduces building costs. Furthermore, the mean and mean plus one standard deviation base shears for both the MCE and DBE hazard levels exceeded the elastic design base shears of both the hybrid timber-steel and steel-only structures.

The foundation forces were concentrated in the column supports of the outer two bays,

Table 4.7: Summary of Seismic Base Shears

Building Type	MCE Base Shear Mean $V_{M\ b,\ MCE}$	MCE Base Shear Mean + SDev. $V_{M+SD\ b,\ MCE}$	DBE Base Shear Mean $V_{M\ b,\ DBE}$	DBE Base Shear Mean + SDev. $V_{M+SD\ b,\ DBE}$
Hybrid Structure	1510	1657	1420	1505
Steel-only Structure	2560	2756	2440	2544

characteristic of the frame geometry of the BRBFs. A summary of the foundation forces is presented in Figure 4.6. The diagonal bracing of the outer bays concentrated the foundation forces in these columns, while the brace orientation provided a slight reduction in the foundation forces on the exterior columns because of the lower force demands required to resist overturning. The middle column foundation forces were attributed to the gravity loads applied to both frames and the storey nodes. The reduced seismic weight and base shear experienced by the hybrid system had a direct affect on the foundation forces. The exterior column of the hybrid structure experienced 32% and 31% reductions in foundation force at the MCE and DBE hazard levels, respectively, compared to the steel-only structure. Additionally, 26% and 25% reductions in the MCE and DBE mean foundation force demands were observed in the interior column of the hybrid braced frame, compared to the steel-only structure. Overall, the lower seismic weight of the hybrid building, compared to the steel-only structure, decreased seismic demands and significantly reduced the base shear and foundation forces. These force reductions could help to improve the feasibility of heavy timber building, by reducing foundation size and member geometry.

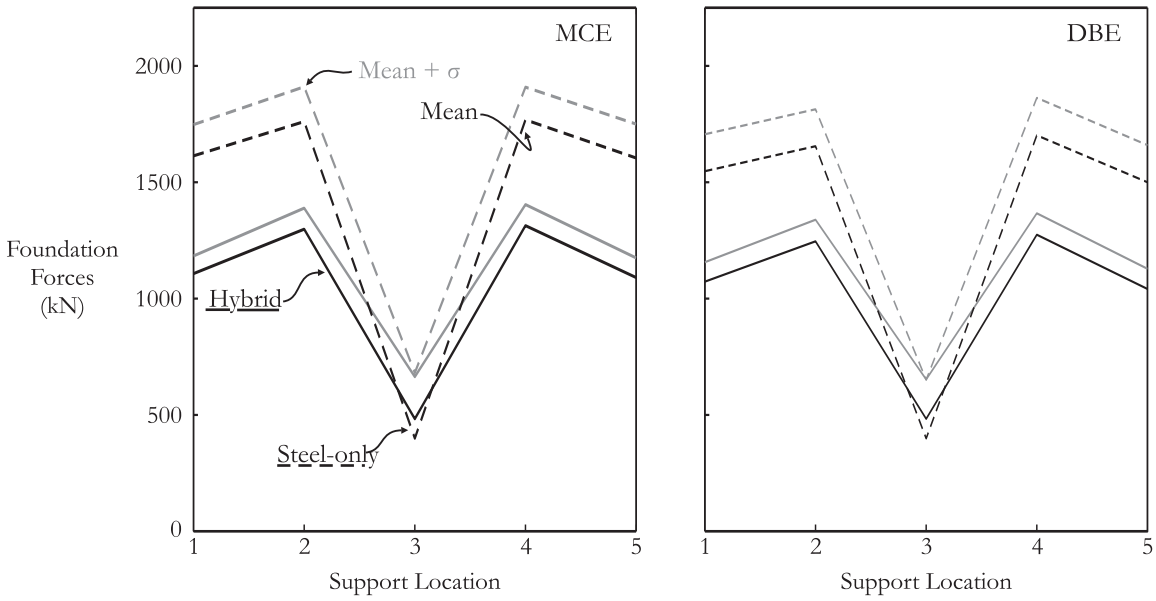

Figure 4.6: Foundation Forces

4.6.2 Interstorey and Residual Drift Response

The overall performance of the hybrid timber-steel and steel-only buildings were similar with respect to drift demands. The peak interstorey drift responses for both BRBFs (hybrid and steel-only) were within the NBCC (2010) requirement of 2.5% for buildings of normal importance. That was because the design of both BRBF systems was governed by strength requirements over drift performance which provided the frames with high lateral stiffness that limited the storey drifts. The interstorey drift responses of the six-storey hybrid and six storey steel-only structures are shown in Figure 4.7 in terms of the mean and mean plus one standard deviation response from the DBE and MCE hazard level earthquakes. The hybrid and steel-only structures had similar mean MCE-level peak interstorey drifts of 1.2% and 1.1%, respectively. The largest interstorey deformations occur in the lower stories of the BRBF due to drift localization caused by P-delta effects acting on the concentrated gravity loads in those stories (Ruiz-Garcia & Miranda, 2006). The DBE level response also showed similar drifts for the two types of BRBF structures. These drifts were well controlled, limiting the mean peak drifts to 0.72% and 0.74% for the hybrid and steel-only BRBFs, respectively.

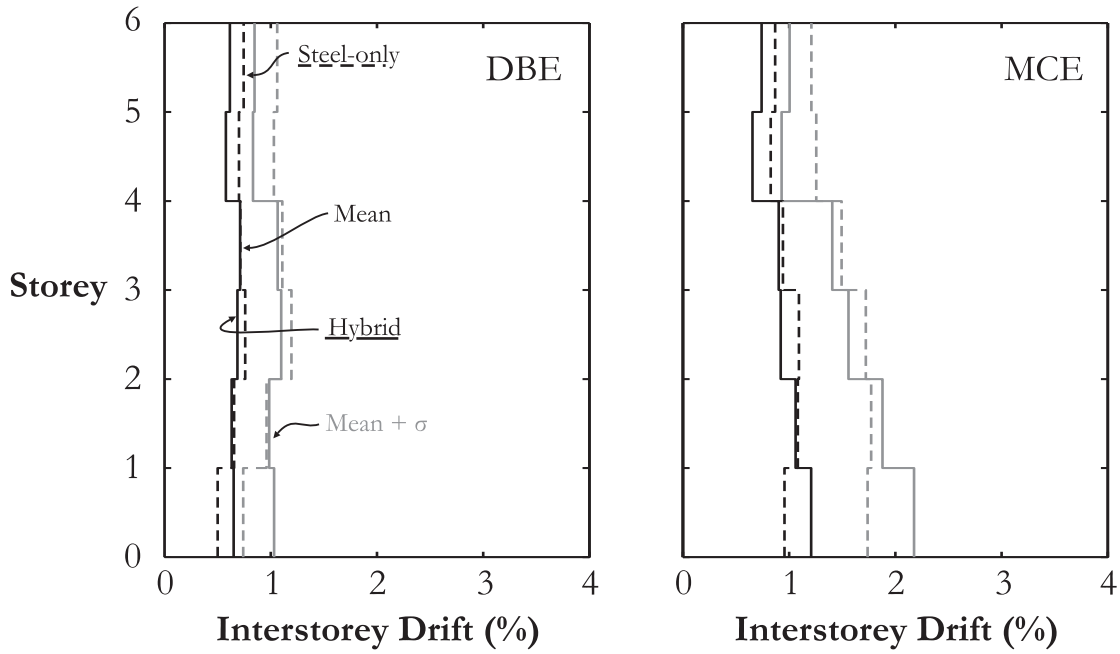

Figure 4.7: Peak Interstorey Drift Response

Since the NBCC (2010) does not explicitly outline allowable residual drift responses as part of performance-based design criteria, acceptable residual drift demands are not clearly defined. However, the residual drift responses may be used to assess the post-disaster performance of the buildings. A previous study conducted by McCormick et al. (2008), found that occupants can detect residual drifts of 0.5% to 0.6%, where residual drifts of 0.8% or greater can cause occupants to become ill and affected overall daily life. Therefore, as a baseline for performance-based design criteria, the authors suggest that residual drift limits remain below 0.5%. Figure 4.8 shows the residual drift responses for the hybrid and steel-only structures. The DBE level ground motions resulted in small mean residual storey drifts, limited to approximately 0.25% for both types of BRBF. Suggesting that post-disaster occupancy of both the hybrid timber-steel and steel-only structures would be plausible after experiencing an excitation of that magnitude. Furthermore, the frames experienced a relatively even distribution of residual drifts throughout the six storeys at these lower intensity earthquakes. At the MCE level, these residual drifts increased to 0.9 and 0.7% for the hybrid and steel-only frames respectively. The MCE responses experienced an uneven distribution in residual drifts that were concentrated in the lower storeys,

characteristic of high intensity earthquakes (Ruiz-Garcia & Miranda, 2006). This distribution, previously observed in the peak interstorey drift responses, is the result of P-Delta effects that localized permanent deformations in the lower storey BRBs. Overall, the hybrid BRBF exhibited equivalent performance but with higher variability (see larger mean plus one standard deviation values) with respect to residual drift to that of the steel-only system.

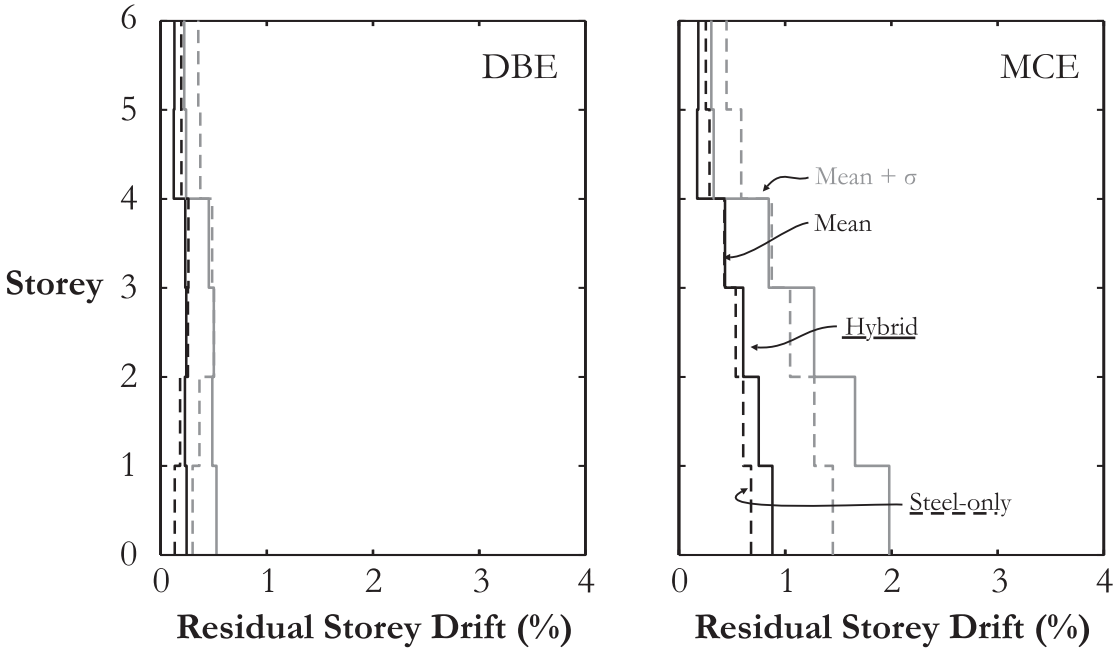

Figure 4.8: Residual Drift Response

4.6.3 Storey Acceleration Response

The BRBFs at both hazard levels experienced maximum absolute storey accelerations that were similar for the hybrid and steel-only systems. Mean and mean plus one standard deviation absolute storey accelerations are presented in Figure 4.9. For the BRBFs, the frames were exposed to MCE scaled mean peak ground accelerations (PGAs) of 0.41g and 0.42g for the hybrid and steel-only structures respectively, resulting in peak storey accelerations of 0.38g and 0.43g respectively. Furthermore, the hybrid and steel-only BRBFs experienced the maximum peak story accelerations of 0.30g and 0.32g, respectively, at the DBE hazard level. These responses correlate to scaled PGAs of 0.27g and 0.28g respectively. The PGAs were exceeded by the hybrid and steel-only BRBF systems in all mean plus one standard deviation responses. There was only slight

variation in the storey acceleration responses which remained below 0.4g and 0.6g respectively, with the greatest acceleration occurring in the lower storeys. Overall, the hybrid and steel-only systems exhibited excellent acceleration control throughout the height of both buildings.

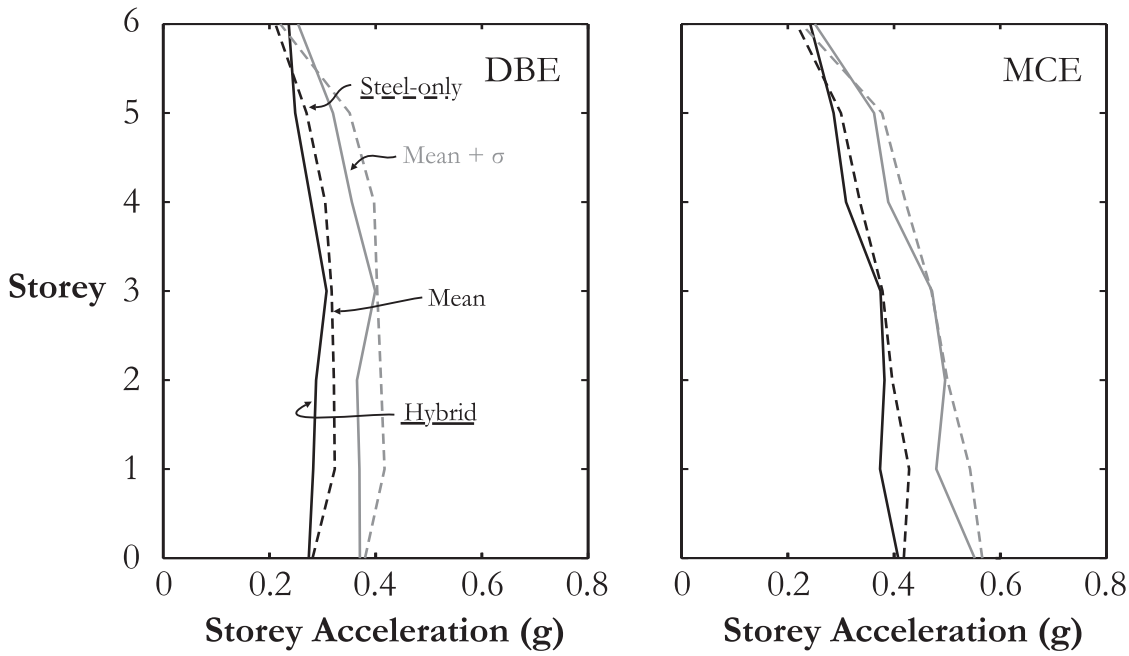

Figure 4.9: Peak Storey Acceleration Response

4.6.4 Member Performance

The structural elements were analysed to validate the capacity design procedure that dictated all structural member would remain elastic at DBE and MCE earthquake intensities. Therefore, the peak mean axial forces were analysed to evaluate if the seismic force demands exceeded the calculated member capacities and yield resistances. The axial forces in the columns and beams of both the hybrid timber-steel and steel-only structures were determined for all 43 earthquake records. A statistical analysis was then conducted to calculate the mean and mean plus one standard deviation force demands. The NBCC (2010) dictates that the mean response of a dynamic time-history analysis can be used to evaluate building performance if the structure is subjected to seven or more ground motions. Therefore, average axial forces were used to evaluate the global member performance and to classify elastic behaviour. Additionally, the mean plus one standard deviation results were used to assess structural resilience and account for variations in earthquake

magnitudes. The mean and mean plus one standard deviation force results showed that all the columns in both the hybrid and steel-only structures remained elastic when subjected to the DBE and MCE hazard level ground excitations. However, as a result of the rigid diaphragm model, axial loads could not be developed in the beam elements due to the restriction of relative axial transformations. This prevented the verification of the capacity design procedure used to determine the final beam geometries. The column response comparison provided confidence in the elastic performance of the two building types and provided insight that suggested the beam sections would also remain elastic.

A response comparison of the first storey BRB from the 1995 Kobe earthquake is presented in Figure 4.10, as expected both braces had a similar hysteresis response characteristics. However, the hybrid brace experienced significantly lower force demands as a result of reduced lateral loads attributed to the 40% reduction in seismic weight. The axial brace deformations of the two systems varied slightly. The hybrid BRB experienced greater compression deformations where the steel-only brace had a slight increase in the tensile direction. This variation in dynamic lateral responses is likely attributed to the difference in elastic stiffnesses between the hybrid and steel-only braces. This brace specific characteristic is attributed to the disparity in lateral stiffnesses of the two structures. Overall, the total energy dissipation of the hybrid brace was approximately half of the steel-only BRB, which was expected considering the different in the seismic response parameters of the hybrid and steel-only structures. Both braces exhibited good cyclic material responses that captured the force-deformation response of typical BRBs.

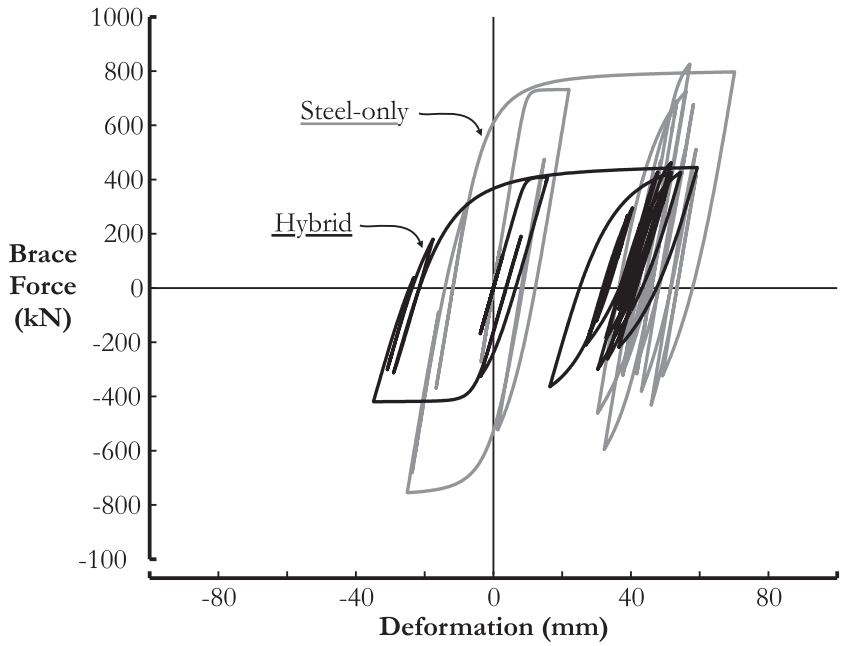

Figure 4.10: First Storey BRB Response

4.7 Summary of Nonlinear Dynamic Analysis

The numerical modelling investigation assessed the seismic performance of the conceptual hybrid timber-steel buckling-restrained brace frame (BRBF) design compared to a steel-only structure containing the same bracing system. The hybrid and steel-only BRBFs were designed using the high force reduction factors of the steel BRB system presented in the NBCC (2010). Each hybrid and steel-only two-dimensional frame was subjected to 44 MCE and 44 DBE level far field earthquake records using OpenSees seismic modelling software.

The nonlinear dynamic time-history analysis of the two six-storey structures showed that hybrid timber-steel structures can have equivalent seismic performance with respect to peak interstorey and residual drifts, and maximum storey accelerations compared to steel-only buildings. Uniaxial material calibration tests and initial brace stiffness characteristics provided excellent material response characteristics of BRBs, even without considering the increased compressive resistance attributed to friction effects. Even with the difference in initial stiffnesses between the hybrid and steel-only systems, the reduction in seismic weight of the hybrid structure provided

comparable seismic performance. This resulted in first and second mode periods of the hybrid structure that were essentially identical to the steel-only building. This reduction in seismic weight, characteristic of the hybrid system and CLT floor slabs, had a direct effect on seismic performance and lateral load demands. As a result, the hybrid system base shear and foundation force demands were significantly lower than the steel-only structure, resulting in smaller member sizes and foundations requirements. That has the potential to offset the costs associated with innovative hybrid timber-steel structures, making these systems a viable design alternative in seismic applications.

Chapter 5: Single Glued-in Rod Specimen Tests

5.1 Objectives

The force-displacement behaviour of the glued-in rod fasteners that were used in the hybrid braced frame tests were first evaluated based on small scale tests. This was done to validate the resistance calculations of the three glued-in rod design methods, because the strength and fracture characteristics used were derived from European materials (Bengtsson & Johansson 2002; Connolly & Mettem 2003; DIN 1052, 2004). Therefore, these tests were necessary to confirm the fastener design utilized in the hybrid timber-steel frame prototype, constructed from a Canadian timber species and epoxy resin, would be capable of resisting the anticipated seismic forces.

The vast majority of previous research into the pull-out resistance of glued-in rod fasteners has been conducted using various monotonic loading protocols to estimate short duration strength characteristics (Serrano 2001; Bengtsson & Johansson 2002; Connolly & Mettem 2003). However, understanding the cyclic response and fastener ductility is vital to evaluating the seismic performance of these connections. The primary goals of this experimental program were to evaluate the monotonic and cyclic behaviour of single rod connections and to assess the effects of pre-tensioning on the connection strength, stiffness and hysteretic behaviour. This information will aid in predicting the dynamic behaviour and inelastic properties of glued-in rods and will provide further guidance for the design of glued in rods, especially for application in seismically active and high-wind regions of Canada. Additionally, the results from these tests will be used to evaluated the force transfer and elastic behaviour of the fasteners in the hybrid connections

designed for seismic resistant cross-braced heavy timber frames.

5.2 Test Assemblage

The testing apparatus was designed to accommodate a compression-pull (C-P) loading condition (presented in Section 2.5.6 of Chapter 2) because this test configuration was used to derive the design equations for both the GIRod report and LICONS Eurocode 5 proposal (Bengtsson & Johansson 2002; Connolly & Mettem 2003). Therefore, this test configuration will provide appropriate evaluation of the various design methods. Additionally, the C-P boundary condition replicates the most severe loading scenario for these connections, capturing the lower bound of the nominal pull-out resistance range of glued-in rod fasteners (Bengtsson and Johansson 2002). The test applied a tensile load (P) to the embedded rod via a transfer washer located below the rod's anchoring nut. The reaction force (w) was applied to the end grain of the glulam specimen surrounding the embeddment hole in bearing, as shown in figure 5.1. To apply this loading condition, the test apparatus consisted of an outer steel support frame that encased the timber specimens and an intermediate steel connection used to load the glued-in rods, as shown in Figure 5.2. The steel testing frame consisted of 12.7 mm ($\frac{1}{2}$ inch) steel side plates welded to 38.1 mm ($1\frac{1}{2}$ inch) end plates and was secured in the testing machine by a 50.8 mm (2 inch) threaded hardened steel cylinder. The intermediate cylindrical connection consisted of an outer steel collar that screwed onto a 25.4 mm (1 inch) thick threaded transfer washer. This connection ensured that the nut was loaded in tension through the transfer washer instead of loading the rod directly. This force transfer was designed to represent the loading scenario the glued-in rods would experience in the associated hybrid braced frame test.

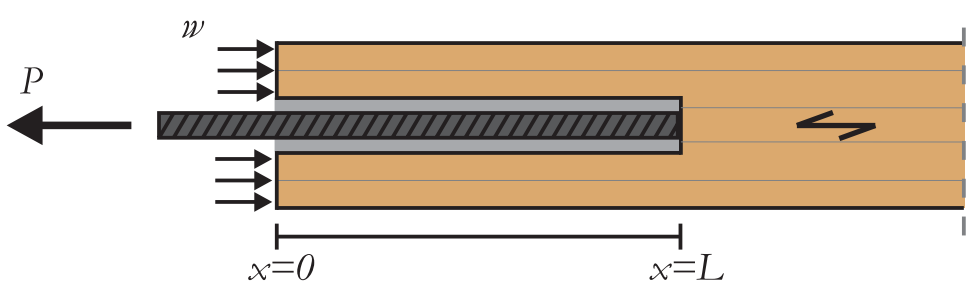

Figure 5.1: Compression-Pull Loading Condition

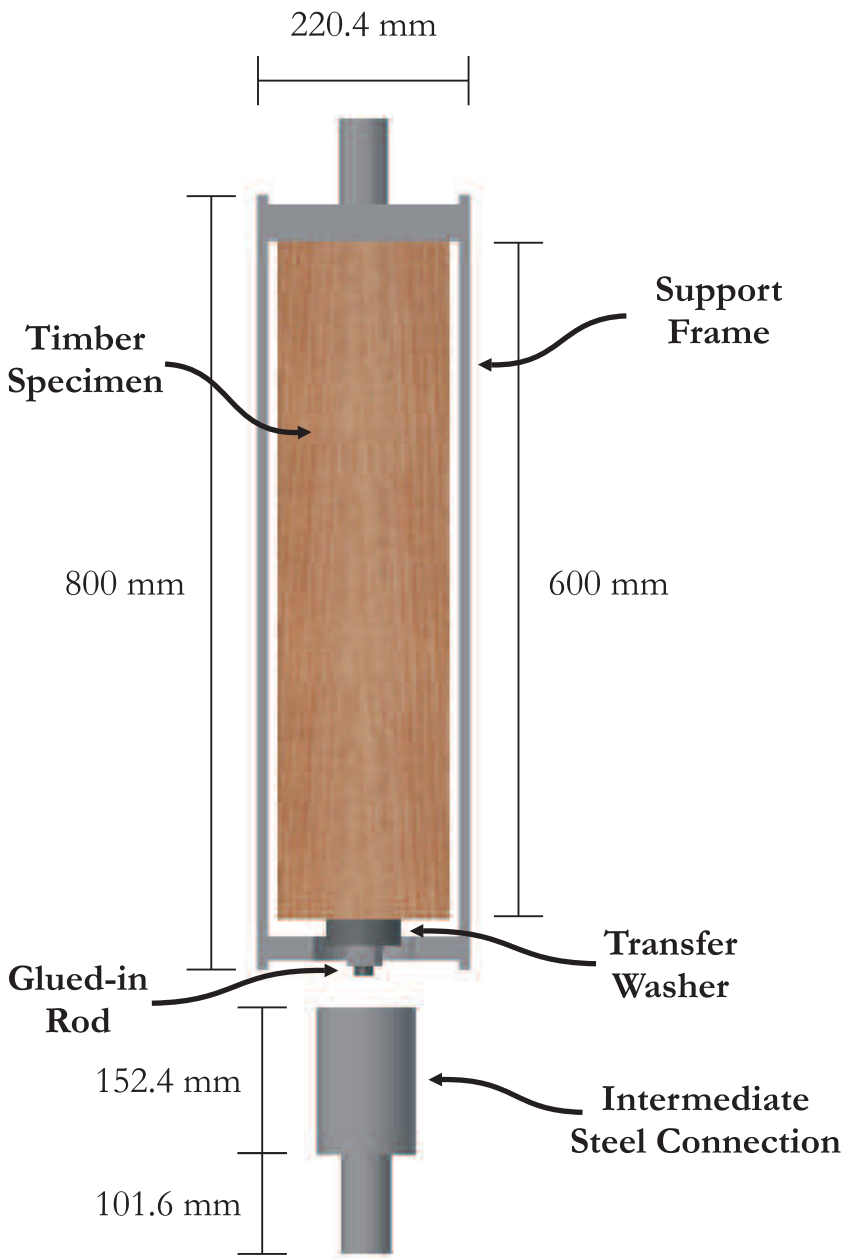

Figure 5.2: Single Rod Specimen Testing Frame

a) b)

c)

Figure 5.3: Intermediate Connection Components
a) and b) Intermediate Steel Cylinder
c) Transfer Washer and Nut Assembly

Figure 5.4: Installed Test Apparatus

5.2.1 Timber and Steel Components Design

The timber sections were designed to remain elastic under the anticipated bearing loads applied to the specimens as a result of the C-P test configuration. The single rod specimens were fabricated from 3.5 meter long 178 mm x 137 mm Nordic lam glue-laminated (Glulam) wood sections, provided by Nordic Structures Inc. The bearing resistance of the timber parallel to grain was calculated to ensure that bearing failure would not occur. An approximate factored bearing resistance of the engaged cross-section of 378.5 kN was determined for short-duration loading conditions.

The external steel testing frame was detailed to accommodate the single rod specimens and provide adequate support to restrain the sections during testing. The steel side plates were designed to resist the applied tension forces to ensure adequate axial stiffness in the apparatus. The side plate width of 137 mm was selected from the width of the timber specimens and a thickness of 12.7 mm ($\frac{1}{2}$ inches) provided adequate tension resistance. The top plate was designed with an internally threaded detail to accommodate the externally threaded 50.8 mm (2 inch) hardened steel anchor rod. The plate thickness was governed by the 50.8 mm (2 inch) thread depth required to elastically transfer the test forces into the hydraulic grips of the test machine and prevent prying action. The bottom plate was machined to accommodate the transfer washer and 101.6 mm (4 inch) intermediate steel connection. The plate was designed to have a high axial stiffness, preventing excessive frame deformations. The transfer washer, attached to the glued-in rod specimens by a high strength nut, was designed to simulate the bearing plates of the connections used in the hybrid braced frame study. The washer thickness was governed by external thread depth and stiffness requirements. The internally threaded intermediate steel connection was detailed to satisfy the thread requirements of the transfer washer and hardened steel support bar. The cylindrical section was bored out to accommodate the 75 mm fastener length of the glued-in rod fasteners. Figures 5.3 and 5.4 shows the individual assemble components of the steel support frame.

5.3 Strength Predictions

The predicted pull-out resistance of the glued-in rod fasteners was determined using three different European developed design methods that have yet to receive Canadian approval. These European design procedures were the GIROD report method (Bengtsson and Johansson 2002), the proposed EURO code method presented in the LICONS report (Connolly and Mettem 2003), and the German approved design method presented in DIN 1052 (NABau 2004). The GIROD report estimated the nominal pull-out resistance of a single rod fastener to be 126 kN due to the slight increase in edge distances of the specimen. The LICONS Report and DIN 1052 methods estimated the factored resistance to be 115 kN and 113 kN, respectively. The pre-tensioning force required for these three methods was calculated as 70 percent of the pull-out resistance were 88.2 kN, 80.5 kN and 79.1 kN, respectively. These resistances, summarized in Table 5.1, were used to evaluate the short duration tension performance of the connections. All of these values are determined from generalized strength characteristic for glued-in rod connections containing epoxy resin adhesives and are therefore approximations of the ultimate strength of the test specimens. This is due to the lack in specific timber/adhesive interface strength characteristics for glued-in rod connections containing Sika AnchorFix©-3001 epoxy.

5.4 Test Specimen Preparation and Assembly

5.4.1 Specimen Geometry

A detail of the single glued-in rod specimens can be seen in Figure 5.5. The fully threaded high strength B7 rods were embedded in 700 mm long 178 mm x 137 mm glulam specimens. This section geometry provided edge distances of 89 mm and 68.5 mm. These distances exceed the allowable minimum edge distance of 48 mm determined from the GIRod Report guideline of $2.5d_r$, dependant of the rod diameter of the fastener (Bengtsson and Johansson 2002). The 675 mm length threaded rods were selected to satisfy the design embedment length of 600 mm and provide adequate fastening length for the transfer washer connection. The 600 mm embedment

Table 5.1: Summary of Strength Predictions

Design Method	Pull-out Resistance (kN)
Nominal Resistance	
GIRod Report	126
LICONS Report	115
German DIN 1052	113
Axial Pre-tensioned Force	
GIRod Report	88.2
LICONS Report	80.5
German DIN 1052	79.1

length was selected to replicate the glued-in rod fasteners utilized in the associated half-scale hybrid braced frame study. This embedment length, in combination with the specimen geometry, resulted in a 100 mm end distance at the undisturbed end grain of the timber, see Figure 5.5. Due to the wide variety of specimen geometries used in previous research there are no guidelines on acceptable minimum undisturbed end length for specimens subjected to compression-pull tests. However, research conducted by Gardell and Morlier (2007) concluded that axial tension stresses in the undisturbed timber has a negligible effect on the axial resistance of glued-in rod connections, provided that the minimum spacing requirements are satisfied. Additionally, the remaining failure mechanisms are not influenced by the end length of the undisturbed portion of the specimen. Therefore, it was accepted that the 100 mm end distance of undisturbed wood would not likely effect the strength behaviour and fastener response during testing. The glued-in rod fasteners contained an approximate bond-line thickness of 1.5 mm, identical to the connections of the associated hybrid timber-steel braced frame study.

5.4.2 Specimen Fabrication

All specimens were comprised of glulam sections 700 mm in length and 675 mm long threaded steel rods with a nominal diameter of 19 mm ($\frac{3}{4}$ inch). The hole diameter of 22.2 mm

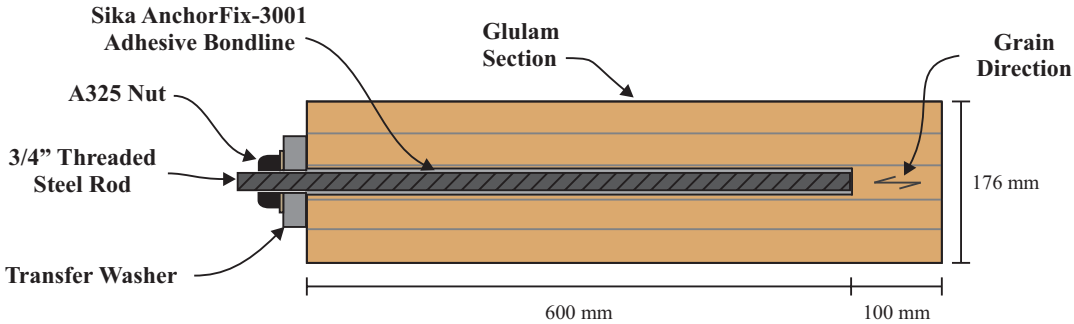

Figure 5.5: Single Rod Specimen Geometry

($\frac{7}{8}$ inches) was used to provide an approximate bond line thickness of 1.5 mm. The five 178 mm x 137 mm Nordic glulam beam sections were received in 3500 mm lengths and had to be cut into 700 mm lengths. This resulted in a total of 25 single rod test specimens. The length of the specimens was selected to maximize the number of specimens cut from each beam while ensuring a suitable end distance of undisturbed material. After the timber sections were cut to size, a manually assisted drill apparatus was used to drill the blind 600 mm embedment holes into the end grain of the test specimens. The dill mount used in the fabrication of the specimens is shown in Figure 5.6. The apparatus was constructed to ensure that embedment holes were straight and consistent, using a drill mount attached to aluminium guide rails, as shown in Figure 5.6. The drill mount consisted of two brackets, a base plate, and a low friction sliding surface. The mounting brackets, milled from solid aluminium blocks, were fastened to the base plate using 6.4 mm ($\frac{1}{4}$ inch) bolts tightened into threaded holes. Spacer plates were used to align the drill bit with the center of the timber sections and ensure the bit remained level during drilling. A low friction material was placed between the base plate and guide rails to allow the drill mount to glide unimpeded along the length of the drilling apparatus. Prior to drilling, the auger bit was placed in a small guide hole tapped by a center punch to prevent the bit from drifting off center during the initial stage of the drilling process. Figure 5.7 shows an example of the center punch and bit alignment technique implemented.

A specimen support frame was constructed to confine the timber section during the drilling process. The timber section was secured within the frame using two 178 mm long 2x4

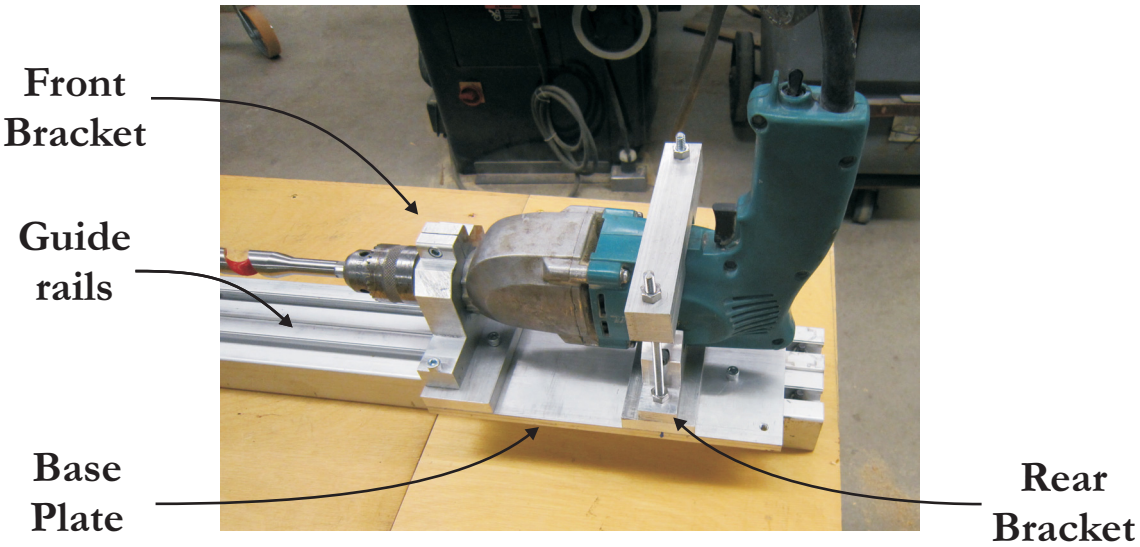

Figure 5.6: Drill Mount Detail

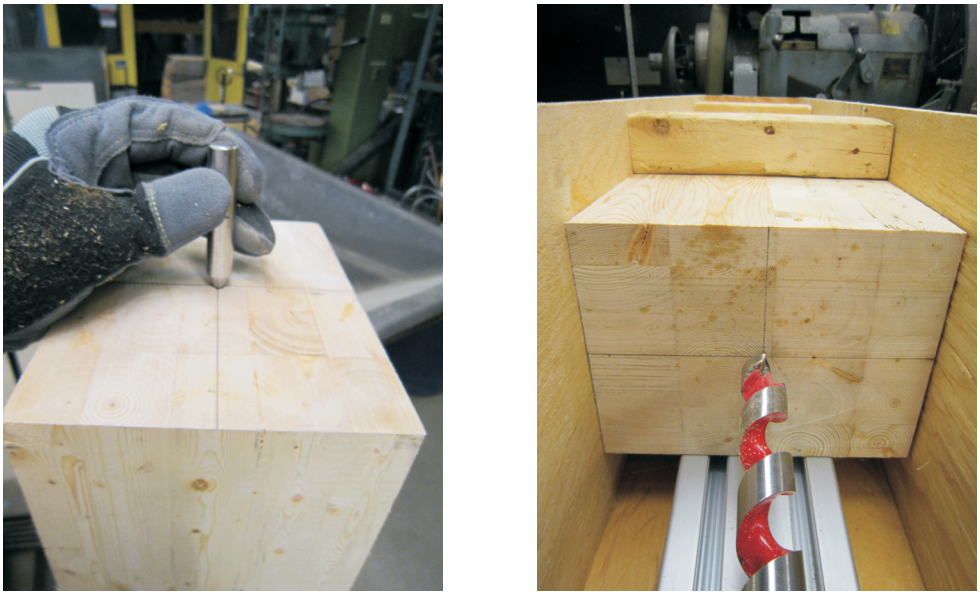

Figure 5.7: Guide hole and Drill Bit Alignment

pieces that were anchored to plywood walls on top of the wood specimens. The entire apparatus was then tied to the fabrication table using ratchet strap tightened around the exterior of the supporting frame. Figure 5.8 shows the various components of this drilling apparatus.

A 22.2 mm ($\frac{7}{8}$ inch) auger drill bit was used in combination with a 304.8 mm (12 inch) machined extension to bore the anchoring holes in the center of the glulam sections. The embedment holes had to be drilled in stages to clear the wood chips and to prevent scoring of the embedment wall and seizing, and redirection of the drill bit. Minimal hole preparation was done to simulate on site construction techniques. An air compression line and meter long hollow extension tube were used to clear the remaining wood chips and debris after drilling was completed. Further embedment surface preparation could be done by manufactures for optimal adhesion of the epoxy to the timber embedment hole.

The 19.1 mm ($\frac{3}{4}$ inch) threaded steel rods were received in 3.7 m (12 ft) sections that were then cut using a steel chop saw into 675 mm lengths to satisfy the embedment length and grip length requirements. The raw ends of the threaded rods and sharp burs were sanded to prevent injury and ensure the nut would be able turn onto the rods. Prior to installation, one end of each rod was machined down to a 5.7 mm x 5.7 mm (0.225 x 0.225 inch) tip using a lath and carbide cutting bit. This tip was designed to center the embedded end of the rod at the bottom of the hole. An example of the machined end can be seen in Figure 5.9. Electrical tape was wrapped around the exposed end of the rod above the 600 mm embedment length to protect the threads against damage and excess epoxy as it exited the hole. The adhesive product was supplied with 300 mm mixing nozzles. However due to the depth of the embedment hole, extension tubes were used to ensure the adhesive was evenly distributed in the base of the hole. The adhesive was injected into the embedment hole using a manual cocking gun. Identifying marks were made on the adhesive cylinder to determine when the required volume had been injected into the hole. The rods were turned in a clockwise direction as they were slowly inserted into the embeddment hole to work the adhesive around the rod and into the threads while prevent air bubbles from being trapped within the adhesive. The rods were centred using a combination of methods to ensure both ends of the rods would sit in the middle in the hole with out any inclination. The blind end of the rod

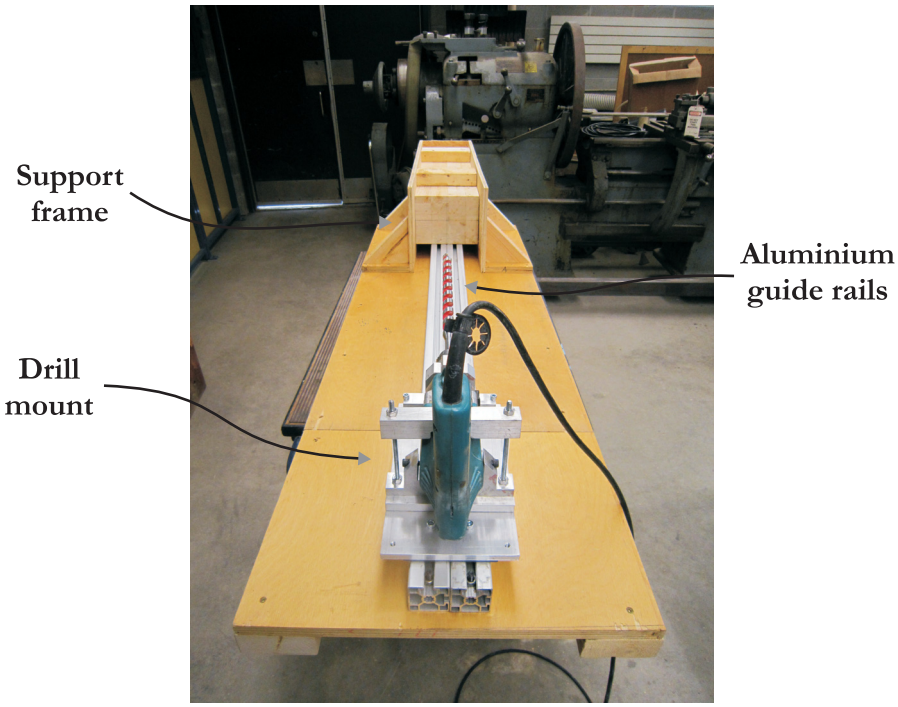

Figure 5.8: Drill Apparatus

was centered by inserting the 5.7 mm (0.225 inch) machined tip into the guide hole at the base of the embendment length provided by the drill bit. Centring at the bottom of the embedment hole prevented unwanted inclination in the rod and ensureed the adhesive was evenly distributed around the rod along the embedment length. The upper portion of the rod was centred at the end of the embedment hole using wood shims to hold the rods during the curing period of the epoxy. Initially, popsicle sticks were used to center the first specimen, however, to minimize disturbance in the adhesive layer small wood shims were used for the remaining specimens. Figure 5.10 shows the centering method used at the exposed end of the rod of the first specimen. Once the epoxy had cured, the electrical tape, centring shims and the excess adhesive, that remained on the timber, were removed prior to attaching the intermediate test connection.

Figure 5.9: Machined Centering Tip of the Embedded Rod End

Figure 5.10: Centering Technique at the Exposed Rod End

5.5 Instrumentation and Test Machine

An MTS 500 kN universal testing machine was used to test the specimens under the required monotonic and cyclic tension loading conditions. The machine was equipped with a load cell and internal displacement recorder to capture the total force and deformation levels achieved during the various tests. The test machine and specimen set-up is presented in Figure 5.11.

An additional externally mounted linear potentiometer (linear pot) was installed between the intermediate steel tension cylinder and the wood sections, as shown in Figure 5.12. The linear pot was used to directly measure the rod elongation and gap formation between the steel transfer washer and timber during the various loading scenarios. All data was recorded at 200 Hz because of the relatively short displacement at ultimate failure. Additionally, this recording frequency would capture the connection behaviour during catastrophic failure of glued-in rod fasteners.

Strain gauges were installed on the rods at the adhesive line of 12 test specimens to analyse the axial tension in the rod due to pre-tensioning force and externally applied force. A belt sander was used to sand the threads to the inner thread diameter minimizing the material removed from the unthreaded rod diameter. The surface was than sanded using a fine grit paper, cleaned, and the gauges were than applied using the adhesive provided. After sealing the gauges with a polyurethane coating, gauze and electrical tape were placed over the instruments to protect them during the embedment process. Furthermore, an investigation into the distribution of axial stresses along the length of the threaded steel rods required additional strain gauges be applied to two rod specimens. The specimens contained four gauges located along the length of the rods and spaced at approximately 200 mm. A minor incision was made through the threads running the entire embedment length. Thin wires were soldered to the gauges and placed in the grove. The wires were than coated using a polyurathane adhesive to secure them to the rod and minimize the impact to the rod/epoxy adhesion. Lastly, a Delmhorst Model RC-IC Solid State Moisture Detector was used to record the wood moisture contents of the test members prior to each test.

Figure 5.11: Single Rod Specimen in Testing Frame

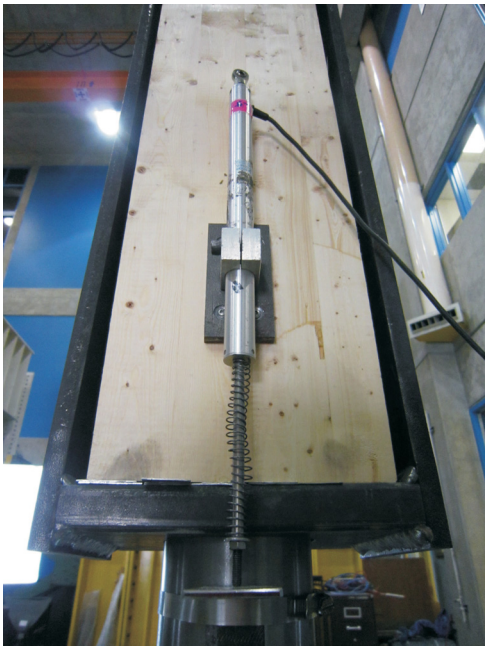

Figure 5.12: Single Rod Specimen External Instrumentation

5.6 Loading Protocol

Two loading protocols were implemented in the study to accurately capture the monotonic and cyclic behaviour of the glued-in rod fasteners. The monotonic loading condition was used to evaluate the accuracy of the resistance calculations and provide important connection stiffness characteristics in the specimens with and without pre-tensioning. The cyclic testing program was used to evaluate the dynamic load reversal behaviour to providing insight into the seismic performance of glued-in rod fasteners. Prior to loading, all specimens had a pre-load of 1 kN to ensure the maximum bearing area of the end grain was in contact with the steel plate. The pre-load also reduced the amount of specimen settlement and minor slip displacements of the testing apparatus during testing.

5.6.1 Monotonic Loading Protocol

The monotonic tests were preformed at a constant grip displacement rate of 1.0 mm/min. This rate is within the loading range of previous studies and was selected to ensure the tests would be completed within a time frame of 5 to 10 minutes (Serrano 2001, Bengtsson and Johansson 2002, Tannert 2014). Therefore, although the tests are monotonic, they are applied at a rate that would be considered short-term loading under the Canadian Wood Design Manual, CSA O86-09.

5.6.2 Cyclic Loading Protocol

The ISO 16670 standard (2003) for the quasi-static reversed-cyclic testing of structural timber joints constructed from mechanical fasteners was used to provide the cyclic displacement increments and loading rate. A tension only cyclic loading protocol was selected for this study to avoid loading the timber in bearing, as this compression loading phase was not expected to affect the connection resistance. Additionally, the difference in relative stiffness between the glued-in rod connection and the timber bearing resistance provided challenges when using displacement control loading in developing accurate bearing loads. The protocol consisted of a required set of loading cycles relative to the ultimate displacement, v_u, of the connection. The mean ultimate displacement of the monotonic tests was determined to be 5.43 mm. In addition to the

required cycles, 11 cycles were added at a constant displacement to replicate the forces that these connections will encounter in the cyclic testing of the full hybrid braced frame. The required displacement to meet this load level depended on the stiffness. The pre-tensioning caused an increase in the connection stiffness which required a stiffness of 49.9 $\frac{\text{kN}}{\text{mm}}$ and 57.5 $\frac{\text{kN}}{\text{mm}}$ for the snug-tight and pre-tensioned test groups. These stiffnesses were used to determine the grip displacements associated with a force development of 50 kN in the sung-tight and pre-tensioned specimens. This increased the probability that the target axial force of 45 kN would be reached during these 11 loading cycles while accounting for strength variabilities and a potential reductions in connection stiffness. Figure 5.13 shows the finalized cyclic loading protocols of the primary test program for the snug-tight and pre-tensioned rod conditions. The loading protocol was preformed at a rate of 0.25 mm/sec, which exceeds the lower bound of 0.1 mm/sec, ensuring that tests were completed within the time limit of "a few minutes," as specified in the standard (ISO 2003). The completion time excluded the additional cycles associated with the brace force simulation.

5.7 Pre-Tensioning

The strength and stiffness characteristics of the glued-in rod specimens were evaluated at two different pre-tensioning levels. To pre-tension the rods the A325 nuts were first hand-tightened onto the threaded rods to establish a secure connection with the transfer washer. The specimens were than restrained to the web of a support column using two 25.4 mm (1 inch) threaded steel rods and steel plates to prevent rotation during pre-tensioning. The pre-tensioning force was then applied using a metric torque wrench, shown in Figure 5.14. All single rod specimens were torqued to a snug-tight pre-tensioning level based on the definition of snug-tight from CSA S16-09 (2009). The estimated torque force required to pre-load glued-in rods to this force level was determined to be 165 N·m (135 ft·lbf). Half of the specimens remained at this force level for testing, however, the remaining specimens were tightened to an elevated pre-tensioning force.

The pre-tension force was applied to the rod by applying a measured torque to the rod's

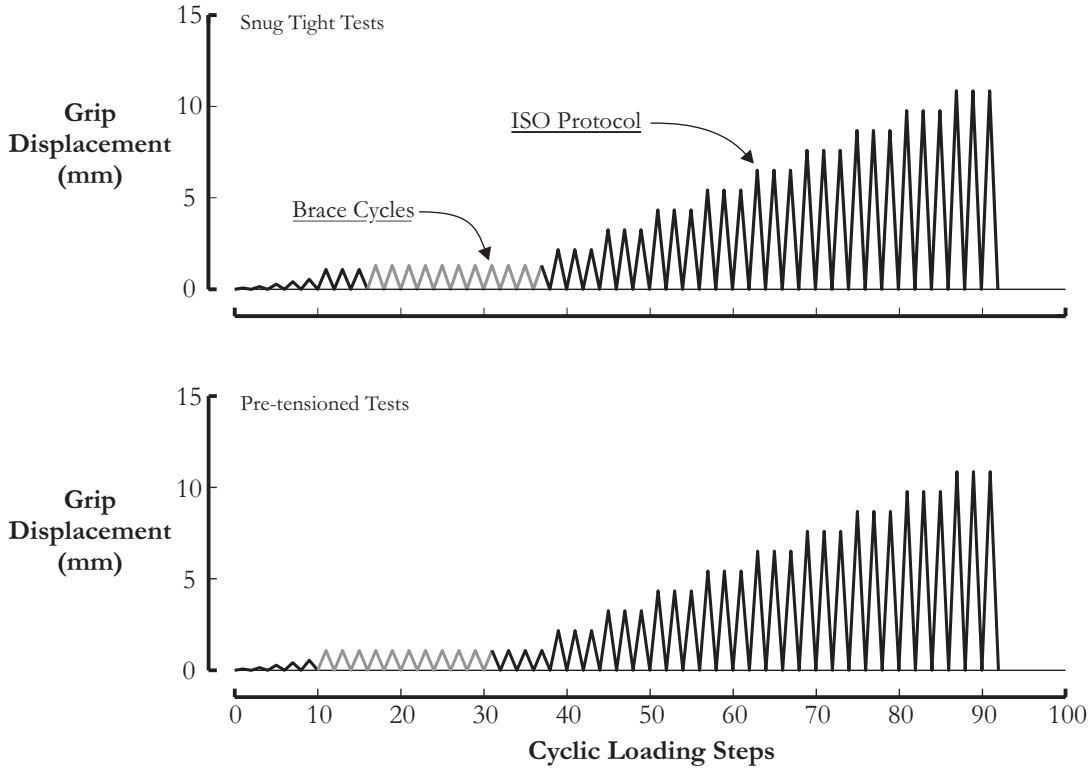

Figure 5.13: Finalized Cyclic Loading Protocols

Figure 5.14: Pre-tensioning of Test Specimens

nut. A pre-tensioning force of 70 % of the calculated connection strength, previously discussed, was applied to the rods. This level of pre-tensioning is equivalent to the pre-tensioning requirements for bolts in tension defined in CSA S16-09 (2009). Based on the median factored resistance, determined from the LICONS Report design method, a required pre-tensioning force of 80.5 kN (18.1 kips) was selected.

The torque required to apply the desired pre-tensioning force in the glued-in rods was initially estimated by Equation (5.1), presented in Fisher and Kloiber (2006):

$$F_{Torque} = 0.12 d_b F_{pt} \tag{5.1}$$

where, F_{Torque} is the torque in inches·kips, d_b is the nominal bolt diameter in inches and F_{pt} in the required pre-tensioning force in kips. This method was developed to determine the torque required to pre-tension anchor rods in concrete. The constant 0.12 is applicable for low friction or well lubricated coatings applied to the thread and nuts. However, a factor of 0.2 is applicable instead for rods that have higher levels of friction or lack lubrication. Based on the two factors for lubricated and non-lubricated surface conditions the torque required to develop a pre-tensioning force of 80.5 kN (18.1 kips) was established to be between 136 ft·lbs and 226 ft·lbs.

A calibration test was conducted using a strain gauged test specimen to determine the torque capable of developing the axial force of 80.5 kN. The torque was applied at increments of approximately 20.5 N·m. A target micro-strain of 2003 was determined using equation (5.2):

$$\epsilon = \frac{F_{pt}}{EA_r} \tag{5.2}$$

where F_{pt} is the required axial force of 80.5 kN, E is the elastic modulus of the threaded rod, and the area of the rod, A_r, was determined from the measured diameter of the reduced cross section of 16.0 mm. The torque of 247 N·m developed an initial micro-strain 1950 $\frac{\text{mm}}{\text{mm}}$ that settled to 1800 $\frac{\text{mm}}{\text{mm}}$ after ten minutes. The next torque level of 267 N·m induced a micro-strain of 2089 $\frac{\text{mm}}{\text{mm}}$ that settled to a strain of 1950 $\frac{\text{mm}}{\text{mm}}$. As a result of this calibration test, an applied torque of 267 N·m was determined to provide the approximate pre-tensioning force required. The strain relaxation was not accounted for when selecting the applied torque of 267 N·m. However, two

long term investigations were conducted to analyse the strain relaxation behaviour of the pre-tension force in glued-in rods. The applied torque suggested that a condition factor of 0.17 would be appropriate for use with equation (5.1). Suggesting that the 0.2 constant for low friction interaction friction is a more accurate representation of the surface conditions that affect the torque required to pre-tension these glued-in rod fasteners. In a select number of specimens the pre-tensioning was confirmed using the strain gauges applied to the rod surface.

5.8 Testing Procedure

The specimens were first restrained in the flange of a steel support column to prevent the specimens from rotating during pre-tensioning. The specimens that contained strain gauges were then wired into the MTS machine to capture the micro-strain induced by the pre-tensioning levels. All specimens were snug-tightened to 165 N·m prior to pre-tensioning. The nut and washer were replaced after each test to prevent strength degradation in these components and avoid skewing the results. The specimens that requires pre-tensioning were then tightened to the required torque of 267 N·m. The intermediate steel collar was then threaded onto the transfer washer and the specimen was placed in the testing apparatus. The specimens were tested immediately following the pre-tensioning to evaluate if the applied torque had an effect on the connection stiffness and capacity. Furthermore, conducing the tests immediately after the pre-tensioning was complete eliminated long term strain behaviour from affecting the test results. Therefore, none of the specimens tested experienced any reduction in the applied pre-tensioning force due to relaxation. Lastly, prior to testing the moisture content of the specimens was recorded using the Delmhorst Model RC-IC Solid State Moisture Detector. The timber members were stored in a conditioned laboratory environment for approximately 7 months prior to testing. The mean recorded moisture contents of the timber specimens was 8.0%

5.9 Acceptance Criteria

The single rod specimens were required to have a higher pull-out resistance than the calculated resistances from the three design methods. This result would validate the assumptions and procedures used in the design of the glued-in rod fasteners for the hybrid braced frame study. Secondly the fasteners had to remain elastic during the brace loading phase of the cyclic testing protocol and withstand the forces that developed during the 11 braced loading cycles without experiencing failure. This would ensure that the fastener design for the hybrid braced brace prototype would provide adequate resistance under the anticipated seismic forces.

5.10 Experimental Results

5.10.1 Preliminary Test Results

For the preliminary testing, five specimens were selected as an initial test set to finalize the cyclic testing program displacements and the required pre-tensioning torque levels. A summary of the preliminary tests conducted on the single rod specimens is presented in Table 5.2. The specimens were all tested under monotonic loading conditions to determine a mean ultimate displacement for the cyclic loading protocol used to test specimen SRT-S5. Additionally, various levels of pre-tensioning were applied to the different specimens to evaluate the effect on connection stiffness. The elastic stiffness , K_e of the tests was determined from the ISO 16670 standard (2003) using equation (5.3):

$$K_e = \frac{0.3F_{max}}{v_{0.4F_{max}} - v_{0.1F_{max}}} \tag{5.3}$$

where F_{max} is the maximum load of the test specimen and $v_{0.4F_{max}}$ and $v_{0.1F_{max}}$ are the displacements associated with 40% and 10% of the maximum load respectively. Lastly, during the pre-tensioning evaluation a gradual drop in the induced strain was observed, because of this behaviour a long term pre-tensioning relaxation test was conducted.

Table 5.2: Preliminary Single Rod Test Summary

Date (D-M-Y)	Specimen	Loading Scenario	Rate (mm/sec)	Comment
11-09-2015	SRT-S0a	Monotonic	0.5	Nut failed in thread shear
14-09-2015	SRT-S0b	Monotonic	0.5	Specimen was tested to failure
14-09-2015	SRT-S1	Monotonic	1.0	Specimen was tested to failure
15-09-2015	SRT-S2a	Monotonic	1.0	Evaluated connection stiffness
17-09-2015	SRT-S2b	Monotonic	1.0	Evaluated connection stiffness
17-09-2015	SRT-S2c	Monotonic	1.0	Specimen was tested to failure
21-09-2015	SRT-S3	Monotonic	1.0	Specimen was tested to failure
24-09-2015	SRT-S4a	Strain Relaxation	1.0	Specimen was tested to failure
27-09-2015	SRT-S4	Monotonic	1.0	Specimen was tested to failure
01-10-2015	SRT-S5	Cyclic	0.25	Specimen was tested to failure

Table 5.3: Preliminary Test Results

Specimen	Pre-Tensioning	Initial Strain (micro $\frac{m}{m}$)	Elastic Stiffness ($\frac{kN}{mm}$)	Ultimate Capacity (kN)	Ultimate Displacement (mm)
SRT-S0a	Snug Tight	-	47.0	188.6	-
SRT-S0b	Snug Tight	-	50.3	171.4	3.87
SRT-S1	Snug Tight	-	49.9	147.0	3.38
SRT-S2a	184 N·m	-	≈50.3	-	-
SRT-S2b	1/8 Turn	-	≈61.8	-	-
SRT-S2c	1/8 Turn	-	65.2	165.6	2.39
SRT-S3	165 N·m	-	57.3	130.7	2.51
SRT-S4a	267 N·m	2089	-	-	-
SRT-S4b	267 N·m	1637	58.1	154.4	2.90
SRT-S5	165 N·m	-1045.8	45.9	151.2	-

A summary of the preliminary glued-in rod test results are presented in Table 5.3. Specimens SRT-S0 and SRT-S1 were loaded monotonicly to evaluate the pull-out resistance of the glued-in rod fasteners under snug-tight pre-tensioning. The first test conducted on specimen S0 (SRT-S0a) resulted in the shear failure in the nut threads at 188.8 kN, due to a lower grade nut being used in the connection assembly. The second test for specimen S0 (SRT-S0b) used the proper A325 high strength nut that resulted in a shear plug failure in the timber/adhesive interface of the fastener providing a tensile resistance of 171.4 kN. This capacity was lower than the previous connection resistance of 188.8 kN because of damage to the fastener prior to failure in the nut. After the test was completed the specimen was found to have a rod inclination of approximately 7.5 degrees. Rod inclinations have been found to increase the pull-out resistance of glued-in rod fasteners and was the likely reason why the fastener resistance was significantly grater than the calculated resistances (Malczyk, 1993). Specimen S1 (SRT-S1) experienced an identical failure mode of shear plug withdrawal at a force of 147.0 kN. The variation in the connection capacity between specimens S0 and S1 was attributed to the shorter lead time between fabrication and testing of specimen S1 that prevented the epoxy from curing completely and the rod inclination in specimen S0.

To test the accuracy of the torque calculation presented by Fisher and Kloiber (2006) for the pre-tensioning force of 80.5 kN, SRT-S2a specimen was sung tightened and then torqued to 165 N·m. The specimen was loaded within the elastic range to a displacement of approximately 1 mm. The results were analysed to determine if the pre-tensioning force could be identified by observing a change in connection stiffness. The fastener had an elastic stiffness of approximately 50.3 $\frac{\text{kN}}{\text{mm}}$. However, due to a lack in prominent stiffness change, the exact magnitude of pre-tensioning force could not be identified from the results. A turn-of-nut approach was then used to estimate the number of required turns based on the expected rod elongation at 80.5 kN as a proportion of the thread angle for specimen SRT-S2b. This calculation resulted in a required $\frac{1}{8}$ turn of the nut to provide the target pre-tensioning force. Again the specimen was loaded within the elastic range to a displacement of 1 mm, resulting in an elastic stiffness of approximately 61.8 $\frac{\text{kN}}{\text{mm}}$. Lastly, SRT-S2c was used to investigate the pre-tensioning affect on ultimate capacity. The nut was tightened first to sung-tight conditions then to the $\frac{1}{8}$ turn and the specimen was loaded

to failure.

The lack of a quantitative definition for snug-tight conditions in CSA S16 (2009) promoted an investigation into the torque required to achieve a snug-tight fit in the glued-in rod connection. The code defines a sung-tight connection as one that has been tightened with an Ironworkers full effort (CSA S16, 2009). Specimen SRT-S3 was first tightened to a torque of 145 N·m, however the nut could still be tightened further. Therefore, the next increment on the torque wrench of 165 N·m was selected as the optimal snug-tight condition. After assembling the connection to a snug-tight fit, the specimen was tested to failure to evaluate its strength characteristics. The fastener had ultimate capacity of 130.7 kN with an initial elastic stiffness of 57.3 $\frac{\text{kN}}{\text{mm}}$. The results of specimen SRT-S3 were included in the statistical analyses presented below.

Because the pre-tensioning force in the three tests conducted in specimen SRT-S2 could not be determined, a more involved analysis was conducted using specimen SRT-S4. This investigation consisted of pre-tensioning the test specimen to torque levels higher than 165 N·m to analyse the strain readings and subsequent induced forces over a period of 10 minutes. Based on the stress-strain compatibility equations, a micro-strain of 2003$\frac{\text{mm}}{\text{mm}}$ was determined as the target strain required for a pre-tensioning force of 80.5 kN. Firstly, the initial torque of 165 N·m was applied to simulate snug-tight conditions. After which, a torque of 247 N·m was applied resulting in an initial micro-strain of 1950$\frac{\text{mm}}{\text{mm}}$ that relaxed to 1800$\frac{\text{mm}}{\text{mm}}$ over the ten minute time frame. The second torque of 267 N·m was then applied that induced an initial strain of 2089$\frac{\text{mm}}{\text{mm}}$ that settled to 1885$\frac{\text{mm}}{\text{mm}}$ micro-strain. Given that the connections were to be tested immediately after pre-tensioning and the required micro-strain of 2003 $\frac{\text{mm}}{\text{mm}}$ was achieved, the 267 N·m torque was chosen as the optimal pre-tensioning torque for the primary investigation. This pre-tension force remained in the specimen and the strain relaxation was recorded for the following four and a half days. This investigation established a relaxation trend that appeared to plateau at approximately 4 days, shown in Figure 5.15. The results were skewed by the fluctuation in the power supply as the energy demand of the building decreased over night. This caused a increase in the voltage readings across the strain gauge that were observed as peaks in the strain readings. In the future long term strain relaxation test this fluctuation behaviour was accounted for through the application of a control gauge placed on an unloaded section of steel. The results from specimen

SRT-S4b were included in the primary test results analysis.

The ultimate displacement presented in Table 5.3 are defined as the grip displacement associated with the initial drop in resistance. This displacement limit was selected because the drop in fastener resistance reached the suggested limit of 0.8 F_{max}, as specified in ISO 16670 (2003), at these corresponding displacements. Where F_{max} in this case was defined as the highest resistance prior to the initial reduction in capacity. The ultimate displacement of the snug-tight connection condition presented in specimen SRT-S3 was used to produce the cyclic loading protocol for test specimen SRT-S5 that was to be tightened to the same condition. Furthermore, the minimum initial stiffness from the monotonic sung-tight specimens of 49.9 $\frac{\text{kN}}{\text{mm}}$ was used to calculate the grip displacement to induced an axial force of 50 kN. However, as a result of the limited number of displacement cycles of the loading protocol used to test specimen SRT-S5, the definition of ultimate displacement was changed. The ultimate displacement was then defined as the grip displacement at fastener pull-out (catastrophic failure), identified as the displacement associated with an immediate drop in fastener resistance of approximately 80 - 90% of the maximum resistance.

5.10.2 Primary Test Results

5.10.2.1 Monotonic and Cyclic Response Characteristics

Prior to conduction the cyclic loading tests, four snug-tight and four pre-tensioned specimens were tested monotonically as part of the primary glued-in rod test program. The results from these tests were used to determine the cyclic loading protocols for the sung-tight and pre-tensioned specimens. Furthermore, the mean connection stiffnesses for snug-tight and pre-tensioned monotonic tests were used to calculate the displacements required to achieve a tensile force of approximately 50 kN, previously discussed in Section 5.6.2.

The results are presented for four different test configurations representing both monotonic and cyclic tests conducted on specimens with and without pre-tensioning. The monotonic tests with and without pre-tensioning consisted of four test specimens each, where both cyclic test configurations (with and without pre-tensioning) were conducted on six specimens each. The median response of the four different test combinations are presented in Figure 5.16. The

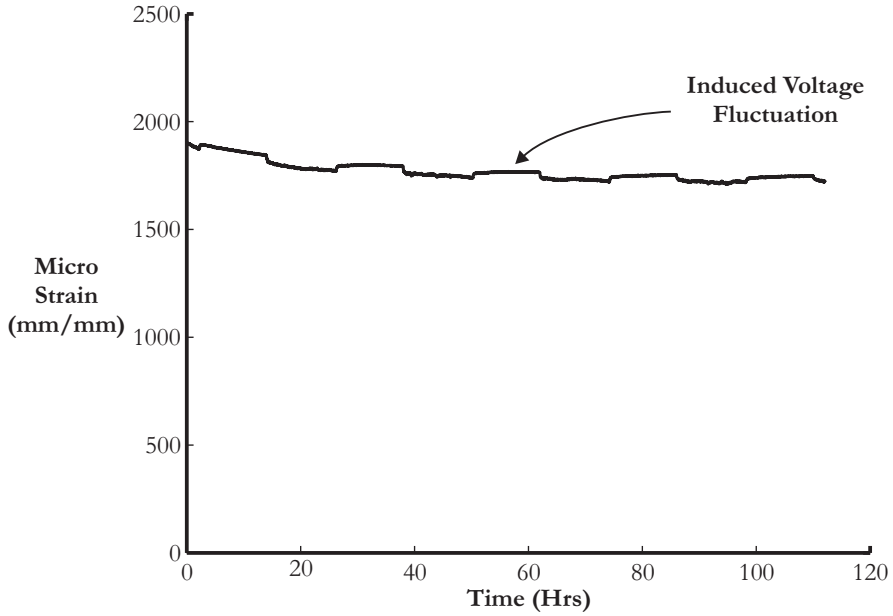

Figure 5.15: SRT-S4a Pre-Tensioning Strain Relaxation

monotonic tests displayed limited ductility due to the brittle failure mode of the timber/adhesive interface. This brittle failure mechanism resulted in catastrophic failures, clearly defined by the instantaneous drops in resistance at the ultimate force resistance.

The cyclic test specimens experienced brittle failure that gradually developed due to micro-fractures along the embedment length in the timber at the timber/adhesive interface. This behaviour limited the energy dissipation associated with the cycles of deformation for each cycle set. This behaviour is defined by the loops in the force-displacement response presented in Figure 5.16 which can primarily be seen in the first cycle of each cycle set. Furthermore, damage primarily occurred as the displacement was increased to the next cycle set, with no significant damage being observed within the subsequent cycles. This suggests that cyclic loading did not result in accumulated damage in the connection, evident when comparing the ultimate deformation results and force-displacement curves of the cyclic tests to the monotonic test responses.

Comparisons of the force-displacement responses of the monotonic and cyclic tests are presented in Figures 5.17 and 5.18. These comparisons provide insight into the effect pre-tension has on the initial stiffness of glued-in rod connections. In both figures, the pre-tensioned specimens had higher initial stiffness of the force-displacement curve than the corresponding specimens

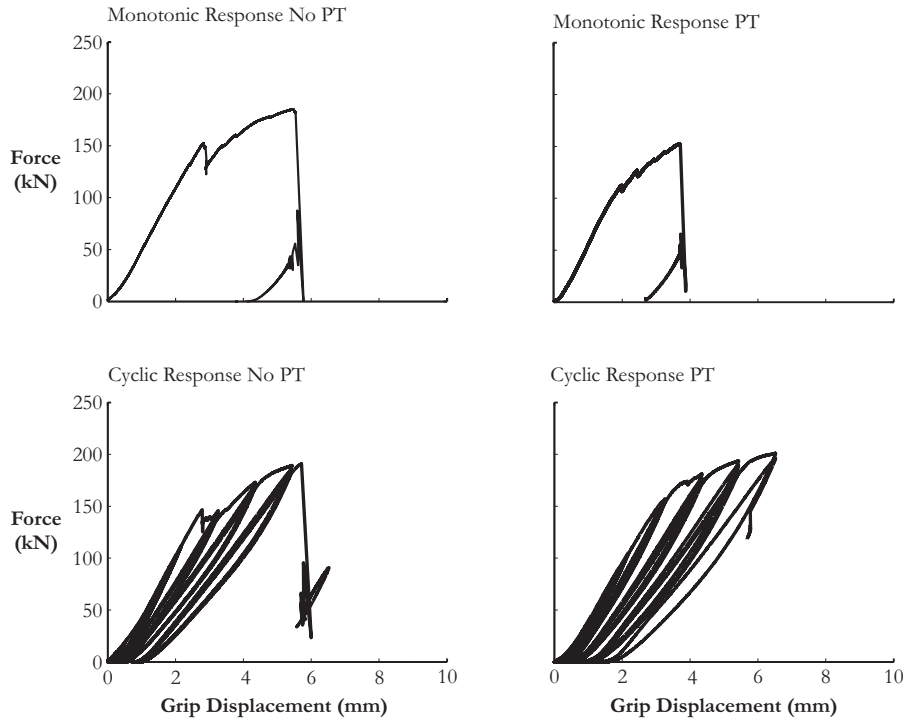

Figure 5.16: Median Rod Response For Monotonic and Cyclic Loading

without pre-tensioning. This increase in stiffness is attributed to the additional bearing stiffness between the end grain and circular steel transfer washer that is in parallel with the rod stiffness when the pre-tensioning force is applied. This added stiffness behaviour is negligible for specimens torqued to snug-tight conditions. However, it is important to note that the pre-tensioned specimens were tested immediately after the pre-tensioning force was applied. This prevented the opportunity for the specimens to relax which may result in a reduction of the pre-tension force and the initial stiffness.

The expected distinction in stiffness change was not observed in the force-displacement responses of the pre-tensioned specimens at the location of the initial pre-tensioning force of approximately 80.5 kN. There was a gradual change in stiffness that could likely be the result of uneven gap formation between the transfer washer and timber end grain as the pre-tensioning force was overcome. This was attributed to minor rod inclinations and/or additional geometric

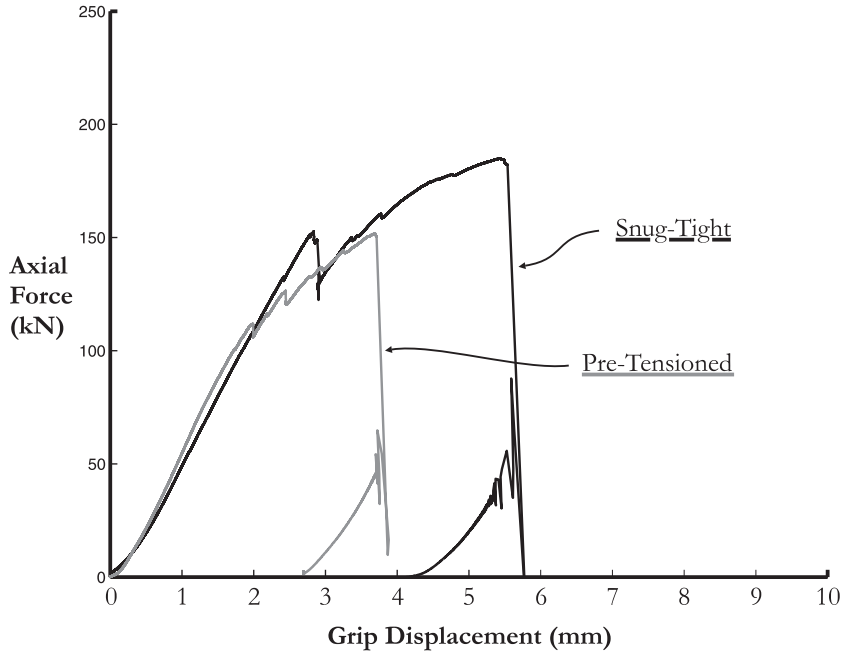

Figure 5.17: Monotonic Response Comparison

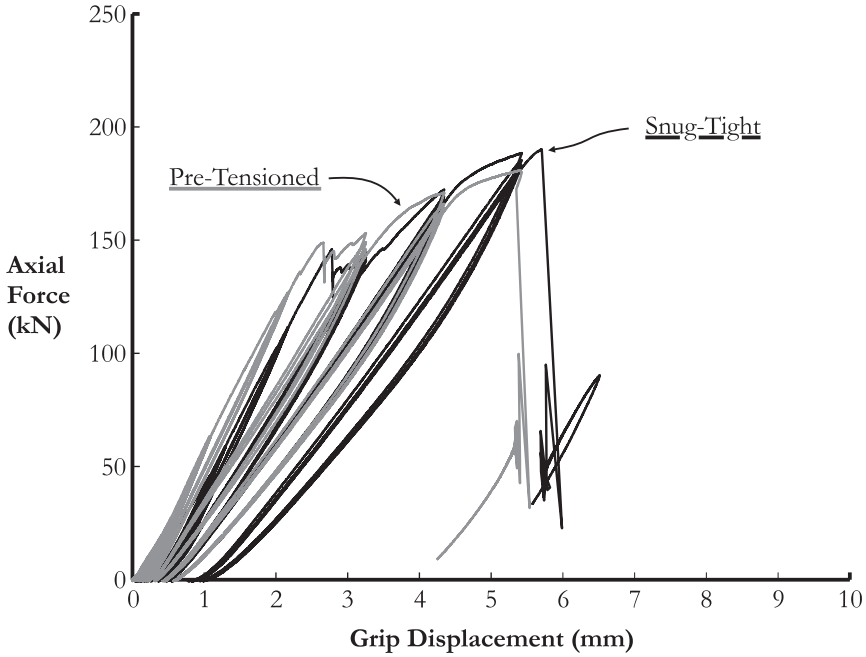

Figure 5.18: Cyclic Response Comparison

eccentricities in the specimens and test assembly that would cause uneven bearing stress distribution between the end grain and transfer washer. These eccentricities can cause localized bearing stress between the two connection components that must be overcome prior to the full gap formation.

Strain gauges were applied to the exposed end of the embedded rod immediately above the bondline in ten of the twenty test specimens. These gauges were used to estimate the initial axial force in the fasteners under the two applied torque levels. The strain gauges were installed on four snug-tight and six pre-tensioned specimens. The rod inclination and initial axial forces determined from the strain readings are presented in Table 5.4. The rod inclination had a clear effect on the variance of the initial axial force in the rod at both the sung-tight and pre-tensioned conditions. A summary of the rod inclinations measured in the test specimens is presented in Table 5.5. This variation in the pre-tensioning force was attributed to induced bending stress in the rod that effected strain readings depending on the gauge location relative to rod inclination. In particular, the gauge attached to the pre-tensioned specimen SRT-S10 was located on the side opposite to the rod inclination of 1.5 degrees. Bending in the pre-tensioned rod induced a compressive force at the gauge location that resulted in an estimated pre-tensioning force of 39.6 kN. Alternatively, the pre-tensioned specimen SRT-S22 was instrumented on the same side of the rod as the 3.5 degree inclination. The positive bending stress in the gauges resulted in an initial micro-strains of 5939 $\frac{\text{mm}}{\text{mm}}$ equating to an axial force of 249.6 kN. The axial force of 81.9 kN was the most accurate representation of the pre-tensioning force associated with the applied torque of 267.1 N·m because this specimen did not have any inclination in the glued-in rod fastener. The majority of the stain data after the initial loading phase was negligible due to damage in the gauges that prevented accurate data collection.

5.10.2.2 Elastic Stiffness Characteristics

The elastic stiffness results determined from the grip displacement verses force responses of the four specimen types, are presented in Tables 5.6 and 5.7. These results were used to evaluate the effect pre-tensioning had on connection stiffness. The stiffness calculations were completed

Table 5.4: Initial Axial Force Results, kN For Monotonic (M) and Cyclic (C) Tests

Specimen ID	Rod Angle* (Degrees)	Axial Force (kN)
No Pre-Tensioning		
SRT-S5(M)	-1.5	38.3
SRT-S15(C)	+2.0	126.4
SRT-S16(C)	+2.5	146.4
SRT-S17(C)	+2.5	161.0
Pre-Tensioned		
SRT-S4(M)	-0.5	69.8
SRT-S9(M)	+0.0	81.9
SRT-S10(M)	-1.5	39.8
SRT-S21(C)	-0.5	60.4
SRT-S22(C)	+3.5	249.6
SRT-S23(C)	+0.5	96.5

*Positive angles induce positive bending in the strain gauges

Table 5.5: Summary of Rod Inclinations

Connection Condition	Specimen ID	Rod Inclination (Degrees)
Monotonic Specimens		
No Pre-Tensioning	SRT-S3	≈0.0
	SRT-S4	0.5
	SRT-S6	≈0.0
	SRT-S7	≈0.0
Pre-Tensioning	SRT-S8	≈0.0
	SRT-S9	≈0.0
	SRT-S10	1.5
	SRT-S11	1.0
Cyclic Specimens		
No Pre-Tensioning	SRT-S12	2.0
	SRT-S13	1.0
	SRT-S14	2.0
	SRT-S15	2.0
	SRT-S16	2.5
	SRT-S17	2.5
Pre-Tensioning	SRT-S18	2.0
	SRT-S19	1.5
	SRT-S20	2.0
	SRT-S21	0.5
	SRT-S22	3.5
	SRT-S23	0.5

using the ISO 16670 stiffness calculation presented in equation (5.3). The results show that the application of pre-tensioning caused an increase in the connection stiffness due to an addition of the bearing stiffness contribution. There was an increase in mean stiffness of 7.3 $\frac{\text{kN}}{\text{mm}}$ and 5.1 $\frac{\text{kN}}{\text{mm}}$ for the monotonic and cyclic pre-tensioned specimens respectively compared to the snug-tight test configurations. This suggests that pre-tensioning caused an increase in the short term elastic stiffness of glued-in rod connections. Additionally, the minimal variation between the monotonic and cyclic loading conditions of the two pre-tensioning levels confirmed the assumption that the loading conditions do not affect connections stiffness.

The theoretical connection stiffness was calculated using equation (5.4) proposed by Jensen (2001) and modified from the GIRod Report design method:

$$k_e = \pi d_h l_a \Gamma \frac{\tanh \varpi}{\varpi} = \pi(23)(600)(29.2)\frac{\tanh(3.71)}{3.71} = 156\ \frac{\text{kN}}{\text{mm}} \tag{5.4}$$

where Γ is defined by the shear strength, τ_f, and fracture energy, G_f, of the bond line defined in equation (5.5). A shear strength and fracture energy of 10.5 MPa and 1.89 $\frac{\text{N}\cdot\text{mm}}{\text{mm}^2}$ were considered for the connections based on the findings of Bengtsson and Johansson (2002).

$$\Gamma = \frac{\tau_f^2}{2G_f} = \frac{10.5^2}{2(1.89)} = 29.2\ \frac{\text{N}}{\text{mm}^3} \tag{5.5}$$

The theoretical stiffness of 156 $\frac{\text{kN}}{\text{mm}}$ was approximately three times the snug-tight and pre-tensioned stiffnesses determined from the grip displacement results. These specimen stiffnesses presented were the series stiffness of the fastener and test frame assembly, therefore, the elastic stiffness from the linear pot displacement would provide a more accurate comparison to the calculated value. The high recording frequency introduced measurement error in the linear pot results that were corrected by taking a moving average of ten data points in each specimen data set. The results of the connection stiffness determined from the linear pot displacement readings are presented in Table 5.8.

Table 5.6: Elastic Stiffness Results, kN/mm

	Monotonic	Cyclic
No Pre-Tensioning	57.3	56.7
	48.4	54.1
	60.0	58.7
	59.4	55.4
		53.9
		55.0
Pre-Tensioning	58.1	64.4
	65.2	62.7
	63.5	63.4
	67.5	61.4
		55.7
		56.8

Table 5.7: Statistical Analysis of Connection Stiffness, kN/mm

	Monotonic		Cyclic	
	Average	Standard Deviation	Average	Standard Deviation
No Pre-Tensioning	56.3	5.4	55.6	1.8
Pre-Tensioning	63.6	4.0	60.7	3.6

Table 5.8: Linear Pot Stiffness Results, kN/mm

	Monotonic	Cyclic
No Pre-Tensioning	131.6	223.0
	111.0	180.1
	105.7	524.2
	164.4	135.3
		102.7
		160.0
Pre-Tensioning	172.8	147.2
	228.6	152.7
	360.7	191.4
	245.4	975.5
		137.2
		169.3

Table 5.9: Statistical Analysis of Linear Pot Stiffness, kN/mm

	Monotonic		Cyclic	
	Average	Standard Deviation	Average	Standard Deviation
No Pre-Tensioning	128.2	26.6	160.2	45.5
Pre-Tensioning	251.9	78.9	159.6	21.3

The mean and standard deviation connection stiffness determined from the linear potentiometer results are presented in Table 5.9. The influence of pre-tensioning on connection stiffness was prominent in the monotonic test comparison for the mean stiffness results. However, this correlation was not present in the mean stiffness results of the cyclicly loaded specimen, where equal mean connection stiffnesses were exhibited in these test specimens for both the snug-tight and pre-tensioned connection conditions. The mean stiffness results for three of the four specimen groups were comparable to the calculated stiffness of 156 $\frac{\text{kN}}{\text{mm}}$. This comparison further validates the accuracy of the four glued-in rod design calculations for connections contained Canadian timber and adhesive types. However, there was variability in the results represented by the standard deviations of the four sample sets, prompting the need for a dedicated study to evaluate the actual connection stiffness of glued-in rods. Furthermore, error in the linear pot readings from two specimens provided results inconsistent with the stiffness behaviour of the remaining specimens. The connection stiffnesses of 524.2 $\frac{\text{kN}}{\text{mm}}$ and 975.5 $\frac{\text{kN}}{\text{mm}}$ for specimens SRT-S14 and SRT-S21 were the result of this error. Therefore, these test specimens were removed from the analysis to prevent skewing of the results.

The test specimens did not experience low cycle fatigue stiffness degradation during the eleven brace force cycles of the hybrid braced frame prototype study. The stiffness behaviour during this loading phase was invariably elastic and consistent throughout the eleven cycles. The stiffness of the first quasi-brace cycle followed the stiffness trajectory of the previous displacement cycle, however the remaining ten cycles settled at a lower yet consistent stiffness. As previously stated this change in the stiffness of the subsequent cycles was characteristic of all the displacement cycles prior to an initial drop in connection resistance. Minor reductions in connection stiffness occurred in specimens that experienced micro-fractures in the timber/adhesive interface due to this localized damage. However, the behaviour was negligible because the cycles before and after this slight reduction in axial strength were elastic. Pre-tensioned specimens did experience a minor reduction in connection stiffness between loading cycles which resulted in slight reductions in the axial force at the maximum displacements. This behaviour was attributed to relaxation in the pre-tensioning force over the duration of the brace force cycles. This expected pre-tensioning relaxation behaviour is most prominent in the first hour after pre-tensioning which was why the

reduction in stiffness was observed during the cyclic testing program. The results of the brace force cycles support the assumptions made in the capacity design process and confirm the elastic performance expectations of the braced hybrid timber frame prototype connections. Figure 5.19 shows a comparison of sung-tight and pre-tensioned response of the braced loading cycles as well as the cycles that proceeded this phase of the cyclic test protocol.

5.10.2.3 Ultimate Capacity

All specimens experienced a shear plug pull-out failure resulting from rupture in the timber at the timber/adhesive interface. Ultimate connection capacities for all the tests are presented in Table 5.10. All of the specimens exhibited a pull-out resistance greater than the calculated nominal strengths of 126 kN, 115 kN and 113 kN. However, there was considerable variability in the data which was attributed to difference in rod inclination and the variation in lead time between fabrication and testing allowing additional adhesive cure time in select specimens. The average and the standard deviation of the pull-out resistances of the four test variations are presented in Table 5.11. All four test configurations had similar strength, considering the standard deviation, which suggests that the application of pre-tensioning does not affect strength. Furthermore, the statistical analysis presents a lower standard deviation and high average resistance for the cyclic loading conditions compared to the monotonicly loaded specimens. Lastly, the strength capacities of the single glued-in rod specimens provided promising results that suggest the glued-in rod fasteners utilized in the associated hybrid braced frame study will resist the anticipated connection forces.

5.10.2.4 Fastener Ductility

The maximum connection ductility provided vital insight into fastener resistance necessary for the capacity design considerations when evaluating seismic force resistance, in particular the fastener's ability to withstand severe ground excitations. The maximum ductility of the monotonic and cyclic specimens were calculated using equation (5.6) (ISO 16670, 2003):

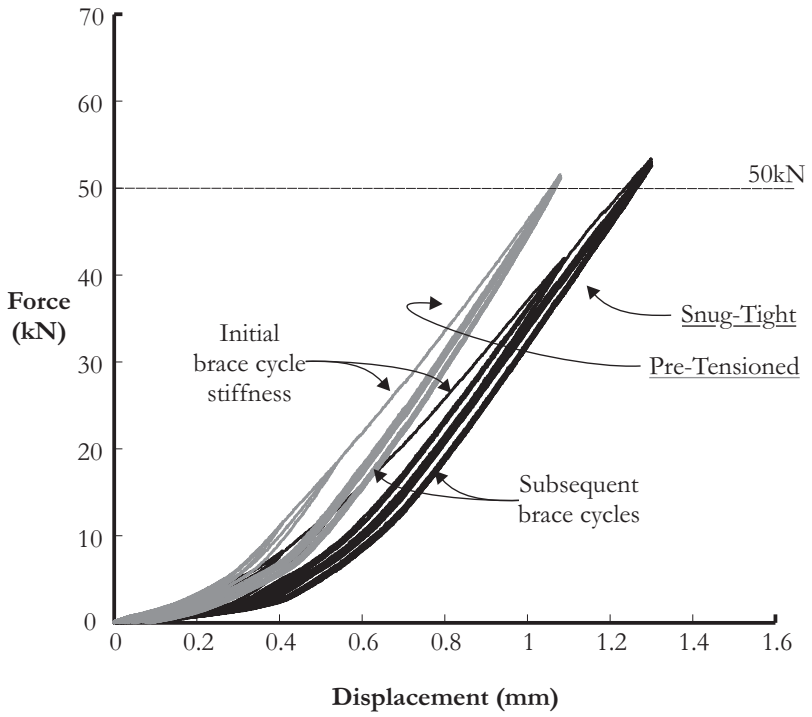

Figure 5.19: Simulated Brace Force Response Comparison

Table 5.10: Ultimate Connection Capacities, kN

	Monotonic	Cyclic
No Pre-Tensioning	130.7	185.3
	198.7	190.9
	185.0	168.4
	200.9	200.7
		167.2
		181.3
Pre-Tensioning	154.4	169.6
	151.9	195.0
	138.5	181.6
	196.6	187.3
		201.0
		177.5

Table 5.11: Statistical Analysis of Resistances, kN

	Monotonic		Cyclic	
	Average	Standard Deviation	Average	Standard Deviation
No Pre-Tensioning	178.8	32.8	182.3	13.0
Pre-Tensioning	160.4	25.2	185.3	11.6

$$\mu = \frac{\delta_{ultimate}}{\delta_y} \tag{5.6}$$

where $\delta_{ultimate}$ is the ultimate displacement of the connections associated with catastrophic failure. The yield displacement, δ_y, was determined graphically as the intersection of the tangents associated with ultimate displacement and the displacement at the onset of initial yielding. The onset of connection yielding was determined from the inspection of the overall force-displacement responses. This was slightly influenced by the application of pre-tensioning as it relates to connection stiffness, however, the onset yield point was not directly influenced by the loading condition applied. Figure 5.20 shows the general method used to determine the yield displacement and individual specimen ductilities.

The brittle pull-out behaviour associated with shear plug failure limited the ductility of glued-in rod connections. The overall mean maximum ductility for the testing program of 1.95 provided a specimen ductility classification of brittle, defined by a mean ductility ≤ 2.0 (Smith et al., 2006). Ductility ratings of the four test groups ranged from brittle to low-ductility ($2 < \mu \leq 4$), showing no significant improvement over the general classification between the specimen configurations. The ductility results showed minor variation in the maximum ductility throughout the various specimen groups, suggesting that pre-tensioning and loading conditions do not affect fastener ductility. This limited ductility is characteristic of the assumed low fracture energy of glued-in rod fasteners containing epoxy resins used in the strength and stiffness calculation previously presented. A summary of the fastener ductilities is presented in Table 5.12, and Table 5.13 shows a statistical analysis of the results.

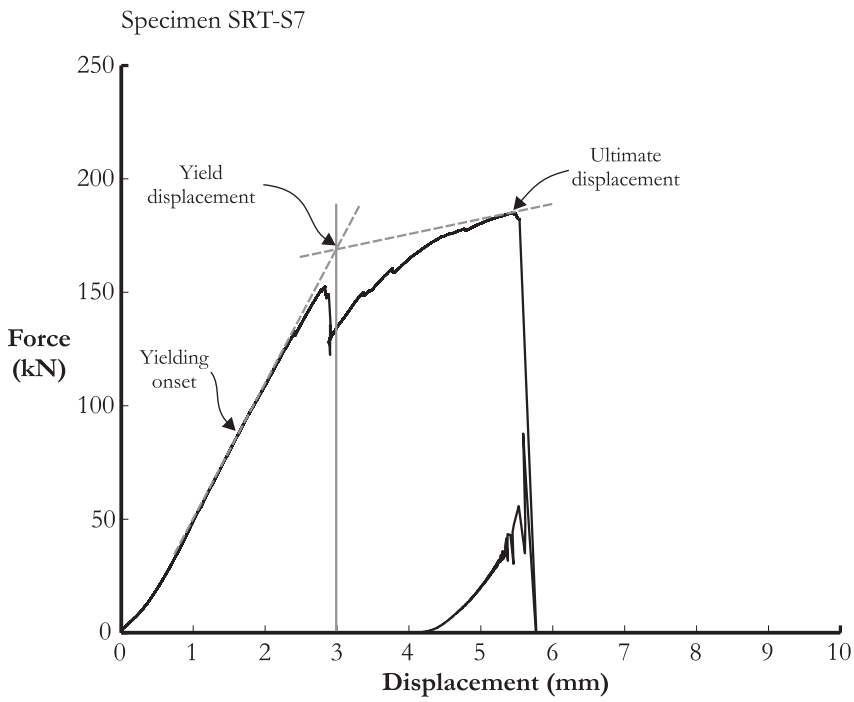

Figure 5.20: General Ductility Method

Table 5.12: Fastener Ductility

	Monotonic			Cyclic		
	δ_{yield} (mm)	δ_{ult} (mm)	μ	δ_{yield} (mm)	δ_{ult} (mm)	μ
No Pre-Tensioning	2.4	3.3	1.4	2.8	5.4	1.9
	3.8	7.4	1.9	3.0	5.7	1.9
	3.0	5.5	1.8	2.5	4.4	1.8
	3.5	8.2	2.3	3.7	8.7	2.4
				2.4	4.4	1.8
				3.0	5.4	1.8
Pre-Tensioning	2.6	4.2	1.6	1.8	3.9	2.2
	2.2	3.7	1.7	2.9	6.5	2.2
	2.0	3.6	1.8	2.5	5.4	2.2
	3.0	7.2	2.4	2.7	5.4	2.0
				3.5	6.5	1.9
				2.6	5.0	1.9

Table 5.13: Statistical Analysis of Ductility

	Monotonic		Cyclic	
	Average	Standard Deviation	Average	Standard Deviation
No Pre-Tensioning	1.9	0.4	1.9	0.2
Pre-Tensioning	1.9	0.4	2.1	0.2

The onset of ductile plastic behaviour was observed in specimens where the axial resistance surpassed the nominal yield resistance, 184 kN, of the threaded rods. However, the elastic stiffness, on-set yield point and catastrophic failure in the timber/adhesive interface limited the ductile behaviour of these specimens. Figure 5.21 shows the limited yielding behaviour captured during the SRT-S11 monotonic and SRT-S15 cyclic tests. These specimens achieved equivalent maximum ductilities of 2.4, resulting in a ductility classification of low. These results were a slight improvement to the overall fastener ductility classification of brittle.

In terms of capacity design considerations, the limited ductility of the test specimens supported the use of fastener detailing techniques to improve the inelastic behaviour of the glued-in rod connections. Designing the glued-in rod fasteners to allow tensile yielding in the rods prior to pull-out failure would improve the seismic performance. This would provide additional energy dissipation capabilities to the seismic force resisting system providing greater capacity protection to the brittle connections and surrounding timber elements during long duration ground motions.

5.10.2.5 Pre-Tension Force Relaxation

In order to determine if relaxation of the pre-tensioning force would occur, one specimen was subjected to a long term strain test. This preliminary test was considered because of the significance load duration and creep have on member strength and connection behaviour in timber. This investigations did not consider environmental effects (such as temperature and moisture) when evaluating the relaxation behaviour in the pre-tensioned specimen. To compensate for the 0.5 degree inclination in the glued-in rod, the specimen was instrumented with a strain gauge on either side of the rod. A control gauge was attached to a 101.6 x 101.6 mm (4 x 4 inch) steel plate

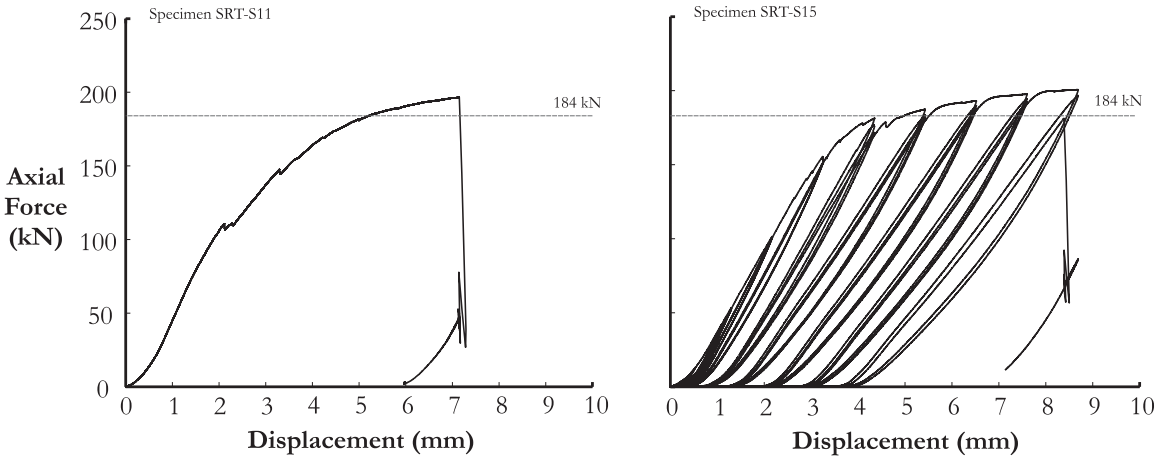

Figure 5.21: Plastic Behaviour

to correct for strain variations associated with fluctuations in voltage and temperature throughout the test period. An initial average pre-tensioning force of 76.7 kN was applied to the glued-in rod fastener and the specimen was left undisturbed for 7 days. Strain readings in the threaded rod were recorded every half hour during the testing period. The raw strain data from the long term test is presented in Figure 5.22. The noise in the raw strain data was filtered by subtracting the control readings from the data captured by the rod gauges, shown in Figure 5.23. Minimal noise still remained in the filtered data due to variation in gauge insulation and environmental exposure between the glued-in rod specimen and the control gauge. This residual error is negligible for the purpose of strain degradation trend analysis. The variation in the strain readings from the rod gauges was attributed to prying action caused by pre-tensioning force and inclined rod. This action induced compression in one side of the rod, underestimating the strain in gauge 2, and subsequently induced tension in the opposing side over estimated the strain in gauge 1. This bending action was corrected by taking the mean of the two data sets, as seen in Figure 5.23.

The force degradation results shown in Figure 5.24 suggest that the pre-tensioning force in glued-in rods has an exponential decay behaviour that had not reached a completely steady state after the 7 day test period. The specimen experienced a 13.9 kN reduction in the pre-tensioning force over the test period resulting in a remaining pre-tensioning force of 62.8 kN. However, the majority of the relaxation occurred within 3.5 days resulting in a force loss of 12.5 kN over

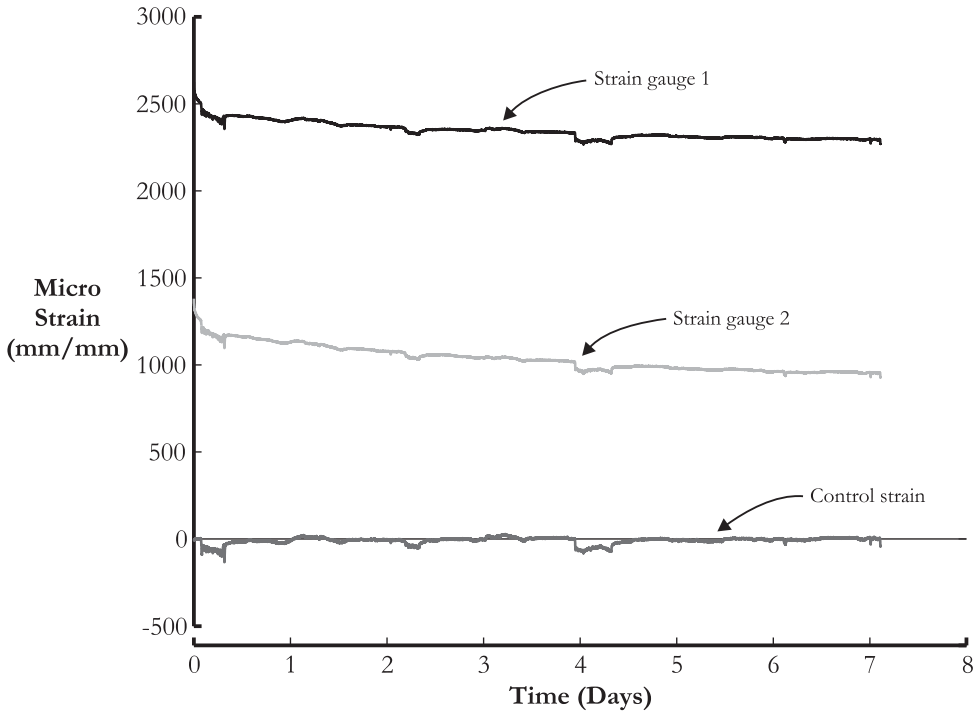

Figure 5.22: Long Term Raw Strain Data

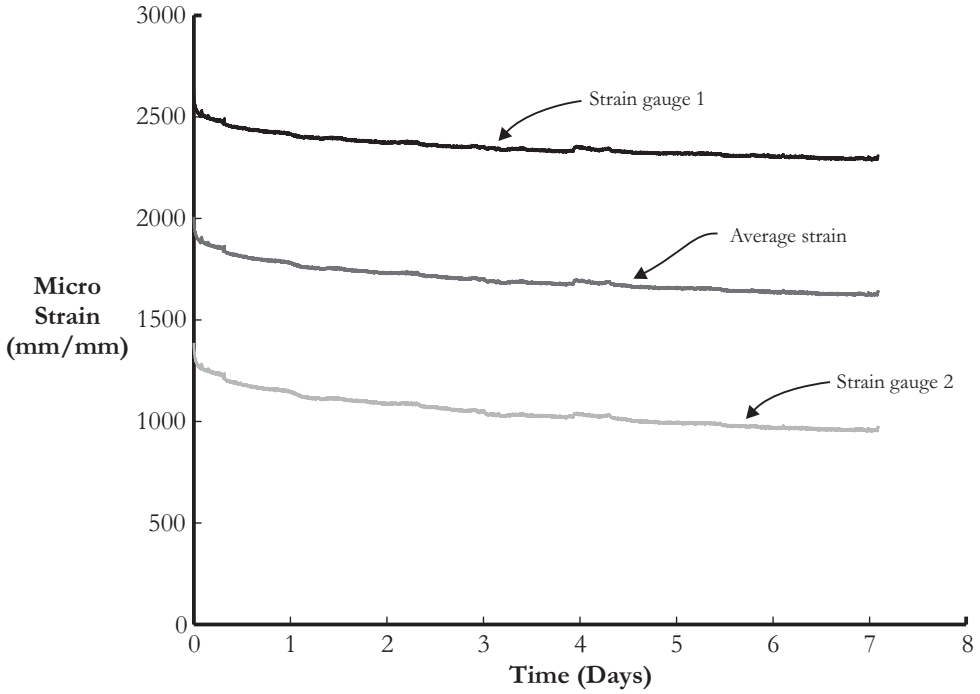

Figure 5.23: Long Term Filtered Strain Data

this period. Considering that one specimen was used to evaluate the approximate long-term creep behaviour of a pre-tensioned glued-in rod connection, a more comprehensive study of this effect is necessary to determine the practical use of pre-tensioned glued-in rod connections and to develop design recommendations.

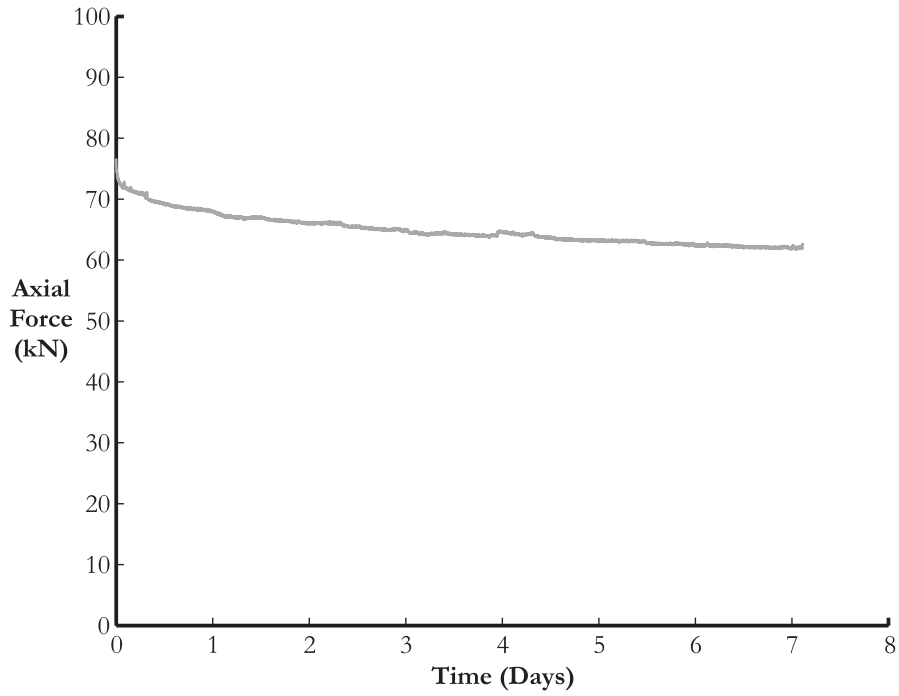

Figure 5.24: Long Term Pre-Tensioned Force Relaxation

5.11 Conclusions

The single rod experimental program has shown that the pull-out resistance of the specified glued-in rod specimens using Sika AnchorFix©-3001 epoxy exceeds the anticipated strength capacities determined from the three existing European design methods. Even though there was a high variance in the strength results for the various loading scenarios, all specimens exceeded the predicted unfactored ultimate strength capacity. The connections exhibited predictable strength behaviour and limited ductility during the monotonic tests that is common for glued-in rod fasteners. Furthermore, the study found that although pre-tensioning does not have an impact on

the ultimate resistance of glued-in rods it does cause an increase in the initial stiffness of the connection. The connections subjected to cyclic loading did not experience any difference in the pull-out resistance as a result of the loading protocol. These specimens exhibited predictably brittle behaviour and low fastener ductility due to the incremental failure of the timber at the timber/adhesive interface, limiting energy dissipation. The results from the cyclic tests provide evidence that shows glued-in rod connections experience negligible impact to stiffness and peak resistance within the elastic range under load reversal. These findings are particularly important for seismic applications and suggest that the glued-in rod fasteners utilized in the associated braced frame study will remain elastic under the anticipated earthquake loads.

5.12 Limitations and Considerations

Based on the findings, this research suggests that the design methods presented may potentially be used to conservatively determine the tensile resistance of glued-in rod connections containing the Sika AnchorFix©-3001 2-component epoxy. However, further investigation into the broad applicability of these calculations is required for specimens with varying embeddment lengths and fastener size, since only one type of failure mode was represented in these tests (failure on the timber-side of the bond line interface). Additionally, an experimental program designed to determine the specified bond line shear strength and geometric parameters of the timber/adhesive interface is required to more accurately predict the pull-out resistance of glued-in rod connections under varying adhesive and timber types. Additional tests containing a set-up with pull-distributed and pull-pull boundary conditions are required to evaluate the strength and stiffness characteristics of glued-in rod specimens with various Canadian materials. These results will validate the Canadian application of the design methodologies presented.

Overall, research into the long term effects of glued-in rods is required to establish connection behaviour and resilience, especially if these fastener types are to be used in vital structural framework such as seismic force resisting systems. Further investigation into pre-tensioning is required to evaluate if it has a long term effects on the connection stiffness or whether the relaxation allows the connection stiffness to settle back to the snug-tight characteristics. These investigations

would provide insight into the effectiveness of pre-tensioning glued-in rod connections exposed to high tensile forces after a prolonged period after installation.

Lastly, high cycle fatigue testing is required to evaluate the strength and stiffness behaviour of glued-in rod fasteners exposed to wind loading scenarios and high frequency vibrations. High cycle fatigue testing was conducted on grouped glued-in rod connections as part of the hybrid timber-steel braced frame study. However, single rod tests would provide detailed results on the fatigue characteristics of the braced frame connections necessary to evaluate wind performance of the connections.

Chapter 6: Testing of Hybrid Braced Frame Prototype

6.1 Objectives

Timber provides attractive earthquake performance characteristics when designing buildings in regions of high seismic risk, such as its high strength-to-weight ratio; however, current timber structures provide limited force reduction factors due to their low inherent ductility. The primary objective of this study is the experimental testing of an advanced structural bracing system adapted into heavy timber frames. This system utilizes energy dissipation to improve the seismic performance of hybrid timber-steel buildings. These seismic systems also provide high force reduction factors (R-factors) that limit seismic design forces and provide improved seismic performance. This study focuses on the design and quasi-static cyclic testing of a friction damping device within a timber frame which will dissipate seismic energy and satisfy performance-based design requirements. The bracing system is incorporated into the timber frame using select steel elements and glued-in rods connections which fasten the steel and timber elements together. The secondary objectives of the testing program are (1) to investigate the effects of pre-tensioning on glued-in rod connection on overall frame performance, and (2) to evaluate high cycle fatigue performance of glued-in rod fasteners subjected to wind loading simulations at differing displacement amplitudes. These findings will aid in establishing design requirements of glued-in rod connections for seismic and wind applications.

6.2 Test Set-up

The hybrid timber-steel braced frame was designed as the primary lateral force resisting system of a six storey heavy timber building located in Victoria, BC. The test specimen was designed to represent a scaled first storey braced connection located on an exterior column and is shown in Figures 6.1 and 6.2. The assembly was tested at half scale to reduce the test assembly foot print. The lateral cyclic loading protocols were applied axially to the beam element through an intermediate force transfer connection. The gravity and seismic axial load contributions in the first storey column were not considered for the experimental program. This ensured the brace would develop higher tension loads in the column connections than if the axial column compression forces were considered, because these compression forces would have eliminate the tension forces in the glued-in rod connections. Additionally, these loads would posed significant experimental challenges with respect to equipment and system control. However, the portion of lateral frame displacement resulting from the P-Delta effects of these concentrated axial loads were included in the dynamic earthquake tests by using simulated first storey displacement histories.

The half scale braced frame prototype was assembled and tested parallel to the strong floor due to laboratory constraints and to simplify frame instrumentation. The prototype was constructed from timber structural elements and intermediate steel connections used to adapt the friction damping device. A set of timber beams and columns were fabricated for each of the two test configurations. The beam and column sections contained grouped glued-in rod connections at each end allowing four connections to be tested simultaneously. The glued-in rods were fabricated from 19.1 mm ($\frac{3}{4}$ inch) fully threaded rods embedded 600 mm into the end grain of the timber sections. The individual glued-in rod fasteners used in the hybrid braced frame were identical to the glued-in rods investigated in the single rod study presented in Chapter 5. Each beam connection contained four glued-in rods where the column joints were fabricated from eight glued-in rod fasteners. The strength and stiffness characteristics of the individual glued-in rod fasteners were evaluated in Chapter 5 by the associated experimental investigation.

The 245 kN (55 kip) actuator with a +/−127 mm (5 inch) inch stroke was attached to the

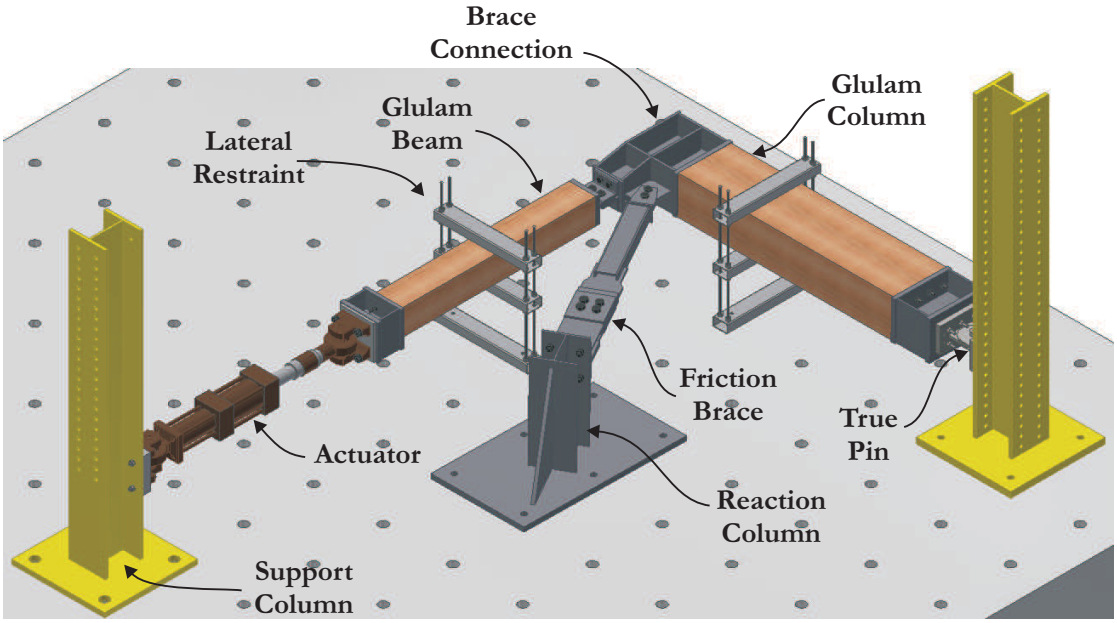

Figure 6.1: Hybrid Braced Frame Assembly

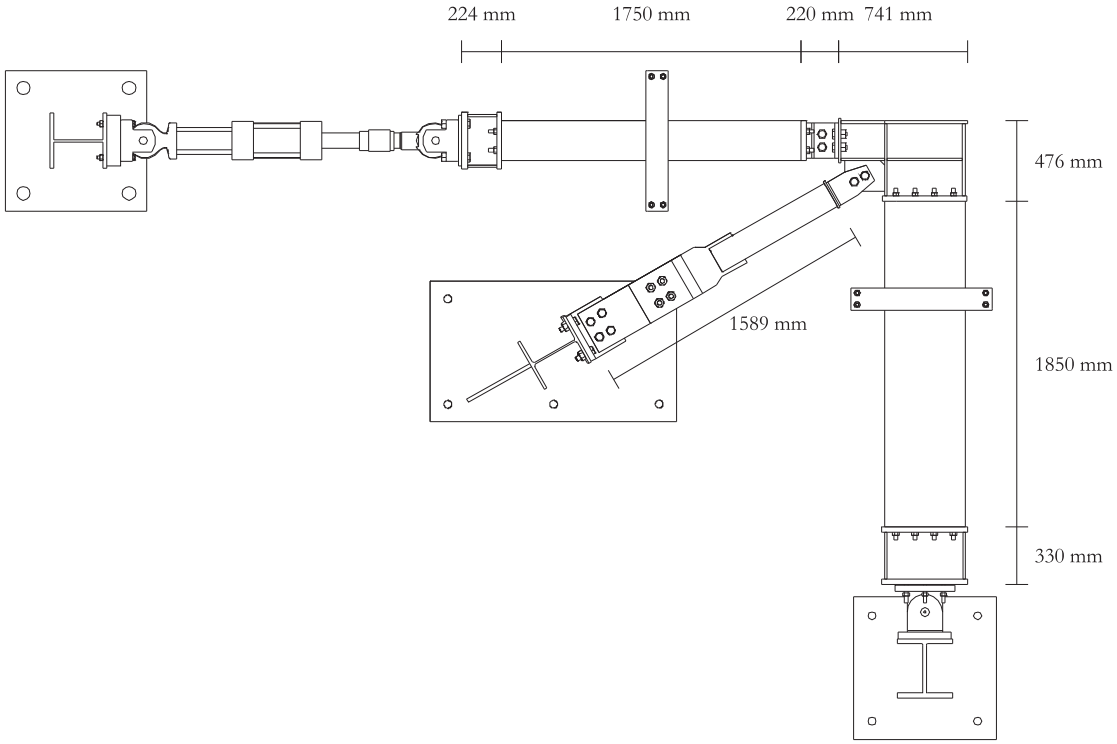

Figure 6.2: Plan View of Hybrid Braced Frame Assembly

timber beam via an intermediate steel section. Support reactions were provided by the support column at the base of the timber column using a true pin connection. The friction brace was mounted to a custom reaction column designed to minimize support movement during the static and dynamic test programs. Lateral restraints were positioned a short distance from the brace connection on each timber section to prevent out of plane movement and support the self weight of the frame. High strength dywidag bars were used to pre-tension the three support columns and lateral restraints to the laboratory strong-floor. To provide a level bearing surface, hydrostone was applied to the strong-floor underneath the support column base plates.

6.2.1 Strength Calculation

The pull-out resistance of the glued-in rod connections were determined from the three design methods described in Chapter 3. The nominal resistance determined by the GIROD Report (Bengtsson and Johansson 2002) method was calculated to 123 kN per fastener. Furthermore, the factored resistances of 115 kN/rod and 113 kN/rod were calculated by the LICONS Report (Connolly and Mettem 2003) and DIN 1052 (NABau 2004) procedures respectively. Therefore the combined beam connection capacity for the GIRod Report, LICONS Report and DIN 1052(2004) were 492 kN, 460 kN, and 452 kN, repectively. The combined column connection resistances of the three design methods were predicted as 1000 kN, 920 kN, and 904 kN, respectively. The high cycle factored fatigue resistances of the glued-in rod connections for SLS design considerations subjected to 2000 loading cycles for the beam connections are 231.2 kN, 216.4 kN and 212.4 kN for the three design methods respectively, where SLS fatigue resistances of the column connections are 407.4 kN, 432.8 kN and 424.8 kN. The ULS considerations provided an additional reduction in fatigue resistance as a result due to uncertainty in the fatigue behaviour of glued-in rod connections that is applicable for fasteners used in vital structural frameworks (Bengtsson and Johansson, 2002). The beam connection resistance of the design procedures for ULS considerations were calculated to be 92.4 kN, 86.4 kN and 84.8 kN. Lastly, the factored ULS fatigue resistances of the column connections are 188 kN, 172.8 kN and 169.6 kN respectively. The ULS high cycle resistances of the beam connection were significantly less than the expected force demand of 159 kN of the wind simulation test. However, the column connections are

expected to remain elastic during the wind loading procedure because the ULS resistances were appropriately twice the predicted connection force demand of 90.5 kN. The fatigue resistance of the connections was evaluated by the wind loading procedure of the ASCE-07 loading protocol and the results was used to validate the high cycle resistance predictions of the three design methods.

6.3 Test Frame Fabrication

Prior to assembly, the 19.1 m ($\frac{3}{4}$ inch) glued-in rod connections were manually fabricated using an assisted drill assembly. The various stages of the fabrication process were completed in the laboratory with minimal surface preparation to simulate on-site conditions. The timber members were donated by Nordic Structures Inc. and pre-cut to the specified lengths. The two-component structural epoxy was provided by Sika Canada Inc. The intermediate steel braced connections were designed and fabricated from G40.21 300W steel in accordance with CSA S16-09 (2009) specifications. Water jet cutting was used in the fabrication of the steel sections which limited the in lab adjustments required to assemble the hybrid frame. However, the cutting process did leave burs in the holes designated for the glued-in rod connections. These were removed with a 20.6 mm ($\frac{13}{16}$ inch) drill bit. Detailed fabrication drawings of the steel sub-assemblies are presented in Appendix A.

6.3.1 Timber Element Fabrication

Minimal preparation was done to the end grain surfaces prior to fabrication. Staples used to secure the protective weather barrier during transportation and storage were removed to prevent damaging the drill bit. Connection dimensions were then marked on the end grain to provide the outline the fastener locations. Guide holes were made at each fastener location using a center punch to prevent straying of the drill bit during the initial drilling stage. A modified version of the manually assisted drilling apparatus described in Chapter 5 was used to drill the embedding holes. Figure 6.3 shows the modified drilling apparatus during fabrication. A support frame and guide rail was fabricated and mounted on the drill apparatus to support the timber elements at

the correct fastener spacings and edge distances. An aluminium angle was secured perpendicular to the guide rails 100 mm from the dill stop to provide a reference against which to align the end grain surface being drilled. Ratchet straps were also used to secure the timber members to the fabrication table throughout the drilling process.

The 600 mm embedment holes were fabricated in stages to prevent the wood chips from redirecting the auger bit during drilling. This also prevented the bit from locking in the hole cause by debris build-up. The 22.2 mm ($\frac{7}{8}$ inch) auger bit was used to drill the initial hole depth of 457 mm (18”) continuously. The longitudinal groves machined into the bit allowed for the wood chips to exit the embedment hole without issue. However, in the latter stages of drilling, a 305 mm (12”) extension was used that required the drill bit be fully extracted periodically to allow the debris to exit the embedment hole. After the holes were drilled, a high pressure air hose was used to remove the remaining debris prior to the installation of the glued-in rod fasteners.

The fully threaded 19.1 m ($\frac{3}{4}$ inch) B7 rods were received in 3.7 m (12 feet) lengths and had to be cut to size. All 48 rods used in the fabrication of the glued-in rod fasteners were cut to consistent length of 675 mm to accommodate embedment length requirements and provide ample fastener length to complete the steel to timber connection. One end of each rods was then machined to a 5.7 x 5.7 mm (0.225 x 0.225 inch) tip to allow for the rods to be centered in the bottom of the embedment hole. Tape was wrapped around a 75 mm section at the end of each rod to mark the end of the 600 mm embedment length and protect the threads during installation.

6.3.2 Glued-in rod Embedment

The timber members were positioned side-by-side vertically to allow for four connections to be embedded in succession. All four members were secured to a work station to prevent the members from shifting during installation. Figure 6.4 shows the fabrication process for the first set of glued-in rod connections. The epoxy was injected into the embedment hole using an two-component adhesive dispenser. A static mixing nozzle and extension tube were attached to the epoxy cartridge port to ensure adhesive was evenly dispensed in the bottom of the 600 mm embedment hole. The initial effluent from each new cartridge was discarded to ensure no streaks

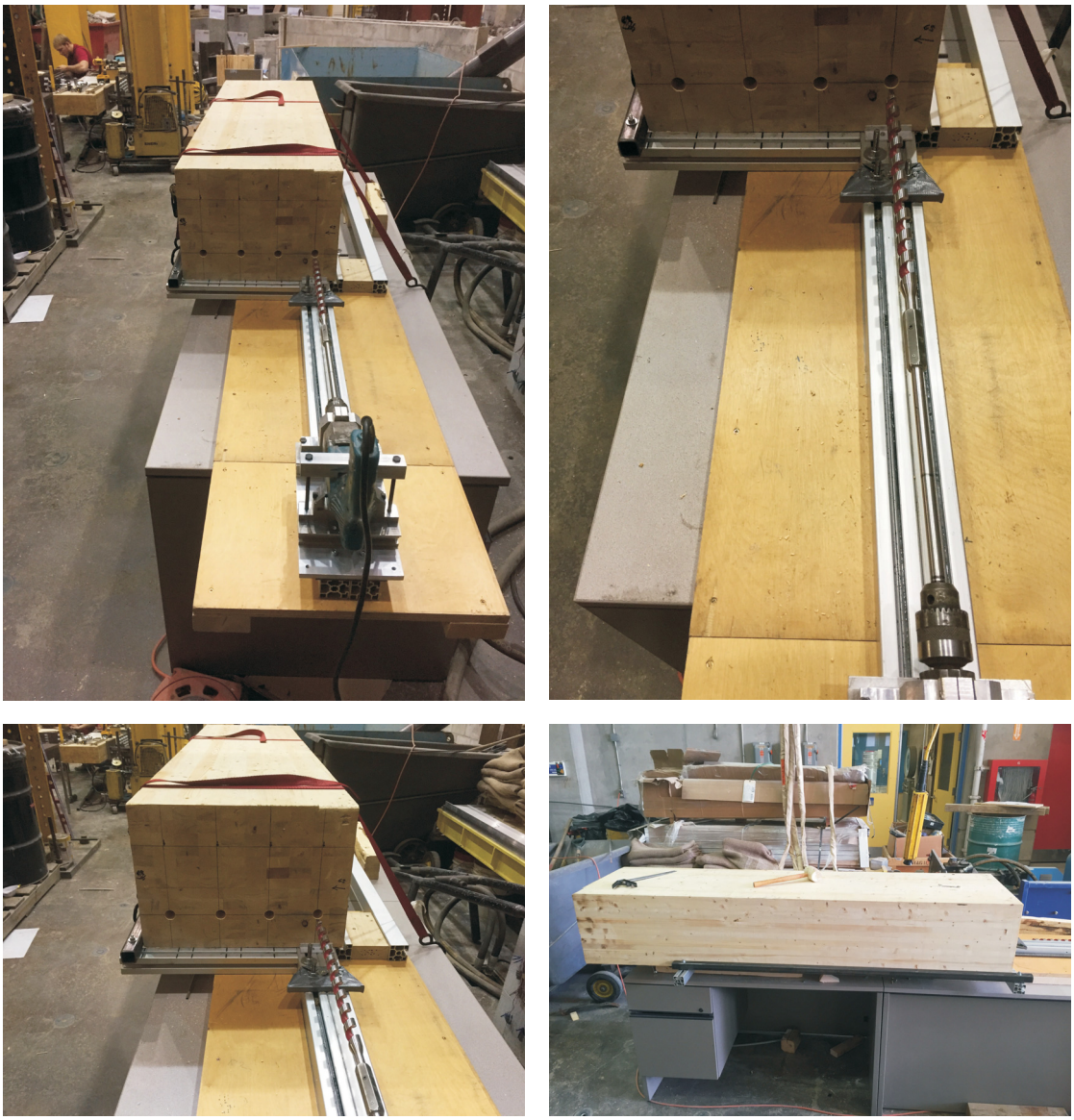

Figure 6.3: Modified Drilling Apparatus

of unmixed adhesive were present, providing a homogeneous consistency. Once the cartridge was primed, four embedment holes were filled in succession prior to replacing the cartridge. The embedment holes were filled to approximately a quarter of the total depth to ensure enough adhesive was in the hole to evenly surround the threaded rod and allow for excess adhesive to flow out the top of the embedment hole. When an anchor hole was filled, a threaded rod was inserted into the hole until initial contact with the adhesive. The rods was then steadily forced into the adhesive and continuously turned clockwise until the rod had reached the full embedment depth. The vertical force remained on the rods until the excess adhesive stopped exiting the embedment hole. The excess adhesive was than removed from the end grain surface using a trowel to prevent the formation of asperities that could affect the contact bearing surface between the timber and base plates of the steel sections. Wood shims were then placed around the rod at the hole opening to center the rod in the embedment hole. Immediately after installation, pre-fabricated spacer templates were positioned over the glued-in rod fasteners and secured to the longitudinal surfaces of timber sections to ensure the rods did not move during the curing process. The templates were fabricated from 19.1 mm ($\frac{3}{4}$ inch) plywood sections and the fastener locations were drilled at the appropriate spacings using a 19.1 mm ($\frac{3}{4}$ inch) drill bit. Figure 6.5 shows the spacer plates and centering shims following fastener installation. The glued-in rods were then set to cure for seven days. After the initial curing stage, the templates were removed and temporary footings were fastened onto the end grain surface. At this point, the members were lowered to the floor and the alternate ends were inverted. Footing supports were fabricated to prevent loading on the glued in rods during the installation of the remaining four connections located at the opposite member end.

6.4 Frame Assembly

After the support columns were positioned and pre-tensioned to the strong-floor, the 245 kN actuator was mounted 638 mm from the floor to the center of the actuator. A pre-fabricated hold-down support was then fastened to the actuator mounting plate and pre-tensioned to the

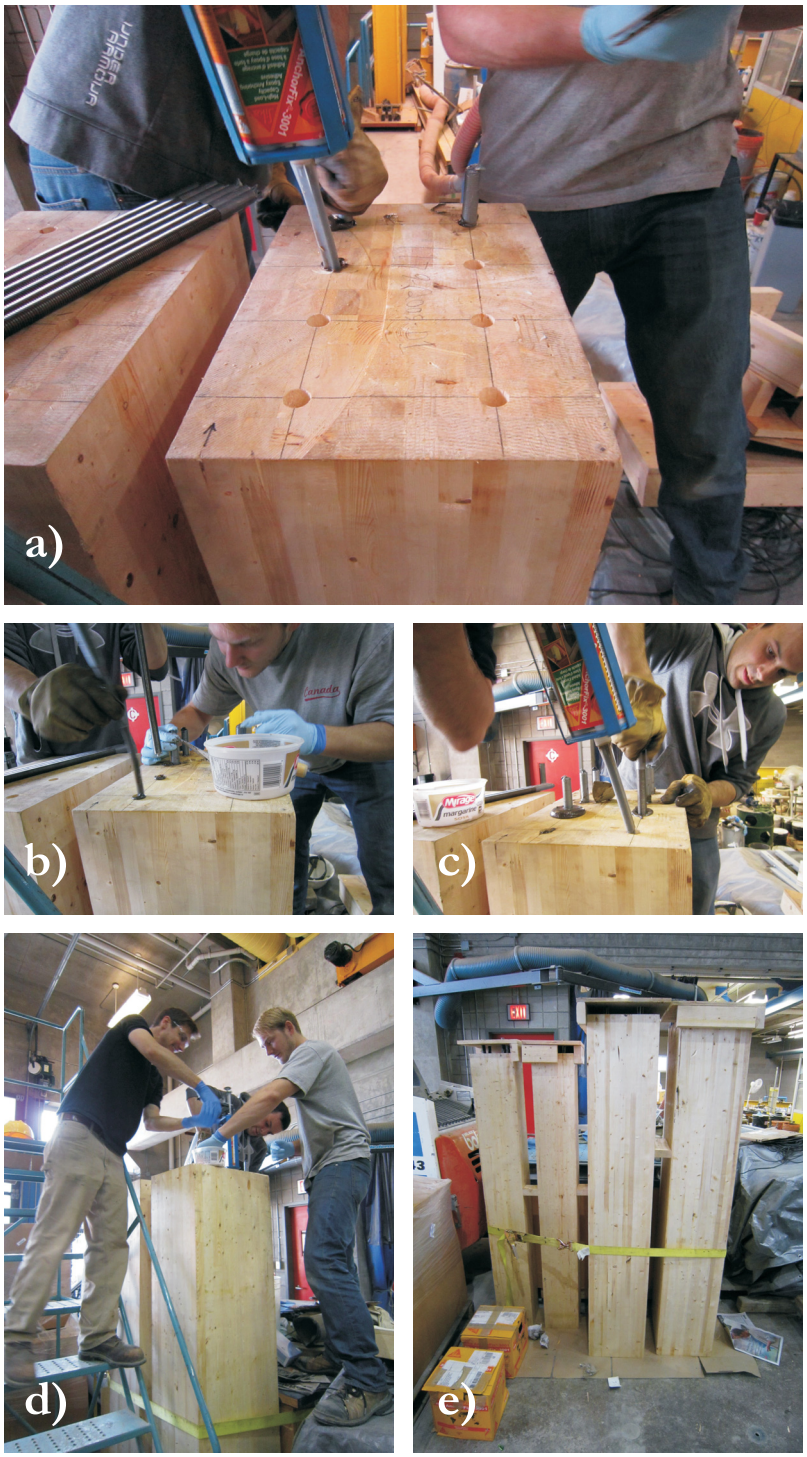

Figure 6.4: Installation of Glued-in Rod Fasteners
a) Embedment holes were Filled Using Extension Tube
b) and c) Rods Were Embedded into the Sections
d) and e) Rods Were Centered and Spacer Templates Were Installed

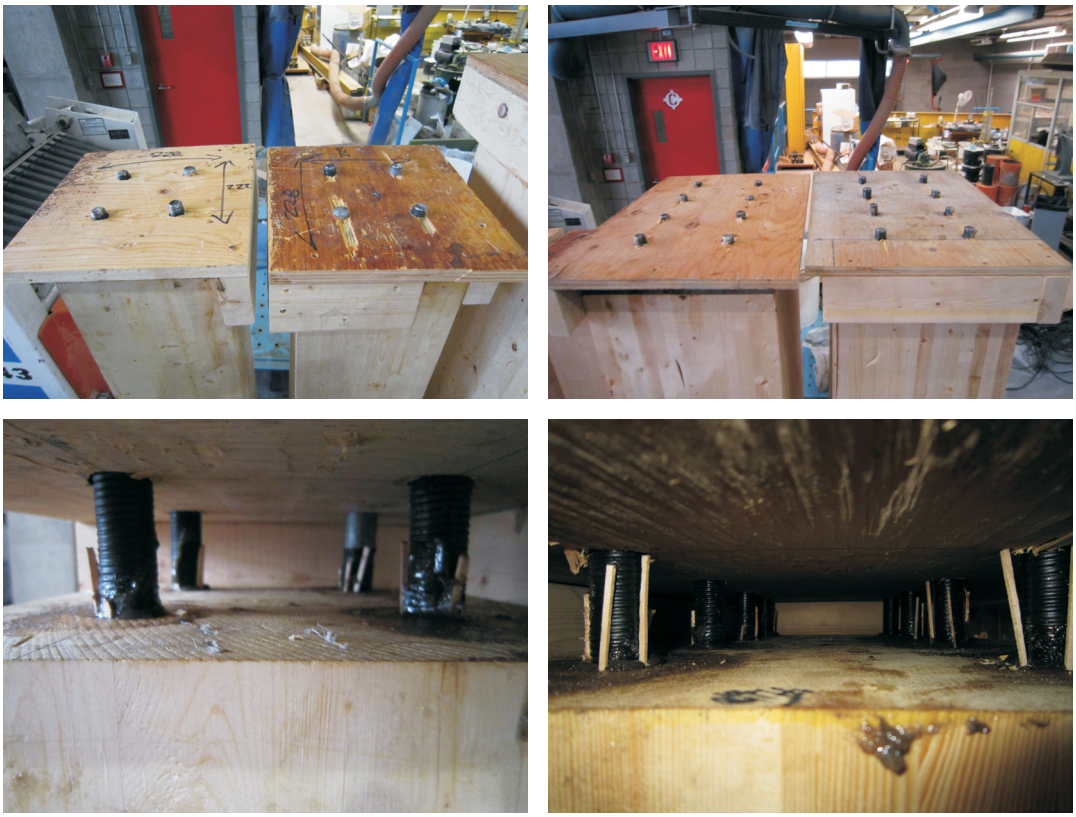

Figure 6.5: Installed Spacer Templates and Centering Shims

floor, shown in Figure 6.7. The hold-down was designed to restrain out-of-plane movement in the actuator and provide an additional fixity to prevent hinging in the actuator socket connected to the support column. The lower support section of the lateral restraints (Shown in Figure 6.7) were positioned at correct heights corresponding to the beam and column members. Prior to positioning the timber sections, the intermediate steel sections (Shown in Figure 6.7) were mounted to timber sections by the glued-in rod connections. The hybrid beam and column sections were then lifted into position and lowered onto the lateral restraints and bolted to the support column connections. Assembly of the friction device then took place with the friction brace first being mounted to the gusset plate connection and supported by the gantry crane. The brass friction plates, steel side plates and washer were then placed on either side of the slotted stainless steel plates and bolted together. The four 25.4 mm (1 inch) friction interface bolts were hand tightened to take the self weight of the brace for the remainder of the frame assembly. No surface conditioning was conducted on the stainless steel and brace plates prior to installation. Figure 6.6 shows the final friction interface assembly prior to instrumentation. All bolted connections were then pre-tensioned using the turn of nut method and the glued-in rods were tightened to snug-tight conditions for the first frame configuration. Lastly, prior to testing, the steel sections, except for the friction brace, were white-washed to help detect if yielding occurs during testing. The final hybrid frame assembly is shown in Figures 6.7 and 6.8

Figure 6.6: Friction Interface Assembly

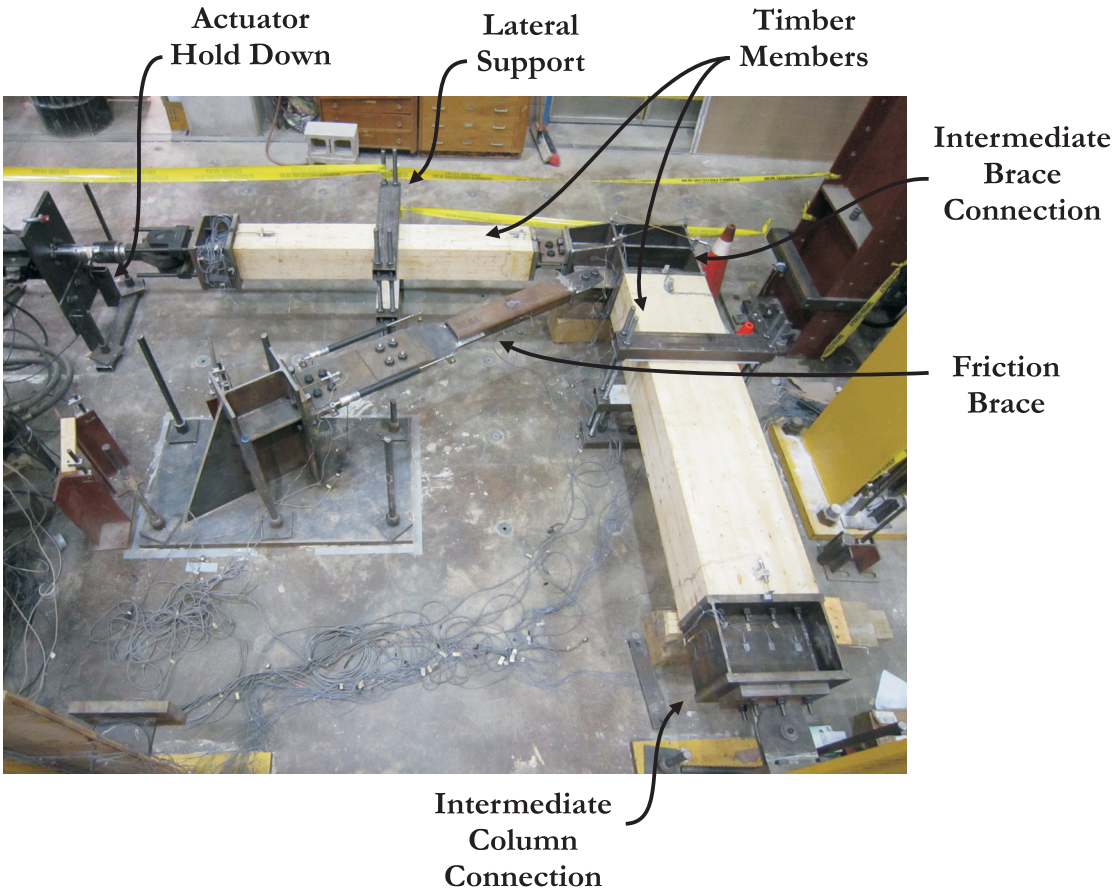

Figure 6.7: Final Hybrid Frame Assembly

prior to white-washing.

6.4.1 Pre-Tensioning of Bolted Connections

CSA S16 (2009) assembly guidelines for bolted steel connections designed for seismic applications require the bolts be pre-tensioned to the specified nut rotations defined by the grip length of the fasteners. These guidelines specify that all bolted connections must first be tightened to snug-tight conditions and than pre-tensioned to the specific force requirement of 70 % of the bolt's tensile resistance (CSA S16, 2009). Therefore, the bolted connections subjected to tension loads were pre-tensioned in accordance with CSA S16-09 (2009) Clause 22.2.2 using the turn of nut method. The connection grip length of the A325 bolts was used to determined the degree of nut rotation defined in Table 8 of CSA S16-09 (2009). The shear pin connection at the beam to intermediate brace connection was pre-tensioned to the specifications of Clause 27.1.6 of CSA S16-09 (2009) for seismic applications. The 95.3 mm (3-3/4 inch) long 225.4 mm (1 inch) A325 bolts were torqued to a nut rotation of $\frac{1}{3}$ as specified by the grip length of 63.5 mm (2-1/2 inches). The pin connection behaviour was closely monitored throughout the testing program to evaluate the accuracy of the assumed pinned restraints used in the frame analysis. The gusset place and brace anchor connection were classified as slip critical and were both pre-tensioned the the appropriate nut rotations specified in Table 8 of CSA S16-09 (2009).

6.4.2 Pre-Tensioning of Glued-in Rods

The findings from the associated study investigating pre-tensioning of glued-in rods discussed in Chapter 5 provided the basis for the pre-tensioning procedure utilized in the frame assemblies. The pre-tensioning forces were applied using a metric torque wrench. Two pre-tensioning levels were selected to evaluate its affect on connection characteristics and the global frame behaviour of the two test configurations. The first set of timber sections were tightened to snug-tight conditions defined by an applied torque of 165 N·m. This applied torque simulated the construction of the hybrid braced frame if pre-tensioning was not implemented. The second glued-in rod configuration was assembled with an applied pre-tensioning torque of 267 N·m.

Figure 6.8: Final Hybrid Frame Assembly

This torque level was determined to induce an approximate pre-tensioning force of 70 percent of the pull-out resistance of the fasteners equal to 80.5 kN. Figure 6.9 shows an example of the beam and column glued-in rod connection that were tightened to the required torque levels. The glued-in rods in the snug-tight test configuration were tightened to the target torque of 165 N·m during the initial frame assembly and were left for the remainder of the test program. The rods were not adjusted because relaxation was not expected to occur in glued-in rods containing low pre-tensioning levels. However, the glued-in rod fasteners in the pre-tensioned test configuration were all initially torqued to the require 267 N·m right before conducting the first wind loading simulation test. Over the course of the four day testing program one beam and column glued-in rod connection was re-torqued to the target pre-tensioning level to allow for the comparison between the initial connection stiffness and the stiffness during relaxation.

6.5 Instrumentation

Prior to assembly, strain gauges were attached to the web and flanges of all the intermediate steel sections to evaluate the axial force transfer through the sections. The web gauges were mounted in line with the glued-in rod fasteners to estimate the axial force distribution in the glued-in rod connections. An example of the strain gauges installed is shown in Figure 6.11. Additionally, the HSS section of the friction brace was gauged on all four sides use to calculate

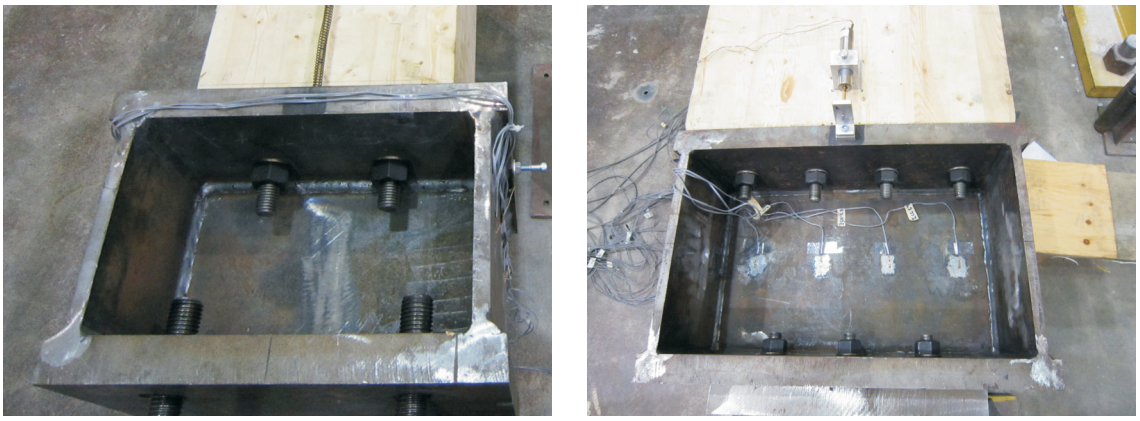

Figure 6.9: Glued-in Rod Beam and Column Connections

the actual brace force during the quasi-static and dynamic tests.

The full frame instrumentation plan is shown in Figure 6.10. Linear variable differential transformers (LVDTs) with a displacement range of ± 6.4 mm (1/4 inch) were used to instrument the glued-in rod connections and steel panel zone of the intermediate brace connection, shown in Figure 6.11. The glued-in rod connection LVDTs were installed to evaluate the stiffness and displacement characteristics of the glued-in rod joints at both applied torque levels during the static and dynamic loading protocols. The steel panel zone instruments were used to determine if any significant shear forces were developed in the panel zone. The presence of shear forces was most likely be the result of an eccentricity in the brace force caused by frame misalignment.

The instrumentation of the friction interface and brace support connection is presented in Figure 6.12. Two ± 152 mm (6 inches) linear potentiometers (linear pots) were used to capture the displacement and rotation in the slotted friction interface. All brace rotation was expected to occur in this location due to the pre-tensioning requirements of the slip-critical connections. Modified 12.7 mm ($\frac{1}{2}$ inch) bolted were used to fasten the linear pots to the mounting brackets welded to the either side of the T-stub brace mounting mechanism and slotted inner place of the friction interface. A spring loaded LVDT mounted to the upper side plate of the friction interface was used to evaluate connection behaviour in the slip-critical connection used to anchor the brace to the reaction column.

Global frame movement was captured by two 152 mm (6 inch) string potentiometers (string pots) mounted to the support columns. A string pot was connected to the conner of the hybrid frame attached to an instrument mount welded to the intermediate brace connections, shown in Figure 6.13. In an attempt to capture displacement in the pinned beam connection, a externally mounted string pot was connected to the intermediate steel beam spacer connection, shown in Figure 6.14. An additional string pot was mounted to the actuator support column following the initial frame tests conducted on the sung tight configuration after observations of movement in the support column. This instrument will capture the displacement behaviour in the reaction column and was used to evaluate the discrepancies between the frame and input

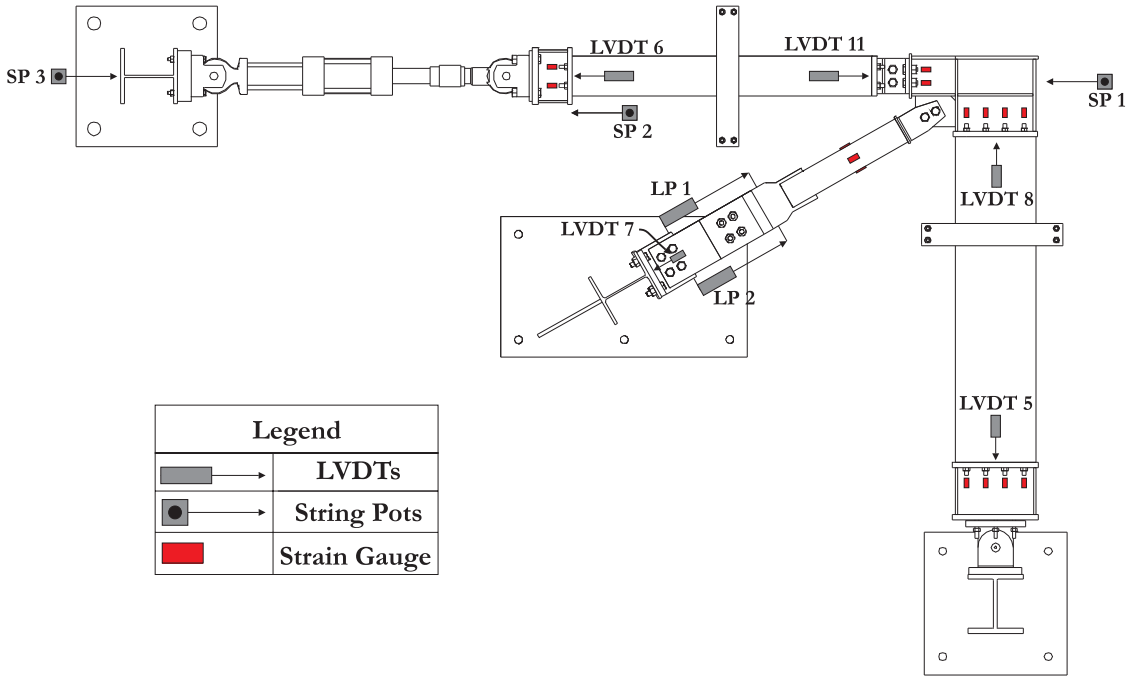

Figure 6.10: Final Instrumentation Plan

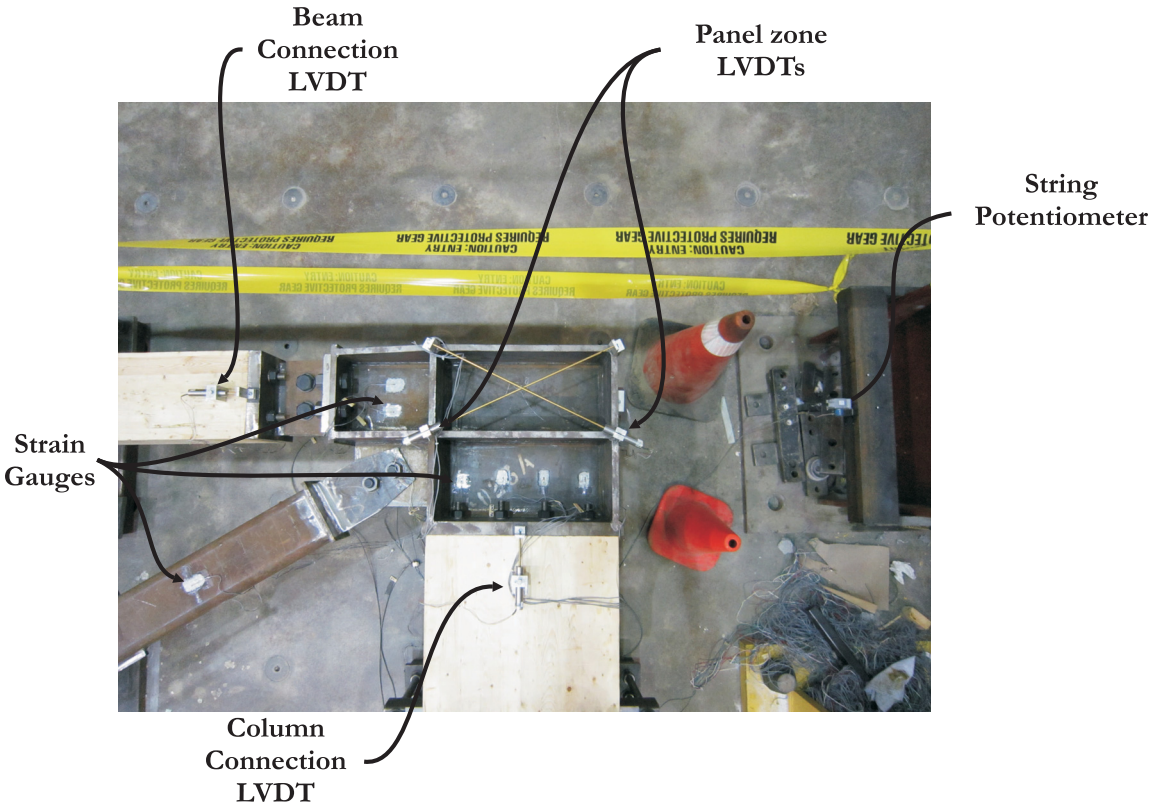

Figure 6.11: Panel Zone and Glued-in Rod Connection Instrumentation

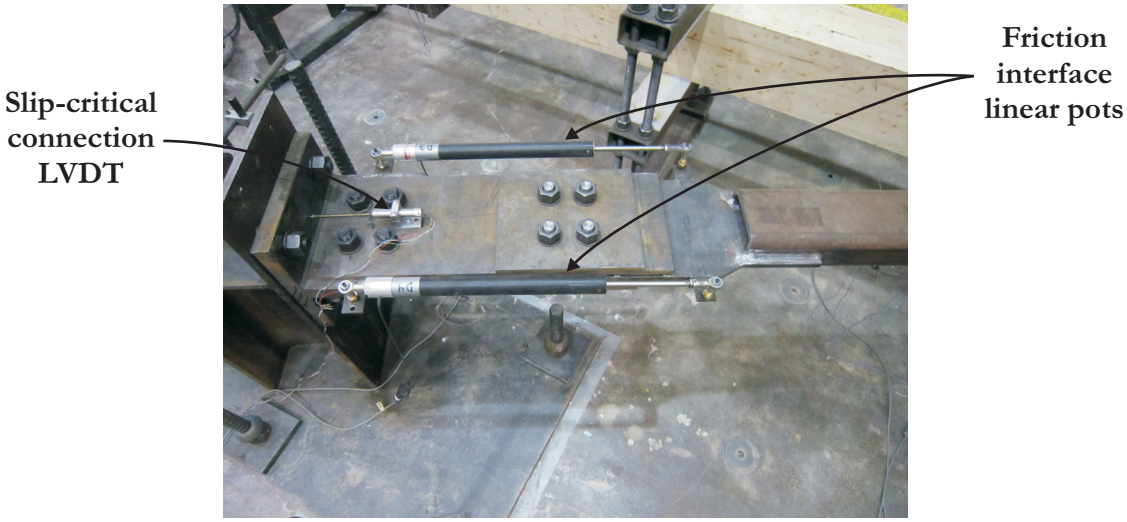

Figure 6.12: Friction Region Instrumentation

displacement-time histories. Lastly, a Delmhorst Model RC-IC Solid State Moisture Detector was used to record the wood moisture contents of the test members prior to each test. The timber members were stored in a conditioned laboratory environment for approximately 9 months prior to testing. The mean recorded moisture contents of the timber specimens used in the snug-tight and pre-tensioned test configurations are presented in Table 6.1.

Table 6.1: Mean Moisture Content Reading of Timber Elements

Timber Member	Moisture Content
Snug-Tight Set-up	
Beam	9.0%
Column	8.5%
Pre-Tensioned Set-up	
Beam	9.5%
Column	9.0%

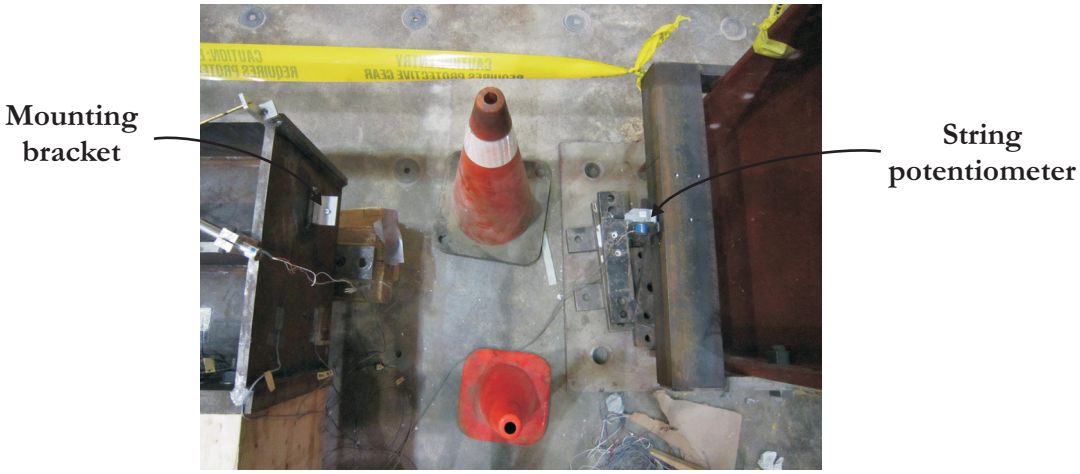

Figure 6.13: Intermediate Brace Connection String Pot Instrumentation

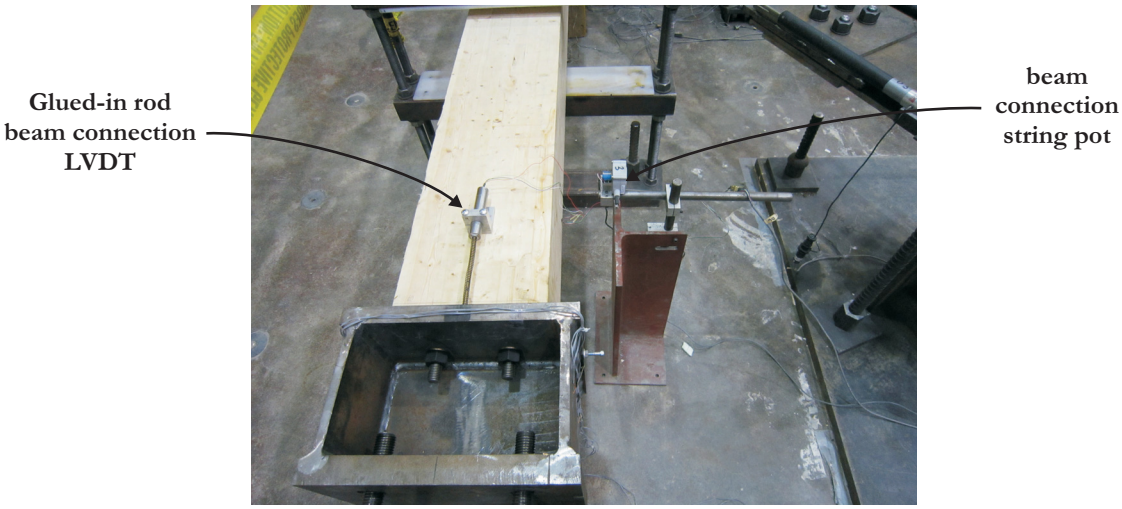

Figure 6.14: Beam Connection String Pot Instrumentation

6.6 Friction Brace Calibration

Before the loading program could be conducted, smaller displacement and rate controlled tests were completed to evaluate the stainless-steel to brass friction brace behaviour. As previously mentioned in Chapter 3, the friction device components include a slotted steel plate, two stainless-steel and brass friction surfaces and two outer steel plates. The friction interface was calibrated to the required half-scale capacity design probabilistic tension and compression brace forces of 183.0 kN and 202.0 kN from the first storey BRB design. The friction interface was calibrated using the actuator load cell to provide a minimum target lateral force of 159.0 kN, determined using the brace angle of 29.7 degrees. The extensive calibration test procedure investigated the effect of velocity and temperature variations on the static and dynamic friction resistance of the stainless-steel on brass interface configuration. The four high-strength 25.4 mm (1 inch) bolts of the friction device were pre-tensioned to various applied torques levels using a manual torque wrench to determine the torque required to generate the target friction force. Additionally, the bolt elongation was measured using a custom-fabricated measuring device with a metric dial gauge. These measurements was used to estimate the coefficient of static and dynamic friction of the stainless-steel and brace interface. Figure 6.15 shows the device used to measure bolt elongation.

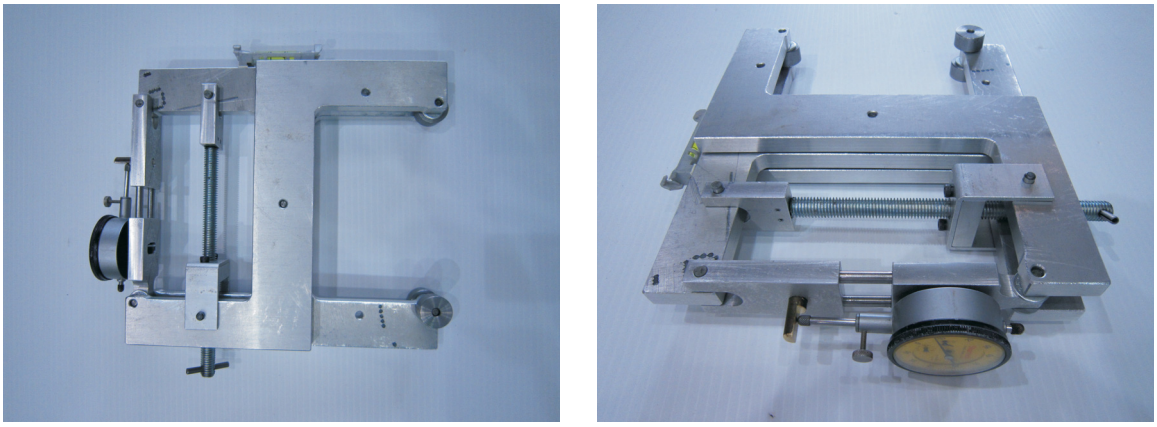

Figure 6.15: Bolt Elongation Measurement Device

6.6.1 Pre-Tensioning Procedure of the Friction Assembly

Prior to torquing the friction interface bolts, calculations were completed to estimate the torque required to reach the target friction force for the assumed friction interface characteristics. This also confirmed that the bolts did not need to be torqued past the maximum allowable torque level. A torque of 1060 N·m (781.5 ft-lbs) determined from equation 6.1 provides the required applied load to pre-tension the 25.4 mm (1 inch) bolts to the standard pre-tensioning force of 60 to 70% of the yield strength outlined in the CSA S16-09 (2009) (Oberg et al., 2008):

$$T = 10^{(b+m*\log d)} \tag{6.1}$$

where b and m are the bolt characteristic specific coefficients of 2.893 and 2.922 respectively, determined from Oberg et al. (2008), for an ASTM A-325 25.4 mm (1 inch) bolts and d is the nominal bolt diameter. This calculation identified the upper torque limit for the brace calibration procedure to ensure the bolts were well within the allowable force range.

The required normal bolt force, F_b, of 120 kN was determined from the friction interface resistance equation presented in Chapter 3 and the static and dynamic friction coefficients of 0.31 and 0.21, respectively (Grigorian 1994). The required normal force in each bolt was estimated using two different methods presented in Oberg et al. (2008). First, various applied torque levels were used to estimate the resulting pre-tensioning force in the 25.4 mm (1 inch) bolts for assumed surface conditions. Second, the axial load in the bolts was determined based on direct elongation measurements of the four pre-stressed bolts at each stage of the calibration process. The first method calculations were completed prior to calibration to estimate the applied torque required to induce a given normal bolt force. The procedure outlined the calculation of the thread and bearing surface friction interactions that contribute to the resistance of the applied torque. This behaviour is represented in equation 6.2, where T_f in the torque applied to the fastener, T_s is the torque resistance provided by the bolt shank, and T_w is the torque resistance contribution attributed to bearing surface and nut interaction (Oberg et al. 2008).

$$T_f = T_s + T_w \tag{6.2}$$

Additionally, the applied torque can be determined from the torque coefficient, K, and bolt diameter d_b, using equation 6.3.

$$T_f = KF_b d_b \tag{6.3}$$

The torque coefficient can be calculated using thread and bearing surface properties as follows:

$$K = \frac{1}{2d_b}(\frac{P}{\pi} + \mu_s d_2 sec\alpha' + \mu_w D_w) \tag{6.4}$$

where μ_s and μ_w are the thread and bearing surface friction coefficients. In addition to the equation, average torque coefficients are tabulated for given thread and bearing surface friction coefficients in Oberg et al. (2008). Based on the information presented in the literature these coefficients were both assumed to be 0.12 for lubricated steel bolts, resulting in an average torque coefficient of 0.164.

Lastly, the following equations (6.5) and (6.6), adapted from the Machinery's Handbook (Oberg et al., 2008), were used to determine effective length, L_b, and applied axial force, F_b, in the A325 bolts using direct elongation measurements:

$$L_b = (\frac{d_{ts}}{d_b})(L_s + \frac{H_B}{2}) + L_J - L_S + \frac{H_N}{2} \tag{6.5}$$

where d_{ts} is the minimum thread diameter of the bolt, d_b is the nominal bolt diameter, L_s is the unthreaded bolt shank length, H_B is the bolt head thickness, L_J in the total joint or grip length, and H_N is the nut thickness (Oberg et al., 2008):

$$F_b = \frac{\delta_b A_b E}{L_b} \tag{6.6}$$

where δ_b is the bolt elongation due to pre-tensioning determined from direct measurement. A_b is the area of the nominal cross-section, and E is the Young's modulus of A325 steel. The method of direct elongation determines the applied axial bolt force within an accuracy of +/− 3-5% (Oberg et al., 2008). The average normal force and expected bolt elongation, determined from the two

calculation methods, of the 25.4 mm (1 inch) A 325 bolts with a pitch of 10 for various applied torque levels are presented in Table 6.2.

Prior to pre-tensioning, the four 25.4 mm (1 inch) A325 bolts used in the friction device assembly were machined to a length of 137.2 mm (5.400 inches) to provide a relatively consistent reference length from which to measure the bolt elongation, as shown in Figure 6.16. This was accomplished by lathing the bolt heads and threaded shaft ends to also ensured a smooth consistent surface to take accurate elongation measurements.

The required pre-tensioning torque was applied to the nuts of the four 25.4 mm (1 inch) A325 bolts by hand using an imperial torque wrench measured in ft-lbs. In addition to the torque wrench a 41.3 mm (1-5/8 inch) wrench was used to prevent bolt head rotation during the pre-tensioning process. The bolts were torqued in an criss-cross order with the procedure beginning and ending with the pre-tensioning of bolt #1 shown in Figure 6.17. This method ensured that all four bolts were pre-tensioned to the target force and guaranteed that the applied normal force was evenly distribute across the entire friction interface.

6.6.2 Frame Calibration Test Results

The calibration tests were conducted using both saw-tooth and sinusoidal displacement functions to evaluate the friction behaviour at varying displacement amplitudes and loading rates. A summary of the calibration tests conducted are presented in Tables 6.3 to 6.6.

The majority of the low velocity calibration tests were conducted using a saw-tooth displacement-time history to evaluate the friction behaviour at a constant loading rate. Three different displacement amplitudes were selected, the first was an arbitrary displacement of 15 mm that was chosen to ensure the elastic stiffness, lateral frame activation and dynamic friction response would be captured within the cyclic loading range. A single calibration test, CT2-D,

Table 6.2: Normal Bolt Forces for Given Values of Applied Torque

Applied Torque (ft-lbs)	Applied Torque N·m (N·m)	Normal Bolt Force (kN)	Exp. Bolt Elongation (mm)
50	67.8	16.3	0.015
100	135.6	32.6	0.029
200	271.2	65.1	0.059
300	406.7	97.6	0.088
320	433.9	104.2	0.094
340	461.0	110.7	0.10
360	488.1	117.2	0.106
380	515.2	123.7	0.112

Figure 6.16: Machined Friction Interface Bolt

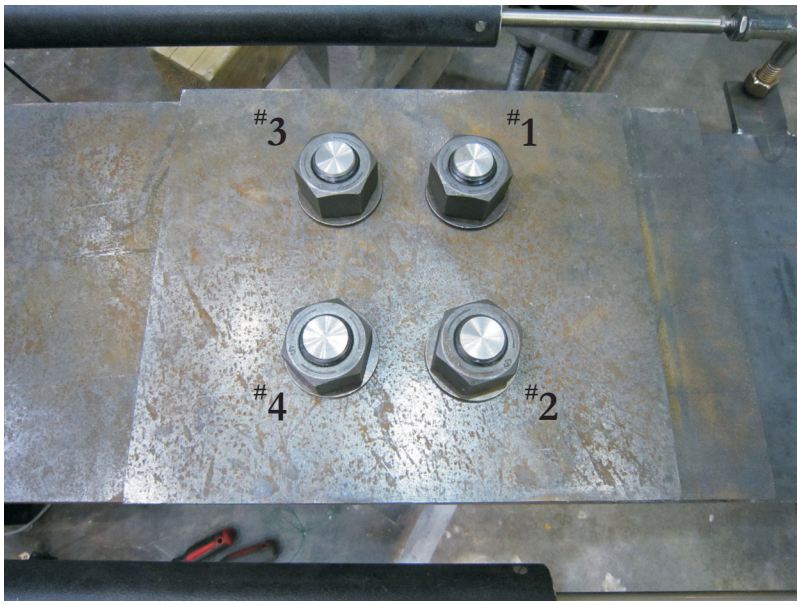

Figure 6.17: Friction Interface Bolt Layout for Per-Tensioning

Table 6.3: Low Velocity Calibration Test Set 1 Summary

Conducted on: 09/12/2016					
Test	cycles	Wave Form	Disp. Ampl. (mm)	Disp. Rate (m/s)	Comments
CT1-A	1	Saw-tooth	+/-15	0.5	Friction resistance evaluation
CT1-B	1	Saw-tooth	+/-15	0.5	Asses Lateral restraint friction
CT1-C	1	Saw-tooth	+/-15	0.5	Asses Lateral restraint friction
CT1-D	1	Saw-tooth	+/-15	0.5	Asses Lateral restraint friction
CT1-E	1	Saw-tooth	+/-15	0.5	Friction resistance evaluation
CT1-F	3	Saw-tooth	+/-15	0.5	Friction resistance evaluation
CT1-G	3	Saw-tooth	+/-15	2	Friction resistance evaluation
CT1-H	1	Saw-tooth	+/-15	0.5	Friction resistance evaluation
CT1-I	3	Saw-tooth	+/-15	2	Friction resistance evaluation

Table 6.4: Low Velocity Calibration Test Set 2 Summary

Conducted on: 10/12/2016					
Test	cycles	Wave Form	Disp. Ampl. (mm)	Disp. Rate (m/s)	Comments
CT2-A	1	Saw-tooth	+/-15	2	Friction resistance evaluation
CT2-B	1	Saw-tooth	+/-15	2	Friction resistance evaluation
CT2-C	1	Saw-tooth	+/-15	2	Friction resistance evaluation
CT2-D	1	Saw-tooth	+/-40.7	1	Asses Lateral restraint friction
CT2-E	1	Saw-tooth	+/-81.4	1	Test Incomplete, time limit Exceeded
CT2-F	1	Saw-tooth	+/-81.4	2	Asses Lateral restraint friction
CT2-G	1	Saw-tooth	+/-81.4	2	Friction resistance evaluation
CT2-H	1	Saw-tooth	+/-81.4	2	Friction resistance evaluation
CT2-I	1	sine wave	+/-15	2	Friction resistance evaluation
CT2-J	5	sine wave	+/-15	2	Friction resistance evaluation
CT2-K	5	sine wave	+/-15	4	Friction resistance evaluation

Table 6.5: Calibration Test Summary Following Stiffener Installation

Conducted on: 16/12/2016					
Test	cycles	Wave Form	Disp. Ampl. (mm)	Disp. Rate (m/s)	Comments
CT3-A	1	Saw-tooth	+/-15	1	Effect of stiffeners evaluated
CT3-B	3	Saw-tooth	+/-15	1	Effect of stiffeners evaluated
CT3-C	3	Saw-tooth	+/-15	2	Effect of stiffeners evaluated

Table 6.6: High Velocity Calibration Tests Summary

Conducted on: 11/01/2016 and 19/01/2016					
Test	cycles	Wave Form	Disp. Ampl. (mm)	Disp. Rate (m/s)	Comments
CT4-A	5	sine w/ cubic	+/-20.35	3.2	Max Velocity of 5 mm/s
CT4-B	5	sine w/ cubic	+/-20.35	6.4	Max Velocity of 10 mm/s
CT4-C	5	sine w/ cubic	+/-20.35	9.5	Max Velocity of 15 mm/s
CT4-D	5	sine w/ cubic	+/-20.35	12.7	Max Velocity of 20 mm/s
CT4-E	5	sine w/ cubic	+/-20.35	15.9	Max Velocity of 25 mm/s
CT4-F	5	sine w/ cubic	+/-20.35	19.1	Max Velocity of 30 mm/s
CT4-G	5	sine w/ cubic	+/-20.35	19.1	Max Velocity of 30 mm/s
CT4-H	5	sine w/ cubic	+/-20.35	19.1	Max Velocity of 30 mm/s
CT5-A	5	sine w/ cubic	+/-20.35	25.5	Max Velocity of 40 mm/s
CT5-B	5	sine w/ cubic	+/-20.35	25.5	Max Velocity of 40 mm/s
CT5-C	5	sine w/ cubic	+/-20.35	31.8	Max Velocity of 50 mm/s
CT5-D	5	sine w/ cubic	+/-20.35	38.2	Max Velocity of 60 mm/s

was conducted at the maximum credible earthquake (MCE) drift displacement of 40.7 mm selected from the results of associated numerical modelling of a six storey hybrid timber structure presented in Chapter 4. Lastly, three tests (CT2-F, CT2-G, and CT2-H) were conducted at a displacement amplitude of two times the maximum MCE drift displacement, 81.4 mm, to investigate if the beam connection and slotted friction detail could satisfy frame rotation demands. A sine-wave function with a displacement amplitude of half the MCE drift displacement was used, in test groups CT3, CT4, and CT5, to evaluate the velocity and temperature dependent friction characteristics of the stainless-steel on brace interface. A cubic function was fitted to the first half cycle of the sine waveform to ensure the initial loading rate of each calibration test started from zero. The results of the various calibration tests were used to characterize the lateral resistance behaviour of the friction brace and establish if the stainless-steel on brass friction configuration was susceptible to velocity and temperature dependant effects.

6.6.2.1 Low velocity Cycles

The low velocity friction calibration tests were performed at loading rates between 1.0 mm/s to 4.0 mm/s. The pre-tensioning torque applied to the four 25.4 mm (1 inch) A325 friction interface bolts was incrementally increased throughout the calibration tests to determine the optimal torque force required to develop a minimum lateral slip force of 159.0 kN. After five calibration steps, the target lateral force was achieved at an applied torque of 217 N·m (160 N·m). The stainless-steel on brass friction interfaces provided predicable and consistent friction behaviour that was expected to withstand the extensive hybrid braced frame testing program with minimal variation in the lateral resistance. Figure 6.18 shows the lateral hysteretic behaviour of the hybrid braced frame responses from tests CT1-E, CT2-A, CT2-B, and CT2-I used to calibrate the friction device. Additionally, there was no significant variation in friction behaviour of the low velocity test when comparing the responses of specimens torqued to identical pre-tensioning forces. The results from the low velocity calibration tests are presented in Tables 6.7 and 6.8.

The force transfer behaviour of braced frame dictates that as the brace is loaded in compression the timber beam and column elements will experience induced tension forces. Therefore, in terms of beam axial force development, the negative forces presented in the lateral force verse

displacement results of the test programs represents tensile loading of the glued in rod connections. This behaviour was defined at the outset to clarify the glued-in rod stiffness comparisons relative to the global lateral frame displacements and force development of the various hysteretic responses.

The pre-tensioning force in the friction interface bolts was removed for calibration tests CT1-B, CT1-C, CT1-D, CT2-D, and CT2-F to quantify the supplemental frame resistance provided by the lateral restraints and rotational friction of the beam shear connection. Additionally, tests CT1-B and CT1-C were conducted without complete contact between the timber sections and the upper crossbar of both lateral restraints. This provided a lower global frame resistance than the subsequent tests. Once the upper supports were in complete contact with the timber members the test set-up provided a mean lateral force resistance of 7.9 kN. Figure 6.19 shows the hysteretic frame behaviour from calibration test CT1-D used to outline the frame behaviour. The friction slip between the timber members and the lateral restraints was visible in the initial stage of loading, shown in the figure. The post-slip frame resistance captured in the curved force-displacement response was attributed to the rotational friction resistance developed in the beam shear connection. The point of beam connection slip and rotation can be seen graphically as the force developed reduces at approximately 3.4 mm.

The bolt normal force, calculated based on the mean bolt elongation measurements, were used to estimate the dynamic friction coefficient of the friction device. A mean dynamic friction coefficient of 0.45 was calculated, using equation (6.7), from the low velocity calibration test results.

$$\mu_{df} = \frac{F_{brace}}{n_b n_{fs} F_b} = \frac{138.0}{(4)(2)36.0} = 0.47 \tag{6.7}$$

where n_b in the number of pre-tension friction interface bolts and n_{fs} is the number of friction surfaces. F_b is the estimated normal bolt force determined from the direct elongation measurements. The mean brace force, F_{brace}, was determined by equation (6.8).

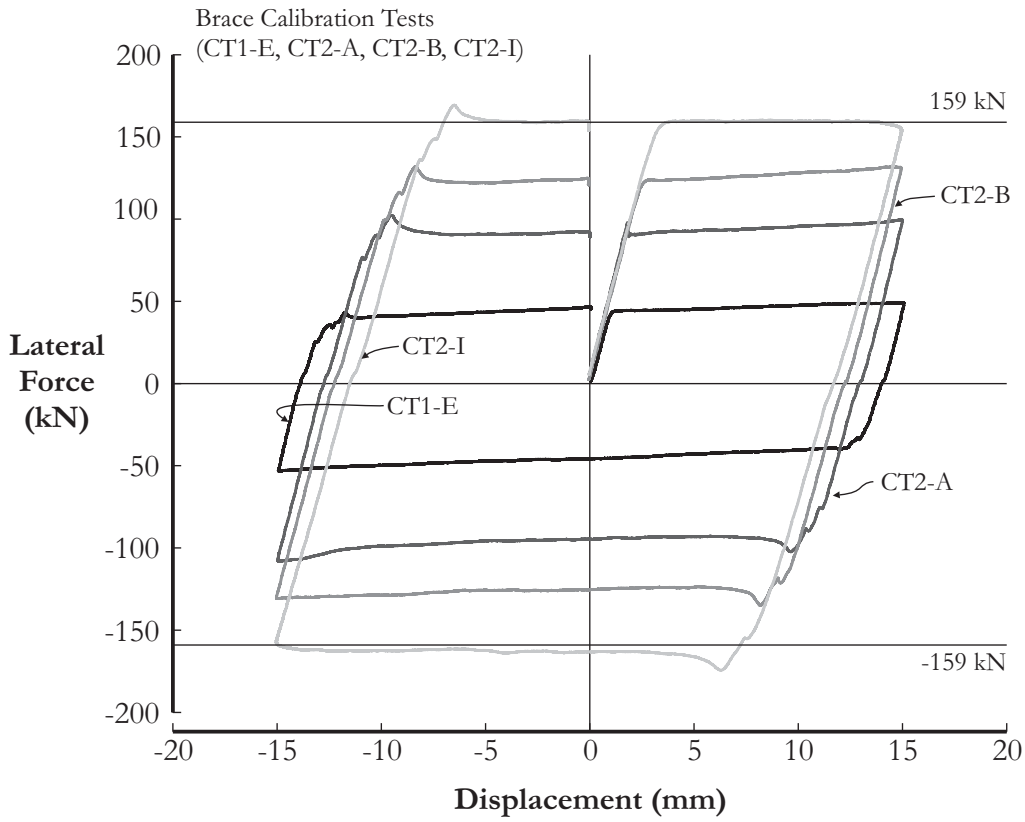

Figure 6.18: Friction Brace Calibration Tests

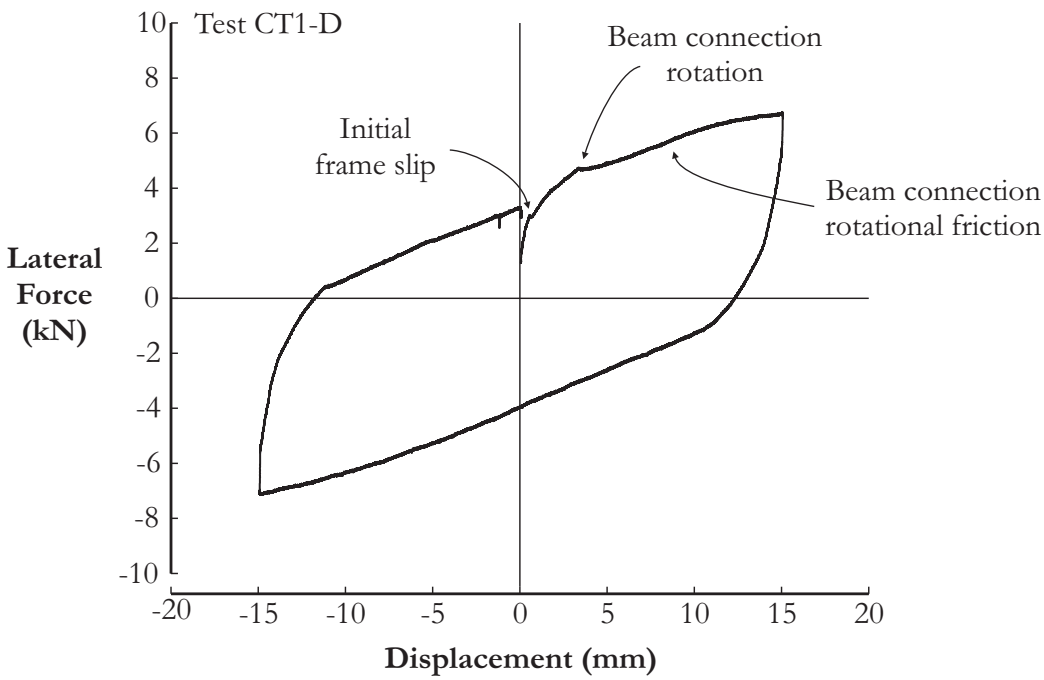

Figure 6.19: Lateral Frame Response (no brace friction)

Table 6.7: Low Velocity Calibration Test Set 1 Results

Test	Mean Applied Torque N·m	Est Bolt Force kN	Mean Slip Force Tension kN	Mean Slip Force Compression kN	Mean Friction Coefficient
Conducted on: 09/12/2016					
CT1-A	68	-	62	58.5	-
CT1-B	0	-	5.2	4.4	-
CT1-C	0	-	5.5	4.6	-
CT1-D	0	-	7.1	6.8	-
CT1-E	68	-	46.5	45	-
CT1-F	68	-	42.7.	41.2	-
CT1-G	68	-	44.3	42.2	-
CT1-H	136	-	95	92.9	-
CT1-I	136	-	101.8	98	-

Table 6.8: Low Velocity Calibration Test Set 2 Results

Test	Mean Applied Torque N·m	Est Bolt Force kN	Mean Slip Force Tension kN	Mean Slip Force Compression kN	Mean Friction Coefficient
CT2-A	136	-	97.3	94	-
CT2-B	170	36.0	127.8	127.8	0.47
CT2-C	203	47.0	160.5	155	0.46
CT2-D	0	-	8.4	7.8	-
CT2-F	0	-	9.7	7.8	-
CT2-G	68	8.3	44.3	43.2	0.62
CT2-H	203	47.0	152.5	148.0	0.45
CT2-I	217	51.5	162.9	159.8	0.43
CT2-J	217	51.5	165.7	163.4	0.44
CT2-K	217	51.5	173.1	167.4	0.45

$$F_{brace} = \frac{F_{lat} - F_{frame}}{cos(\theta_{brace})} = \frac{127.8 - 7.9}{cos(29.65)} = 138.0 \text{ kN} \tag{6.8}$$

The lateral force contribution of the brace force, F_{lat}, was calculated as the difference between the average sustained lateral tension and compression resistances and the mean lateral supplementary frame resistance of 7.9 kN. A displaced frame brace angle of 29.7 degrees used to calculate the various maximum frame displacement amplitudes. For example the mean bolt elongation of 0.0475 mm measured at the applied torque of 217 N·m resulted in the normal bolt force of 51.5 kN. The calculated mean normal bolt forces were validated for each test using equation 6.9 at the corresponding applied torque.

$$F_b = \frac{T_f}{K d_b} \tag{6.9}$$

A torque coefficient, K, of 0.164 was assumed for the connection surface conditions (Oberg et al.). The mean friction coefficient of 0.45 was accepted as an accurate dynamic friction characterization coefficient for the stainless-steel on brass friction interface assembly. This kinetic friction coefficient was greater than both the 0.31 and 0.21 static and dynamic friction coefficients used in the design of the friction interface. Out-of-plane movement of the friction brace was observed during the earthquake records applied in the preliminary stages of hybrid braced frame testing program. To reduce this movement, additional steel stiffeners were welded to the bottom side plate to prevent plastic hinge formation in either of the side plates or inner slotted plate of the friction assembly. After the modifications were complete, additional calibration tests were conducted to evaluate if the stiffeners would affect the friction resistance of the hybrid braced frame. These test results are presented in Table 6.9. The initial test, CT3-A, shows an approximate drop in dynamic friction resistance of 52 kN, compared to the results of the last three calibration tests from test group CT2. This reduction in lateral resistance was attributed to insufficient pre-tensioning of the four 25.4 mm (1 inch) bolts, this was confirmed when the torque levels were checked using the torque wrench. The pre-tensioned bolts of the friction device were then re-torqued to 217 N·m and the remaining two calibration tests were conducted. The mean lateral frame forces in tests CT3-B and CT3-C were essentially identical to the three

average lateral resistance results from the previous test group. This supported the assumption that the stiffeners would not affect frame performance.

6.6.2.2 High Velocity and Temperature Assessment Tests

High velocity calibration tests were conducted to evaluate velocity and temperature effects on the friction material behaviour. The maximum loading rates were calculated to capture the scaled peak velocities of the dynamic earthquake record tests. These tests were conducted to characterize the expected friction behaviour and global seismic frame response of the dynamic earthquake tests. A summary of the velocity dependent calibration test results is presented in Table 6.10.

The hysteretic comparison of the selected test results in Figure 6.20, shows the lateral frame behaviour at incremental maximum loading rates. Reductions in the dynamic friction behaviour can be observed at the location of maximum loading rate, near zero displacement. There was a slight reduction in the friction resistance at high velocity when compared to the low velocity hysteretic response at the maximum displacement amplitudes. After each calibration test, the residual brace force was released prior to loading in all but one test. This force was not released prior to test CT5-C which resulted in the absence of elastic stiffness prior to brace activation. A varying degree of stick-slip behaviour was observed throughout the high velocity calibration tests. This behaviour is most prominent in the first loading cycle of the hysteretic response in

Table 6.9: Calibration Test Results Following Stiffener Installation

Test	Mean Applied Torque N·m	Est Bolt Force kN	Mean Slip Force Tension kN	Mean Slip Force Compression kN	Mean Friction Coefficient
CT3-A	217	51.5	114.7	111.8	0.33
CT3-B	217	51.5	159.8	159.8	0.42
CT3-C	217	51.5	164.6	162.9	0.44

Table 6.10: High Velocity Calibration Tests Results

Test	Mean Applied Torque N·m	Est Bolt Force kN	Mean Slip Force Tension kN	Mean Slip Force Compression kN	Mean Friction Coefficient	Temp. Before Test ˙c	Temp. After Test ˙c
CT4-A	217	51.5	155.6	152.5	0.41	21.0	23.3
CT4-B	217	51.5	167.0	164.5	0.44	25.5	25.0
CT4-C	217	51.5	166.5	164.5	0.44	23.5	26.4
CT4-D	217	51.5	175.7	171.8	0.46	25.0	28.2
CT4-E	217	51.5	161.2	158.1	0.42	26.0	28.9
CT4-F	217	51.5	178.8	175.0	0.47	26.0	29.1
CT4-G	217	51.5	179.8	175.7	0.47	26.6	29.4
CT4-H	217	51.5	177.7	176.6	0.47	27.0	30.2
CT5-A	217	51.5	162.9	160	0.43	-	-
CT5-B	217	51.5	170.2	163.2	0.44	19.9	23.8
CT5-C	217	51.5	171.7	166.3	0.45	23.7	26.6
CT5-D	217	51.5	172.4	165.8	0.45	25.4	27.9

the tests loaded to maximum velocities of 30 mm/s and greater. However, this behaviour was also present in the post activation friction response of each half cycle. The severity of stick-slip behaviour between the interface materials was directly related to the increase in sliding velocity. The initial slip force of the first cycle was consistently less than the subsequent cycles. An increase in dynamic resistance was observed in each loading cycle of the high velocity tests. This was attributed to localized surface damage induces ploughing effects and mechanical interlock between the asperities that develop in the interface surfaces (Christopoulos and Filiatrault, 2006). This behaviour was observed in slotted friction connections tested by Tremblay (1993), where the increase in specimen slip resistance occurred consecutively up to as many as 27 cycles before decreasing. The five cycle loading sequence of the individual high velocity calibration tests provided a limited frame of reference that was unable to capture the reduction in sliding resistance after this ploughing behaviour subsided. The increase in loading rate of each test induced more dynamic stick-slip behaviour that most likely caused an increase in the surface damage that prevented the slip force reduction due to temperature effects from being observed in the later high velocity calibration tests. This was supported by the increase in mean slip forces results of the later velocity dependent tests presented in Table 6.10. Furthermore, a consistent increase in surface temperature was observed in all but one of the high velocity calibration tests. However, the stick-slip behaviour and increased friction resistance of the later cycles prevented the observation of temperature dependent effects at these low temperature changes. The effect the velocity dependant stick-slip and ploughing behaviours have on lateral resistance and seismic performance of the hybrid system will be discussed in the future section related to the dynamic earthquake tests.

6.7 Hybrid Braced Frame Tests

Four loading procedures were applied to the hybrid timber-steel braced frame prototype to investigate the seismic and wind performance of the timber-steel connections, the intermediate brace connection, and the friction brace design. Additionally, the affects of pre-tensioning on the glued-in rod connections was evaluated under both the low and high cycle loading scenarios. The

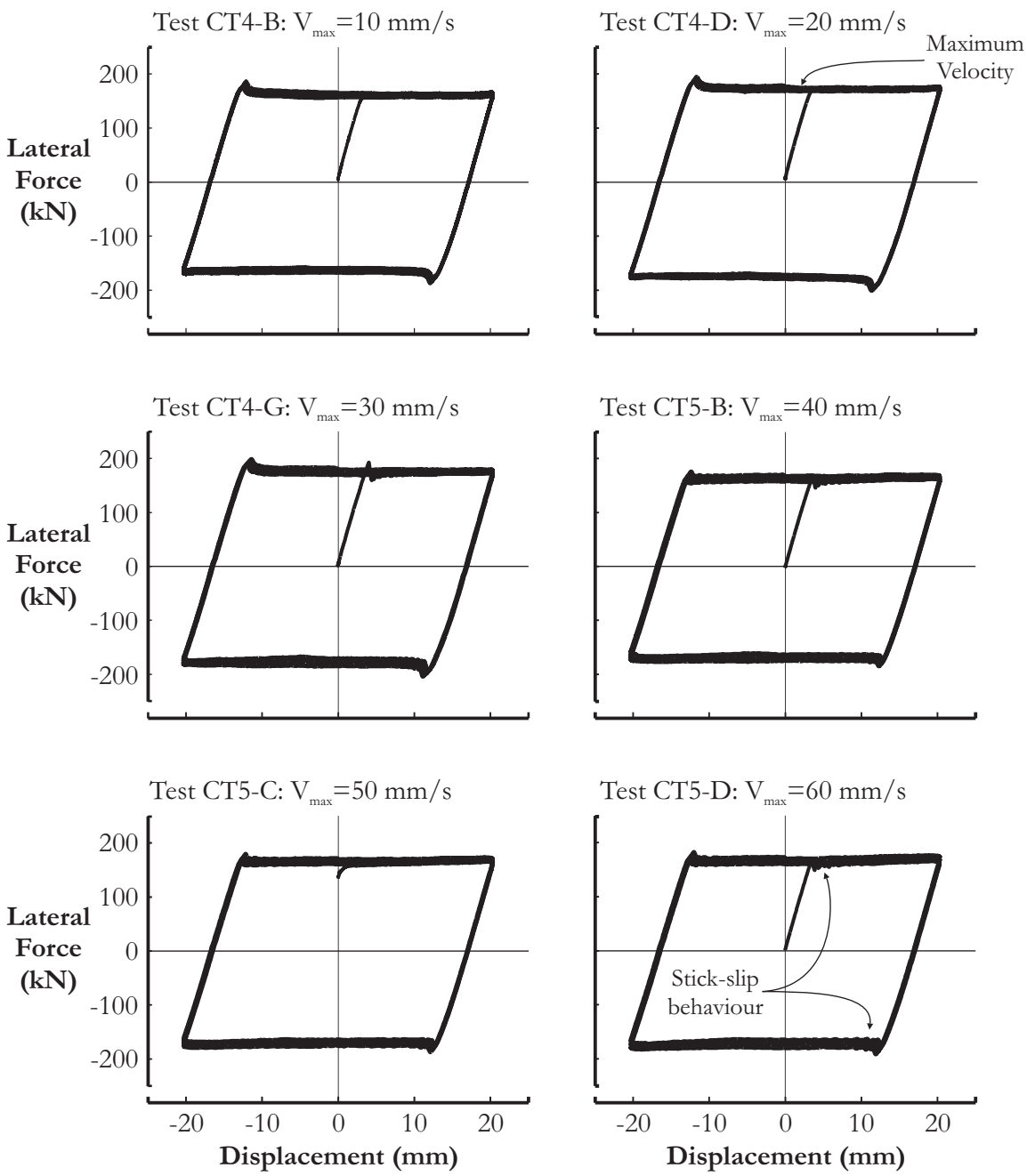

Figure 6.20: Velocity Dependent Hysteretic Responses

test programs used to assess frame performance were (1) the ASCE 7-05 (2005) wind loading protocol, (2) a combined quasi-static cyclic loading protocol, (3) Dynamic earthquake response tests, and (4) pre-tensioning connection stiffness characterization tests. However, prior to testing, the elastic stiffness, k_e, and activation (slip) displacement, Δ_a, of the hybrid frame were determined from the calibration test results. An elastic stiffness of 50.5 $\frac{\text{kN}}{\text{m}}$ was calculated from the displacements associated with 10% and 40% of the mean dynamic friction force equal to 166.5 kN. The dynamic friction force was selected as the activation force because of a lack in discrepancy between static and dynamic friction behaviour in the hysteretic response of some calibration tests. This resulted in a conservative lateral slip displacement of 3.30 mm that was used to define the displacement amplitudes of the wind loading protocol and the initial stage of the combined brace loading protocol. Lastly, the 245 kN actuator capacity prevented the testing of the bolted gusset plate connection as a secondary failure mechanism to provide supplemental energy dissipation if the target calibrated brace force is exceeded. Further investigation into the energy dissipation capabilities of this connection is required to evaluate the capacity design concepts used to detail the gusset plate as a secondary failure mechanism.

6.7.1 Wind Loading Protocol

The ASCE 7-05 (2005) wind loading procedure was selected to investigate the elastic lateral resistance of the hybrid braced frame while evaluating the high cycle fatigue behaviour of the glued-in rod fasteners with and without pre-tensioning. The two wind loading simulation sets were applied at 50% and 95 % of the lateral activation displacement, resulting in target frame displacement amplitudes of 1.65 mm and 3.13 mm, respectively. These loading sets consisted of a thousand loading cycles applied at the scaled fundamental period of the six-storey structure presented in Chapter 4 to satisfy the required two thousand cumulative wind cycles. The fundamental period of 1.51 sec from the preliminary numerical modeling investigation of a six storey hybrid timber structure had to be scaled in accordance with the procedure outlined in Chapter 3. Therefore, all wind cycles were applied at the scaled period of 1.06 s resulting in input loading rates of 6.2 mm/s and 11.8 mm/s for the two peak wind displacement cycle sets respectively. The hysteretic responses of the two wind simulation tests are compared in Figure 6.21. The glued-in

rod connections of test WLT1 were fastened to snug-tight condition where the pre-tensioning torque of 267 N·m was applied to the WLT2 test configuration.

The hysteretic responses of the two wind simulations test groups demonstrated fully elastic behaviour at both displacement amplitudes with no degradation of the response. The lateral frame stiffnesses were essentially identical for both the test set-ups, establishing that the pre-tensioning of the glued-in rod connections does not effect elastic frame stiffness. During the wind loading simulations, minimal gap formation was observed in the glued-in rod connection zones between the steel base plates and timber end grain in the pre-tensioned connections. This behaviour did not affect the hysteretic responses which suggests gap formation did not effect the global frame performance. Additionally, after analysis of the panel zone instrumentation data, it was clear that no inelastic action occurred in the panel zone during the wind simulation tests. These finding were further supported by the lack of white-wash flacking in the panel zone region.

A comparison of the glued-in rod connection responses during the wind loading simulations are shown in Figure 6.22. A clear increase in connection stiffness can be observed in the pre-tensioned connection configuration of test WLT2 when compared the stiffness of the snug-tight connection conditions of test WLT1. The connection response plots captured the differences in stiffness between the glued-in rod fasteners and the end-grain bearing action (associated with positive displacements). The mean peak axial forces developed in the beam connection glued-in rods during the $0.5\Delta_a$ of the two test configurations, was approximately equal to the mean ULS wind loading fatigue resistance of 87.6 kN. Furthermore, the mean peak axial force of approximately 146.8 kN was developed in the beam connection during the $0.95\Delta_a$ displacement cycles for both test configurations. This force development exceeded the calculated fatigue resistance of 87.6 kN for the grouped glued-in rod connection. Considering that the connections did not experience reductions in fastener strength or stiffness, this suggests the SLS design calculation could be a more accurate representation of the high cycle fatigue resistance of these fasteners; as these resistances were greater than the force demands developed in the connections during the wind simulation tests. Lastly, the glued-in rod connection did not experience any strength or stiffness degradation

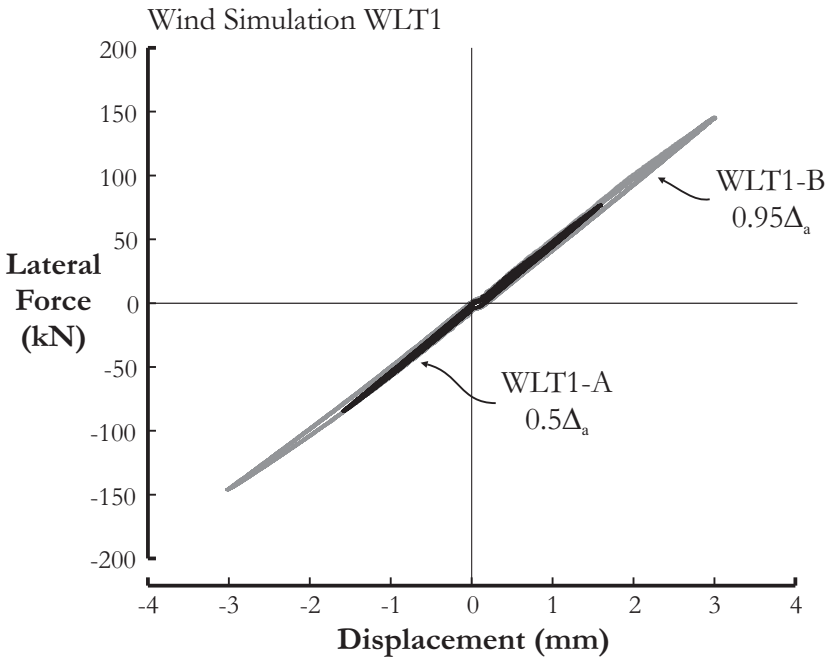

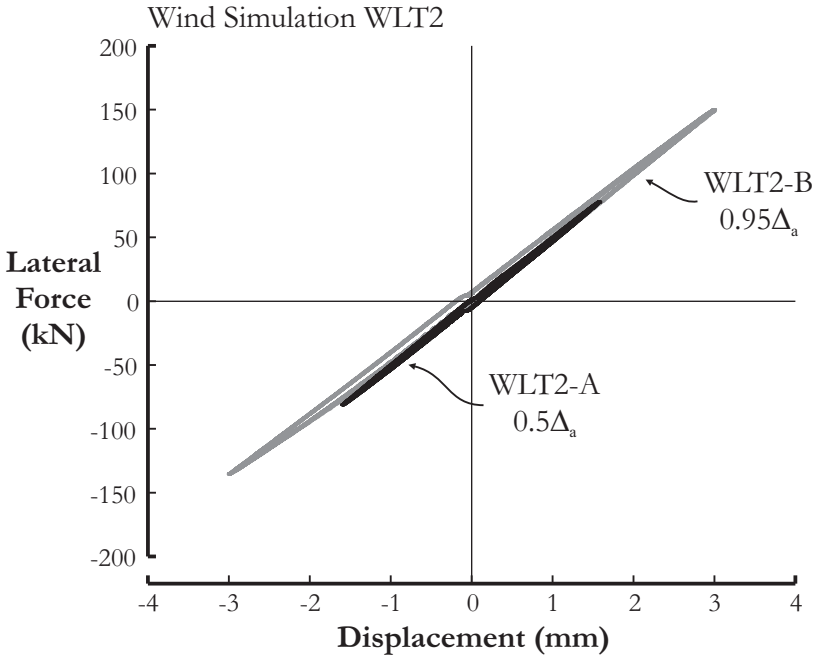

Figure 6.21: Wind Loading Simulation Response Comparison

at the two displacement amplitudes in either test configurations. These findings related to fastener resilience provide significant evidence that suggests glued-in rod connection can be utilized in the design of lateral force resisting systems.

Friction characterization cycles were conducted to evaluate the brace response before and after the wind loading simulations to establish if the high cycle elastic loading effects friction resistance. A comparison of the hysteresis friction behaviours of the two test conflagrations are presented in Figure 6.23. These results shows that the friction resistance was not affected by the high cycle wind loading simulations.

6.7.2 Quasi-Static Cyclic Loading Tests

The primary goal of the testing program required the hybrid braced frame to be subjected to a combined buckling restrained brace loading protocol complied from the AISC 341-05 (2005) and ASCE 7-05 (2005) testing standards described below. The combined testing protocol would allow for the seismic performance evaluation of the friction damping device and glued-in rod connections. Furthermore, the overall frame response was analysed to assess whether the pinned connection assumptions are valid as well as determining if the beam pin connection and slotted friction interface can satisfy the localized rotation demand at two times the MCE drift displacement.

The AISC 341-05 consists of the following deformation sets (AISC, 2005):

1. 2 loading cycles at a deformation amplitude of $\Delta_b = \Delta_a$
2. 2 loading cycles at a deformation amplitude of $\Delta_b = 0.5\Delta_{bm}$
3. 2 loading cycles at a deformation amplitude of $\Delta_b = 1.0\Delta_{bm}$
4. 2 loading cycles at a deformation amplitude of $\Delta_b = 1.5\Delta_{bm}$
5. 2 loading cycles at a deformation amplitude of $\Delta_b = 2.0\Delta_{bm}$

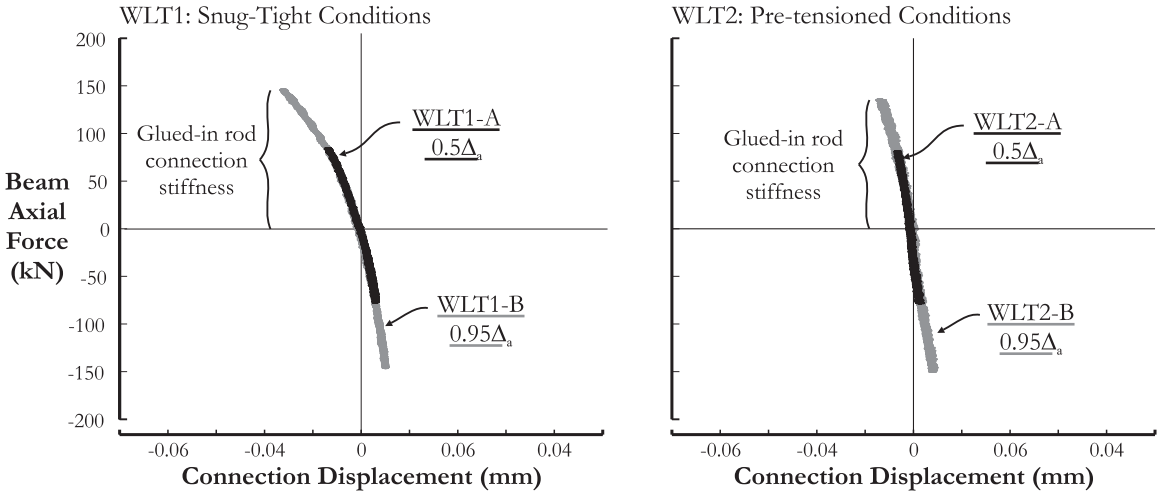

Figure 6.22: Glued-in Rod Beam Connection Response Comparison

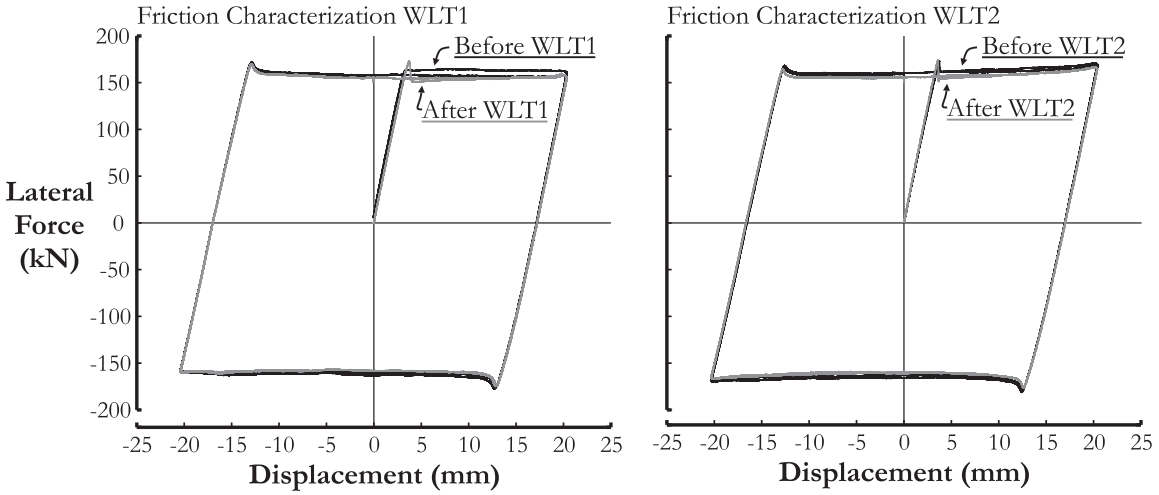

Figure 6.23: Friction Characterization Response Comparison

6. Additional loading cycles at a deformation amplitude of $\Delta_b = 1.5\Delta_{bm}$ are required if the cumulative inelastic brace deformation experience during sequences 1 - 5 does not exceed $200\Delta_a$.

The ASCE 7-05 testing program specifies the following three sequences (ASCE, 2005):

1. The first sequence consists of 2000 wind cycles that are to be applied at the natural frequency of the structure. This loading sequence is only required if the design wind load is greater than the activation or yield force of the test system.

2. The second sequence requires five MCE hazard level deformation cycles to be applied at the fundamental period of the structure.

3. The third sequence requires that five MCE deformation cycles are repeated at the first mode period and 0.4 times the first mode period of the structure. This sequence is not required if the force-deformation properties of the system are not sensitive to loading frequency.

The second sequence from the testing protocol in Chapter 18 of ASCE 7-05 (2005) was selected as part of the quasi-static loading protocol of the hybrid braced frame prototype. The maximum credible earthquake (MCE) drift displacement, Δ_{bm}, was selected as 2.2% from the associated numerical modelling results of a six-storey hybrid timber structure from Chapter 4. This was determined from the mean plus one standard deviation first storey maximum drift response from the MCE earthquake records. The activation drift displacement Δ_a was assumed to be 3.30 mm as previously mentioned. Additional cycles at $1.5\Delta_{bm}$ were not required because the combined inelastic deformation of the combined loading protocol exceeded $200\Delta_a$ as specified. The finalized displacement amplitudes and equivalent cycle displacements of the combined brace loading protocol are presented in Table 6.11. Due to the limitations of the testing equipment, the deformation cycles were applied at the constant rate of 1 mm/sec. Additionally, the data acquisition system was set to a constant recording frequency of 10 Hz in order to capture the dynamic friction response during the cyclic loading program.

Table 6.11: Combined AISC and ASCE Brace Loading Protocol

Cycles	Amplitude	Drift %	Displacement mm
2	Δ_a	0.002	3.30
2	$0.5\Delta_{bm}$	1.1	20.35
5	$1.0\Delta_{bm}$	2.2	40.7
2	$1.5\Delta_{bm}$	3.3	61.05
2	$2.0\Delta_{bm}$	4.4	81.7

6.7.2.1 Frame Response

The snug-tight frame configuration was subjected to two full combined brace loading protocol tests, BLP1-A and BLP2-A, to evaluate the frame response and glued-in rod connection behaviour before and after the wind loading simulation tests. Additionally, in the lead time between the snug-tight frame tests BLP1-A and BLT2-A, stiffeners were welded to the bottom side plate of the friction interface to provide additional bending resistance during the dynamic testing protocols. The pre-tensioning frame set-up was subjected to a single brace loading protocol test, BLP3-A, because the initial findings of the two snug-tight tests proved that the high cycle wind simulations did not effect the overall seismic performance of the frame. The hysteresis responses for the combined protocol tests are presented in Figures 6.24 and 6.25. These results were determined from the lateral force and frame displacements record by the actuator load-cell and string pot mounted to the intermediate brace connection. The hybrid braced frame was capable of satisfying the displacement demands of all the loading cycles through rotations in the beam shear connection and slotted friction interface. Figure 6.26 shows the global frame displacements at the maximum and minimum amplitudes of the $2.0\Delta_{bm}$ displacement cycles. The elastic stiffness and activation displacement of the two frame configurations were equal to 50.5 $\frac{\text{kN}}{\text{m}}$ and 3.30 mm, respectively, suggesting that the pre-tensioning of glued-in rod connections did not effect the elastic frame behaviour and initial lateral resistance of the hybrid braced frame.

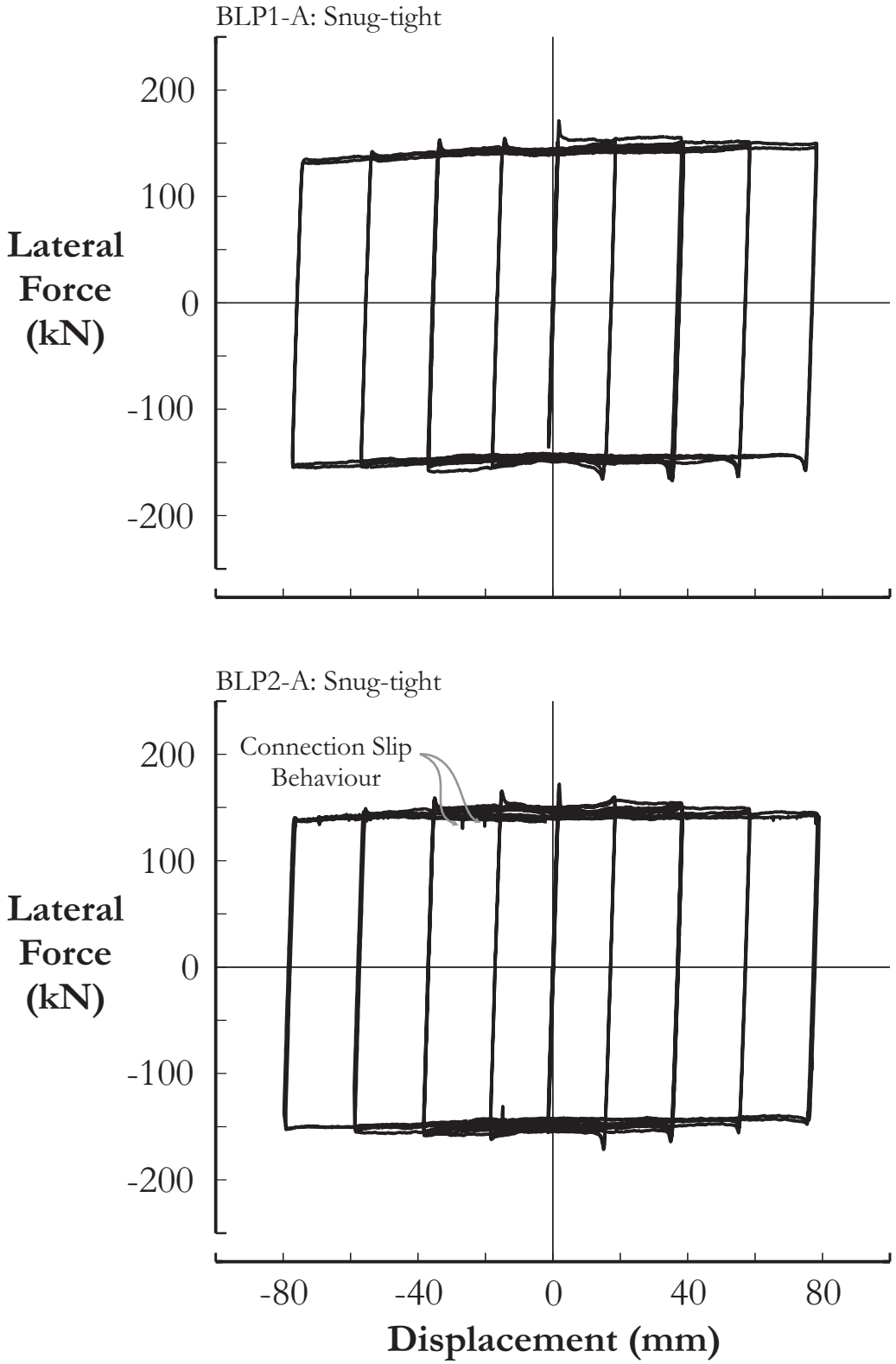

Figure 6.24: Combined Brace Loading Protocol Hysteresis

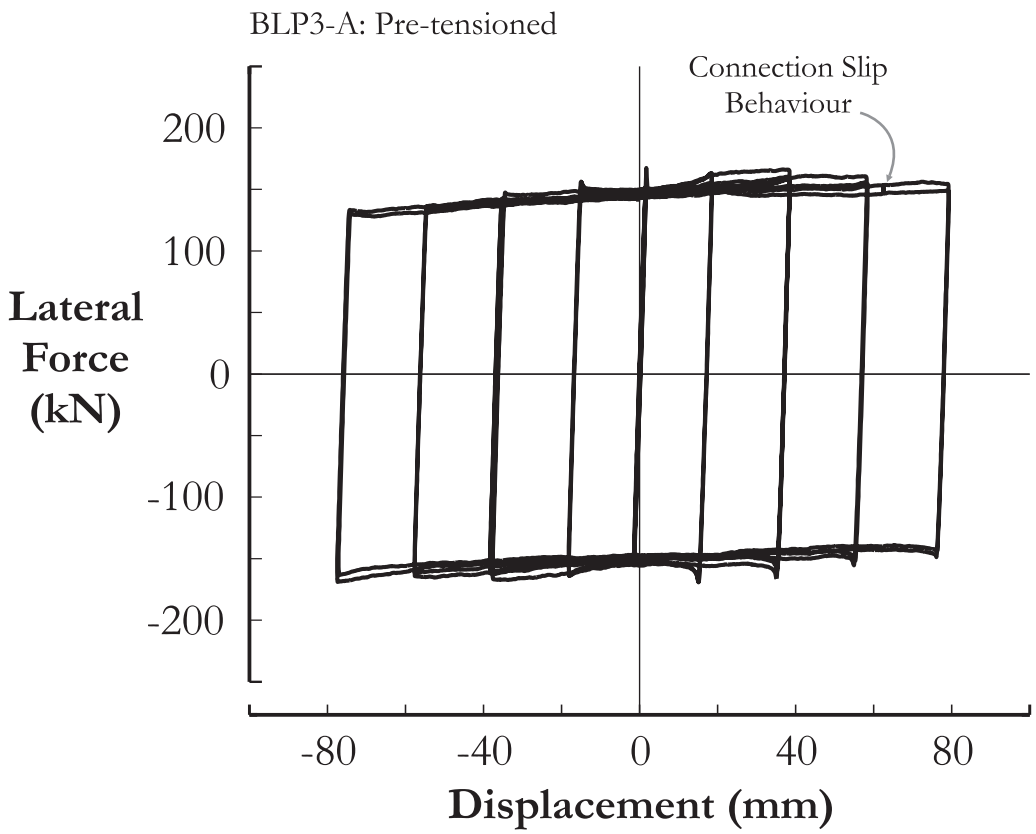

Figure 6.25: Combined Brace Loading Protocol Hysteresis of Pre-tensioned Set-up

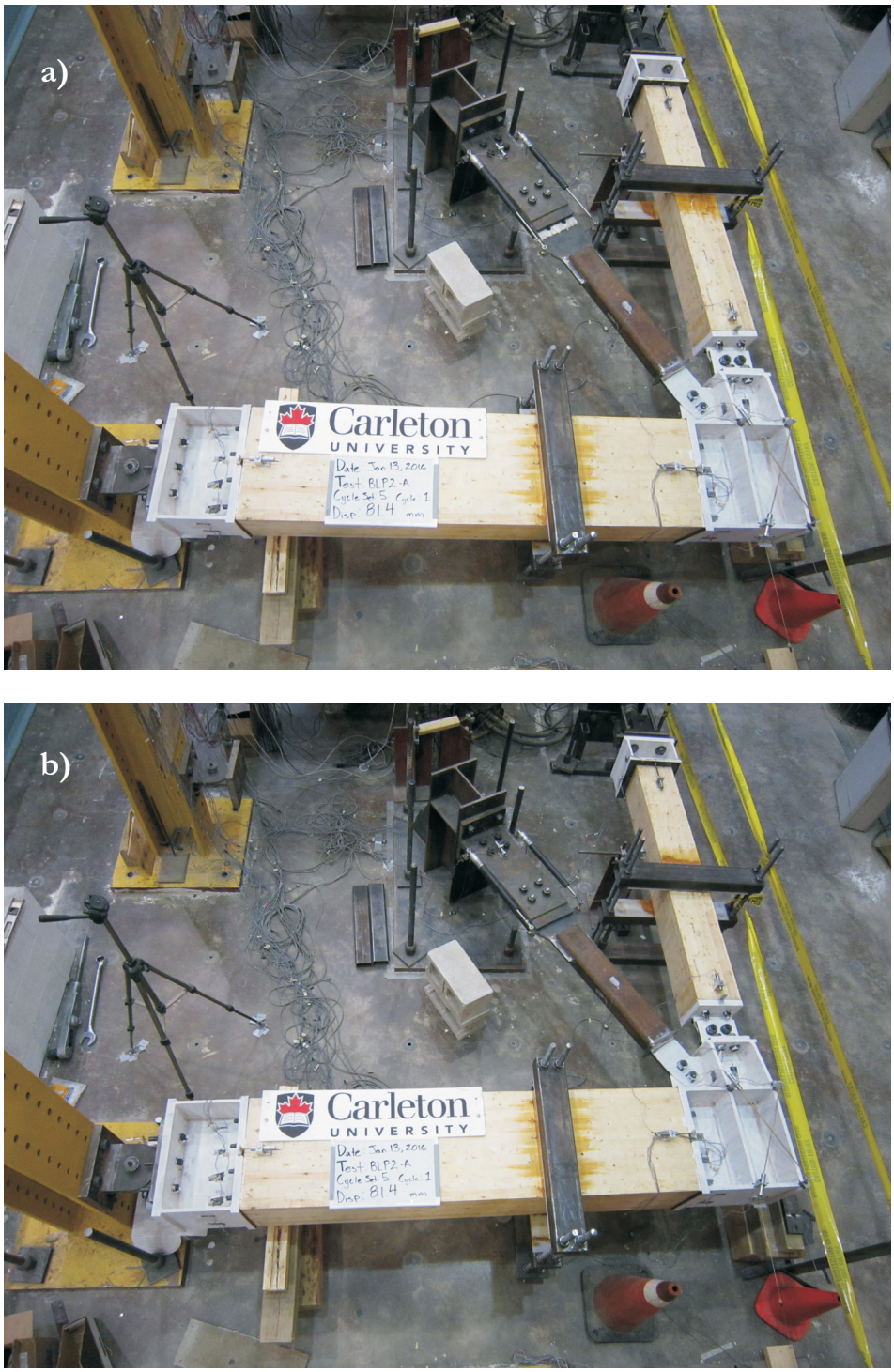

Figure 6.26: Frame Positioning at ± $2.0\Delta_{bm}$

There was a difference in the fiction behaviour of all three tests because the pre-tensioned friction interface bolts were released between the test programs. This allowed for the release of the residual force that had developed in the frame. The friction device was than re-calibrated to the required pre-tensioning force by torquing the bolts to 217 N·m. In all tests, the friction device exhibited excellent lateral sliding resistance slightly less than the target slip force of 159.0 kN. The early displacement cycles provided clear distinctions in the static and dynamic friction. However, the static friction force and activation behaviour were significantly reduced in the $1.5\Delta_{bm}$ and $2.0\Delta_{bm}$ displacement cycles. This behaviour was the result of a reduction in surface roughness and the development of debris build-up that isolated the friction interfaces and reduced the static friction coefficient (Christopoulos and Filiatrault, 2006). In support of these findings, debris formation was visible on the slotted stainless-steel plate at the large displacement cycles as shown in Figure 6.27. Furthermore, temperature induced reductions in lateral resistance can be seen in the hysteresis responses of all three tests when comparing the dynamic friction behaviour of the initial displacement cycles to the resistance of the later loading stages. This phenomenon was the result of heat flux increase in the faying surfaces that caused a reduction in the coefficient of friction (Christopoulos and Filiatrault, 2006). The mean dynamic friction forces and surface temperature results of the three combined protocol tests are presented in Table 6.12.

The beam connection slip behaviour was represented by the sudden drops in lateral resistance which was most prominent in the hysteretic response of test BLP2-A, shown in Figure 6.24. This behaviour was also present in the later stage of the $2.0\Delta_{bm}$ displacement cycle of the BLP3-A hysteretic response, shown in Figure 6.25. During both tests, noise coming from the beam pin connection was assumed to be the result of the slip response. This slip behaviour is discussed in detail in section 6.7.2.2. Lastly, the three hysteresis responses did not show any signs of plastic behaviour in the panel zone, nor was there any evidence of inelastic action in the force-displacement responses of the panel zone instrumentation. This was supported by the absence of white-wash flaking in the web throughout the brace loading protocol test.

Initially, the hysteresis brace responses were calculated using the brace strain gauge readings; however, variability in the data introduce significant error in the BLP1-A and BLP2-A

Table 6.12: Combined Brace Loading Protocol Test Results

Cycles	Amplitude	Displacement mm	Mean Slip Force Compression kN	Mean Slip Force Tension kN	Temp. Before ˙c	Temp. After ˙c
			Test: BLP1-A			
2	Δ_a	3.30	-	-	20.9	-
2	$0.5\Delta_{bm}$	20.35	-150.1	149.7	-	-
5	$1.0\Delta_{bm}$	40.7	-148.7	144.6	-	-
2	$1.5\Delta_{bm}$	61.05	-146.8	142.3	-	-
2	$2.0\Delta_{bm}$	81.7	-146.0	139.3	-	27.3
			Test: BLP2-A			
2	Δ_a	3.30	-	-	20.2	20.2
2	$0.5\Delta_{bm}$	20.35	-155.2	151.9	20.4	20.3
5	$1.0\Delta_{bm}$	40.7	-151.1	147.5	20.3	23.1
2	$1.5\Delta_{bm}$	61.05	-148.9	143.3	23.3	24.8
2	$2.0\Delta_{bm}$	81.7	-145.1	139.8	25.2	26.4
			Test: BLP3-A			
2	Δ_a	3.30	-	-	20.9	20.8
2	$0.5\Delta_{bm}$	20.35	-156.1	153.2	20.7	21.3
5	$1.0\Delta_{bm}$	40.7	-152.7	148.3	21.6	24.3
2	$1.5\Delta_{bm}$	61.05	-152.0	145.7	24.5	26.0
2	$2.0\Delta_{bm}$	81.7	-149.0	139.4	26.6	27.8

Figure 6.27: Brass Flake Debris and Friction Interface Condition at $2.0\Delta_{bm}$

results. Therefore, further evaluation of the seismic performance of the friction device could not be conducted. However, the response comparisons presented in Figure 6.24 provided sufficient evidence to suggest the friction brace exhibited excellent seismic performance capable of satisfying and exceeding the 4.0 ductility demand represented in the buckling restrained brace design. Comparisons of the friction characterization tests before and after the BLP2-A and BLP3-A combined protocol tests are presented in Figure 6.28. The reduction in the lateral brace resistance was due to temperature and surface conditioning experienced during the tests.

The connection response comparison of the beam to actuator glued-in rod connection from the three tests in Figure 6.29 shows a significant variation in stiffness. This was most likely the result of connection eccentricities that caused asymmetric gap formation between the intermediate steel section and the timber end-grain. This action prevented an accurate quantification of the glued-in rod connection stiffness. Movement was also captured in the column connection behaviour during the snug-tight test configurations that prevented an accurate representation of the connection stiffness. The pre-tensioned column connections experienced considerably less

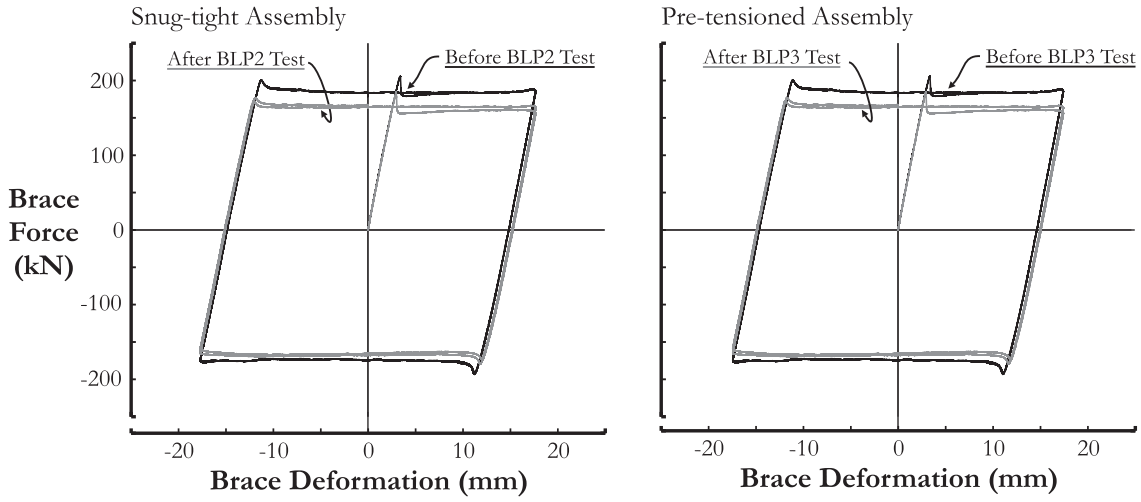

Figure 6.28: Friction Characterization Test Comparisons Before and After Protocol Tests

movement in the intermediate steel sections due to the increase in connection stiffness associated with the application of pre-tensioning in glued-in rod connections. Figure 6.30 shows a comparison in the column connection response for the snug-tight and pre-tensioned fastener conditions.

Prior to testing, the glued-in rod connection at the base of the column was re-torqued to the required pre-tensioning force, while the top connection was left undisturbed. The column connection responses were used to assess if stiffness relaxation had occur in the upper connection since the frame was assembled. A comparison in the two column connection responses of the pre-tensioned set-up is presented in Figure 6.31. There is a clear variation in the glued-in rod connection stiffness that provides evidence of relaxation in the pre-tensioning force when comparing the elastic behaviour of these two connections. However, the stiffness comparison was not as evident in the pre-tensioned beam connection responses due to eccentricities in the frame assembly that cause abnormal displacement behaviour between in the relaxed connection. Additionally, both column connections experienced minimal displacement and rotation behaviour in the intermediate steel sections, this provides evidence to suggests that gap formation and frame eccentricity is reduced with the application of pre-tensioning.

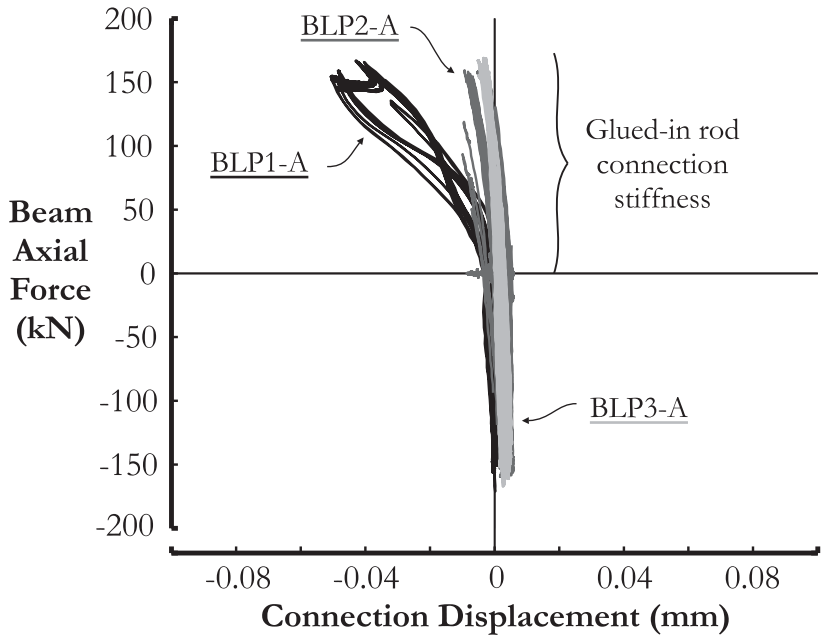

Figure 6.29: Glued-in Rod Beam Connection Response Comparison

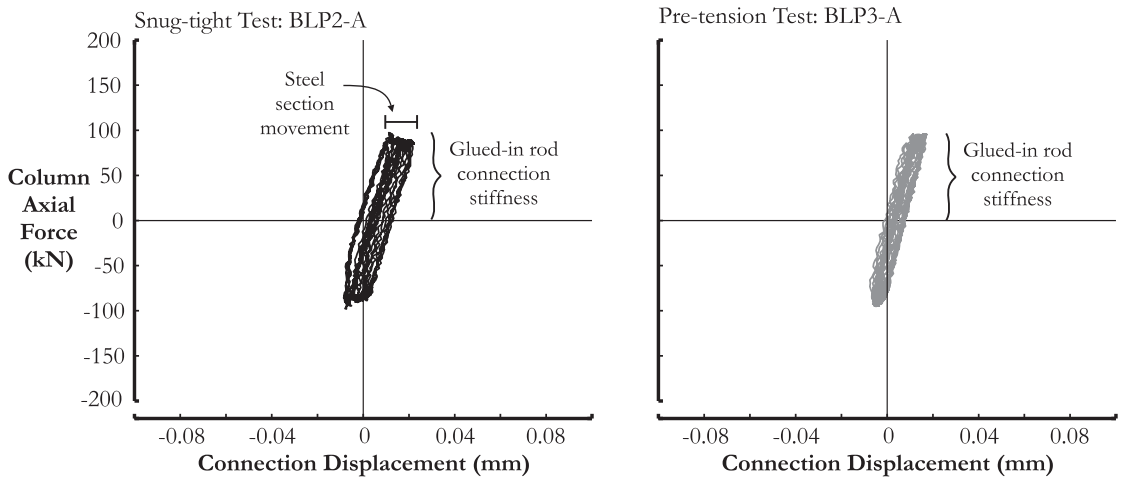

Figure 6.30: Pre-tensioning effects on Column Connection Behaviour

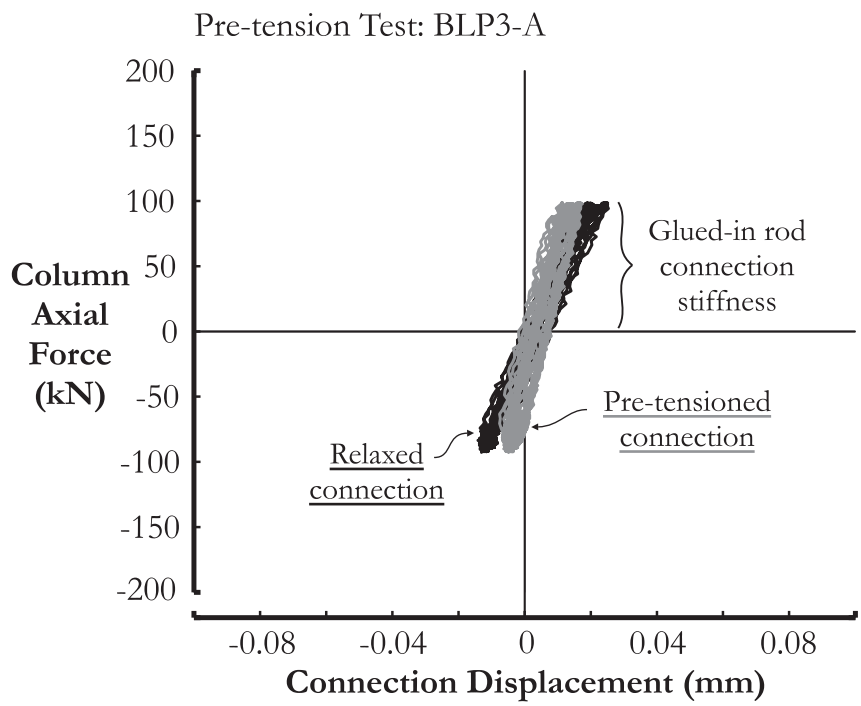

Figure 6.31: Column Glued-in Rod Connection Stiffness Comparison

6.7.2.2 Beam Connection Behaviour

Throughout the testing of both frame configurations, observations were made which suggested that rotation in the beam shear connection was occurring without any visible effect on frame performance. Figure 6.32 shows the connection rotation at the maximum negative displacement of -2.0Δ_{bm} (left), the connection position at zero displacement (center), and the induced connection rotation at the maximum displacement of $+2.0\Delta_{bm}$. A clear comparison can be made that shows the beam shear connection was capable of satisfying the frame rotation demands.

6.7.2.3 Deformation Response of Slotted Friction Device

The slotted bolt hole detail of the friction device satisfied the elongation demands of the brace at all displacement amplitudes of the combined brace loading protocol. Figure 6.33 Shows the friction device positioning at the maximum and minimum displacements equal to 2.0Δ_{bm}. According to the linear pot data analysis, the friction interface experienced maximum rotations of ± 1.7 degrees and ± 1.0 degrees at the 2.0Δ_{bm} and 1.5Δ_{bm} displacement cycles, respectively.

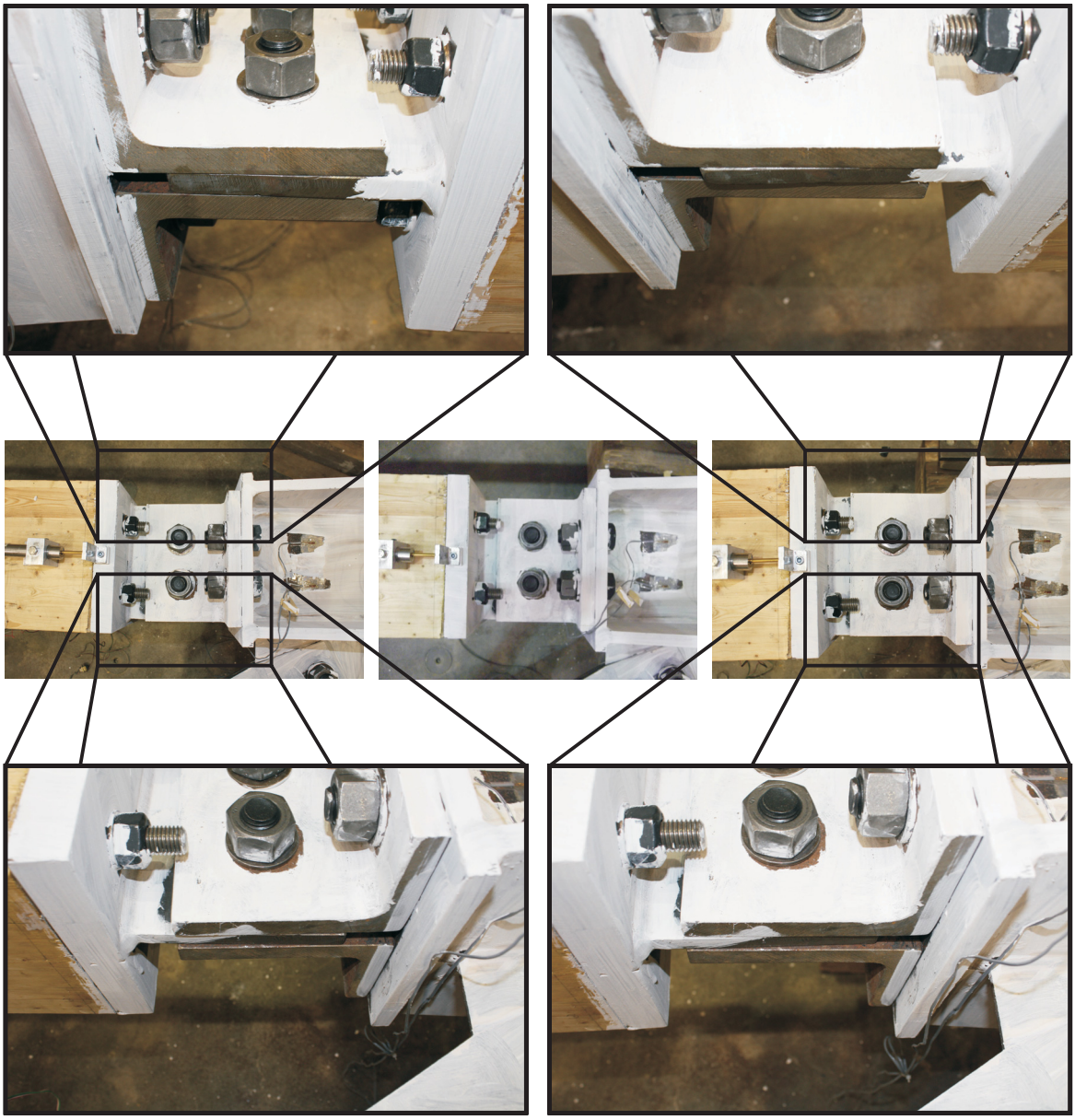

Figure 6.32: Beam Connection Rotation at Maximum Displacements

Manual measurements of the relative displacement between the side plate and the two slotted hole locations, presented in Figure 6.34, estimated an interface rotation of 1.1 degrees at the $1.5\Delta_{bm}$ displacement cycles, supports the rotation demands determined from the linear pot measurements. Figure 6.35 shows clear evidence of rotation in the friction device proving that the slotted bolt hole design is capable of satisfying the brace rotation demands. Further evidence was provided by visual inspection of the brace anchor and gusset plate connections that showed no signs of rotation in either connection zone.

6.7.3 Dynamic Earthquake Response

After completing the wind simulation and combined brace loading protocol tests, six earthquake deformation records were applied to the two braced frame prototype configurations. Three design-basis earthquake (DBE) and three maximum-considered earthquake (MCE) records were selected from the nonlinear dynamic analysis results from the numerical modelling investigation presented in Chapter 4. The earthquake records selected from the FEMA P695 far field record set were chosen based on earthquake intensity, acceleration content and historical significance. In all cases, the most severe first storey braced deformation response of the bi-directional ground accelerations was selected as the governing record. The DBE records considered were the ATC F05 1979 Imperial Valley, ATC F07 1995 Kobe and ATC F22 1976 Friuli earthquakes. The records selected for the MCE seismic evaluation tests were the ATC F01 1994 Northridge, ATC F07 1995 Kobe and ATC F20 1999 Chi-Chi earthquakes. The record set selected for the seismic hazard assessment provides a variety of fault types and ground motions recorded at varying epicentral distances.

Prior to testing, the response records were scaled using the dynamic scaling factors presented in Chapter 3. The deformation response of the first storey brace was converted into lateral frame displacement by dividing by the deformation-time history by $\cos(\theta_b)$, where θ_b is the frame bracing angle of the frame, 29.7 degrees. The displacement-time histories were then scaled to half-scaling by multiplying that records by the displacement and time scaling factors

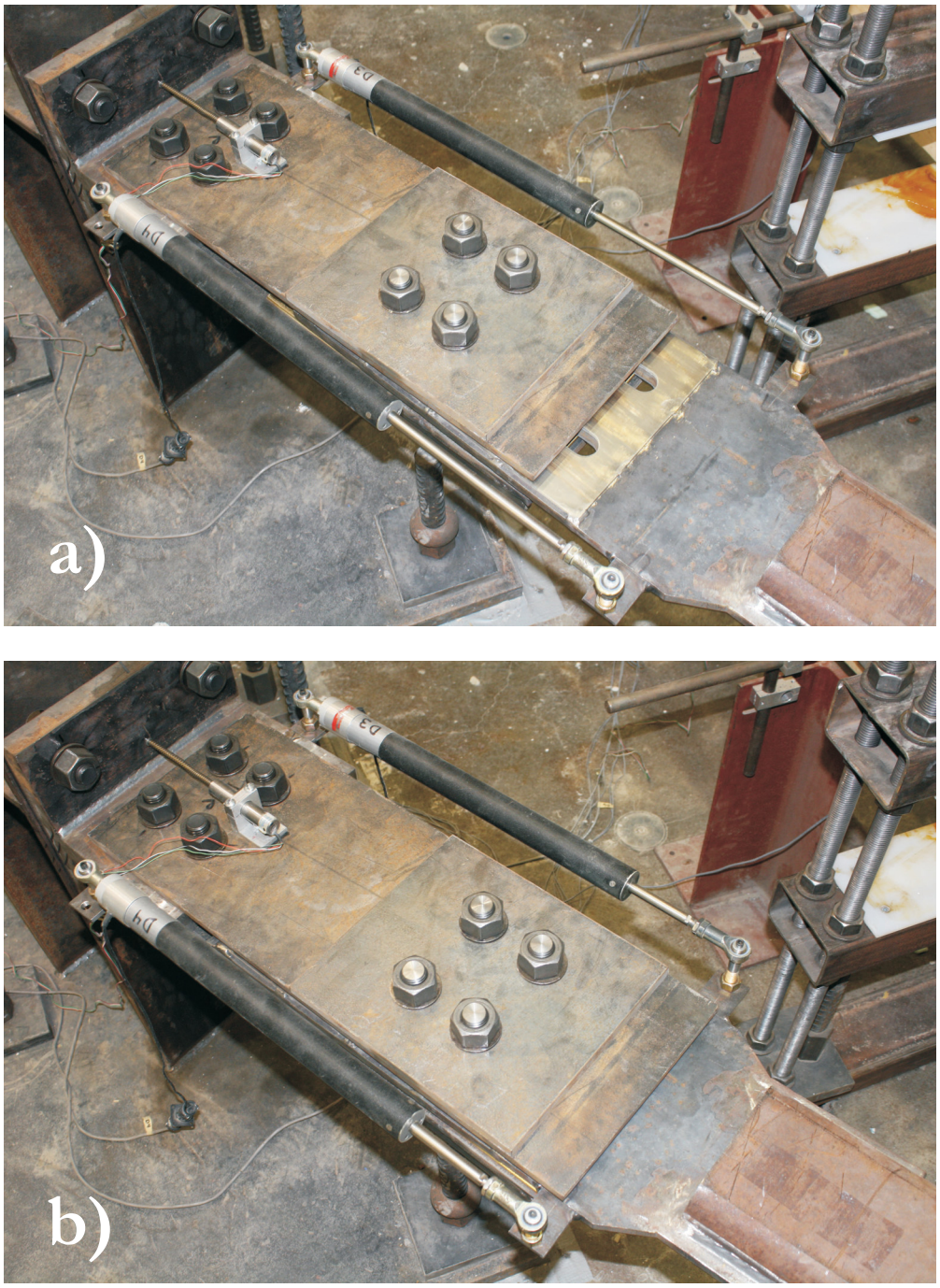

Figure 6.33: Friction Brace Displacement
a) Brace Elongation at $+2.0\Delta_{bm}$ and b) Brace Elongation at $-2.0\Delta_{bm}$

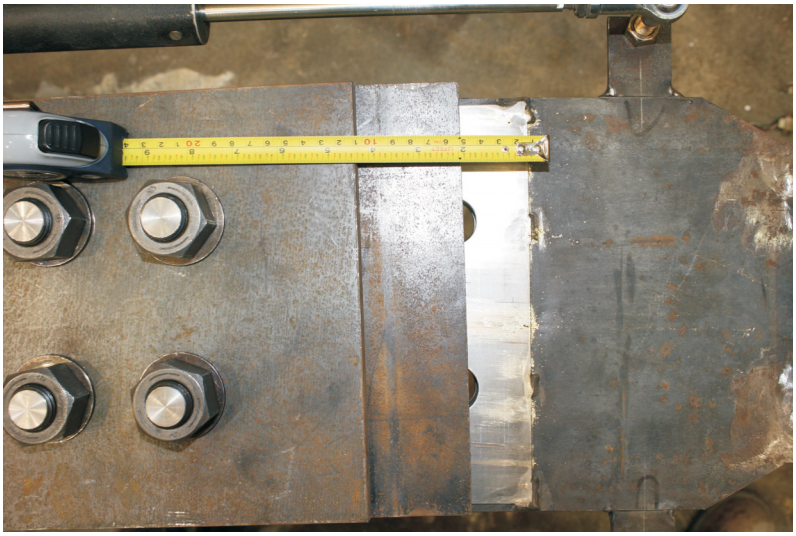

Figure 6.34: Measurement of Friction Brace Displacement

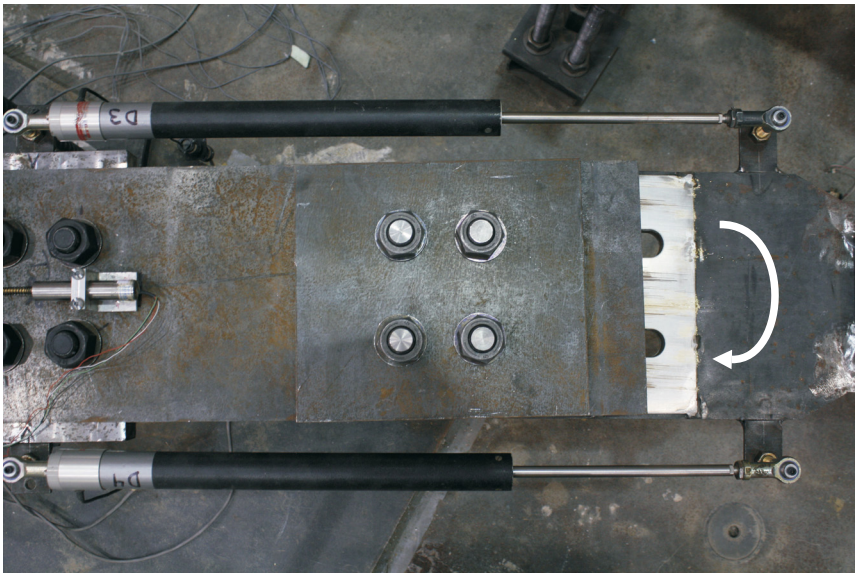

Figure 6.35: Rotation Behaviour in the Friction Interface

of 0.5 and 0.707, respectively. The velocity content of the six frame displacement histories was calculated to determine if time-step scaling was necessary to satisfy the loading rate limitations of the test actuator. As a result of this evaluation, time-step reduction factors of 3.0 and 2.0 were be applied to the MCE and DBE responses, resulting in scaled time steps of 0.0042 and 0.0028 seconds respectively. A comparison of the half-scale and velocity limited lateral displacement-time histories of the six records is shown in Figure 6.36.

6.7.3.1 Dynamic Earthquake Response: Design Basis Earthquake

The hysteretic response of the DBE earthquake record tests, in terms of inter-storey drift of the snug-tight and pre-tensioned frame configurations, are presented in Figure 6.37. The results show identical hysteretic responses of the snug-tight and pre-tensioned test configurations for the three earthquake tests. This supports the previous finding that the application of pre-tensioning in glued-in rod connections does not effect the seismic performance of the hybrid brace frame. The hybrid frame experienced peak inter-storey drifts of 1.40 %, 0.72 % and 0.60 % for the ATC F05, ATC F07 and ATC F22 tests, respectively. As a result, both test setups experienced effective ductilities of 7.8, 4.0 and 3.4 for the three records respectively, calculated from the peak inter-storey drifts and frame slip displacement. The earthquake simulations resulted in an increase in the activation and dynamic friction resistances compared to the target calibrated resistance of 159.0 kN. This increase in lateral resistance was attributed to an increase in faying surface roughness that induced ploughing behaviour. The surface roughness effect was most prominent in the static friction resistance in the snug-tight ATC F05 hysteretic response. The hybrid braced frame prototype did not experience any damage as a result of the increased force demands. Furthermore, the frame geometry dictates that brace force demands are approximately 15% greater than the developed lateral forces (storey shear). This resulted in gusset plate forces greater than the factored connection resistance of 215 kN. However, this increase in force demand did not cause inelastic behaviour in the gusset plate connection. It is important to note that these force demands are greater than the scaled DBE brace forces of 116.6 kN, 110.4 kN and 103.2 kN from the first storey brace responses of the hybrid timber-steel building presented in Chapter

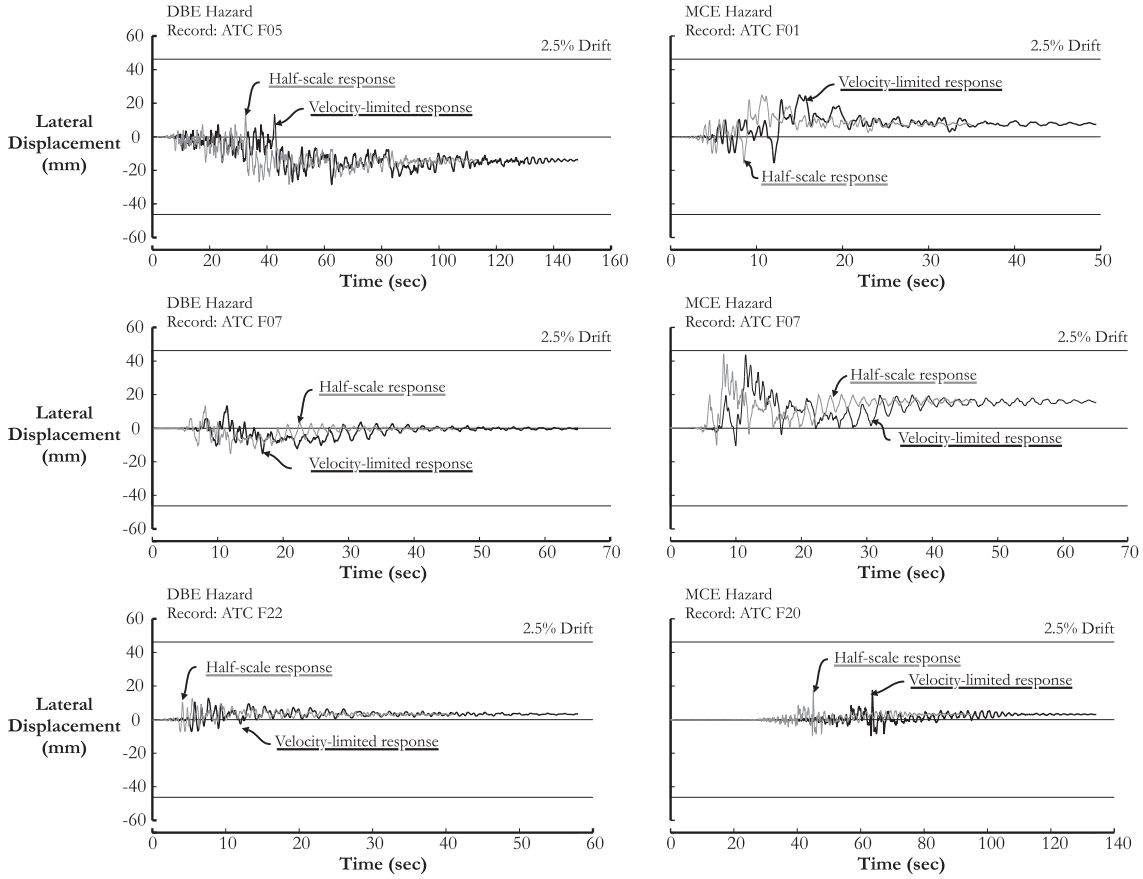

Figure 6.36: DBE and MCE Scaled Displacement Time Histories

4 for the three earthquake records, receptively. Additionally, marginal stick-slip behaviour can be seen in the hysteric responses of the six tests due to the relatively low peak velocities of the DBE records. Mean maximum support column movement of 1 mm was recorded at the peak dynamic displacements of the lateral deformation records which caused a 0.05 % reduction in the storey drift displacement. This minimal reaction column interference did not effect the overall frame performance. Furthermore, in all six tests, the expected residual drift displacements of the numerical model was achieved. The DBE seismic hazard assessment resulted in excellent overall lateral frame performance provided by the friction damping device. The resilient glued-in rod connections were able to resist the increased dynamic force demands without sustaining any damage. Furthermore, the hybrid braced frame was capable of satisfying the lateral displacement and rotation demands of the three seismic records.

A comparison of the brace friction characterization before and after the DBE earthquake records is presented in Figure 6.38. There was an increase in the tensile resistance of the brace in the snug-tight assembly after being subjected to the DBE hazards. This was most likely the result of the formation of asperities on the friction surfaces during these short-term dynamic tests. However, there was no distinction between the pre- and post-test friction resistance for the pre-tension test set-up as a result of the DBE earthquake records.

6.7.3.2 Dynamic Earthquake Response: Maximum-Considered Earthquake Records

Excellent seismic performance was observed for the snug-tight and pre-tensioned set assemblies under the MCE hazard level earthquakes. Hysteretic responses of the various MCE earthquake tests are presented in Figure 6.39. The stainless-steel on brass friction assembly provided consistent lateral resistance with no reduction in the friction performance during the dynamic tests. Stick-slip behaviour can be seen in the post-activation response of the friction device as a result of high loading velocities. However, this behaviour is limited due to the velocity controlled MCE deformation histories that were applied because of actuator limitations. Generally there was a slight reduction in the slip resistance of the pre-tensioned frame configuration compared to the snug-tight tests due to the recalibration of the friction device that occurred after swapping the

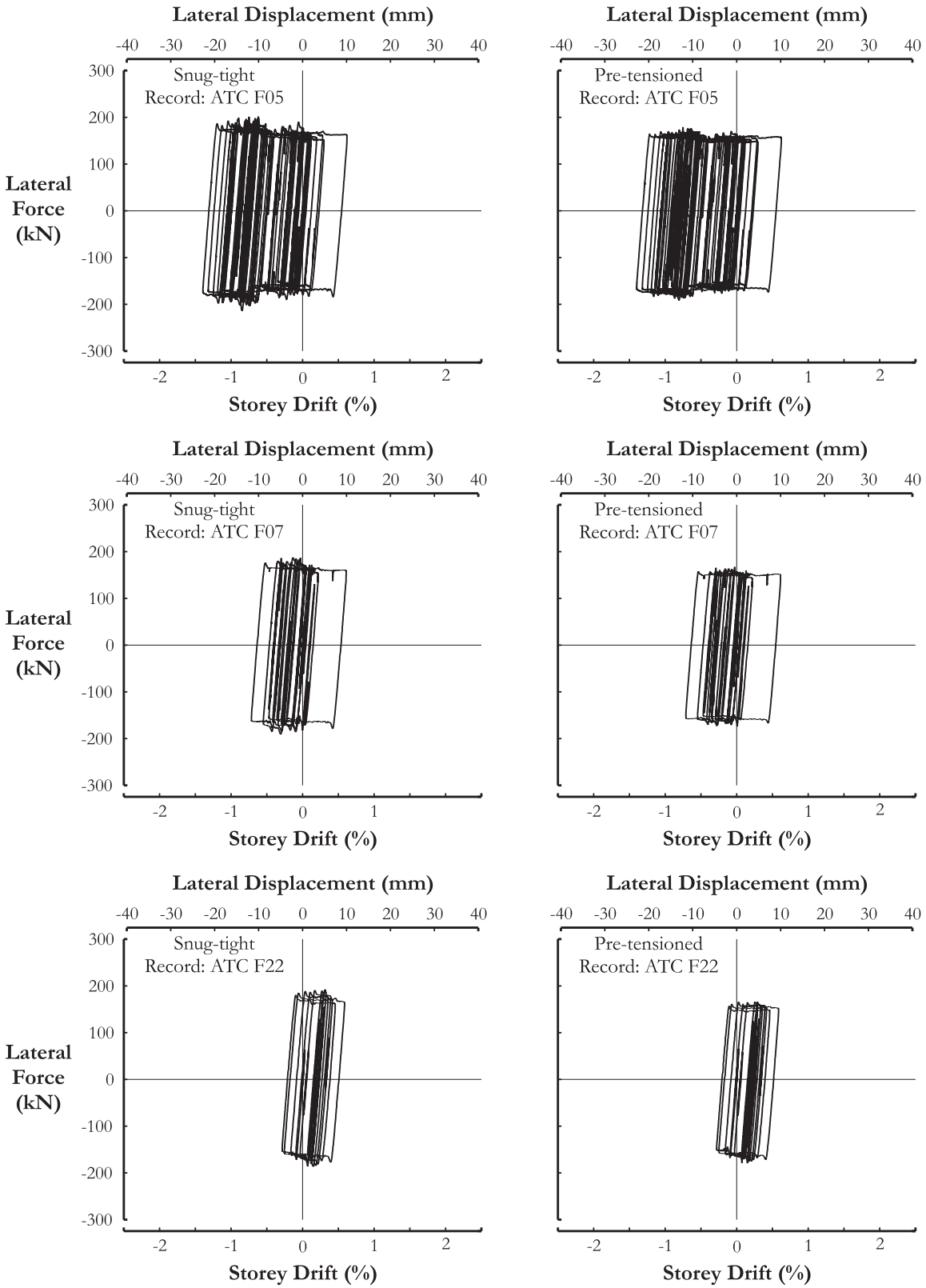

Figure 6.37: Hysteretic Response comparison for DBE Hazard Assessment

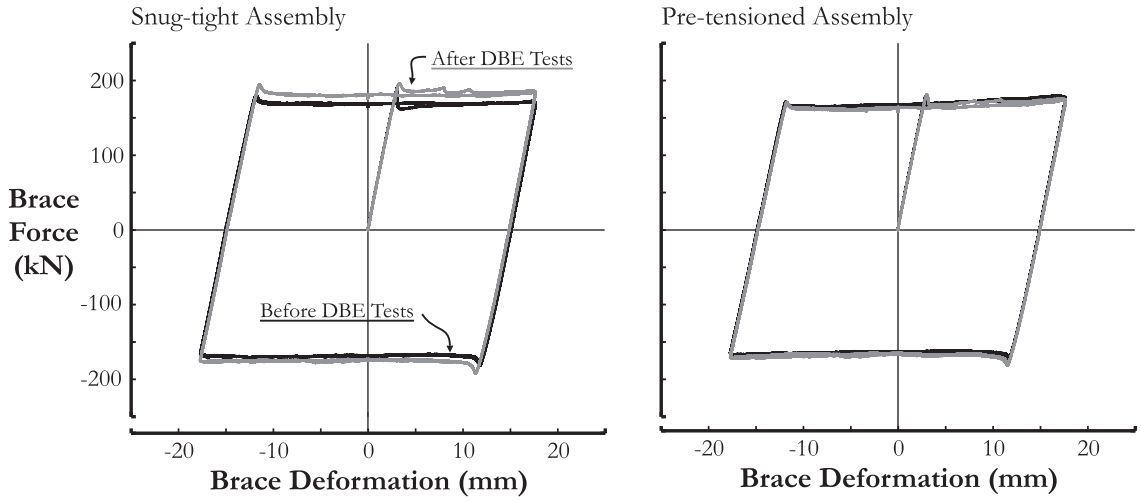

Figure 6.38: Friction Characterization Test Responses for DBE Hazard Assessment

frame assemblies. Additionally, the hysteretic responses of the F01 and F07 pre-tensioned frame tests have a minor unbalanced characterization in the friction response. This phenomenon was attributed to out-of-plane movement in the friction device that caused the side plates to confine the inner stainless-steel friction interfaces resulting in the increase in siding resistance in the positive drift displacements. Peak inter-storey drifts of 1.24 %, 2.20 % and 0.83 % were achieved for the ATC F01, ATC F07 and ATC F20 tests, respectively, in the snug-tight and pre-tensioned test conditions. These peak inter-storey drifts resulted in effective ductilities of 7.0, 12.3 and 4.7 for the three MCE hazards respectively. The target brace force was exceeded in all of the MCE earthquake tests without causing damage to the gusset connection. The over-strength characteristics of the factored connection resistance prevented the activation of the intended secondary failure mechanism. Improvements to the gusset plate connection could be made by designing a 19.1 mm ($\frac{3}{4}$ inch) bolt configuration to establish an unfactored row-shear resistance closer to the capacity design forces. This would allow for an investigation into the supplementary energy dissipation capabilities of the ductile gusset plate connection.

The friction characterisation responses before and after the MCE earthquake records are presented in Figure 6.40. There was slight difference in the brace friction performance as a result of the MCE earthquake hazard tests. This discrepancy was significantly less than the difference experience in the snug-tight brace characteristics following the DBE tests. After the final MCE

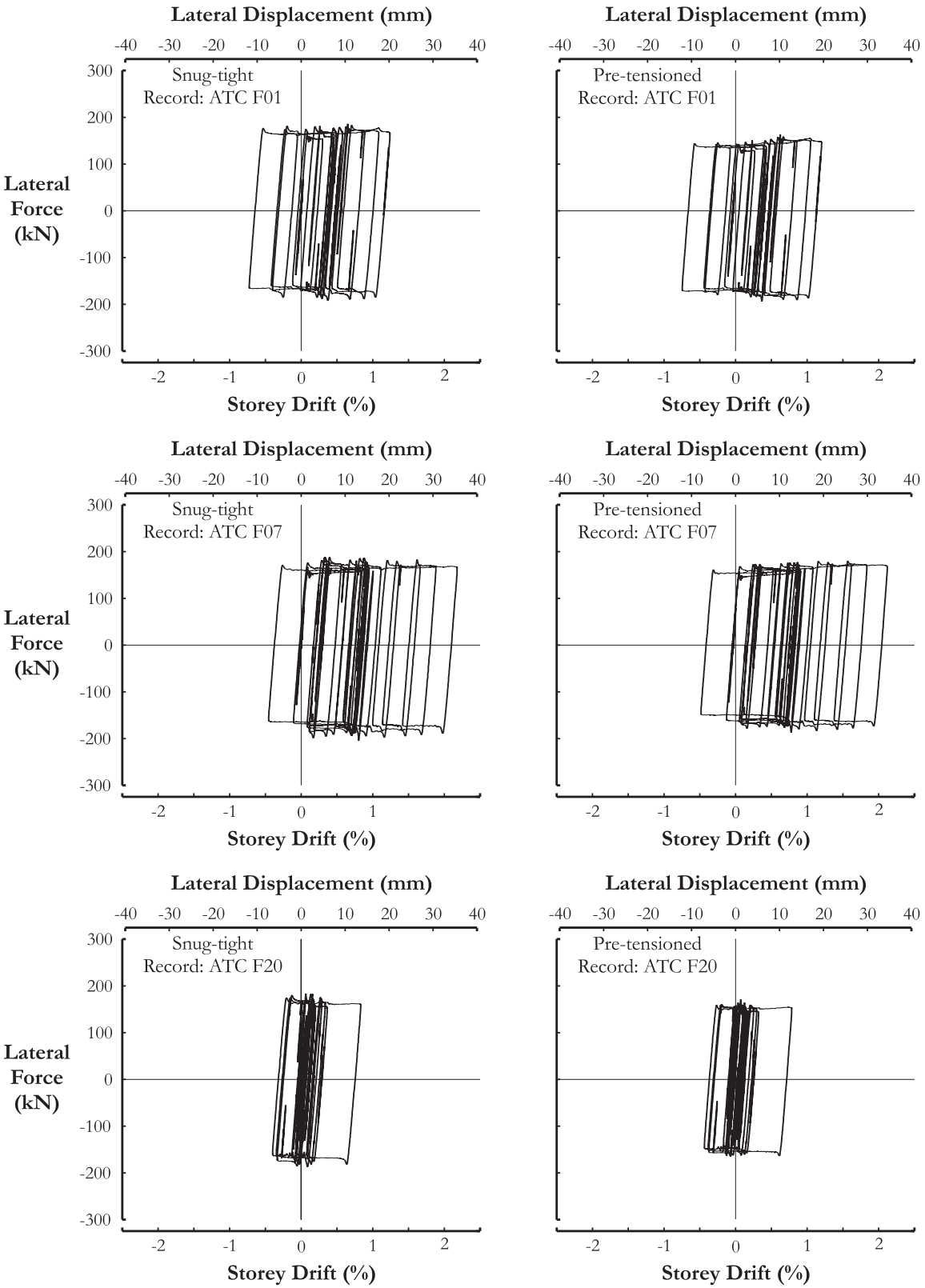

Figure 6.39: Hysteretic Response comparison for MCE Hazard Assessment

earthquake test the snug-tight and pre-tensioned test configurations were both subjected to an additional MCE ATC F07 Kobe earthquake record. The investigations were used to assess the hybrid system's ability to withstand two severe earthquake records applied in short succession. Figure 6.41 shows the response comparisons of the first and second ATC F07 tests for the snug-tight and pre-tensioned glued-in rod connection conditions. Both test configurations had identical seismic performances when comparing results from the initial and final ATC F07 responses. During this additional ATC F07 test performed on the pre-tensioned glued-in rod test set-up, gap formation was observed in one of the angle sections that make up the intermediate brace connection portion of the beam shear connection. This connection deformation behaviour was the result of a gradual release in the bolt pre-tensioning force over the course of the full test program of this set-up configuration. However, the glued-in rods and timber elements of both the snug-tight and pre-tensioned glued-in rod test configurations did not sustain any damage as a result of either two intense earthquake tests. Considering all the inelastic demands being satisfied by the friction brace, these additional tests further support the application of the capacity design principles used in the design of the hybrid system.

6.7.4 Connection Stiffness Characterization Tests

An investigation to characterize the effect that pre-tensioning has on the fastener stiffness of grouped glued-in rod connections was conducted on the beam-to-actuator glued-in rod connection show in Figure 6.42. Short duration wind loading simulation tests consisting of twenty-five cycles were applied to the hybrid braced frame at the half-scale fundamental period of 1.06 s. The beam connection was pre-tensioned to eight torque levels ranging for 64 N·m (47 ft·lbs) to 348 N·m (257 ft·lbs) with an incremental torque step of 41 N·m (30 ft·lbs). The applied torque range investigated was limited by the capacity of the torque wrench used to tighten the nuts of the glued-in rod fasteners. The pre-tensioning force of the previous test was released prior to tightening the connection to the next torque level. Prior to testing, the friction device was locked by pre-tensioning the 25.4 mm (1 inch) friction interface bolts to approximately 542 N·m (400 ft·lbs) to ensure a lateral force resistance greater than the actuator capacity which would prevent

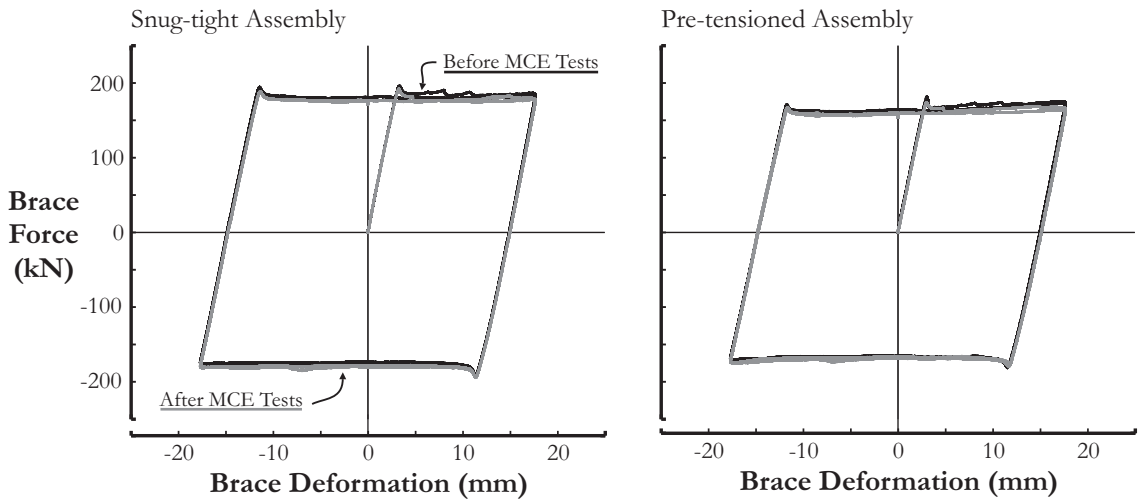

Figure 6.40: Friction Characterization Test Responses for MCE Hazard Assessment

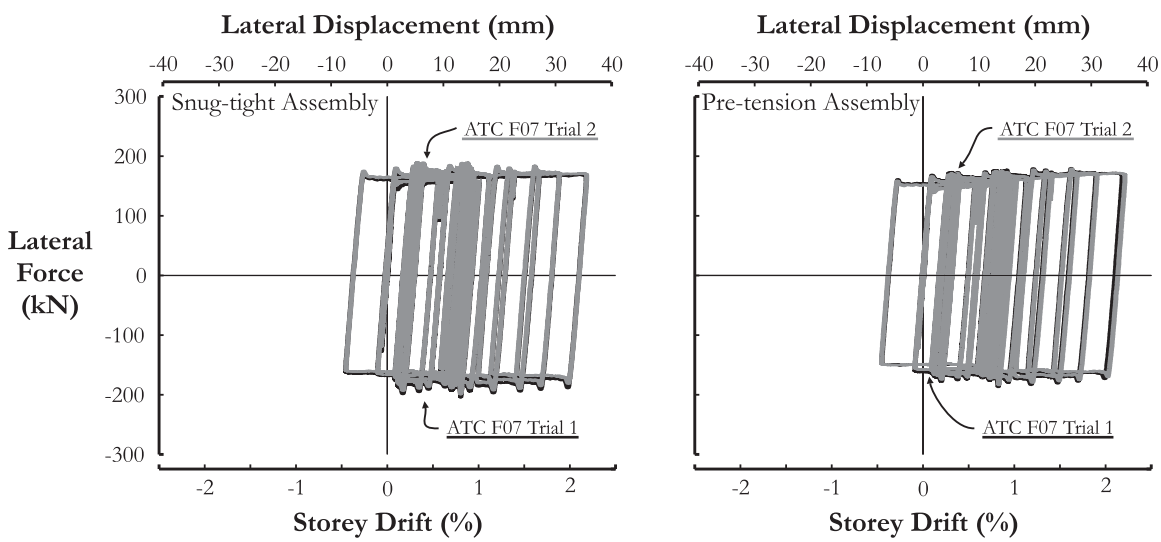

Figure 6.41: ATC F07 MCE Responses Comparison

frame activation. Additionally, another LVDT was mounted to the underside of the timber beam at the actuator end and spring loaded to the bearing plate of the intermediate steel connection. The connection stiffnesses were quantified from the axial beam forces from the actuator load cell and mean response from the LVDT displacements captured on either side of the timber beam. Four test groups consisting of three connection configurations were evaluated to quantify elastic stiffness characteristics of the glued-in rod connection. The first and last test groups, PTC1 and PTC4, were conduced on the complete glued-in rod connection, where the second and third sets, PCT2 and PCT3, tested partial connection geometries by disengaging two of the four glued-in rods. Figure 6.43 shows the connection configuration of test groups PCT2 and PCT3. It is important to note that even though connection orientation dictates that negative deformations in the connection result in tension loading, the results are presented in this section represents positive deformations associated with tensile (positive) connection loads to standardize the stiffness calculations and response comparisons. Fastener stiffness results were determined from the forces and deformations associated with 10% and 40% of the maximum tensile connection force experienced during the cyclic tests of each test group. Additionally, based on the findings from the individual glued-in rod specimens presented in Chapter 5, a mean ultimate resistance of the group connection was estimated at 705 kN assuming group effect phenomenon does not dictate the connection pull-out resistance. Therefore, the tests were expected to experience elastic behaviour throughout the first and last test groups. However, based on the single glued-in rod responses presented in Chapter 5, it is plausible that the partial connection configurations could experience minor damage as a result of increased tension forces in the fasteners.

The glued-in rod fasteners of the PCT1 full connection configuration remained elastic at all pre-tension levels. The hysteretic comparison of the PCT1 mean connection response of the PTC1-A, PTC1-D, PTC1-F and PTC1-H test specimens is shown in Figure 6.44. The pre-tensioning torques applied to the glued-in rod connection for these test configurations were 63 N·m, 186 N·m, 267 N·m and 348 N·m, respectively. The response comparison shows a trend that suggests glued-in rod connection stiffness increases with the application of a higher pre-tensioning force. This finding supports the initial results on the effect of pre-tensioning in the

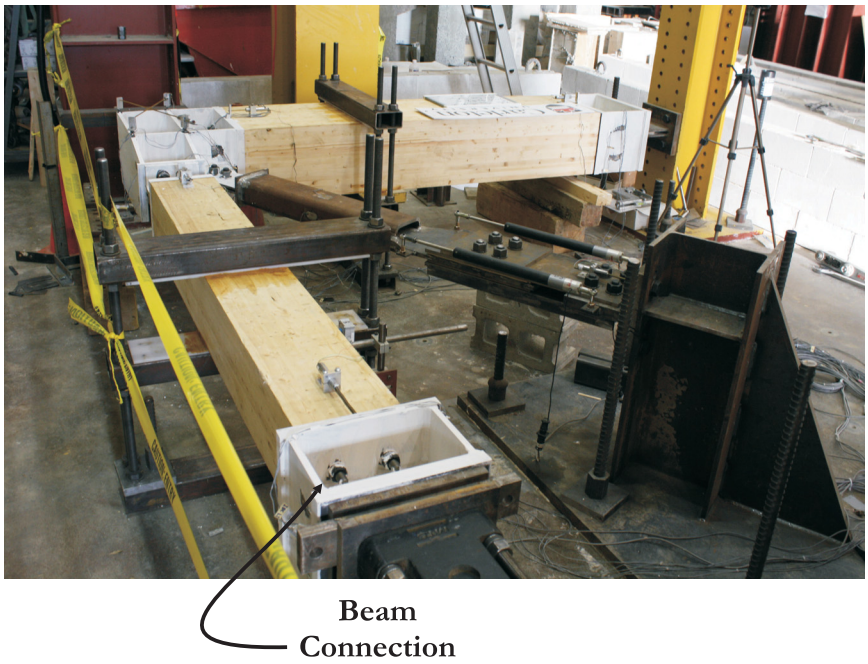

Figure 6.42: Beam Glued-in Rod Connection

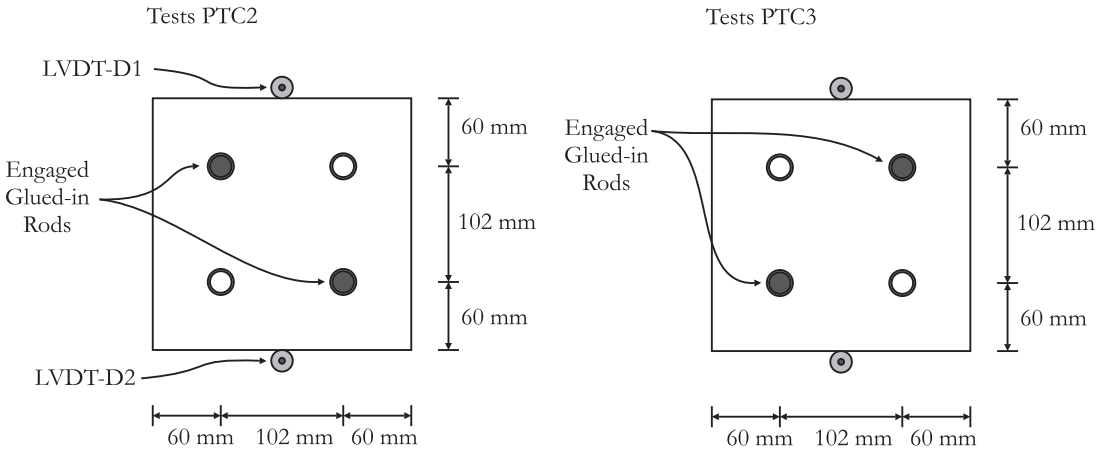

Figure 6.43: PTC2 and PTC3 Glued-in Rod Connection Test Configurations

single glued-in rod specimens discussed in Chapter 5. Furthermore, the tests results showed an increase in the bearing stiffness developed with an increase in the applied pre-tensioning torque. At low levels of pre-tensioning (below snug-tight conditions) the stiffness was attributed to the steel plate bearing directly on the end-grain in the tests. However, as the applied pre-tensioning is increased the glued-in rods stiffness contributes to the bearing stiffness as the glued-in rods and timber both resist the compression loads, since the nut remains engaged during the compression loading phase.

The quantified connection stiffness characteristics of test group PTC1 are presented in Table 6.13. The connection was subjected to a mean peak axial force of 209.8 kN during the cyclic tests that resulted in an induced fastener force of 52.4 kN. These stiffness characterization results show that stiffness increased relative to the applied pre-tensioning force of the elastic fastener responses. This positively correlated relationship is validated by the linear trend observed between the change in connection stiffness and the increase in applied torque in Figure 6.45. Based in the findings, a mean change in stiffness of 1482 $\frac{\text{kN}}{\text{mm}}$ was determined for the 41 N·m incremental increase in the applied torque with a standard deviation of 905 $\frac{\text{kN}}{\text{mm}}$.

The PCT2 and PCT3 partial connection tests experienced uneven gap formation as a result of out-of-plane rotation in the intermediate steel section that concentrated axial forces in one of the two rods due to prying action. This eccentric loading behaviour observed in the PCT2 and PCT3 test groups is shown in Figure 6.46. Even with uneven connection movement the mean stiffness responses suggest that the engaged glued-in rods experienced low levels of damage during the twenty-five loading cycles. This behaviour is visible in the mean hysteretic response comparisons of the test specimens for the PTC3 test group presented in Figure 6.47. The response of the lowest applied torque test (PTC3-A) resembles the cyclic behaviour of the single glued-in rod test specimens presented in Chapter 5. The stiffness of the initial loading cycle is greater than the subsequent cycle responses, suggesting that micro-fracturing of the timber-adhesive interface occurred due to the uneven connection force distribution. Research into quantifying this

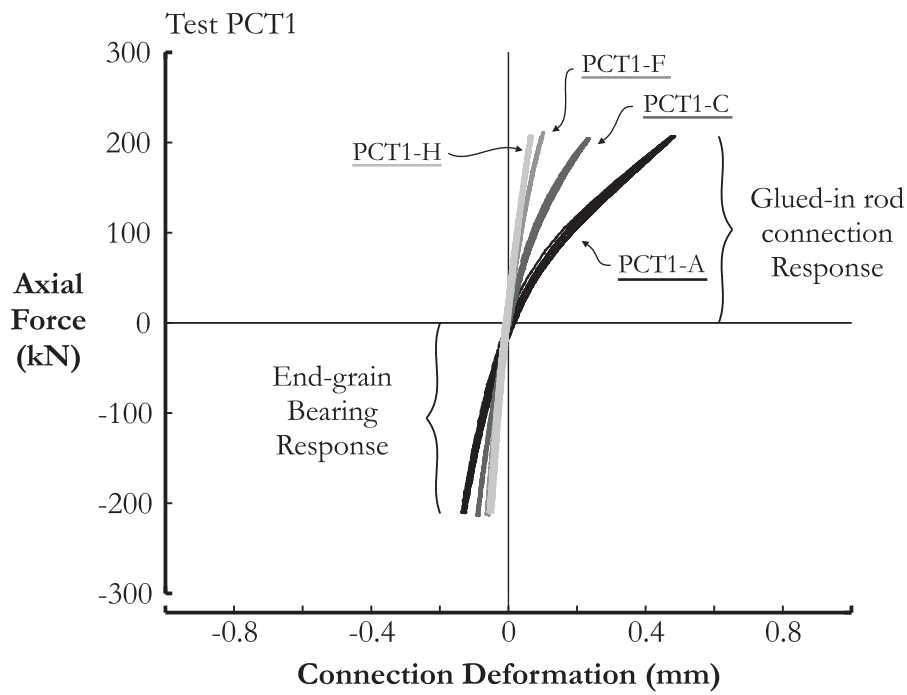

Figure 6.44: Hysteretic Response Comparisons of PTC1 Test Specimens

Table 6.13: Stiffness Analysis results for PCT1 Test

Test Specimen	Maximum Applied Torque N·m	Maximum Elastic Force kN	Maximum Elastic Stiffness $\frac{kN}{mm}$
PTC1-A	64	207	2534
PTC1-B	104	216	3969
PTC1-C	145	205	5355
PTC1-D	186	209	8132
PTC1-E	226	213	9662
PTC1-F	267	211	10169
PTC1-G	308	209	12603
PTC1-H	348	207	12915

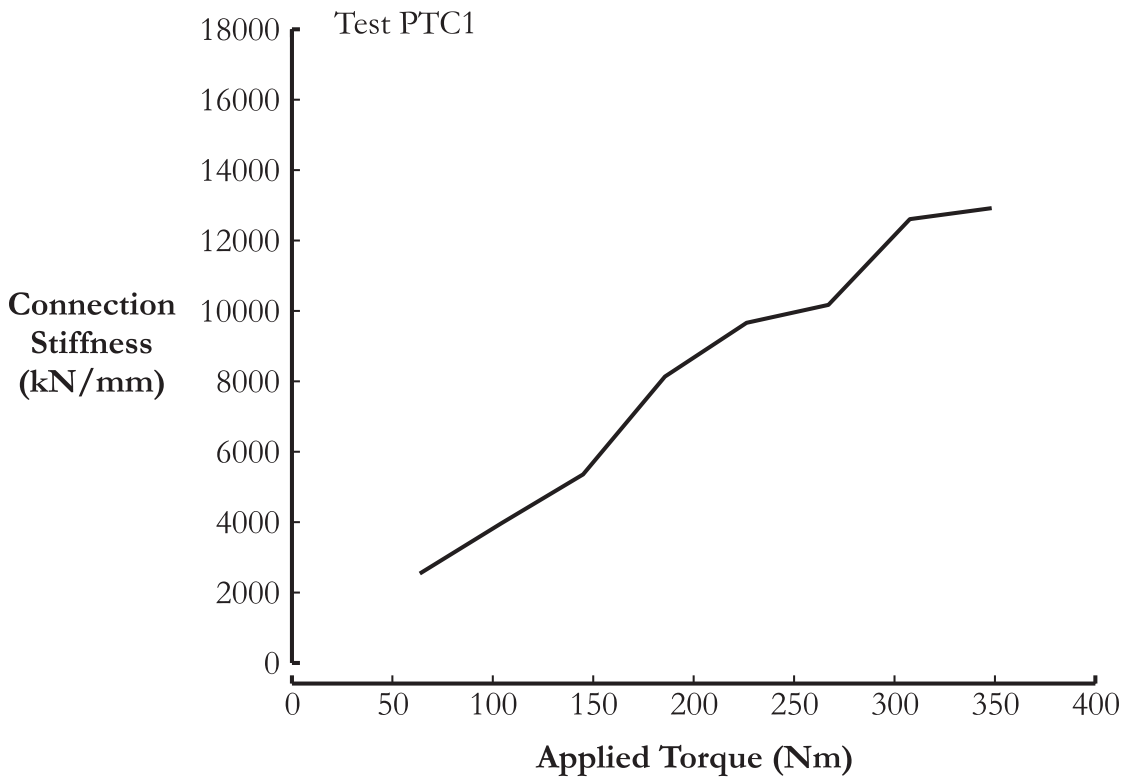

Figure 6.45: Relationship Between Connection Stiffness and Torque for Test PTC1

force distribution behaviour is important to establishing resistance modification factors that accounts for prying action and accidental eccentricities that could effect the strength and stiffness characteristics of grouped glued-in rod connections.

The final test group, PCT4, did not experienced an overall reduction in connection stiffness following the partial connection tests. A comparison of the mean connection responses of a select PTC4 test specimens captures the pre-tension induced incremental stiffness trend is presented in Figure 6.48. The lower torque test PTC4-A experienced minor damage in the first loading cycle. This is represented by the reduction in fastener stiffness of the subsequent loading cycles.

The connection stiffness characteristics for the PTC4 test group are presented in Table 6.14. The stiffness results were calculated from the connection responses based on a mean peak axial force of 205.1 kN. This resulted in 51.3 kN axial force in each of the four glued-in rod fasteners. The stiffness characteristics further validate the presence of a relationship between connection stiffness and an increase in applied torque. A comparison of the connection stiffness and applied torque relationship between tests PTC1 and PTC4 is presented in Figure 6.49. There is slight reduction in connection stiffness of the initial torque level of the PCT4 test group results compared to the initial PTC1 test set. This is likely the result of the minor damage sustained during the partial connection tests that affected the timber-adhesive interface. However, the linear incremental stiffness tread representative of the increase in pre-tensioning force is still present. Comparing the stiffness trend of the PCT4 tests results to the PCT1 test group, a more consistent positively correlated increase in stiffness is obvious in the last test group (PTC4). The change in stiffness is substantially lower in the first two test results due to the low pre-tensioning force at the applied torques. The mean stiffness increase of 2246 $\frac{\text{kN}}{\text{mm}}$ and the 414 $\frac{\text{kN}}{\text{mm}}$ standard deviation determined from the stiffness characteristics of test group PTC4 is representative of this more consistent incremental stiffness trend.

In general, the application of pre-tensioning in glued-in rod fasteners increased the stiffness of the grouped connection. This pre-tensioning also reduced the connection gap deformations as

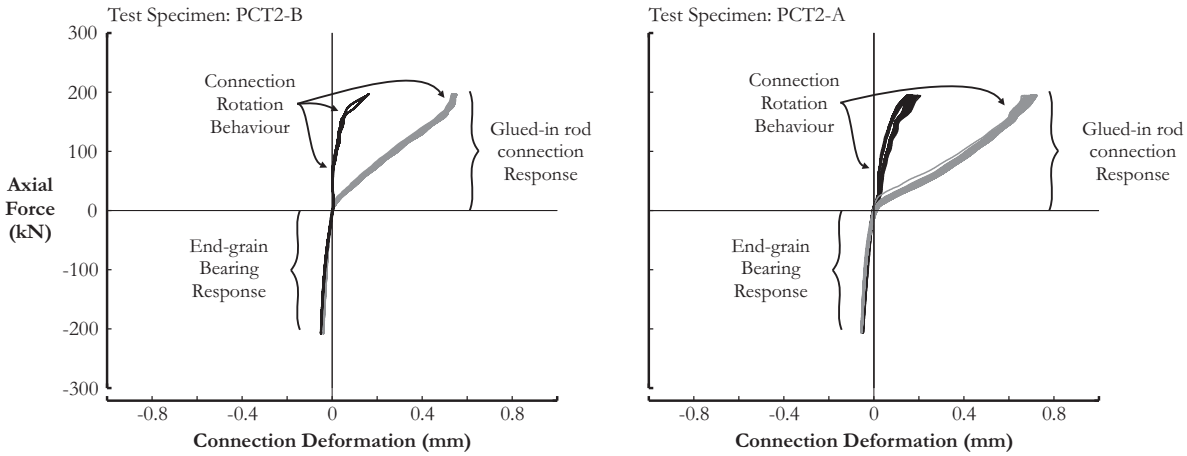

Figure 6.46: Prying Response in Partial Connection Tests

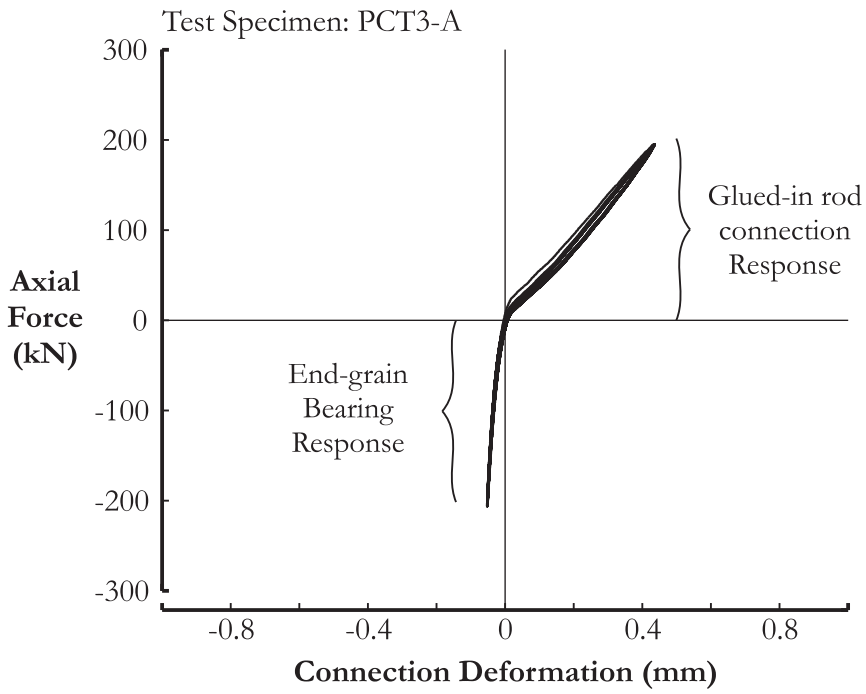

Figure 6.47: Mean PTC3-A Specimen Response

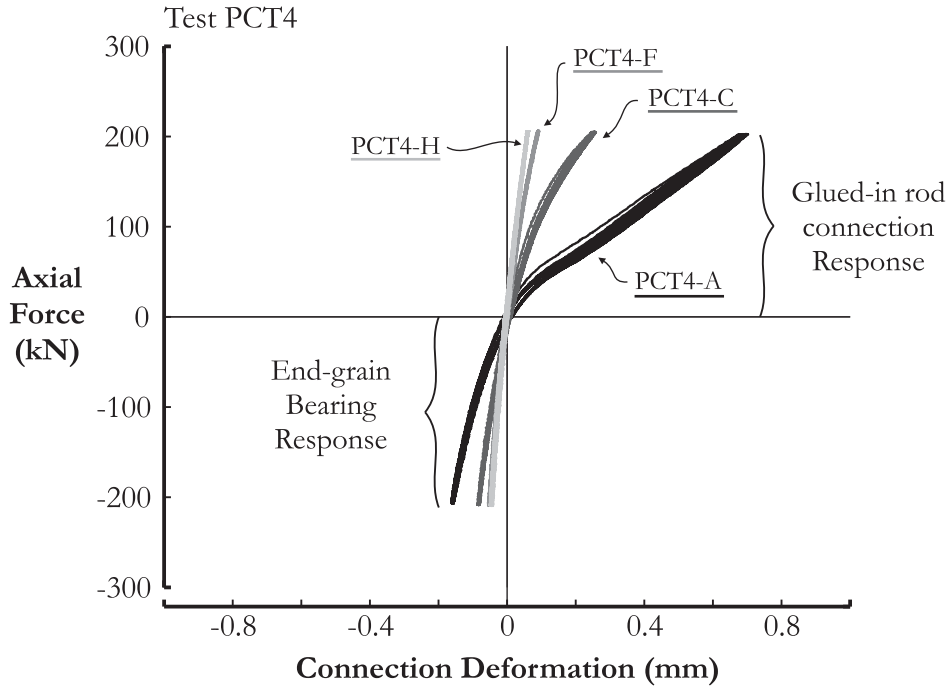

Figure 6.48: Hysteretic Response Comparisons of PTC4 Test Specimens

Table 6.14: Stiffness Analysis results for PCT4 Test

Test Specimen	Maximum Applied Torque N·m	Maximum Elastic Force kN	Maximum Elastic Stiffness $\frac{kN}{mm}$
PTC4-A	63.7	202.5	1220.4
PTC4-B	104.4	203.7	3476.8
PTC4-C	145.0	204.8	5657.0
PTC4-D	185.7	205.7	7964.6
PTC4-E	226.4	205.9	9852.5
PTC4-F	267.1	206.1	11547.7
PTC4-G	307.7	206.1	13939.7
PTC4-H	348.4	205.9	16940.0

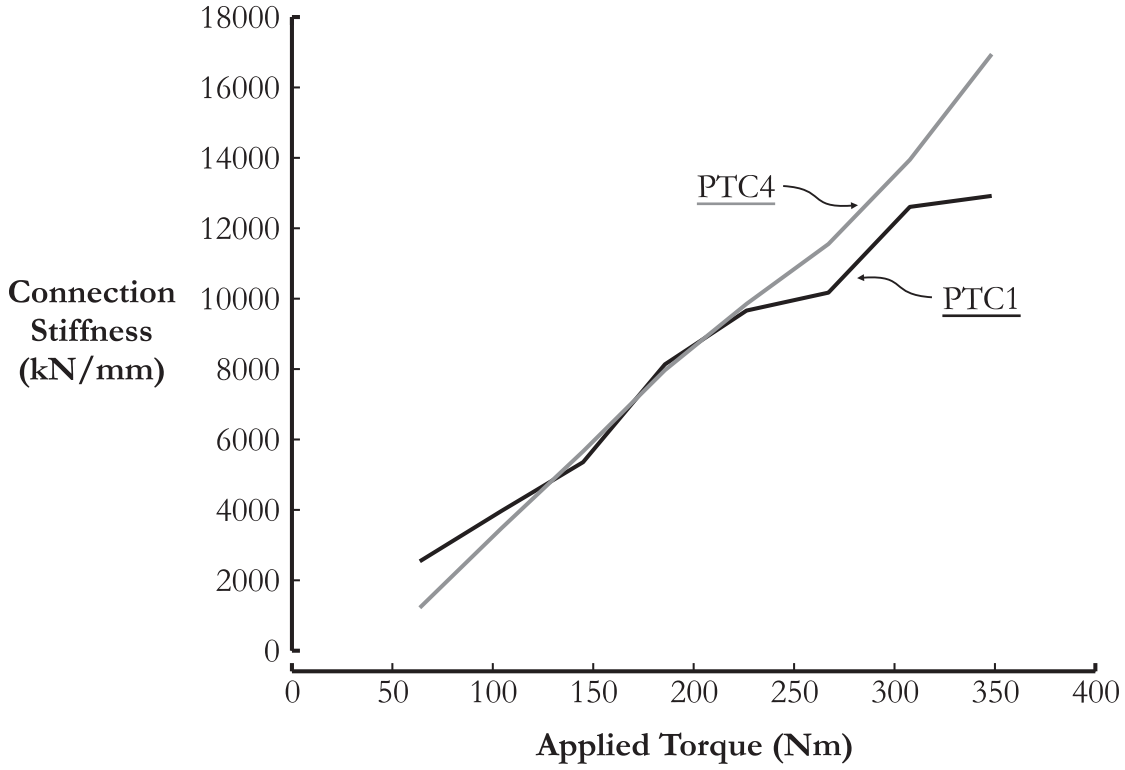

Figure 6.49: Connection Stiffness and Torque Relationship Comparison

a result of the increased tension forces in the glued-in rod fasteners at equilibrium. This information provides insight into the short-term stiffness characteristics of glued-in rod connection. However, relaxation behaviour could reduce the stiffness trends shown in the test results. Therefore, long-term pre-tensioning tests are required to fully evaluate the stiffness characteristic of grouped glued-in rod connections.

6.8 Post-Test Inspection

After completion each test configuration, the frame, glued-in rod fasteners, connection surfaces and friction interfaces were inspected to assess if the individual components sustained any damage. The beam connection was disassembled and inspected to determine what effect the rotation demands had on the connection interface. Figure 6.50 shows the significant levels of surface abrasion sustained by the outer angle (left) and inner plate (right) of the connection interface after the snug-tight and pre-tensioned brace loading protocol tests were completed. The

surface has distinct curved ploughing and asperity characteristics that suggests the damage was caused by rotational friction. The visual observations of connection rotation and presence of surface damage on the connection interface verifies the pinned fixity assumption of the beam shear connection. The gusset plate was inspected to determine if plastic behaviour or rotation occurred in this connection zone. There was no obvious evidence that the force demands of the testing program exceeded the yield strength of the connection, as shown in Figure 6.51. Flaking was not visible in the white-wash that was applied to the brace plates and gusset plate of the connection prior to testing. Additionally, there was no localized damage or surface abrasion in the gusset to brace connection interface, supporting test observations that suggest the slotted bolt hole detail of the friction brace satisfied the rotation demands of the brace.

The set of brass and stainless-steel faying surfaces of the friction device were used throughout the entire testing program for the snug-tight and pre-tensioned glued-in rod connection configurations. As a result, the post-test inspection of the friction interface surfaces show that significant surface damage was sustained by the brass plates. Figure 6.52 shows the post-test condition of the upper brass plate and slotted stainless steel plate, similar damage was observed on the brass and stainless steel plates from lower friction interface. The localized damage in the brass plates were the result of friction interface interaction during the extensive testing program. The damage was concentrated on the brass plates because of the lower material strength and difference in material hardness of brass compared to stainless-steel. This significant surface damage was

Figure 6.50: Damage in the Beam Connection Interface

Figure 6.51: Post-Test Condition of the Gusset Plate Connection

also attributed to the severe stick-slip response of the dynamic earthquake and high velocity tests that induced ploughing behaviour. The longitudinal gouge formations at the edge of the brass plates were attributed to the perimeter welds on the stainless-steel plate scoring the brass plates during the large displacement amplitudes of the combined brace loading protocol. Furthermore, brass flakes were observed around the edge of the upper stainless-steel plate. The presence of this debris supports the force reduction findings in the later stages of the combined brace loading protocol due to interface isolation and rolling resistance behaviour caused by debris development in between the friction surfaces.

Lastly, the glued-in rod connections of both sets of timber members were inspected to determine if localized damage could be seen in the timber-adhesive interface. The observations concluded that none of the glued-in rod connection experienced any surface damage or splitting as a result of the testing programs. This supports the design assumptions used in the capacity protection procedure that these connections would remain elastic while resisting the high tension forces developed in the timber members.

6.9 Summary of Results

The hybrid frame design demonstrated excellent seismic performance during all three lateral loading programs. The beam shear connection and slotted bolt hole detail of the friction device was capable of satisfying the rotation demand caused by global frame movement at two times the MCE drift displacement limits experienced in the combined loading protocol tests. The glued-in rod connection did not suffer any damage during the static and dynamic loading programs. The test results showed that the pre-tensioning of glued-in rod fasteners did not affect the global frame behaviour or elastic stiffness of the hybrid system. However, the findings suggest pre-tensioning could be used to prevent gap formation between the connection components and increase connection stiffness. The gap formation that occurred in the snug-tight connections could affect the seismic performance by increasing lateral frame displacements. Shake-table tests and force controlled loading protocols could be used to evaluate the impact connection separation has on the hybrid braced frame behaviour. Additionally, the fasteners were able to satisfy

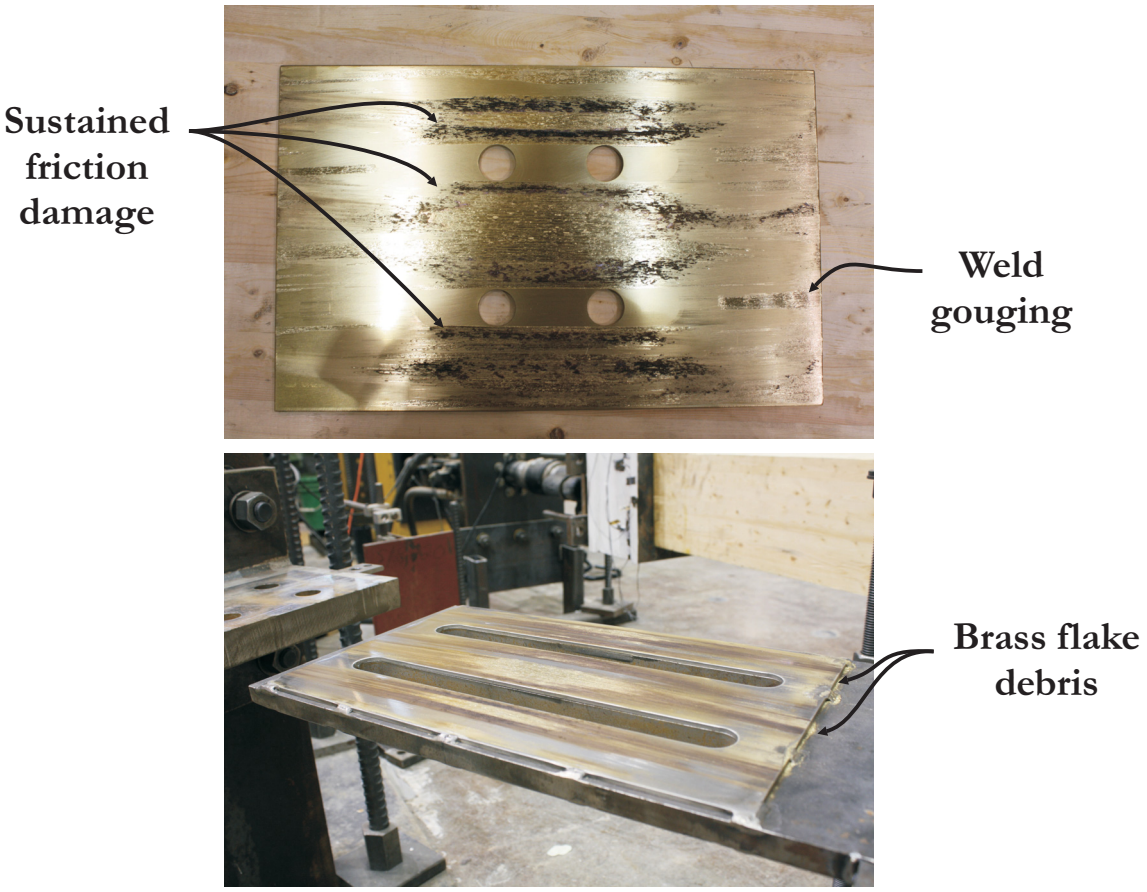

Figure 6.52: Post-test surface conditions of the friction interface

the high cycle load demands of the wind simulation tests without suffering measurable damage. These findings suggest that the GIROD Report, LICONs Report and DIN 1052 design methods are applicable to the design of glued-in rod fasteners in Canada. However, further testing is required to characterize the ultimate and fatigue resistances of grouped glued-in rod connections subjected to seismic and wind loading scenarios.

The stainless-steel on brass friction brace preformed well throughout the extensive testing program. However, minor reductions in the lateral resistance were experienced during the higher displacement cycles of the combined brace loading protocol test that was attributed to an increase in debris build-up between the faying surfaces and increase in interface temperatures. These surface conditions did not effect the overall seismic performance of the hybrid system allowing the friction device to satisfy and in some cases exceed the effective ductility requirements of the bucking restrained brace design.

Lastly, the results of the short-term connection stiffness characterization test provided insight into the effect pre-tensioning has on connection stiffness. The tests showed an increasing trend in the relationship between connection stiffness and applied pre-tensioning force. The two full connection configuration tests provided mean stiffness increases of 1482 $\frac{\text{kN}}{\text{mm}}$ and 2246 $\frac{\text{kN}}{\text{mm}}$ for an increase in that applied torque of 41 N·m. Additionally, the increase in applied pre-tensioning reduced overall connection deformations and prevented gap formation between the bearing plate and timber end-grain at moderate force levels.

Overall, the lack of damage and excellent seismic performance of the hybrid braced frame supports the application of the hybrid and capacity design concepts used in the adaptation of advanced structural bracing systems into heavy timber frames. These tests provided promising results which suggest that high force reduction factors can be used in the seismic design of heavy timber buildings through the application of advanced seismic force resisting systems.

Chapter 7: Conclusions

7.1 Summary of Findings

The primary goal of this research was the development of an innovative hybrid design concept for the adaptation of advanced structural bracing systems for seismic applications in heavy timber buildings. These advanced ductile steel systems provide high force reduction factors that allow for the reduction of seismic forces in building design. A nonlinear dynamic analysis and two experimental investigations were used to evaluate the seismic performance of the hybrid timber-steel braced frame. The findings provided insight into the efficacy of hybrid and capacity design principles and suggest that the improvements in seismic performance could offset the apparent economy associated with the fabrication and construction of hybrid timber-steel buildings.

7.1.1 Numerical Modelling Results

The numerical modelling investigation assessed the seismic performance of the conceptual hybrid timber-steel buckling-restrained brace frame (BRBF) design compared to a steel-only structure containing the same bracing system. The buckling-restrained braced frame models provided insight into the seismic performance of these advanced bracing systems. The nonlinear dynamic time-history analysis of the two six-storey structures showed that hybrid timber-steel structures can have equivalent seismic performance with respect to peak interstorey and residual drifts, and maximum storey accelerations compared to steel-only buildings. The interstorey drift responses of both the hybrid timber-steel and steel-only structures remained well within the NBCC (2010) allowable drift limit of 2.5%. Furthermore, the high lateral stiffness of both systems resulted in mean peak residual drifts of 0.7 and 0.9% observed at the MCE hazard level

in the hybrid and steel-only structures respectively. The hybrid structure had a 40% reduction in seismic weight attributed to the CLT floor slab systems that reduced the base shear forces to 60% of the steel-only building. The reduction in seismic weight had a direct affect on the foundation forces and seismic loads that reduced the geometry of the structural components and helped to optimize the hybrid system design. The findings suggested hybrid system are capable of excellent seismic performance by satisfying the life safety requirements of the NBCC (2010).

7.1.2 Experimental Glued-in Rod Investigation Findings

The single glued-in rod investigation validated the strength predictions of the three European methods (GIROD Report, LICONS Report, and DIN 1052) for the glued-in rod fasteners containing structural epoxy resins. These fasteners were used to predict the elastic behaviour and cyclic performance of the hybrid braced frame connections. In an attempt to characterize the cyclic response of these connections, brace loading simulation tests were conducted that verified the elastic behaviour required to satisfy the capacity design procedure. The single glued-in rod connections exhibited brittle fastener behaviour attributed failure in the timber/adhesive interface. Ultimate capacity and strength governing failure mechanisms of the glued-in rod specimens were not influenced by cyclic loading or applied pre-tensioning. These findings are particularly important for seismic applications and suggest that the glued-in rod fasteners utilized in the associated braced frame study would remain elastic under the anticipated earthquake loads.

Although pre-tensioning was not found to influence fastener capacity, it was linked to short-term increases in fastener stiffness. Preliminary investigations into the long-term behaviour of pre-tensioned glued-in rod connections shows exponential relaxation behaviour in the induced axial forces that did not stabilize after seven days.

7.1.3 Experimental Hybrid Braced Frame Results

The three component experimental testing program was implemented to evaluate the wind and seismic performance of the hybrid braced frame prototype. Findings showed that rotation demands at the MCE and two times the MCE drift limits were satisfied by the beam shear and slotted friction connections, without impacting global frame performance. Overall, the hybrid

timber-steel design exhibited excellent seismic performance characteristics capable of satisfying the NBCC (2010) drift and strength requirements. Ideal friction resistance characteristics were seen throughout the hybrid braced frame investigation. Calibration tests established a dynamic friction coefficient of 0.45 for the stainless-steel in brass friction interface. The friction device provided predictable static and dynamic friction behaviour with frame activation occurring at 3.30 mm of lateral displacement. Reductions in sliding resistance were observed at larger displacement cycles of the combined brace loading protocol tests, attributing to reductions in the friction coefficient due to temperature effects and faying surface isolation caused by debris accumulation. Furthermore, increases in dynamic friction resistance occurred during the dynamic earthquake record tests as a results of increased surface wear and stick-slip behaviour. These surface conditions did not effect the overall seismic performance of the hybrid braced frame system, allowing the friction device to satisfy and in some cases exceed the effective ductility requirements of the bucking restrained brace design.

The glued-in rod connections did not suffer any observable damage or reductions in stiffness as a result of the extensive testing programs. Axial forces developed in the connections during the dynamic wind simulation tests exceeding the high cycle fatigue resistances without failure. These findings suggest that the GIROD Report (2002), LICONS Report (2003) and DIN 1052 (2004) design methods are applicable to the design of glued-in rod fasteners in Canadian. Lastly, short-term connection stiffness characterization tests provided insight into the effect pre-tensioning has on connection stiffness. The full connection tests showed an increase in stiffness attributed to higher levels of applied torque. Stiffness characteristics and higher pre-tensioning forces reduced overall connection deformations and limited connection gap formation, which improved axial force distribution throughout the connection.

7.2 Future Research

Based on the findings and short comings of the experimental and numerical modelling investigations, the following suggestions are presented as areas of future research:

- Nonlinear dynamic analysis and seismic response comparison of multi-storey hybrid

braced frame structures

- Experimental investigations into the long-term relaxation behaviour of pre-tensioned glued-in rod fasteners
- Experimental investigations into the high cycle fatigue characteristics of glued-in rods that could aid in establishing validate Canadian design methods.
- Load duration effects on glued-in rod fasteners.
- Development of glued-in rod pre-tensioning calculation method and design rules
- Optimization of the hybrid braced frame glued-in rod design
- Experimental validation of the hybrid braced frame glued-in rod design and strength predictions.
- Development and testing into the energy dissipation capabilities of ductile gusset plate connections.

References

American Institute of Timber Construction (AITC) (2005). *Timber Construction Manual, Fifth Edition.* John Wiley & Sons, Inc. New Jersey, USA.

American Society of Civil Engineers (ASCE 7-05) (2005).*Minimum Design Loads for Buildings and Other Structures*, ANSI/SEI7-05 Including Supplement No.1. Chicago: American Society of Civil Engineers.

American Institute of Steel Construction (AISC 341-05) (2005). *Seismic Provisions for Structural Steel Buildings*, ANSI/AISC 341s1-05 Including Supplement No.1. Chicago: American Institute of Steel Construction Inc.

Aicher, S., Dull-Langer, G. (2001). *Influence of Moisture, Temperature and Load Duration on Performance of Glued-in Rods.* Proceedings International RILEM Symposium on Joints in Timber Structures. (Edited by: Aicher, S. and Reinhardt, H.-W.). PRO 22, RILEM Publications, 383-392.

Aicher, S., Hofflin, L. (2009). *Glulam Beams With Holes Reinforced by Steel Bars.* International Council for Research and Innovation in Building and Construction. CIB-W18, Switzerland, August 248-261.

Andreolli, M., Piazza, M., Tomasi, R., Zondonini, R. (2011). *Ductile Moment-Resistant Steel-Timber Connections.* Institution of Civil Engineers Proceedings, Structures and Buildings, Vol. 164, SB2, 65-78.

Ashtari, S. (2009). *In-plane Stiffness of Cross-Laminated Timber Floors*. Vancouver: University of British Columbia, B.C.

Astaneh-Asl, A. Cochran, M. L., Sabelli, R. (2006). *Seismic Detailing of Gusset Plates for Special Concentrically Braced Frames*. Steel Technical Information and Product Services, Report. December.

Barillas, E., G. (2015). *Performance of Timber Connections with Single and Multiple Glued-in Threaded Steel Rods.* MASc. Thesis. Department of Civil Engineering, The University of British Columbia, Vancouver, Canada, September.

Blaß, H.J., Laskewitz, B. (1999). *Effect of Spacing and Edge Distance on the Axial Strength of Glued-in Rods*. CIB W18 Meeting, Paper 32-7-12.

Blaß, H.J., Laskewitz, B. (2001). *Effect of distance between rods and between rods and timber edge on the axial strength*. Technical report for WP 3. Versuchsanstalt fur Stahl, Holz und Steine, Universitat Fridericiana, Karlsruhe, Germany.

Bengtsson, C., Johansson, C., (2002). *GIROD - Glued-in Rods for Timber Structures*, Swedish National Testing and Research Institute, Borås, Sweden, August 2002.

Bhat, P., Azim, R., Popovski, M., Tannert, T. (2014). *Experimental and Numerical Investigation of Novel Steel-Timber-Hybrid Systems.* World Conference on Timber Engineering. August, Quebec City, Canada.

Borzouie, J., MacRea, G.A., Chase, J.G., Rodgers, G.W., Clifton, G.C. (2015). *Experimental Studies on Cyclic Performance of Column Base Weak Axis Aligned Asymmetric Friction Connection*. Journal of Constructional Steel Research. 112, 252-262.

Bouchair, A., Racher, P., Bocquet, J.F. (2007). *Analysis of Dowelled Timber to Timber Moment-Resisting Joints.* Materials and Structures, 40, 1127-1141

British Standards Institution, BSI (1979). *Commentary on Corrosion at Bimetallic Contacts and its Alleviation*. Standard PD 6484:1979, Londan, UK.

Broughton, J. G., Hutchinson, A. R., (2001). *Pull-out Behaviour of Steel Rods Bonded into Timber.* Materials and Structures, March, 34, 100-109.

Bruneau, M., Uang, C.-M., Whittaker, A., (1998). *Ductile Design of Steel Structures*, McGraw-Hill, New York, USA.

Buchanan, A. H., Barber, D. J. (1996). *Fire Resistance of Epoxied Steel Rods in Glulam Timber.* New Zealand Timber Design Journal, Issue 2, Volume 5, 12-18.

Butterworth, J. (2000). *Ductile Concentrically Braced Frames Using Slotted Bolted Joints*. Journal of the Structural Engineering Society New Zealand (SESOC Journal), April, 13, 1, 39-48.

Camino G., Tartaglione G., Frache A., Maniferti C., Costa G., (2005). *Thermal and Combustion Behaviour of Layered Silicate-Epoxy Nanocomposites.* Polymer Degradation and Stability. 90, 354-362.

Canadian Standards Association (CSA), (2009). CAN/CSA S16-09 *Limit States Design of Steel Structures*, Canada, 2010.

Canadian Standards Association (CSA), (2009). CAN/CSA O86-09 *Wood Design Manual*, Canada, 2010.

Choi, H., Erochko, J., Christopoulos, C., & Tremblay, R. (2008). *Comparison of the Seismic Response of Steel Buildings Incorporating Self-Centering Energy-Dissipative Braces, Buckling Restrained Braces and Moment-Resisting Frames.* (Report No. 05-2008). Toronto: Dept. of Civ. Eng. University of Toronto, ON.

Christopoulos, C. and Filiatrault, A. (2006). *Principles of Passive Supplemental Damping and Seismic Isolation*. IUSS Press, Pavia, Italy.

Christopoulos, C., Tremblay, R., Kim, H.-J., Lacerte, M. (2008). *Self-Centering Energy Dissipative Bracing System for the Seismic Resistance of Structures: Development and Validation*. Journal of Structural Engineering, ASCE, January, 96-107

Connolly, T., Mettem, C. J., (2003). *Development of Eurocode-Type Design Rules for Axially Loaded Boned-in Rods*, Low Intrusion Conservation Systems for Timber Structures (LICONS), October.

Decker, L., Ellis, P., Fleming, K., Campbell, K. et al. (1995). *The January 17, 1995 Kobe Earthquake an EQE Summary Report*. EQE International Ltd. United Kingdom, April.

Della Corte, G., D'Aniello, M., Landolfo, R., Mazzolani, F. M., (2011). *Review of Steel Buckling-Restrained Braces*. Steel Construction 4, No.2.

Deng, J. X. (1997). *Strength of Epoxy Bonded Steel Connections in Glue Laminated Timber.* Research Report 97/4. Department of Civil Engineering, University of Canterbury, Christchurch, New Zealand.

Di Sarno, L., Elnashai, A.S., (2005). *Innovative Strategies for Retrofitting of Steel and Composite Structures.* Progress in Structural Engineering and Materials. Journal, May, Issue 7, 115-135.

Erochko, J., Christopoulos, C., Tremblay, R., Choi, H. (2011). *Residual Drift Response of SMRFs and BRB Frames in Steel Buildings Designed According to ASCE 7-05.* Journal of Structural Engineers, ASCE. Vol. 137, No. 5, May, 589-599.

Erochko, J. (2013). *Improvements to the Design and Use of Post-Tensioned Self-Centering Energy-Dissipative (SCED) Braces*. PhD Thesis, Department of Civil Engineering, University of Toronto. Canada.

Faghani, P. (2013). *Experimental and Numerical Investigations of Pull-Out Strength of Timber Joints with Glued-in Rods.* MASc. Thesis. Department of Civil Engineering, the University of British Columbia, Vancouver, Canada, August.

Faherty, K. F., Williamson, T. G. (1995). *Wood Engineering and Construction Handbook.* Second Edition. McGraw-Hill, Inc. New York, USA.

Fahnestock, L. A, Ricles, J. M, Sause, R. (2007). *Experimental evaluation of a large-scale buckling-restrained braced frame*. Journal of Structural Engineering, 133, pp. 1205-1214.

Federal Emergency Management Agency [FEMA] (2009). *Quantification of Building Seismic Performance Factors*, FEMA-P695. Washington DC: Federal Emergency Management Agency.

Filiatrault, A., Tremblay, R., Christopoulos, C., Folz, B., Pettinga, D. (2013). *Elements of Earthquake Engineering and Structural Dynamics*. Third Edition. Presses Internationales Polytechnique.

Canada.

Fisher, J. M., Kloiber, L. A. (2006). Steel Design Guide, Base Plate and Anchor Rod Design, Second Edition. American Institute of Steel Constuction, Inc. May, USA.

FPInnovations. 2010. *Cross Laminated Timber Handbook*. FPInnovations, SP-528E, Canada.

Frangi A, Fontana M (2010). *Fire Safety of Multistorey Timber Buildings*. Structures Build 163(4):213-226

Gardelle, V., Morlier, P. (2006). *Geometric Parameters which affect the short term resistance of an axially loaded glued-in rod.* RILEM, Materials and Structures, 40, 127-138.

Gilbert, C., Gohlich, R., Erochko, J. (2015). *Nonlinear Dynamic Analysis on Innovative High R-Factor Hybrid Timber-Steel Buildings.* The 11th Canadian Conference on Earthquake Engineering. July, Victoria, British Columbia.

Gohlich, R (2016). *Development of an Innovative Hybrid Timber-Steel Moment-Resisting Frame for Seismic-Resistant Heavy Timber Structures*. (Master's Thesis) Dept. of Civ. and Env. Eng., Carleton University, Ottawa, Canada.

Grigorian, C (1994). *Energy Dissipation with Slotted Bolted Connections*. University of California, Berkeley. PhD Thesis, Engineering, Civil Engineering.

Gustafsson, P.J. (2002). *Tests and Test Results on Mechanical Properties of Adhesive Bond lines.* European Cooperation in Science and Technology (COST), Action E13. Wood Adhesion and Glued Products, State of the Art Report, Edited by Johansson, C.-J., Pizzi, T., Van Leemput, M., August.

Gustafsson, P.J., Serrano, E., Aicher, S., Johansson, C.-J. (2001). *A Strength Design Equation for Glued-in Rods.* Proceedings International RILEM Symposium on Joints in Timber Structures. (Edited by: Aicher, S. and Reinhardt, H.-W.). PRO 22, RILEM Publications, 323-332.

Harris, S. (2004). *Fire Resistance of Epoxy-Grouted Steel Rod Connections in Laminated Veneer Lumber (LVL).* M.Eng. Thesis, University of Canterbury, New Zealand, June.

Harrison, K.W. (1986). *Application of epoxy and acrylic adhesives*. Proceedings of the international conference on structural adhesives in engineering. Institution of Mechanical Engineers publication 1986-6.

Hergenrother P, Thompson C, Smith J, Connell J, Hinkley J, Lyon R, Moulton R. (2005). *Flame Retardant Aircraft Epoxy Resin Containing Phosphorous.* Ploymer,46, 5012-5024.

International Standard ISO 16670 (2003). Timber Structures - Joints made with mechanical fasteners Quasi-static reversed-cyclic test methods. Switzerland, ISO 16670:2003.

Jamil, M., Quenneville, P., Clifton, C. (2012). *Low-Damage Moment Resisting Timber Multi-Storey Buildings.* World Conference on Timber Engineering, July, Auckland, New Zealand.

Jeng R, Shau S, Lin J, Su W, Chiu Y. (2002). Flame Retardant Epoxy Polymers Based on all Phosphorous-containing Components. European Polymer Journal. 38, 683-693.

Jensen, J. L., Koizumi, A., Sasaki, T., Tamura, Y., Iijima, Y. (2001). *Axially Loaded Glued-in Hardwood Dowels.* Wood Science and Technology, 35, 73-83.

Kassner, M.E., Geantil, P., Levine, L.E., Larson, B.C. (2009). *Back stress, the Bauschinger Effect and Cyclic Deformation*. Material Science Form, Vol 604-605, 39-51.

Kemmsies M. (1999). *Comparison of pull-out strengths of 12 adhesives for glued-in rods for timber structures.* Swedish National Testing and Research Institute, Building Technology. BorÃěs, Sweden.

Kim, H.-J., Christopoulos, C., Tremblay, R. (2004). *Experimental Characterization of Boltstressed Non-asbestos Organic (NAO) Material-to-steel Interfaces*. (Report). Department of Civil Engineering, University of Toronto, Canada.

Kiwelu, H. (2013). *Finite Element Models of Effects of Moisture on Bolt Embedment and Connection*

Properties of Glulam. PHD Thesis, Graduate Academic Unit of Forestry and Environmental Management, University of New Brunswick, Canada.

Komatsu, K., Mori, T., Kitamori, A., Araki, Y. (2014). *Evaluation on Dynamic Performance of Glulam Frame Structure Composed of Slotted Bolted Connection System.* World Conference on Timber Engineering. August, Quebec City, Canada.

Kulak, G.L., Grondin, G. Y. (2010). *Limit States Design in Structural Steel*. Ninth Edition. Canadian Institute of Steel Construction (CISC). October, Canada.

Lam, F., Li, Z., He, M., Li, M. (2015). *Comparison of Tow Reliability Assessment Methods for the Seismic Performance of Timber-Steel Hybrid Structures*. 12th International Conference on Applications of Statistics and Probability in Civil Engineering, ICASP12. Vancouver, Canada.

Lartigau, J., Coureau, J-L, Moral, S., Galimard, P., Maurin, E. (2012). *Effect of Temperature on the Load Bearing Capacity of Glued-in Rods.* 10th World conference on Timber Engineering, July, Auckland, New Zealand.

Latour, M., Piluso, V., Rizzano, G. (2013). *Experimental Behaviour of Friction T-Stub Beam-to-Column Joints Under Cyclic Loads*. Steel Construction, 6, 1, 11-18.

Latour, M., Piluso, V., Rizzano, G. (2014). *Experimental Analysis on Friction Materials for Supplemental Damping Devices.* Construction and Building Materials, 65, 159-176.

Liu L-Y., Wei W.-L., Hsu K.-Y., Ho W.-H. (2004). *Thermal Stability of Epoxy-Silica Hybrid Materials by Thermogravimetric Analysis.* Thermochimica Acta. 412, 139-147.

McCormick, J., Aburano, H., Ikenaga, M., & Nakashima, M. (2008). *Permissible Residual Drift Deformation Levels for Building Structures Considering Both Safety and Human Elements.* 14th World Conference on Earthquake Engineering. (Paper No. 05-06-0071). Beijing, China.

McKenna, F., Fenves, G. L., Scott, M. H., Jeremic, B. (2000). *Open System for Earthquake Engineering Simulation (OpenSees) [Computer Software]*. Pacific Earthquake Engineering Research Center,

University of California, Berkeley, CA. Available from: http://opensees.berkeley.edu/.

Michaud, D., & Léger, P. (2012). Ground Motions Selection and Scaling for Nonlinear Dynamic Analysis of Structures Located in Eastern North America. *Canadian Journal of Civil Engineering*. 41, 232-244.

Milke, J. (2002). *Analytical Methods for Determining Fire Resistance of Steel Members.* In P. DiNenno, SFPE Handbook of Fire Protection Engineering (pp. 4:209-4:238). Quincy, Massachusetts: Society of Fire Protection Engineers.

Mitchell, D., Tremblay, R., Karacabeyli, E., Paultre, P., Saatcioglu, M., Anderson, D. L. (2003). *Seismic Force Modification Factors for the Proposed 2005 Edition of the National Building Code of Canada*. Canadian Journal of Civil Engineering, 30, 308-327.

Motosaka, M., Mitsuji, K. (2012). *Building Damage during the 2011 off the Pacific coast of Tohoku Earthquake*. Soils and Foundations, December, 52, 929-944.

Nakatani, M., Mori, T., Komatsu, K. (2012). *Development of Cross Embedded Joint Using Lagscrew-bolt.* World Conference on Timber Engineering. July, Auckland, New Zealand.

National Research Council of Canada [NRC](2010). *National Building Code of Canada (NBCC)*. Ottawa, ON. Canada.

Nordic Engineered Wood. (2013a). *Nordic X-Lam Slabs*. Nordic Wood Structures Technical Note S23. Nordic Structures.

Nordic Engineered Wood. (2013b). *Design Properties, Nordic Lam*. Nordic Wood Structures Technical Note S01. Nordic Structures.

Normenausschuss Bauwesen (DIN 1052) (2004) *Design of Timber Structures - General Rules and Rules for Buildings*. DIN 1052, August.

Oberg, E., Jones, F. D., Horton, H. L., Ryffel, H. H., McCauley, C. J. (Ed.), Heald, R. M. (Ed.),

Hussain, M. I. (Ed.). (2008). *Machinery's Handbook (28th Ed.).* New York: Industrial Press.

Popovski, M (2000). *Seismic Performance of Braced Timber Frames*. PhD Thesis, Department of Civil Engineering, The University of British Columbia. Vancouver Canada.

Popovski, M., Prion, H. G. L., Karacabeyli, E. (2002). *Seismic Performance of Connections in Heavy Timber Construction*. Canadian Journal of Civil Engineering, October, 29, 389-399.

Popovski, M., Prion, H. G. L., Karacabeyli, E. (2003). *Shake Table Tests on Single-Storey Braced Timber Frames.* Canadian Journal of Civil Engineering, December, 30, 6, 1089-1100.

Popovski, M., Karacabeyli, E. (2008). *Force Modification Factors and Capacity Design Procedures for Braced Timber Frames.* 14th World conference on Earthquake Engineering, October, Beijing, China.

Reghunadhan Nair, C.P., Bindu, R.L., Ninan, K.N., (2001). *Thermal Characteristics of Addition-Cure Phenolic Resins.* Polymer Degradation and Stability, 73, 251-257

Riberholt H (1988). *Glued bolts in glulam-proposals for CIB code.* Paper 21-7-2. In: Proceedings of the 21st conference of CIB-W18, Parksville, Canada.

Rossignon, A., Espion, B. (2008). *Experimental Assessment of the Pull-out Strength of Single Rods Boned in Glulam Parallel to the Grain.* Springer-Verlag, Holz Roh Werkst, August, 66, 419-432.

Ruiz-Garcia, J. & Miranda, E (2006). *Evaluation of Residual Drift Demands in Regula Multi-Storey Frames for Performance-Based Seismic Assessment*. Earthquake Engng. Struct. Dyn. 35, 1609-1629

Sabelli, R., Roeder, C. W., Hajjar, J. F. (2013). *Seismic Design of Steel Special Concentrically Braced Frame Systems*. NEHRP Seismic Design Technical Brief No. 8, produced by the NEHRP Consultants Joint Venture, a partnership of the Applied Technology Council and the Consortium of Universities for Research in Earthquake Engineering, for the National Institute of Standards and Technology, Gaithersburg, MD, NIST GCR 13-917-24.

Serrano, E. (2001a). *Glued-in Rods for Timber Structures - a 3D Model and Finite Element Parameter Study.* International Journal of Adhesion & Adhesives, 21, 115-127.

Serrano, E. (2001b). *Glued-in Rods for Timber Structures - An Experimental Study of Softening Behaviour.* Materials and Structures, May, 34, 228-234.

Sika Canada Inc. (2014). *Sika Anchorfix-3001 High-Strength, High-Load Capacity and Low-VOC, Pure Epoxy Anchoring Adhesive with Extended Working Time*. Product Data Sheet Ed. 12-2014/v1.

Smith, I., Asiz, A., Snow, M., Chui, I. (2006). *Possible Canadian / ISO approach to deriving design values from test data*. In: Proceedings of the meeting 39 of Working Commission W18 - Timber Structures, CIB, Florence, Italy, August.

Steiger, R., Serrano, E., Stepinac, M., Raijcic, V., O'Neill, C., McPolin, D., Widmann, R. (2015). *Strength of Timber Structures with Glued-in Rods.* Construction and Building Materials, 1-16.

Stepinac, M., Hunger, F., Tomasi, R., Serrano, E., Rajcic, V., van de Kuilen, J-W. (2013). *Comparison of Design Rules for Glued-in Rods and Design Rule Proposal for Implementation in European Standards*. CIB-W18, Paper 46-7-10. August, Vancouver, Canada.

Tannert, T., Faghani, P., Zhu, H., Garekani, A., Vallee, T. (2014). *Timber Joints with Glued-in FRP Rods*. 14th World Conference on Timber Engineering, Quebec, August, PAP351.

Thakur, A., Nemat-Nasser, S., Vecchio, K. S. (1996). *Dynamic Bauschinger Effect*. Acta mater, 44, 7, 2797-2807.

Tjahyadi, A. (2002). *Slotted-Bolted Friction Damper as a Seismic Energy Dissipator in a Braced Timber Frame.* MSc. Thesis, Wood Science and Civil Engineering, Oregon State University, March, Oregon, USA

Tlustochowicz, G., Serrano, E., Steiger, R. (2011). *State-of-the-Art Review on Timber Connections with Glued-in Steel Rods*. Materials and Structures, 41, 997-1020.

Tremblay R., (1993). *Seismic Behaviour and Design of Friction Concentrically Braced Frame for Steel Buildings*. PHD Thesis, Department of Civil Engineering, University of British Columbia. Canada.

Tremblay, R., Poncet, L., Bolduc, P., Neville, R. and Devall, R. (2004). *Testing and Design on Buckling Restrained Braces for Canadian Application*. 13th World Conference on Earthquake Engineering, Vancounver, BC, August, PN 2893.

Townsend, P.K: (1990). *Steel Dowels Epoxy Bonded in Glue Laminated Timber.* Research Report 90-11, Department of Civil Engineering, University of Canterbury, Christchurch, New Zealand.

Tsai, K.C., Hsiao, P.C. (2008). *Pseudo-dynamic Test of a Full-Scale CFT/BRB Frame - Part II: Seismic Performance of Buckling-Restrained Braces and Connections.* Earthquake Engineering and Structural Dynamics, 37, 1099-1115.

Welch, D., Sullivan, T., & Filiatrault, A. (2014). *Equivalent Structural Damping of Drift-Sensitive Nonstructural Building Components*. 10th U.S. National Conference on Earthquake Engineering. Anchorage, Alaska.

Widmann, R., Steiger, R., Gehri, E. (2007). *Pull-out Strength of Axially Loaded Steel Rods Bounded in Glulam Perpendicular to the Grain*. Materials and Structures, 40, 827-838.

Yeboah, D., Taylor, S., McPolin, D., Gilfillan, R. (2013). *Pull-out Behaviour of Axially Loaded Basalt Fibre Reinforced Polymer (BFRP) Rods Bonded Perpendicular to Grain of Glulam Elements*. Construction and Building Materials, 38, 962-969.

Appendix A: Fabrication Drawings

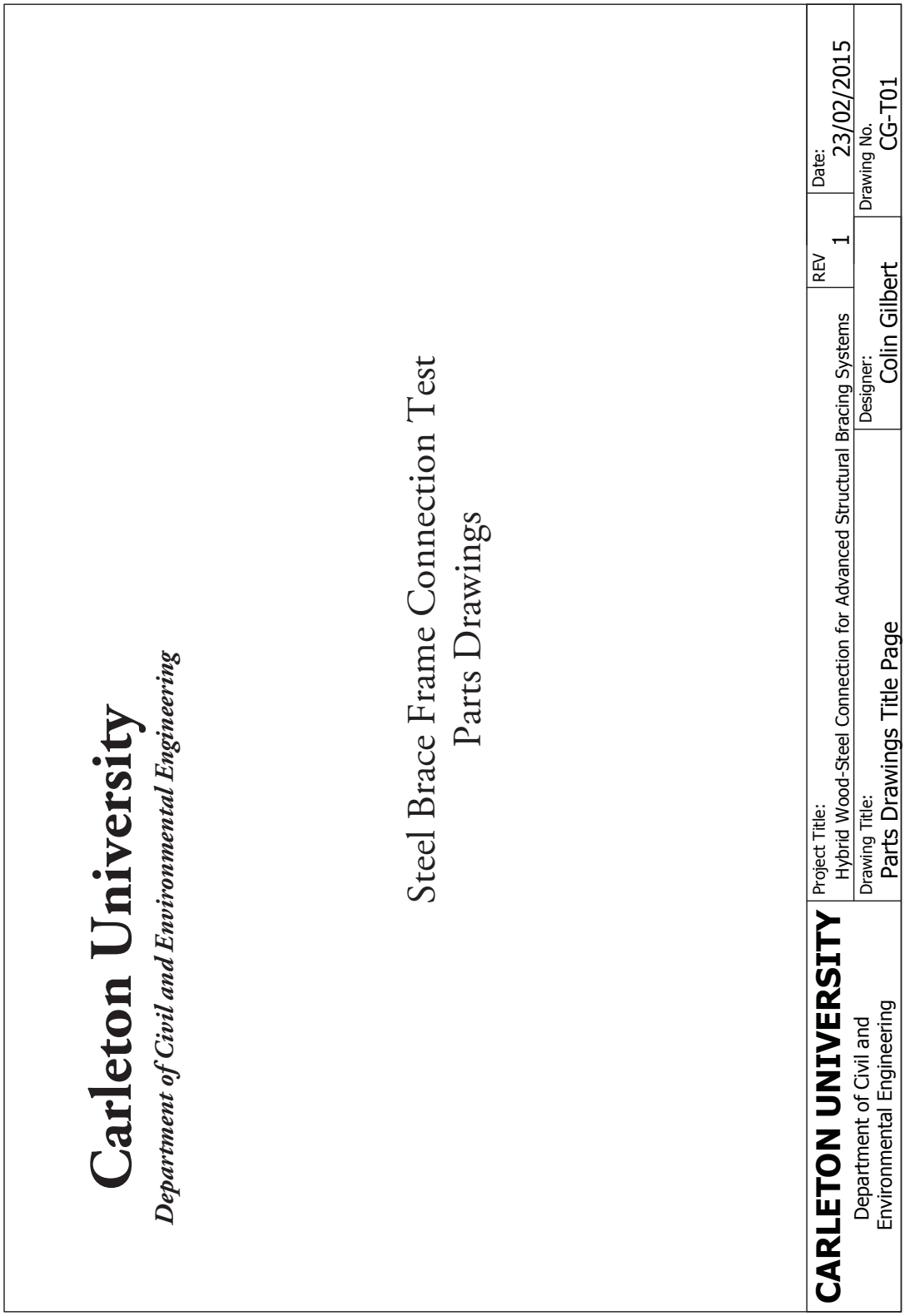
Carleton University
Department of Civil and Environmental Engineering
Steel Brace Frame Connection Test
Parts Drawings
CARLETON UNIVERSITY
Department of Civil and
Environmental Engineering
Project Title:
Hybrid Wood-Steel Connection for Advanced Structural Bracing Systems
REV
1
Date:
23/02/2015
Drawing Title:
Parts Drawings Title Page
Designer:
Colin Gilbert
Drawing No.
CG-T01

Bill of Materials (by Part)

Part #	Description	Page	Weight (kg)	# Required	Total Weight (kg)	Material
IBC-P1	Column Web Section	PT1A	22.6	1	22.6	300W
IBC-P2	Beam End Bearing Plate	PT1A	6.3	1	6.3	300W
IBC-P3	Beam Bearing Plate	PT1B	12.6	1	12.6	300W
IBC-P4	Column Bearing Plate	PT1B	36.6	1	36.6	300W
IBC-P5	Beam Stiffener	PT1C	8.3	2	16.6	300W
IBC-P6	Upper Gusset Bearing Plate	PT1C	8.6	1	8.6	300W
IBC-P7	End Plate	PT1C	16.7	1	16.7	300W
IBC-P8	Pin Connection Inner Plate	PT1D	3.7	1	3.7	300W
IBC-P9	Pin Connection Angle Side Plate	PT1D	7.2	2	14.4	350W
IBC-P10	Top Plate	PT1D	29.5	1	29.5	300W
IBC-P11	Inner Stiffener Plate	PT1E	16.5	1	16.5	300W
IBC-P12	Gusset Plate	PT1F	1.9	2	3.8	300W
IBC-P13	Beam Web Section	PT1F	4.8	1	4.8	300W
BSC-P1	Column Base Plate	PT2A	332.2	1	332.2	300W
BSC-P2	Support Column	PT2A	113.3	1	113.3	350W
BSC-P3	T-Section Back Plate	PT2B	20.4	1	20.4	300W
BSC-P4	T-Section Middle Plate	PT2B	15.3	1	15.3	300W
BSC-P5	Column Stiffener	PT2C	29.9	1	29.9	300W
ICC-P1	Column Bearing Plate	PT3A	36.6	1	36.6	300W
ICC-P2	Pin Connection Bearing Plate	PT3A	36.7	1	36.7	300W
ICC-P3	Side Plate	PT3B	8.7	2	17.4	300W
ICC-P4	Web Plate	PT3B	8.6	1	8.6	300W
IBPC-P1	Actuator Bearing Plate	PT4A	21.8	1	21.8	300W
IBPC-P2	Beam Bearing Plate	PT4A	17.7	1	17.7	300W
IBPC-P3	Flange Plate	PT4B	5	2	10	300W
IBPC-P4	Web Plate	PT4B	4.5	1	4.5	300W
FDD-P1	Friction Device Side Plate	PT5A	16.4	2	32.8	300W
FDD-P2	Friction Device Center Plate	PT5B	19.8	1	19.8	300W
FDD-P3	Washer Side Plates	PT5B	6.7	2	13.4	300W
FDD-P4	Friction Damper Support Tube	PT5C	18.8	1	18.8	350W
FDD-P5	Gusset Plate Side Plates	PT5E	3.4	2	6.8	300W
FDD-P6	HSS End Plate	PT5E	2.2	1	2.2	300W
FDD-P7	Stainless Steel Friction Surface	PT5F	1.9	2	3.8	300W
	TOTAL				**950.9**	

CARLETON UNIVERSITY Department of Civil and Environmental Engineering	Project Title: Hybrid Wood-Steel Connection for Advanced Structural Bracing Systems	REV 1	Date: 23/02/2015
	Drawing Title: Bill of Materials (By Part)	Designer: Colin Gilbert	Drawing No. CG-BM1

Bill of Material
(by Type)

Type	Length	Area	Gross Weight (kg)	Material
Steel Section				
W310x143 (W12x96)	0.8m (2.6 ft)		113.3	350W
HSS 152x102x13 (HSS 6 x 4 x 0.5)	0.752 (2.47 ft)		18.8	350W
L 152x102x19 (L 6 x 4 x 0.75)	0.2 (0.656 ft)		14.4	350W
Steel Plate				
1 1/2"		1.12 sqm (12.06 sqft)	335	300W
1 3/8"		0.058 sqm (0.624 sqft)	15.9	300W
1 1/4"		0.705 sqm (7.59 sqft)	175.72	300W
1"		0.248 sqm (2.66 sqft)	49.35	300W
5/8"		0.869 sqm (9.36 sqft)	116.7	300W
1/2"		0.667 sqm (7.18 sqft)	104	300W
1/4"		0.0394 sqm (0.424 sqft)	3.93	300W
3/8"		0.152 sqm (1.63 sqft)	14.1	300W
Stainless Steel				
1/8"		0.0912 sqm (0.982 sqft)	4.52	Stainless Steel
	TOTAL		965.72	

CARLETON UNIVERSITY Department of Civil and Environmental Engineering	Project Title: Hybrid Wood-Steel Connection for Advanced Structural Bracing Systems		REV 1	Date: 23/02/2015
	Drawing Title: Bill of Materials (By Type)	Designer: Colin Gilbert		Drawing No. CG-BM2

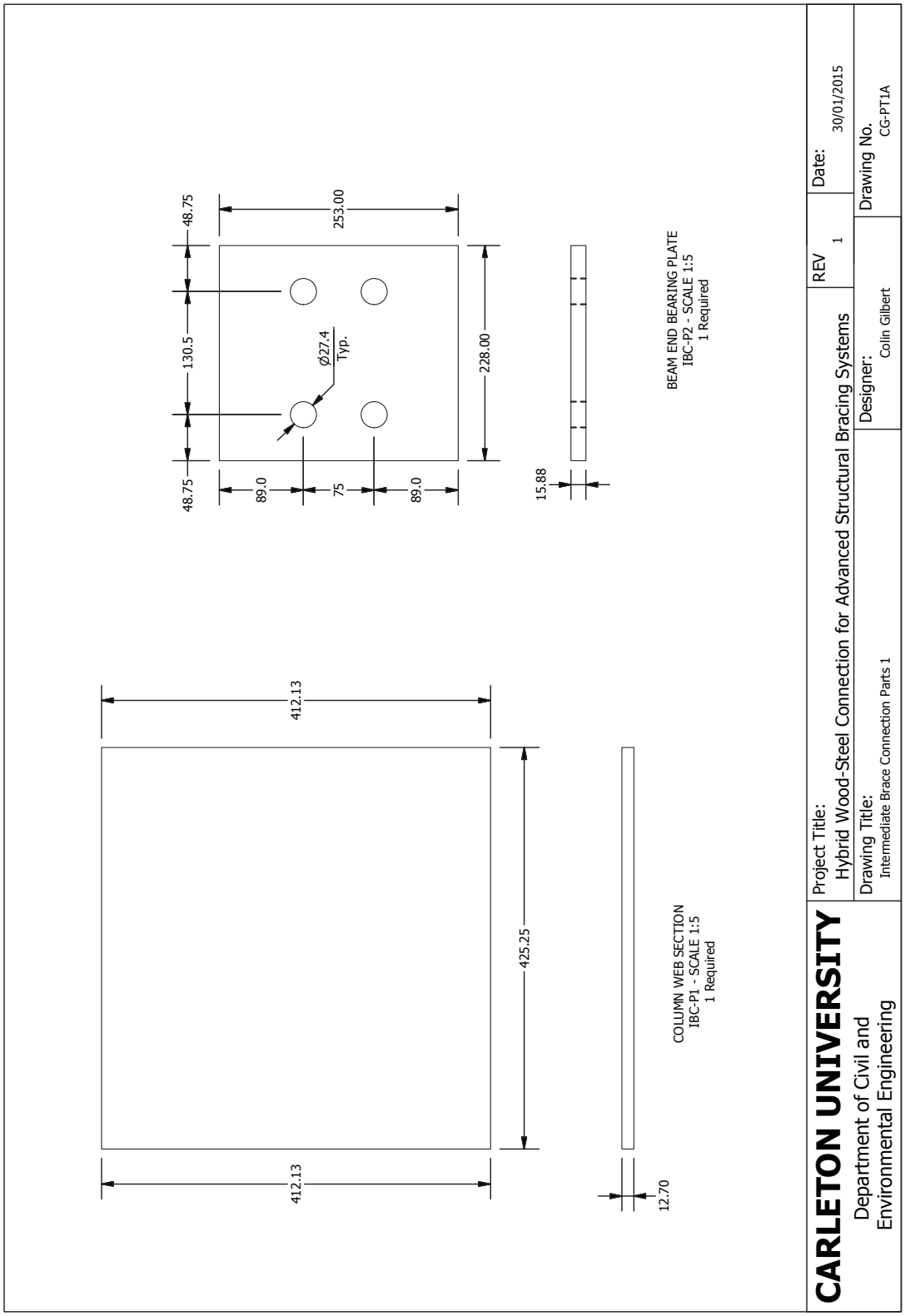
48.75
130.5
48.75
253.00
Ø27.4
Typ.
228.00
89.0
75
89.0
15.88
BEAM END BEARING PLATE
IBC-P2 - SCALE 1:5
1 Required
412.13
412.13
425.25
12.70
COLUMN WEB SECTION
IBC-P1 - SCALE 1:5
1 Required
CARLETON UNIVERSITY
Department of Civil and
Environmental Engineering
Project Title:
Hybrid Wood-Steel Connection for Advanced Structural Bracing Systems
Drawing Title:
Intermediate Brace Connection Parts 1
Designer:
Colin Gilbert
REV
1
Date:
30/01/2015
Drawing No.
CG-PT1A

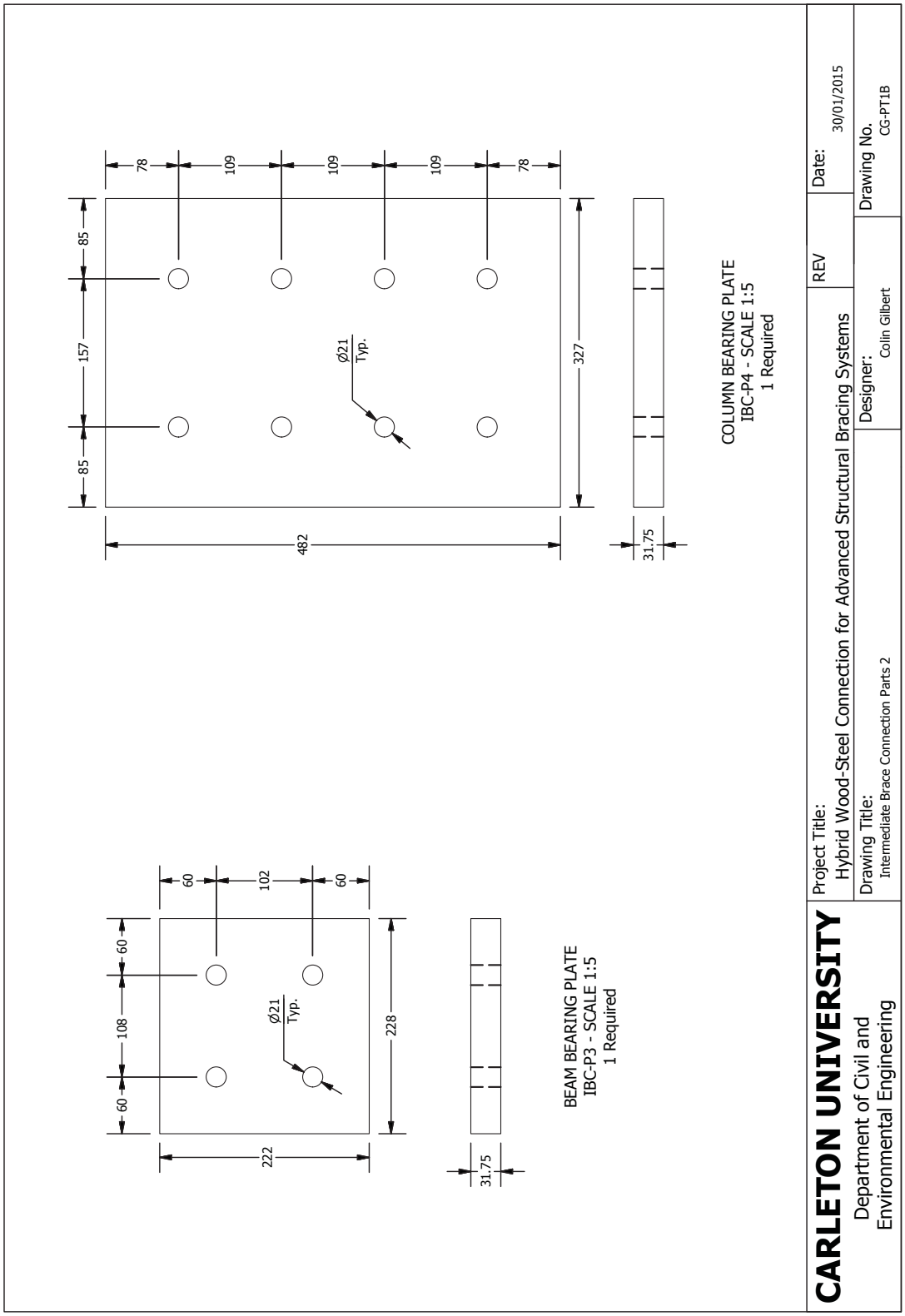
78
109
109
109
78
85
157
85
Ø21
Typ.
327
482
31.75
COLUMN BEARING PLATE
IBC-P4 - SCALE 1:5
1 Required
60
102
60
60
108
60
Ø21
Typ.
228
222
31.75
BEAM BEARING PLATE
IBC-P3 - SCALE 1:5
1 Required
CARLETON UNIVERSITY
Department of Civil and
Environmental Engineering
Project Title:
Hybrid Wood-Steel Connection for Advanced Structural Bracing Systems
Drawing Title:
Intermediate Brace Connection Parts 2
Designer:
Colin Gilbert
REV
Date:
30/01/2015
Drawing No.
CG-PT1B

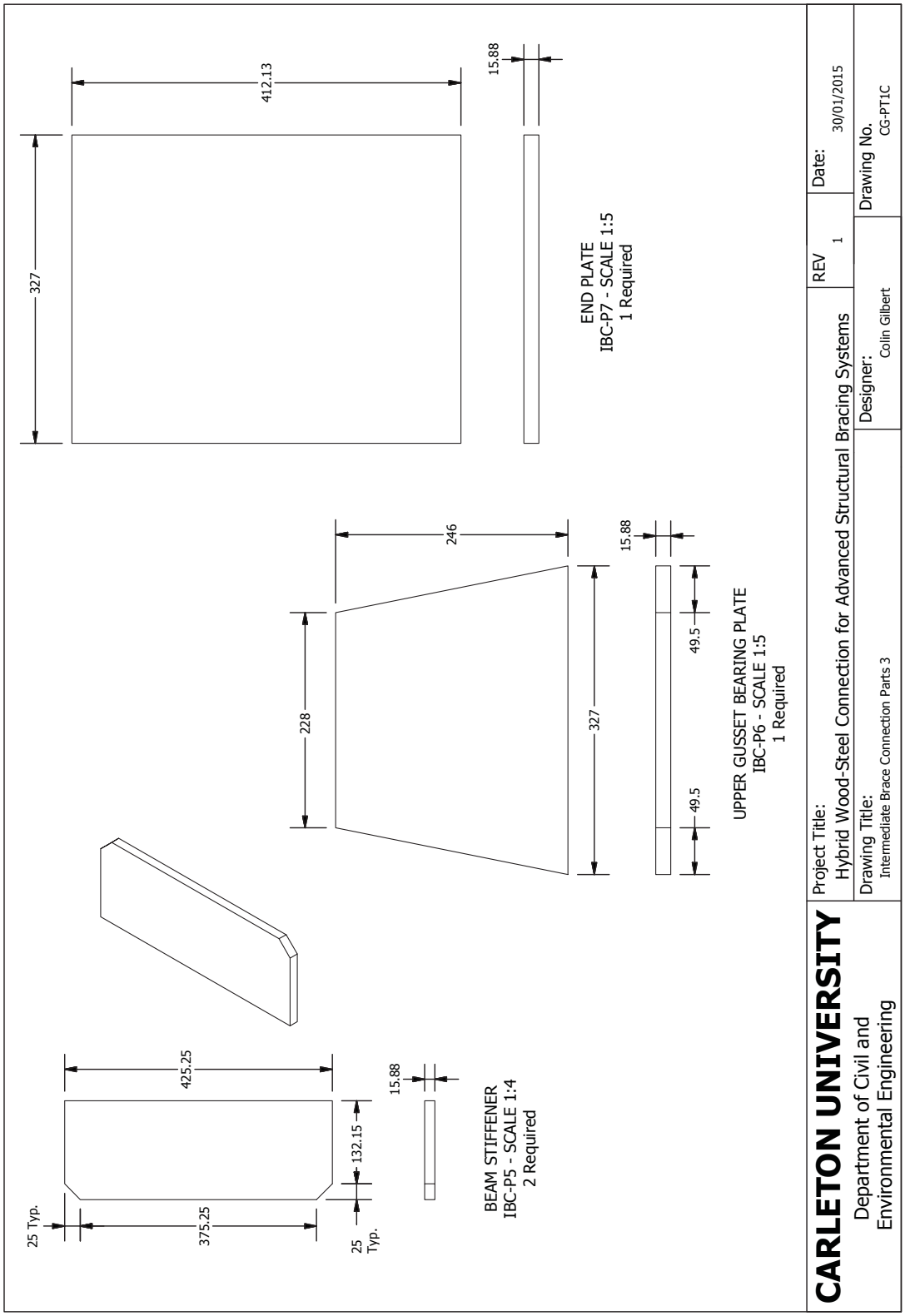
327
412.13
15.88
END PLATE
IBC-P7 - SCALE 1:5
1 Required
228
246
327
15.88
49.5
49.5
UPPER GUSSET BEARING PLATE
IBC-P6 - SCALE 1:5
1 Required
25 Typ.
375.25
425.25
132.15
25 Typ.
15.88
BEAM STIFFENER
IBC-P5 - SCALE 1:4
2 Required
CARLETON UNIVERSITY
Department of Civil and Environmental Engineering
Project Title:
Hybrid Wood-Steel Connection for Advanced Structural Bracing Systems
Drawing Title:
Intermediate Brace Connection Parts 3
Designer:
Colin Gilbert
REV
1
Date:
30/01/2015
Drawing No.
CG-PT1C

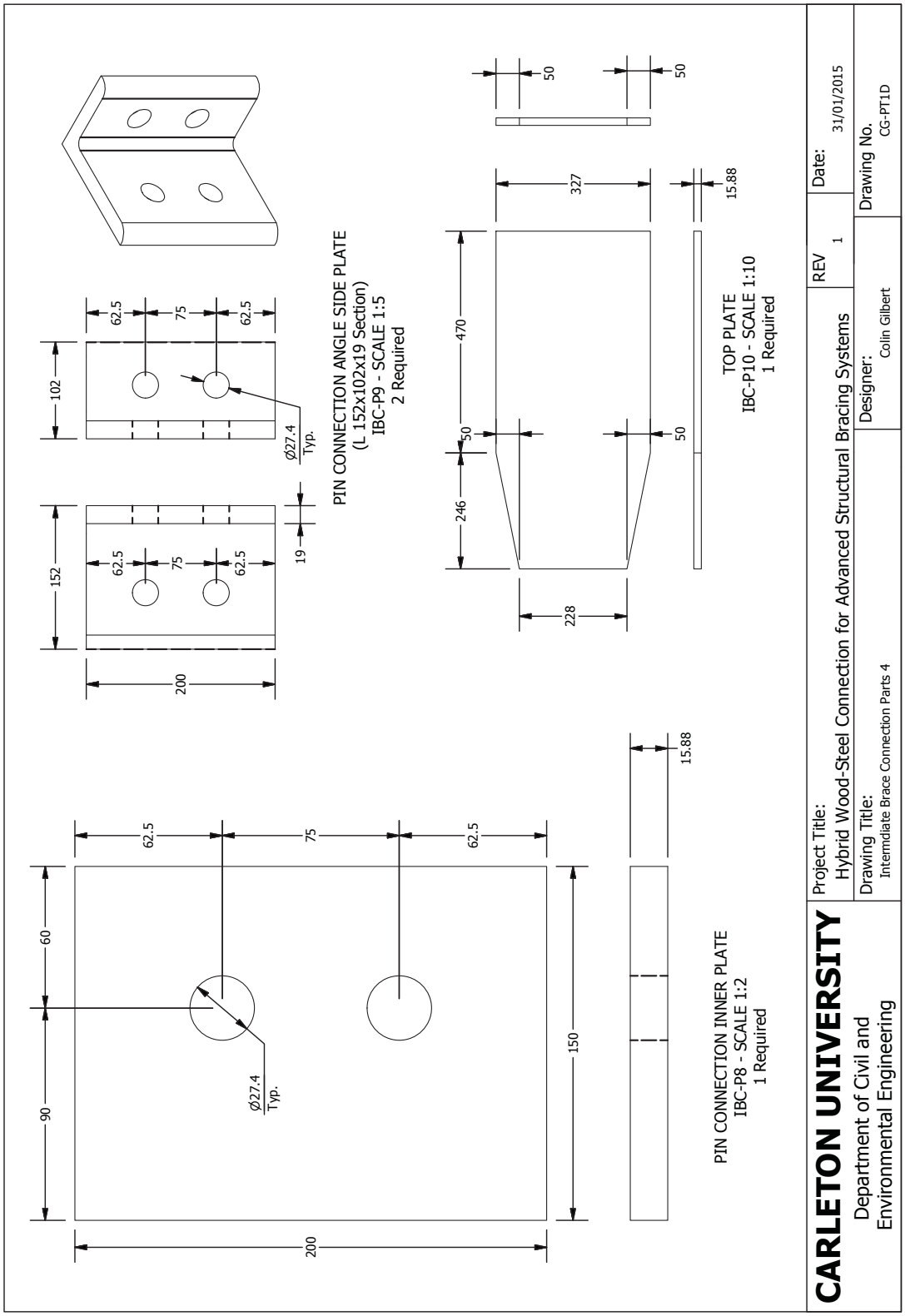
PIN CONNECTION ANGLE SIDE PLATE
(L 152x102x19 Section)
IBC-P9 - SCALE 1:5
2 Required
TOP PLATE
IBC-P10 - SCALE 1:10
1 Required
PIN CONNECTION INNER PLATE
IBC-P8 - SCALE 1:2
1 Required
Ø27.4
Typ.
CARLETON UNIVERSITY
Department of Civil and
Environmental Engineering
Project Title:
Hybrid Wood-Steel Connection for Advanced Structural Bracing Systems
Drawing Title:
Intermediate Brace Connection Parts 4
Designer:
Colin Gilbert
REV
1
Date:
31/01/2015
Drawing No.
CG-PT1D

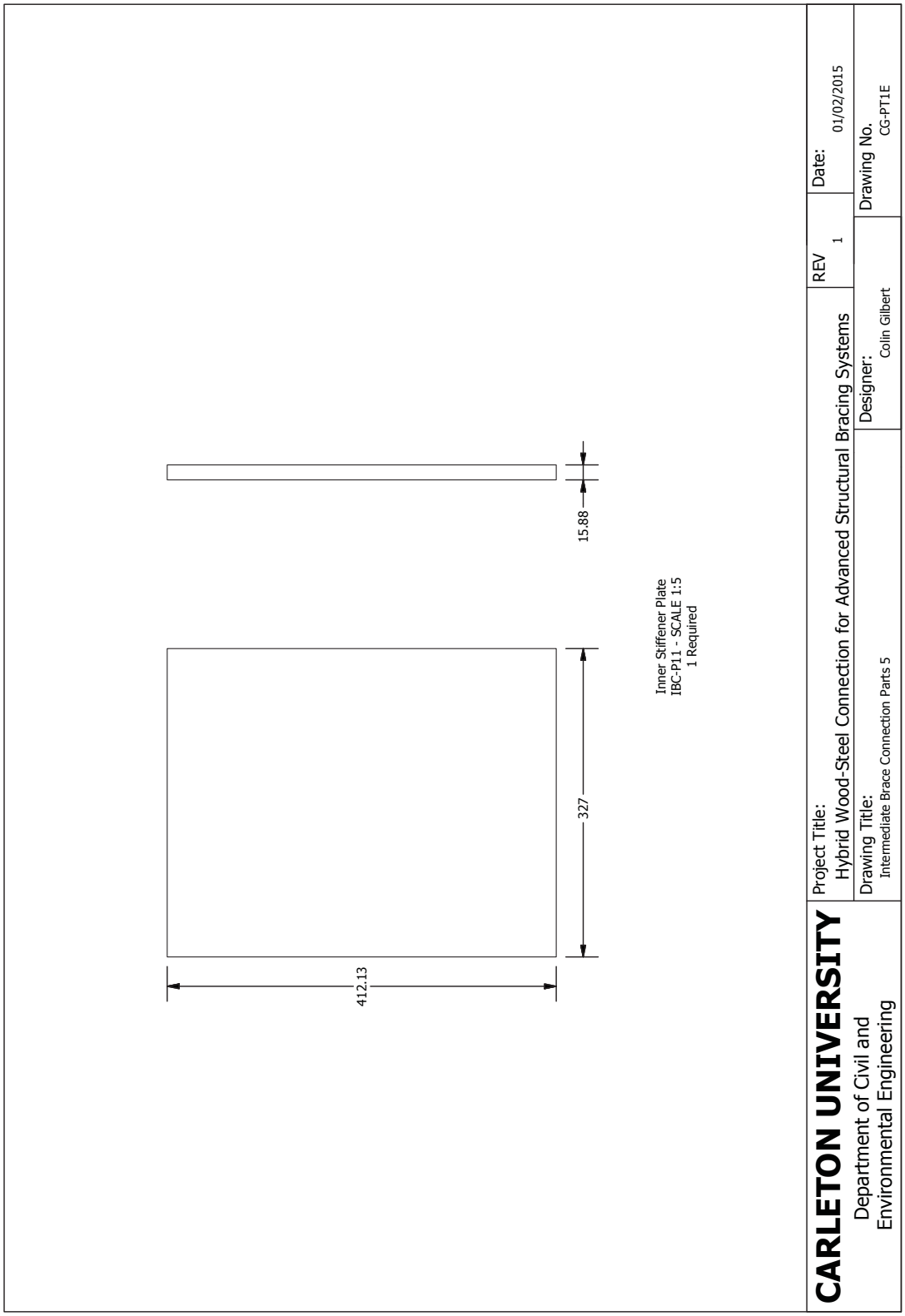
15.88
327
412.13
Inner Stiffener Plate
IBC-P11 - SCALE 1:5
1 Required
CARLETON UNIVERSITY
Department of Civil and
Environmental Engineering
Project Title:
Hybrid Wood-Steel Connection for Advanced Structural Bracing Systems
Drawing Title:
Intermediate Brace Connection Parts 5
Designer:
Colin Gilbert
REV
1
Date:
01/02/2015
Drawing No.
CG-PT1E

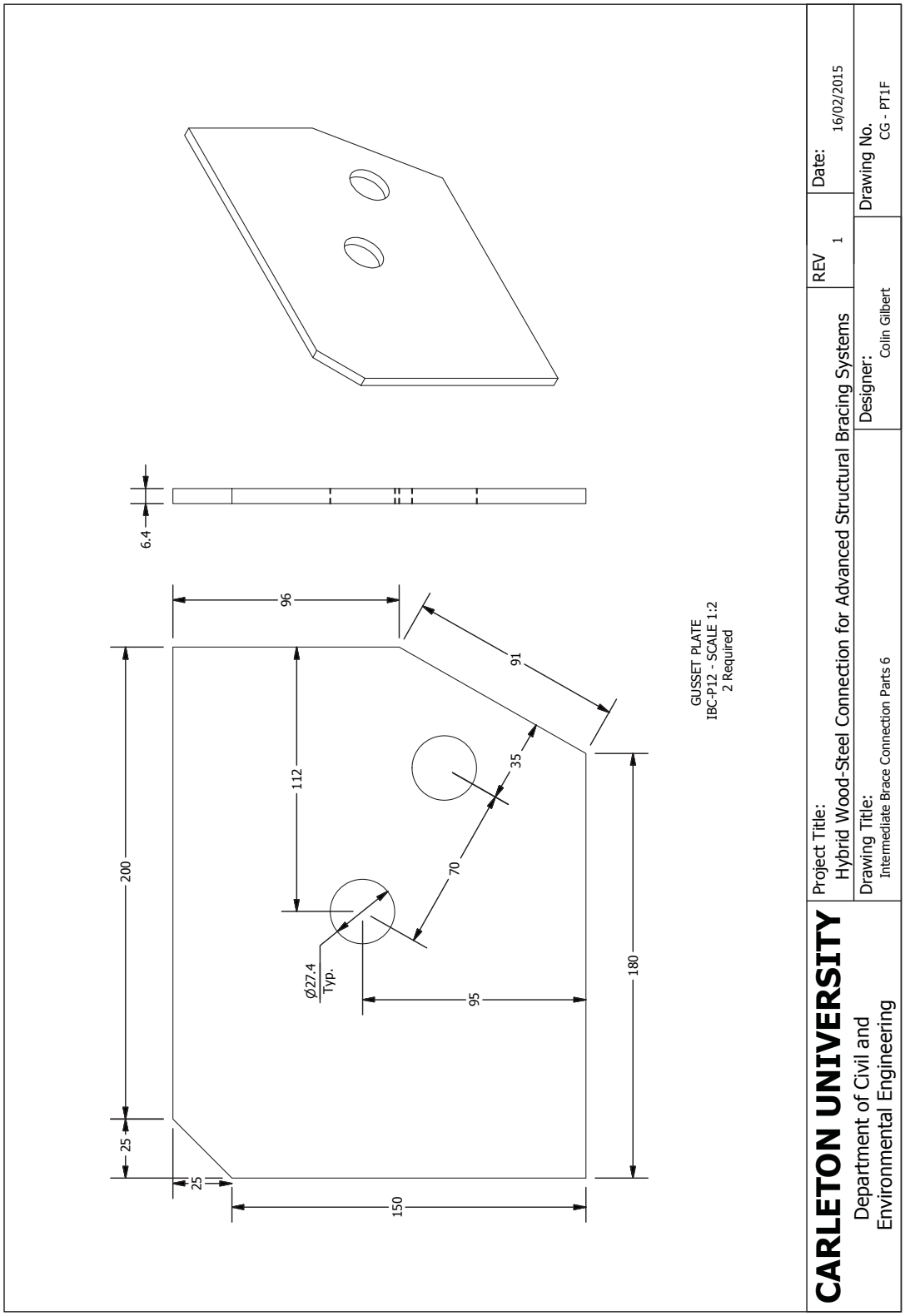
6.4
96
91
200
112
35
70
Ø27.4
Typ.
95
180
25
25
150
GUSSET PLATE
IBC-P12 - SCALE 1:2
2 Required
CARLETON UNIVERSITY
Department of Civil and
Environmental Engineering
Project Title:
Hybrid Wood-Steel Connection for Advanced Structural Bracing Systems
Drawing Title:
Intermediate Brace Connection Parts 6
Designer:
Colin Gilbert
REV
1
Date:
16/02/2015
Drawing No.
CG - PT1F

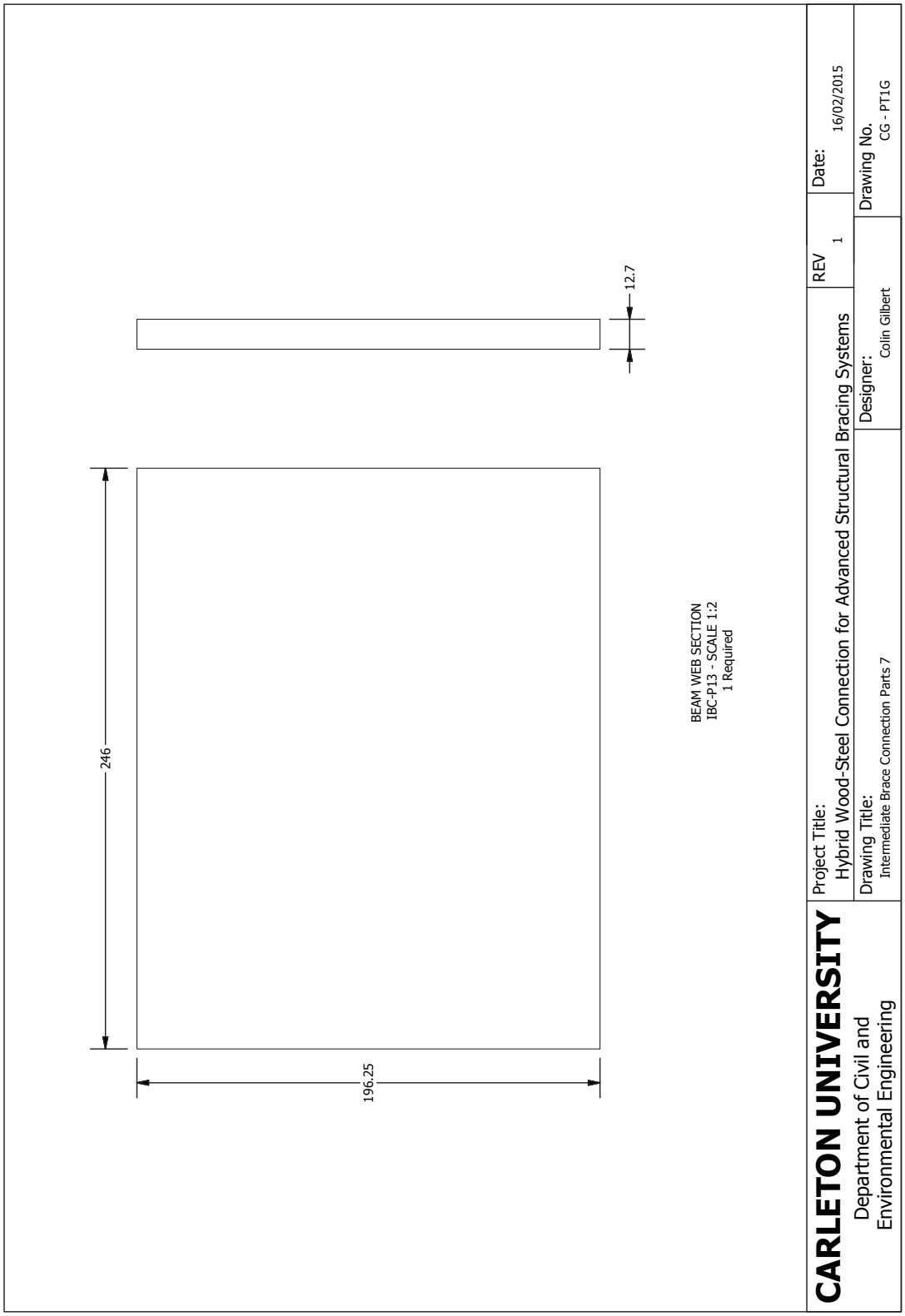
246
196.25
12.7
BEAM WEB SECTION
IBC-P13 - SCALE 1:2
1 Required
CARLETON UNIVERSITY
Department of Civil and
Environmental Engineering
Project Title:
Hybrid Wood-Steel Connection for Advanced Structural Bracing Systems
Drawing Title:
Intermediate Brace Connection Parts 7
Designer:
Colin Gilbert
REV
1
Date:
16/02/2015
Drawing No.
CG - PT1G

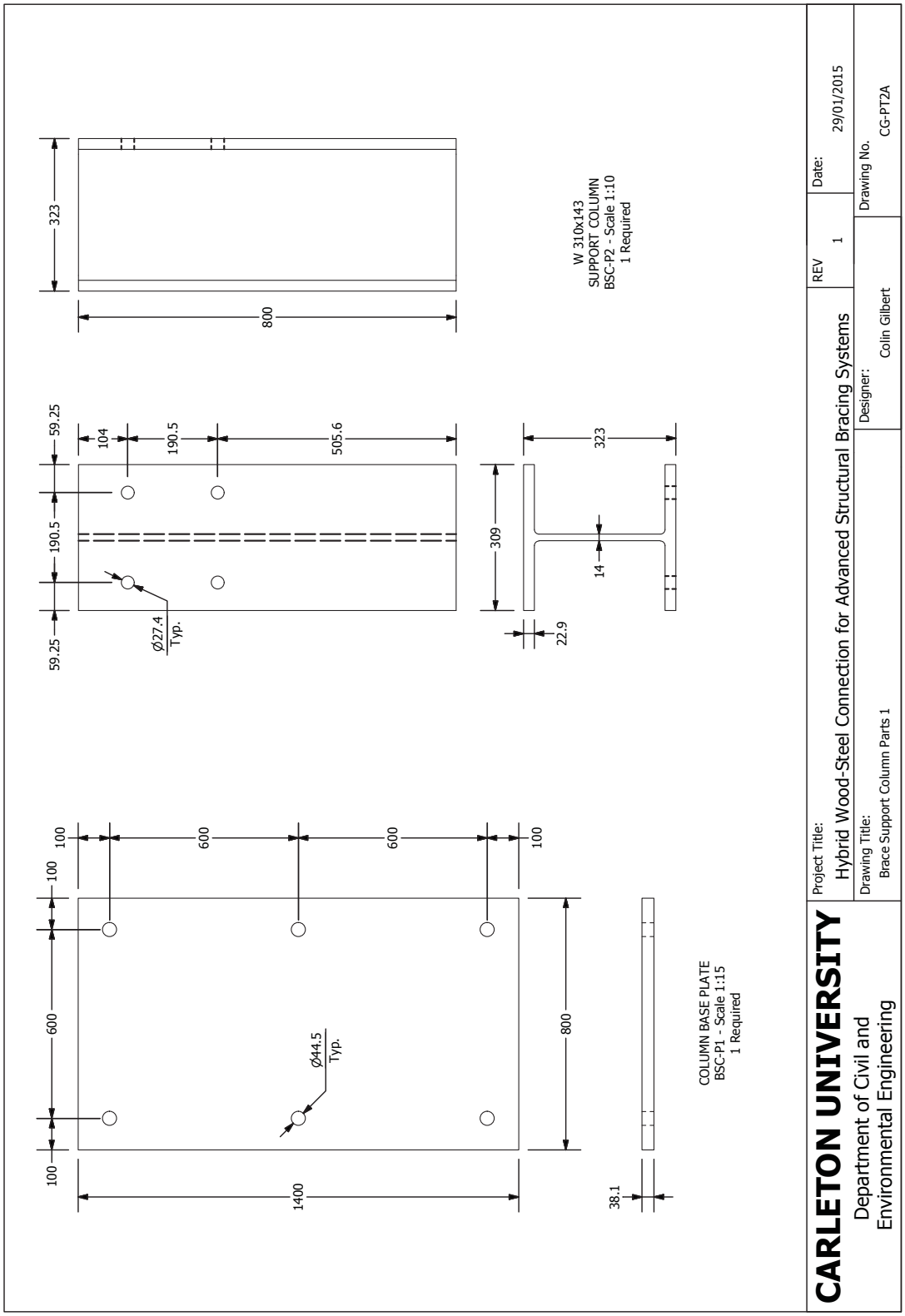
323
800
W 310x143
SUPPORT COLUMN
BSC-P2 - Scale 1:10
1 Required
59.25
104
190.5
505.6
190.5
59.25
Ø27.4
Typ.
309
323
14
22.9
100
600
600
100
100
600
100
Ø44.5
Typ.
800
1400
38.1
COLUMN BASE PLATE
BSC-P1 - Scale 1:15
1 Required
CARLETON UNIVERSITY
Department of Civil and
Environmental Engineering
Project Title:
Hybrid Wood-Steel Connection for Advanced Structural Bracing Systems
Drawing Title:
Brace Support Column Parts 1
Designer:
Colin Gilbert
REV
1
Date:
29/01/2015
Drawing No.
CG-PT2A

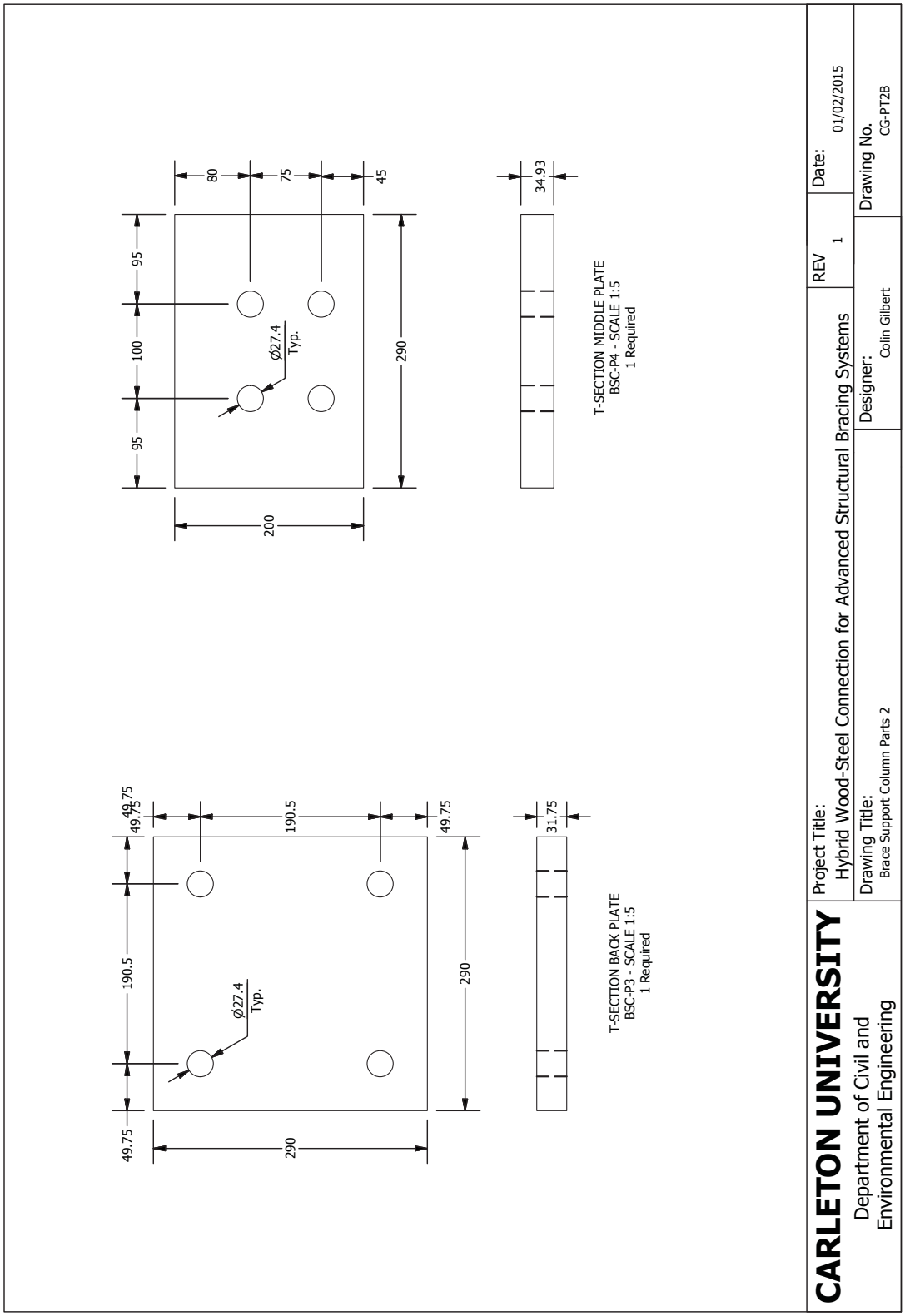
80
75
45
95
100
95
Ø27.4
Typ.
200
290
34.93
T-SECTION MIDDLE PLATE
BSC-P4 - SCALE 1:5
1 Required
49.75
49.75
190.5
49.75
190.5
Ø27.4
Typ.
49.75
290
290
31.75
T-SECTION BACK PLATE
BSC-P3 - SCALE 1:5
1 Required
CARLETON UNIVERSITY
Department of Civil and
Environmental Engineering
Project Title:
Hybrid Wood-Steel Connection for Advanced Structural Bracing Systems
REV
1
Date:
01/02/2015
Drawing Title:
Brace Support Column Parts 2
Designer:
Colin Gilbert
Drawing No.
CG-PT2B

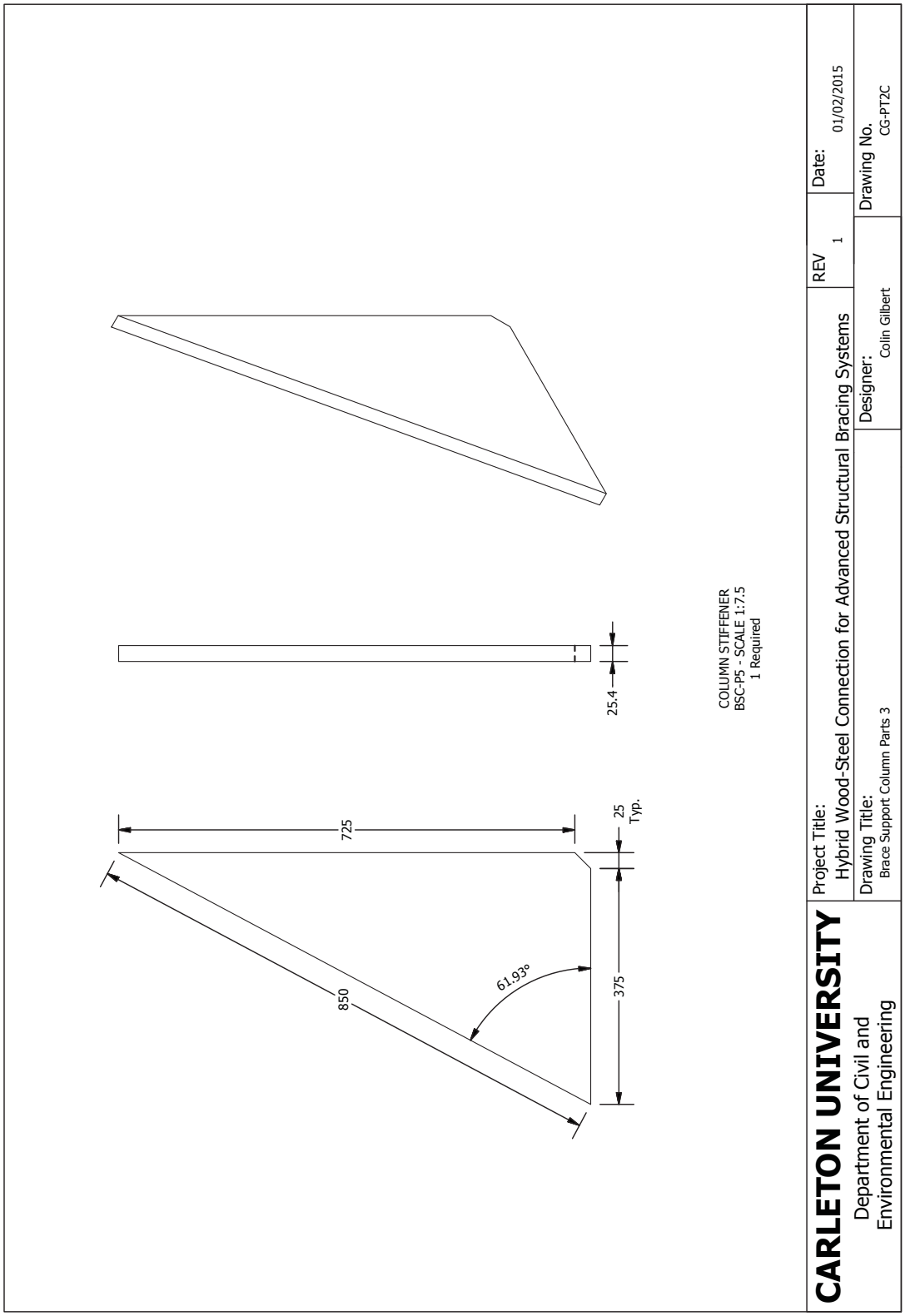
850
725
61.93°
375
25
Typ.
25.4
COLUMN STIFFENER
BSC-P5 - SCALE 1:7.5
1 Required
CARLETON UNIVERSITY
Department of Civil and
Environmental Engineering
Project Title:
Hybrid Wood-Steel Connection for Advanced Structural Bracing Systems
Drawing Title:
Brace Support Column Parts 3
Designer:
Colin Gilbert
REV
1
Date:
01/02/2015
Drawing No.
CG-PT2C

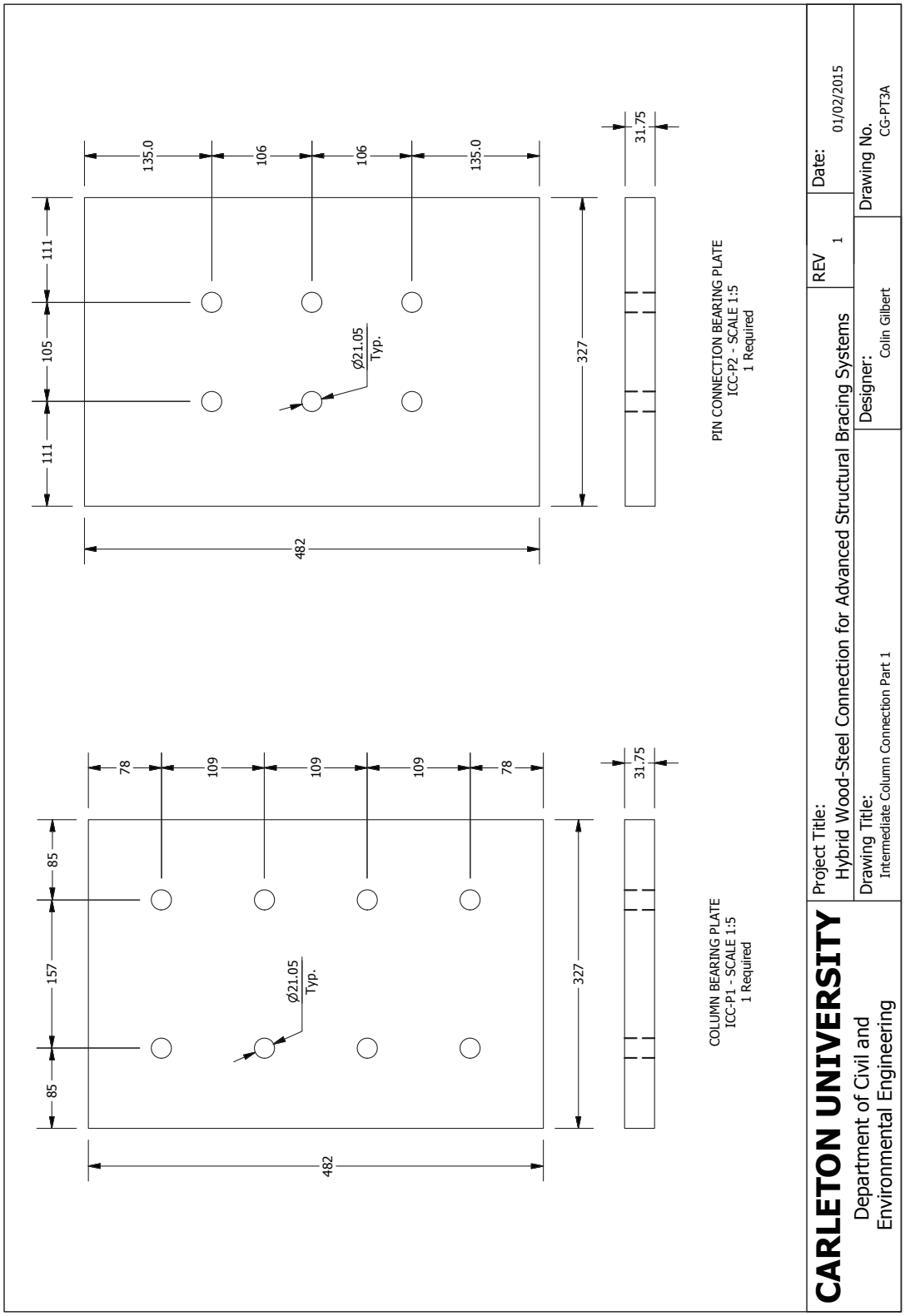
135.0
106
106
135.0
111
105
111
Ø21.05
Typ.
482
327
31.75
PIN CONNECTION BEARING PLATE
ICC-P2 - SCALE 1:5
1 Required
78
109
109
109
78
85
157
85
Ø21.05
Typ.
482
327
31.75
COLUMN BEARING PLATE
ICC-P1 - SCALE 1:5
1 Required
CARLETON UNIVERSITY
Department of Civil and
Environmental Engineering
Project Title:
Hybrid Wood-Steel Connection for Advanced Structural Bracing Systems
REV
1
Date:
01/02/2015
Drawing Title:
Intermediate Column Connection Part 1
Designer:
Colin Gilbert
Drawing No.
CG-PT3A

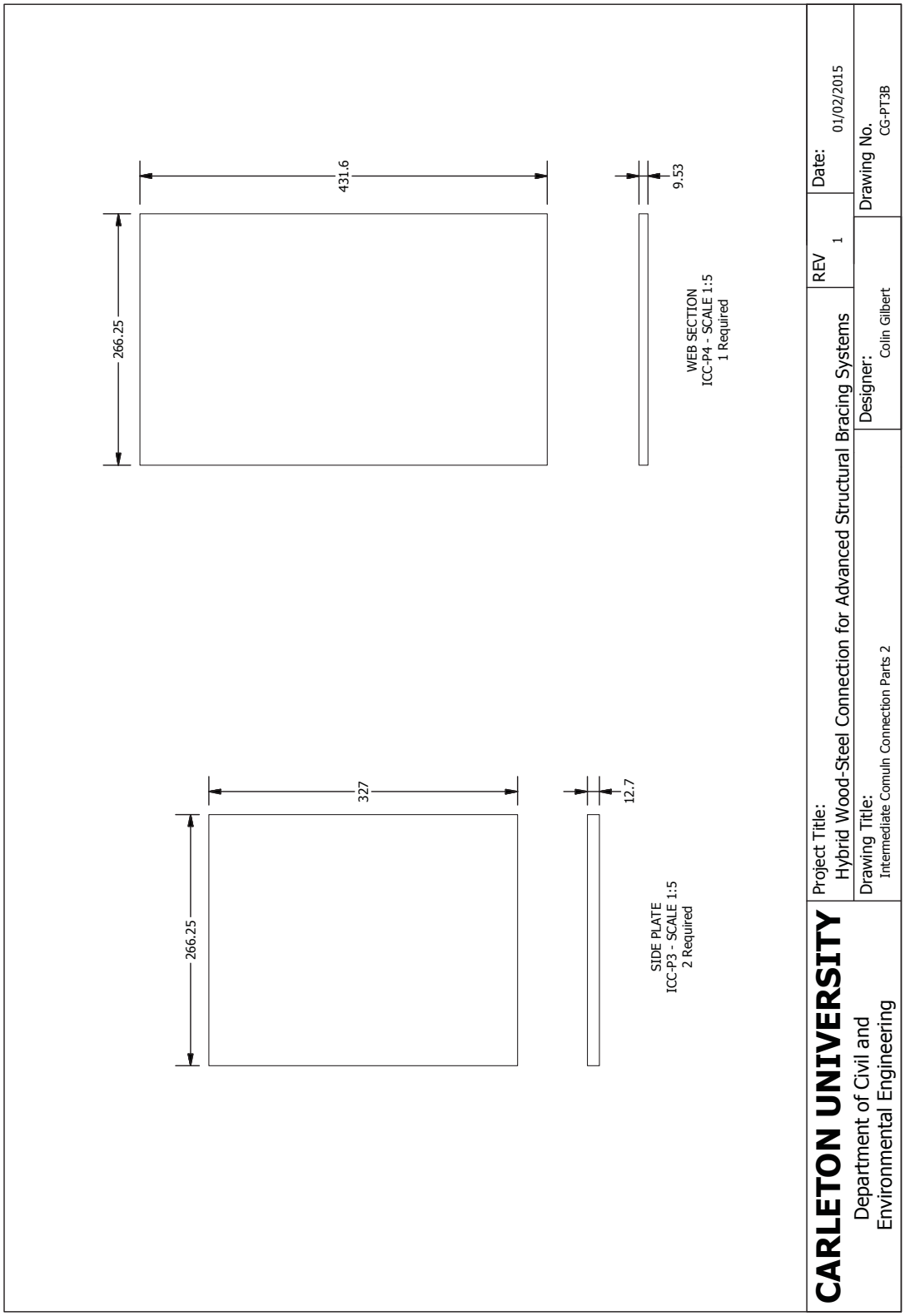
266.25
431.6
9.53
WEB SECTION
ICC-P4 - SCALE 1:5
1 Required
266.25
327
12.7
SIDE PLATE
ICC-P3 - SCALE 1:5
2 Required
CARLETON UNIVERSITY
Department of Civil and
Environmental Engineering
Project Title:
Hybrid Wood-Steel Connection for Advanced Structural Bracing Systems
Drawing Title:
Intermediate Comuln Connection Parts 2
Designer:
Colin Gilbert
REV
1
Date:
01/02/2015
Drawing No.
CG-PT3B

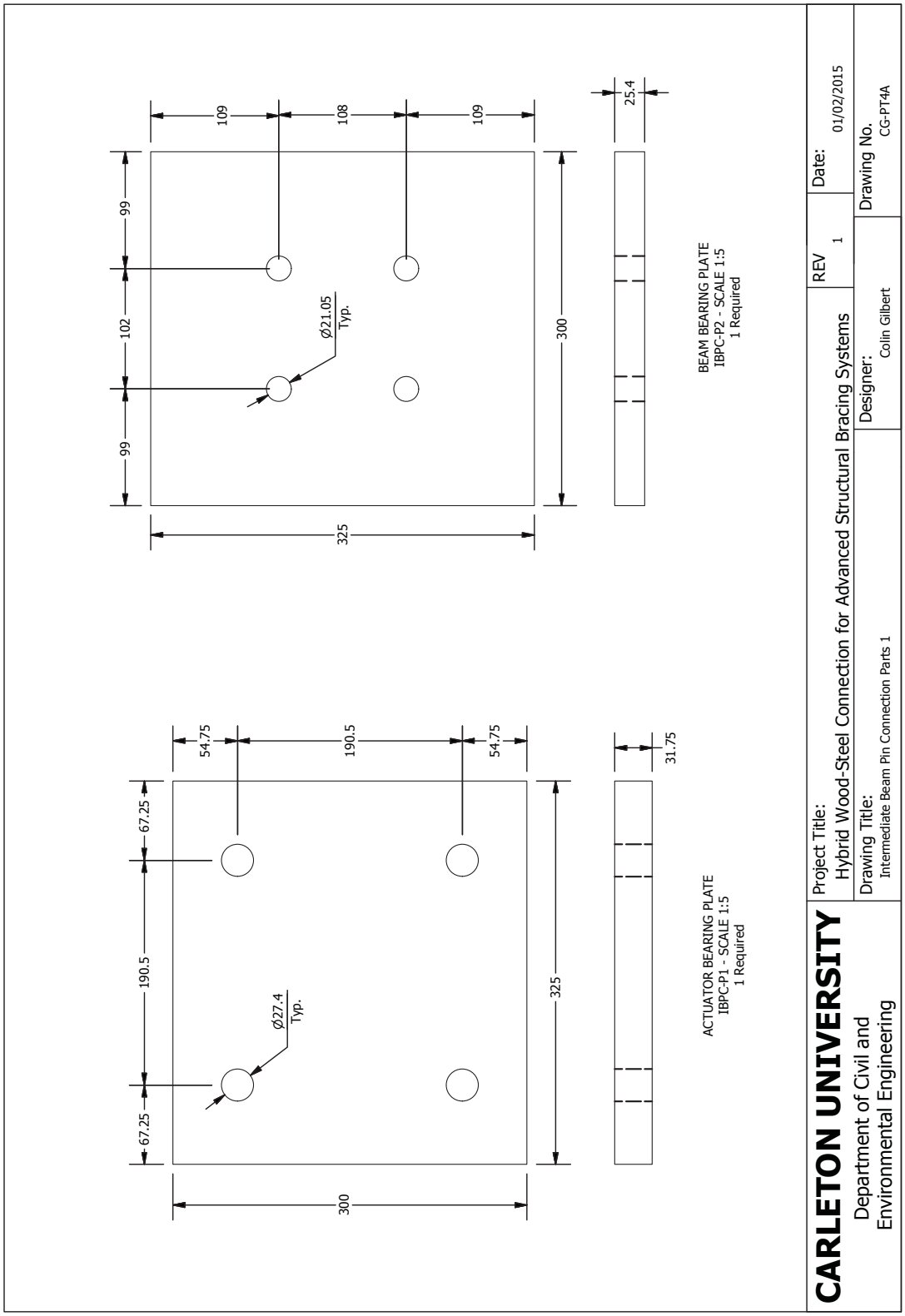
109
108
109
25.4
99
102
99
Ø21.05
Typ.
300
325
BEAM BEARING PLATE
IBPC-P2 - SCALE 1:5
1 Required
54.75
190.5
54.75
31.75
67.25
190.5
67.25
Ø27.4
Typ.
325
300
ACTUATOR BEARING PLATE
IBPC-P1 - SCALE 1:5
1 Required
CARLETON UNIVERSITY
Department of Civil and
Environmental Engineering
Project Title:
Hybrid Wood-Steel Connection for Advanced Structural Bracing Systems
REV
1
Date:
01/02/2015
Drawing Title:
Intermediate Beam Pin Connection Parts 1
Designer:
Colin Gilbert
Drawing No.
CG-PT4A

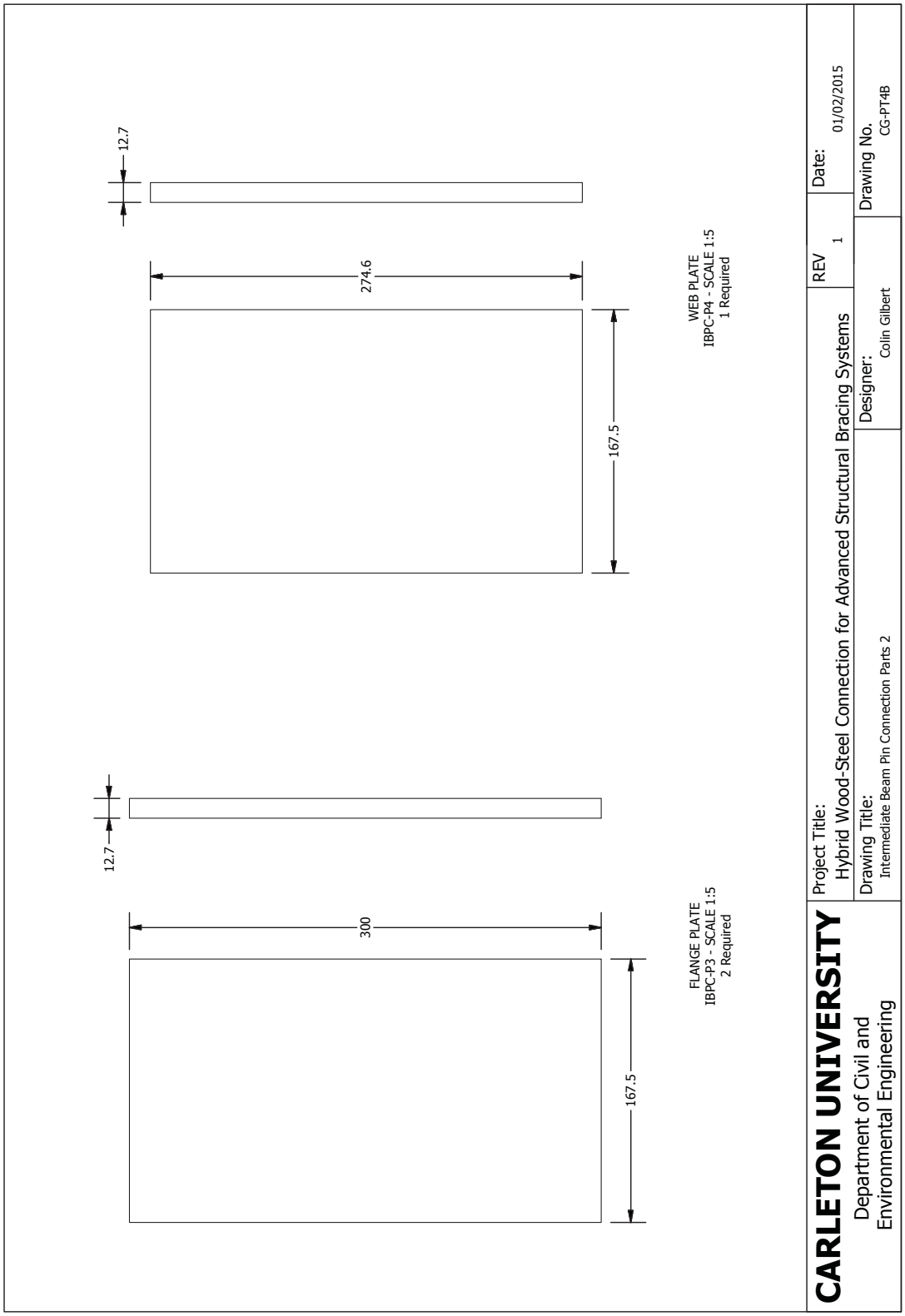
12.7
274.6
167.5
WEB PLATE
IBPC-P4 - SCALE 1:5
1 Required
12.7
300
167.5
FLANGE PLATE
IBPC-P3 - SCALE 1:5
2 Required
CARLETON UNIVERSITY
Department of Civil and
Environmental Engineering
Project Title:
Hybrid Wood-Steel Connection for Advanced Structural Bracing Systems
Drawing Title:
Intermediate Beam Pin Connection Parts 2
Designer:
Colin Gilbert
REV
1
Date:
01/02/2015
Drawing No.
CG-PT4B

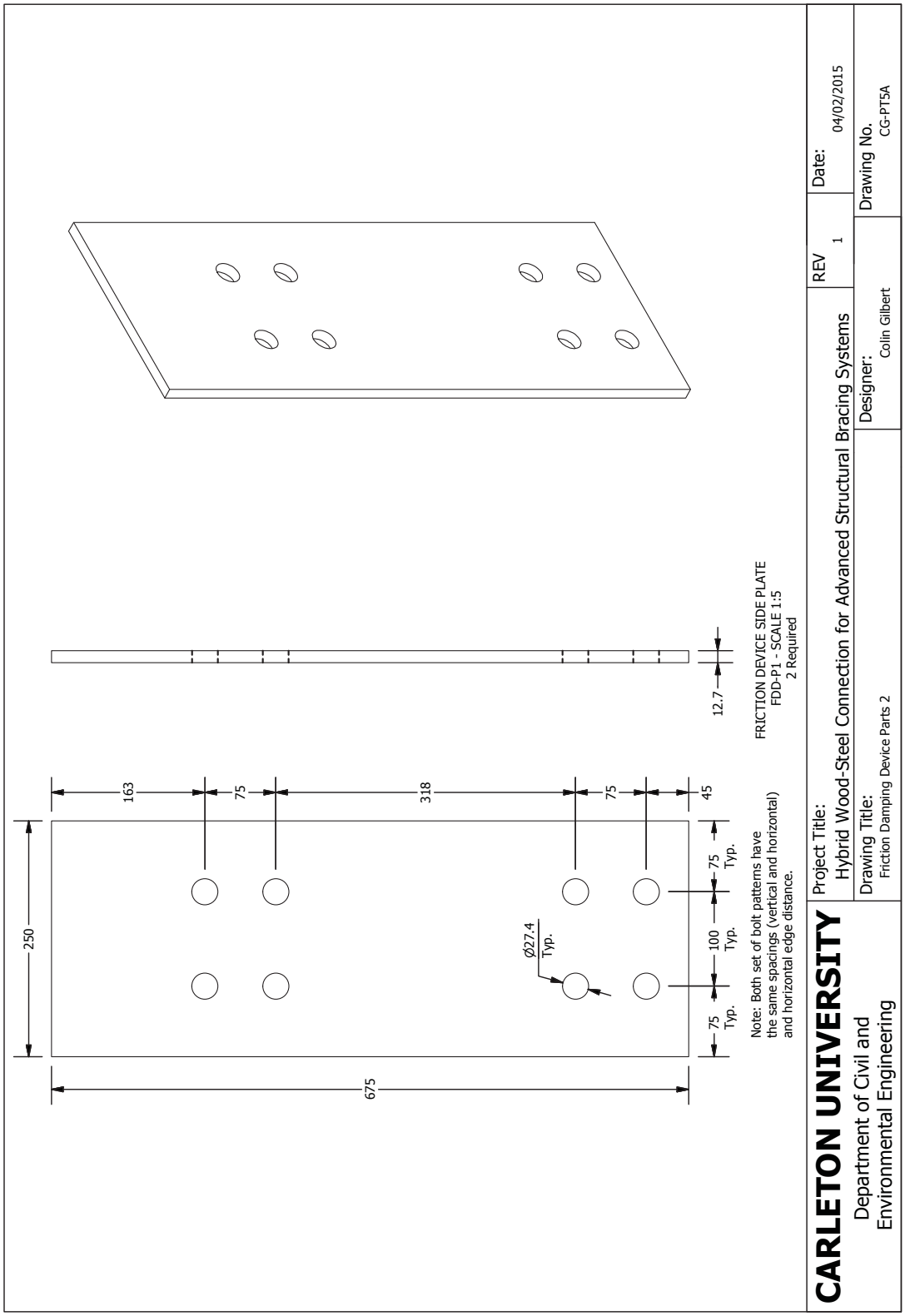
250
675
163
75
318
75
45
75 Typ.
100 Typ.
75 Typ.
Ø27.4 Typ.
12.7
Note: Both set of bolt patterns have the same spacings (vertical and horizontal) and horizontal edge distance.
FRICTION DEVICE SIDE PLATE
FDD-P1 - SCALE 1:5
2 Required
CARLETON UNIVERSITY
Department of Civil and Environmental Engineering
Project Title:
Hybrid Wood-Steel Connection for Advanced Structural Bracing Systems
Drawing Title:
Friction Damping Device Parts 2
Designer:
Colin Gilbert
REV
1
Date:
04/02/2015
Drawing No.
CG-PT5A

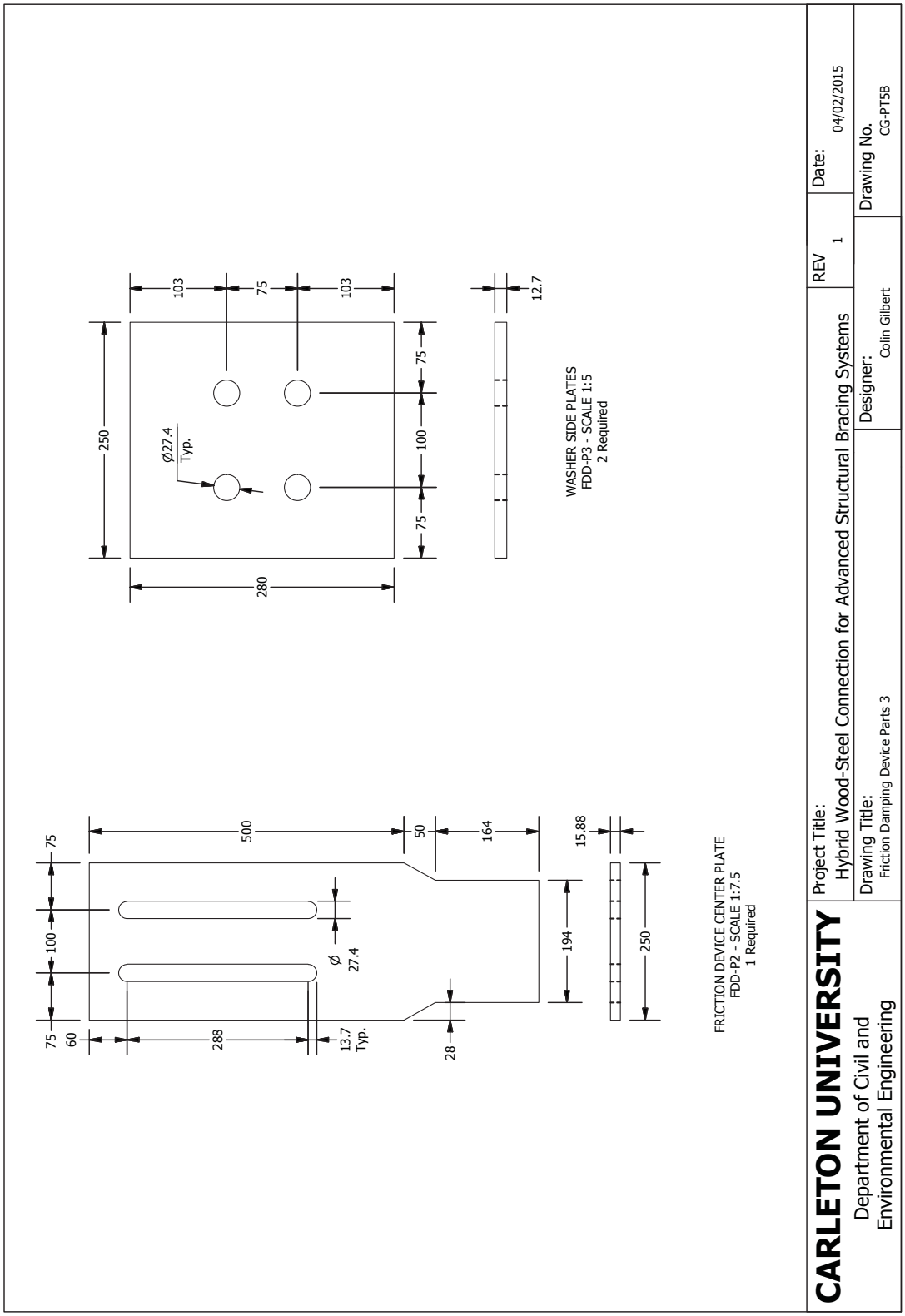
250
103
75
103
Ø27.4
Typ.
75
100
75
280
12.7
WASHER SIDE PLATES
FDD-P3 - SCALE 1:5
2 Required
75
100
75
60
500
50
164
Ø
27.4
288
13.7
Typ.
28
194
15.88
250
FRICTION DEVICE CENTER PLATE
FDD-P2 - SCALE 1:7.5
1 Required
CARLETON UNIVERSITY
Department of Civil and
Environmental Engineering
Project Title:
Hybrid Wood-Steel Connection for Advanced Structural Bracing Systems
REV
1
Date:
04/02/2015
Drawing Title:
Friction Damping Device Parts 3
Designer:
Colin Gilbert
Drawing No.
CG-PT5B

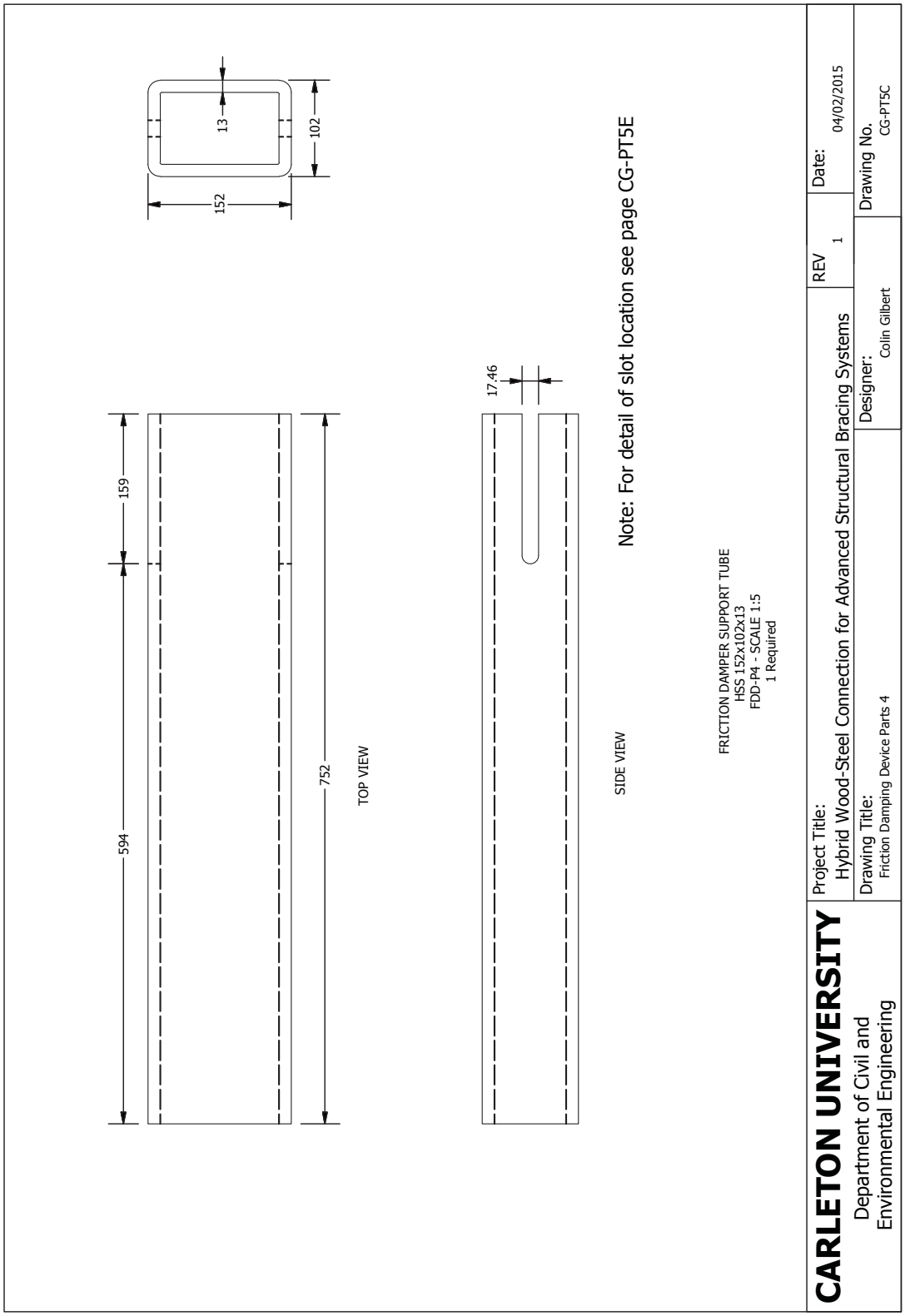
13
102
152
159
594
752
TOP VIEW
17.46
SIDE VIEW
Note: For detail of slot location see page CG-PT5E
FRICTION DAMPER SUPPORT TUBE
HSS 152x102x13
FDD-P4 - SCALE 1:5
1 Required
CARLETON UNIVERSITY
Department of Civil and
Environmental Engineering
Project Title:
Hybrid Wood-Steel Connection for Advanced Structural Bracing Systems
REV
1
Date:
04/02/2015
Drawing Title:
Friction Damping Device Parts 4
Designer:
Colin Gilbert
Drawing No.
CG-PT5C

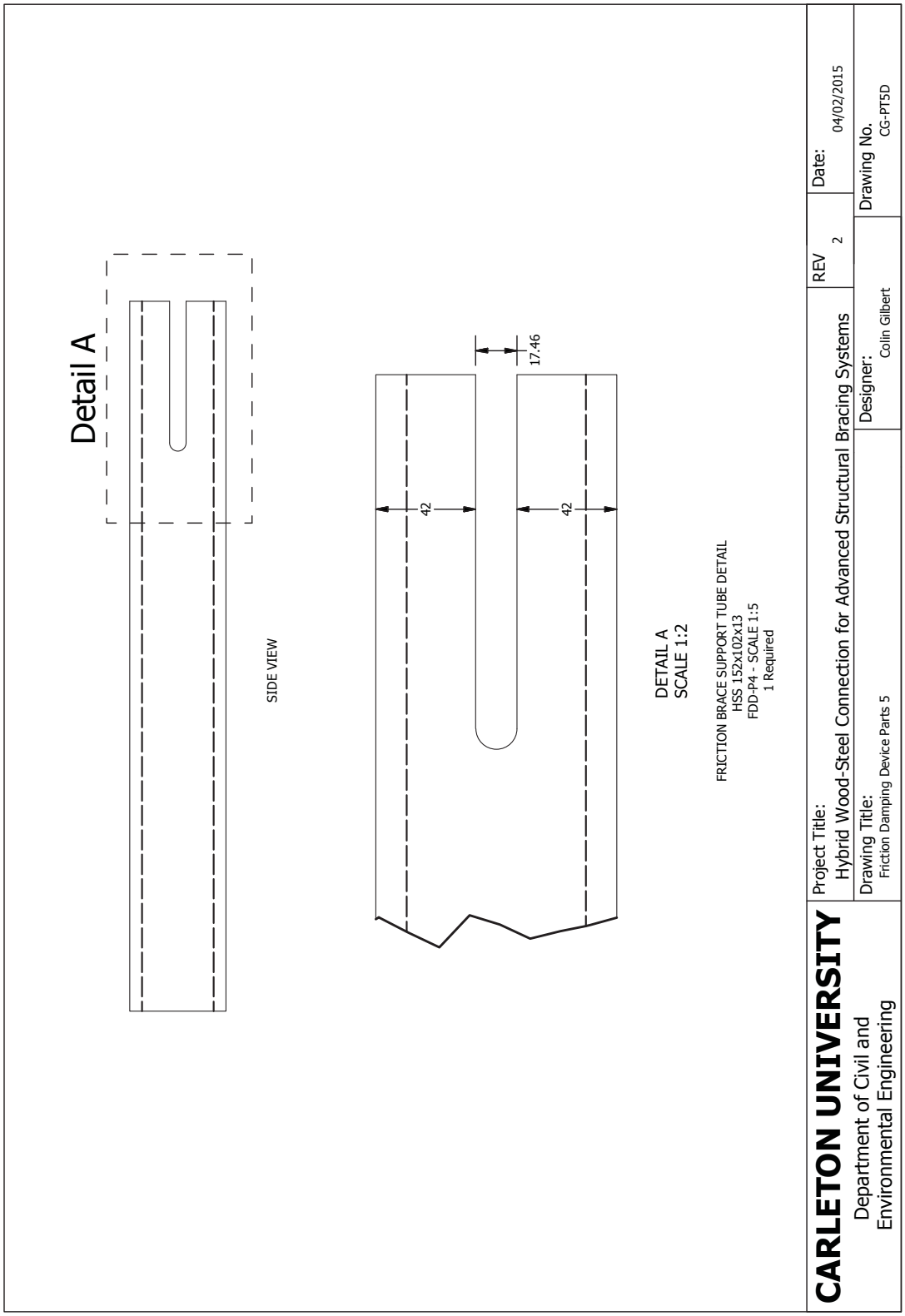
Detail A
SIDE VIEW
17.46
42
42
DETAIL A
SCALE 1:2
FRICTION BRACE SUPPORT TUBE DETAIL
HSS 152x102x13
FDD-P4 - SCALE 1:5
1 Required
CARLETON UNIVERSITY
Department of Civil and
Environmental Engineering
Project Title:
Hybrid Wood-Steel Connection for Advanced Structural Bracing Systems
Drawing Title:
Friction Damping Device Parts 5
Designer:
Colin Gilbert
REV
2
Date:
04/02/2015
Drawing No.
CG-PT5D

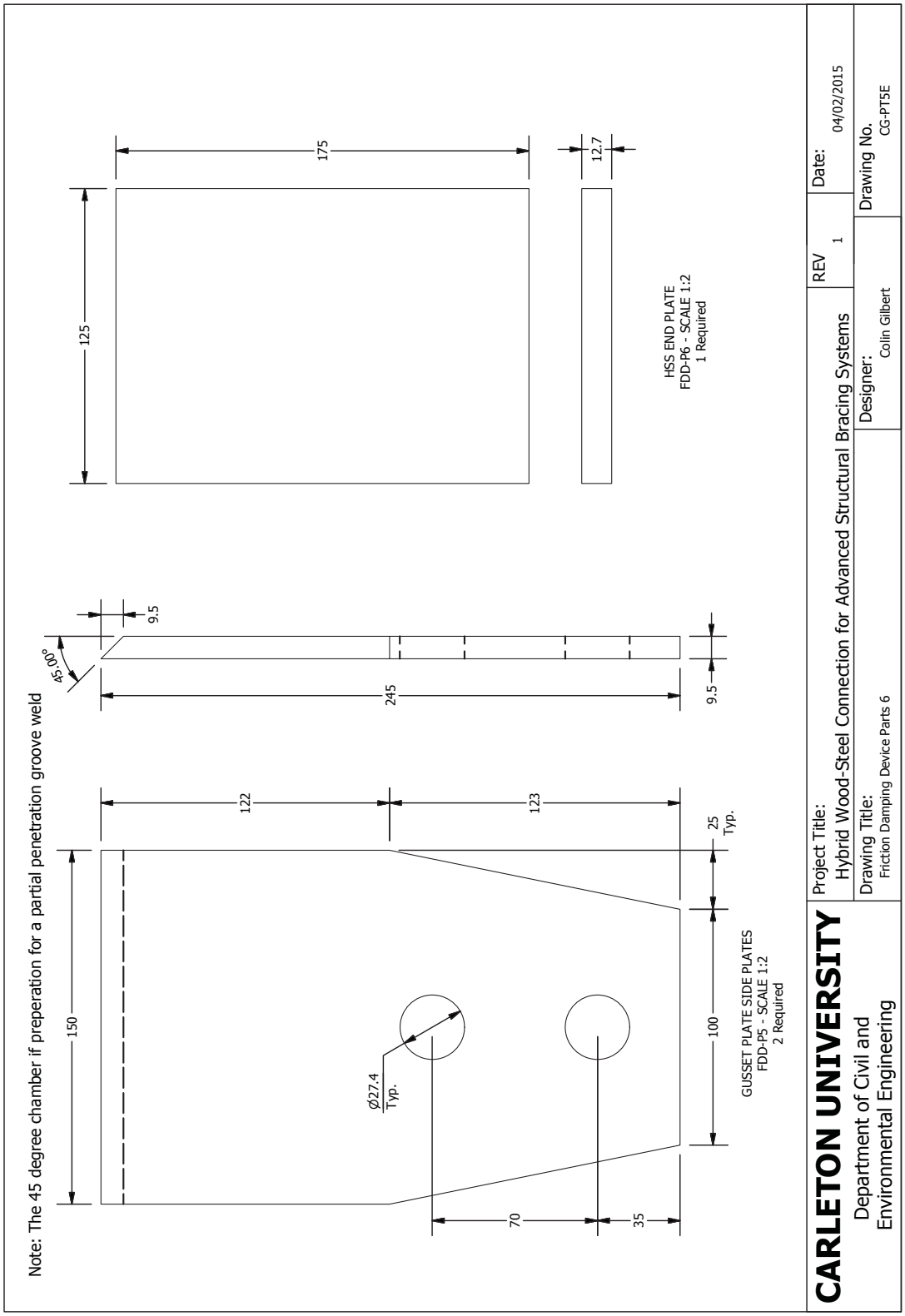
Note: The 45 degree chamber if preperation for a partial penetration groove weld
45.00°
9.5
245
9.5
122
123
25
Typ.
150
100
Ø27.4
Typ.
70
35
GUSSET PLATE SIDE PLATES
FDD-P5 - SCALE 1:2
2 Required
125
175
12.7
HSS END PLATE
FDD-P6 - SCALE 1:2
1 Required
CARLETON UNIVERSITY
Department of Civil and
Environmental Engineering
Project Title:
Hybrid Wood-Steel Connection for Advanced Structural Bracing Systems
REV
1
Date:
04/02/2015
Drawing Title:
Friction Damping Device Parts 6
Designer:
Colin Gilbert
Drawing No.
CG-PT5E

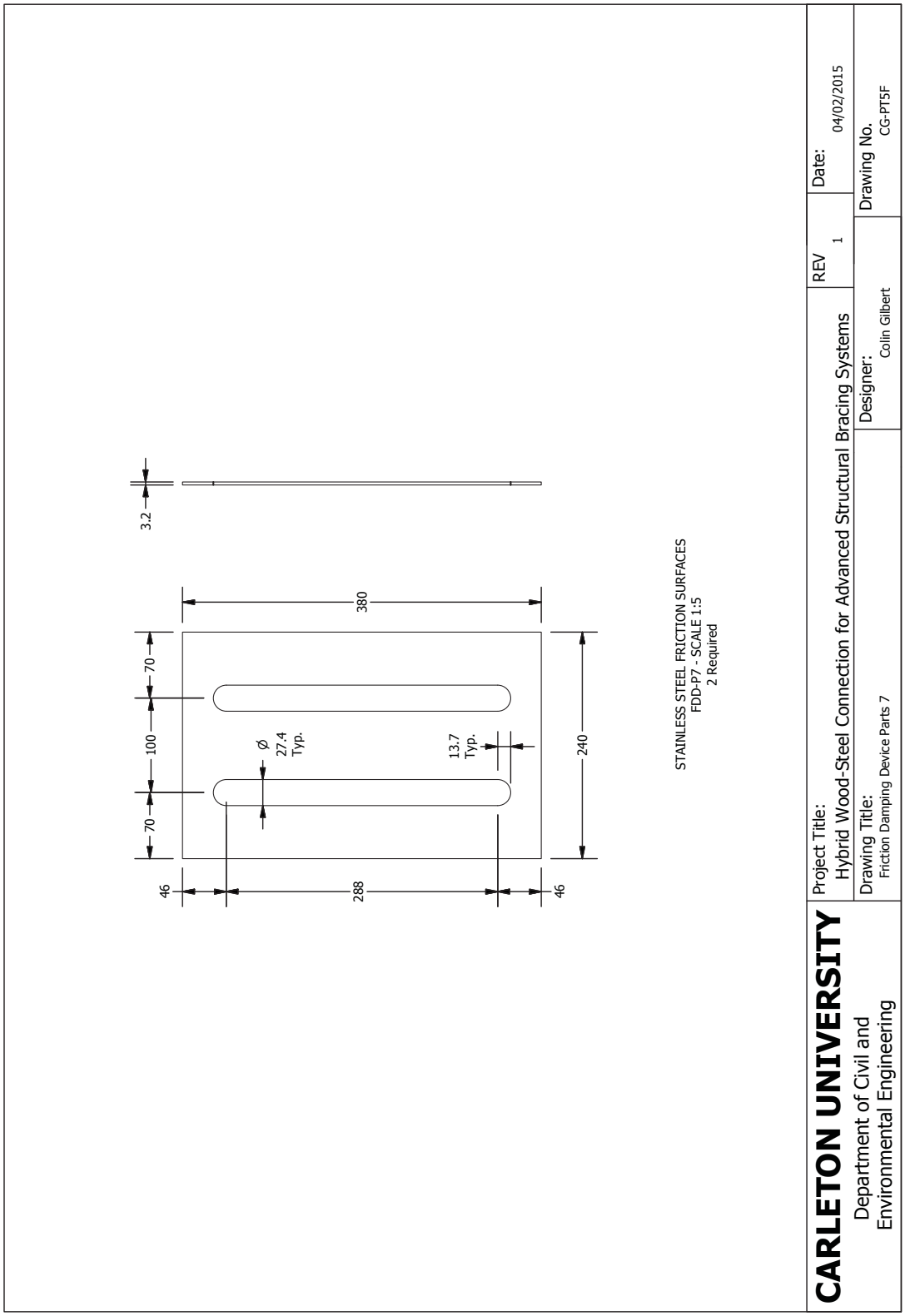
3.2
380
70
100
70
Ø
27.4
Typ.
13.7
Typ.
240
46
288
46
STAINLESS STEEL FRICTION SURFACES
FDD-P7 - SCALE 1:5
2 Required
CARLETON UNIVERSITY
Department of Civil and
Environmental Engineering
Project Title:
Hybrid Wood-Steel Connection for Advanced Structural Bracing Systems
REV
1
Date:
04/02/2015
Drawing Title:
Friction Damping Device Parts 7
Designer:
Colin Gilbert
Drawing No.
CG-PT5F

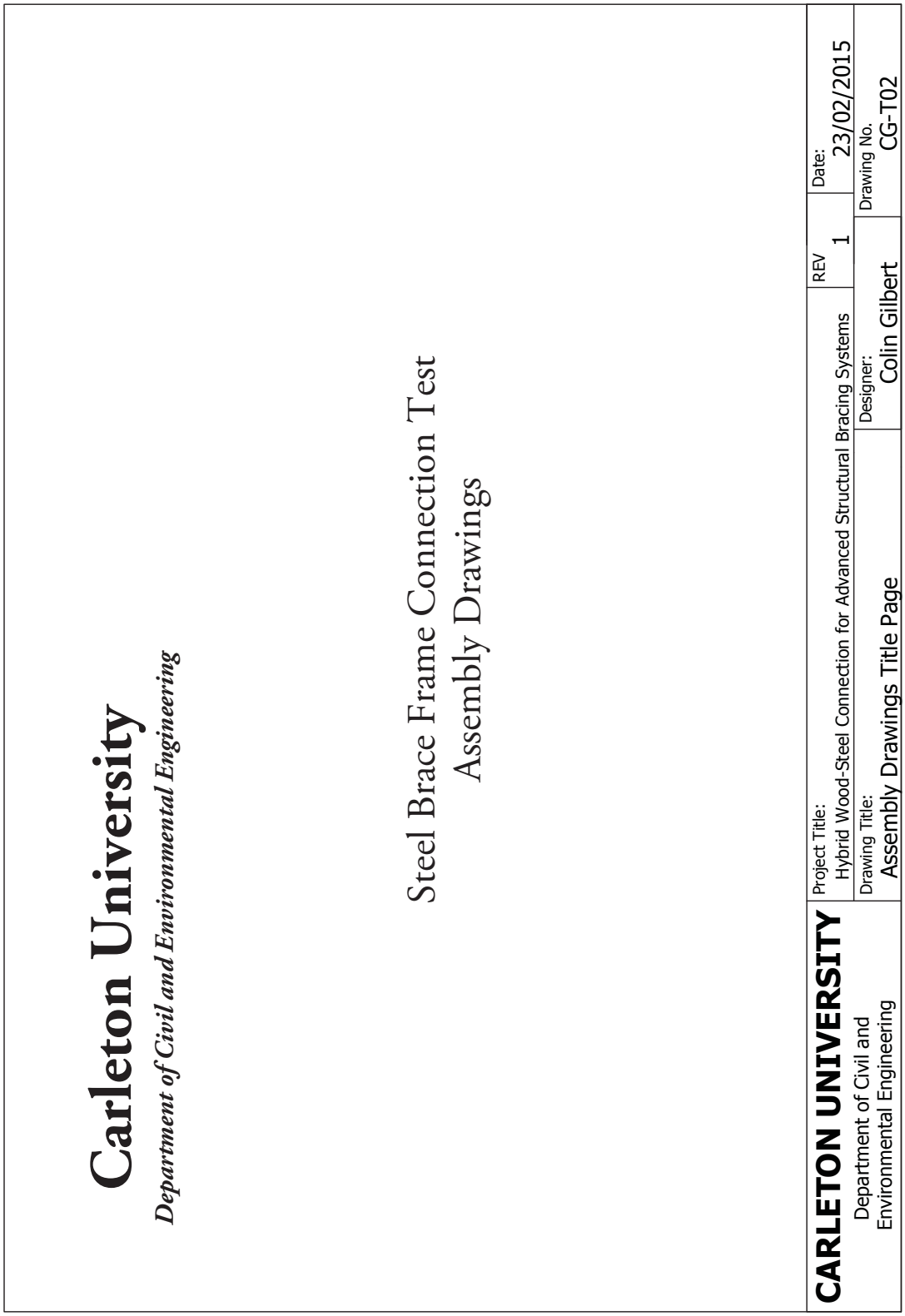
Carleton University
Department of Civil and Environmental Engineering
Steel Brace Frame Connection Test
Assembly Drawings
CARLETON UNIVERSITY
Department of Civil and
Environmental Engineering
Project Title:
Hybrid Wood-Steel Connection for Advanced Structural Bracing Systems
REV
1
Date:
23/02/2015
Drawing Title:
Assembly Drawings Title Page
Designer:
Colin Gilbert
Drawing No.
CG-T02

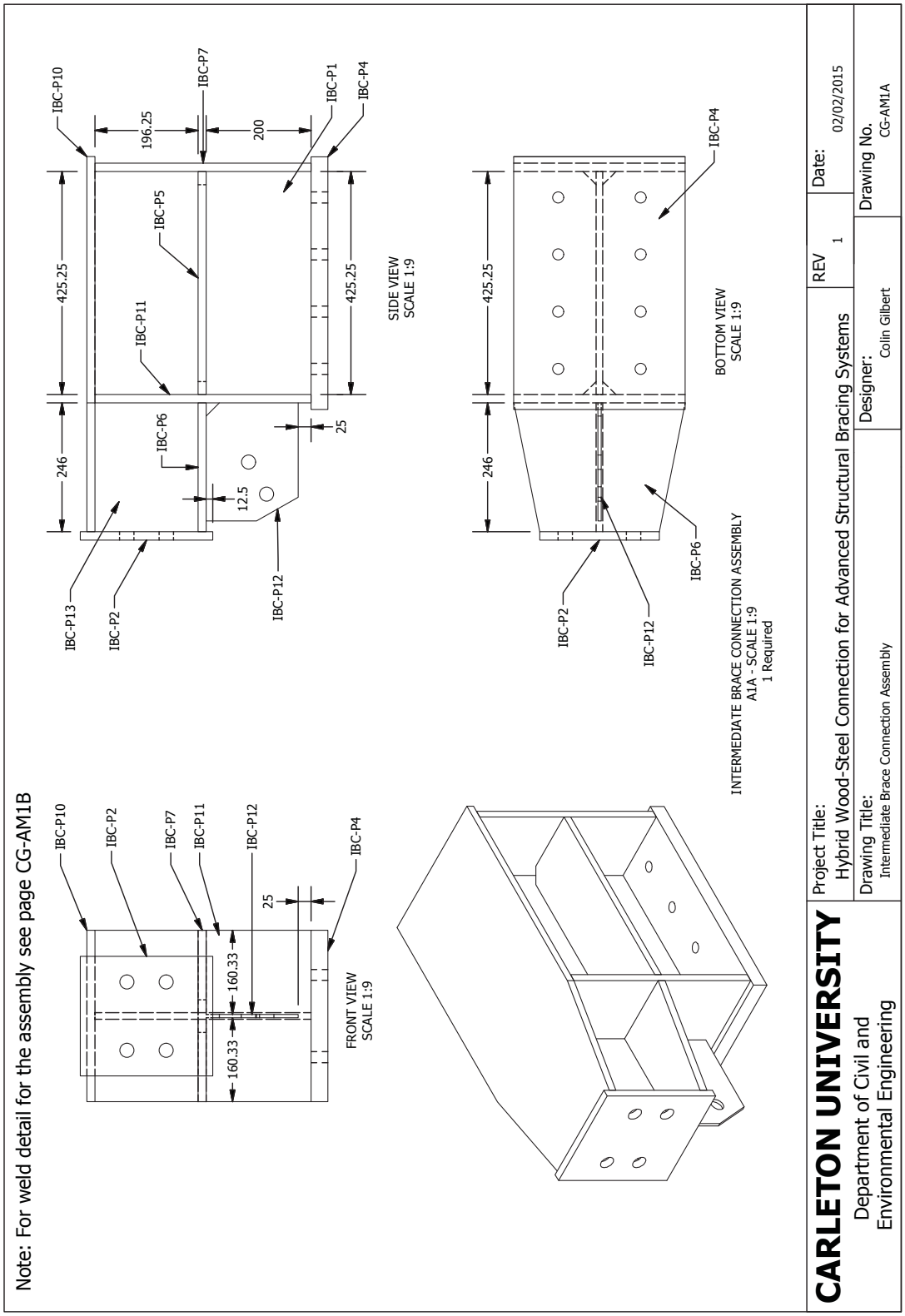
Note: For weld detail for the assembly see page CG-AM1B
IBC-P10
IBC-P2
IBC-P7
IBC-P11
IBC-P12
IBC-P4
25
160.33
160.33
FRONT VIEW
SCALE 1:9
IBC-P10
IBC-P7
IBC-P1
IBC-P4
196.25
200
IBC-P5
IBC-P11
IBC-P6
425.25
246
425.25
25
12.5
IBC-P13
IBC-P2
IBC-P12
SIDE VIEW
SCALE 1:9
IBC-P4
425.25
246
IBC-P2
IBC-P12
IBC-P6
BOTTOM VIEW
SCALE 1:9
INTERMEDIATE BRACE CONNECTION ASSEMBLY
A1A - SCALE 1:9
1 Required
CARLETON UNIVERSITY
Department of Civil and
Environmental Engineering
Project Title:
Hybrid Wood-Steel Connection for Advanced Structural Bracing Systems
REV
1
Date:
02/02/2015
Drawing Title:
Intermediate Brace Connection Assembly
Designer:
Colin Gilbert
Drawing No.
CG-AM1A

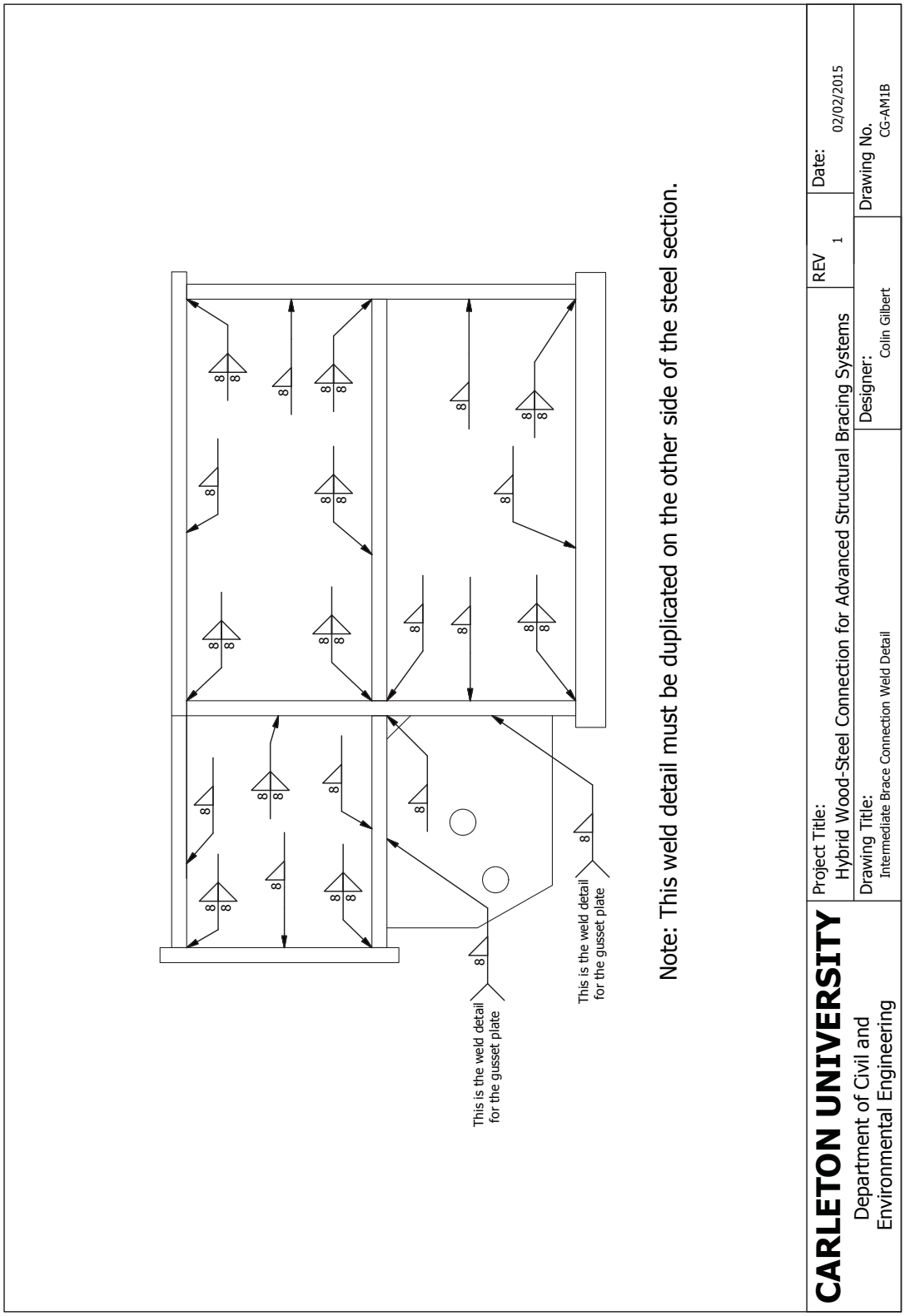
This is the weld detail for the gusset plate
This is the weld detail for the gusset plate
Note: This weld detail must be duplicated on the other side of the steel section.
CARLETON UNIVERSITY
Department of Civil and Environmental Engineering
Project Title:
Hybrid Wood-Steel Connection for Advanced Structural Bracing Systems
REV
1
Date:
02/02/2015
Drawing Title:
Intermediate Brace Connection Weld Detail
Designer:
Colin Gilbert
Drawing No.
CG-AM1B

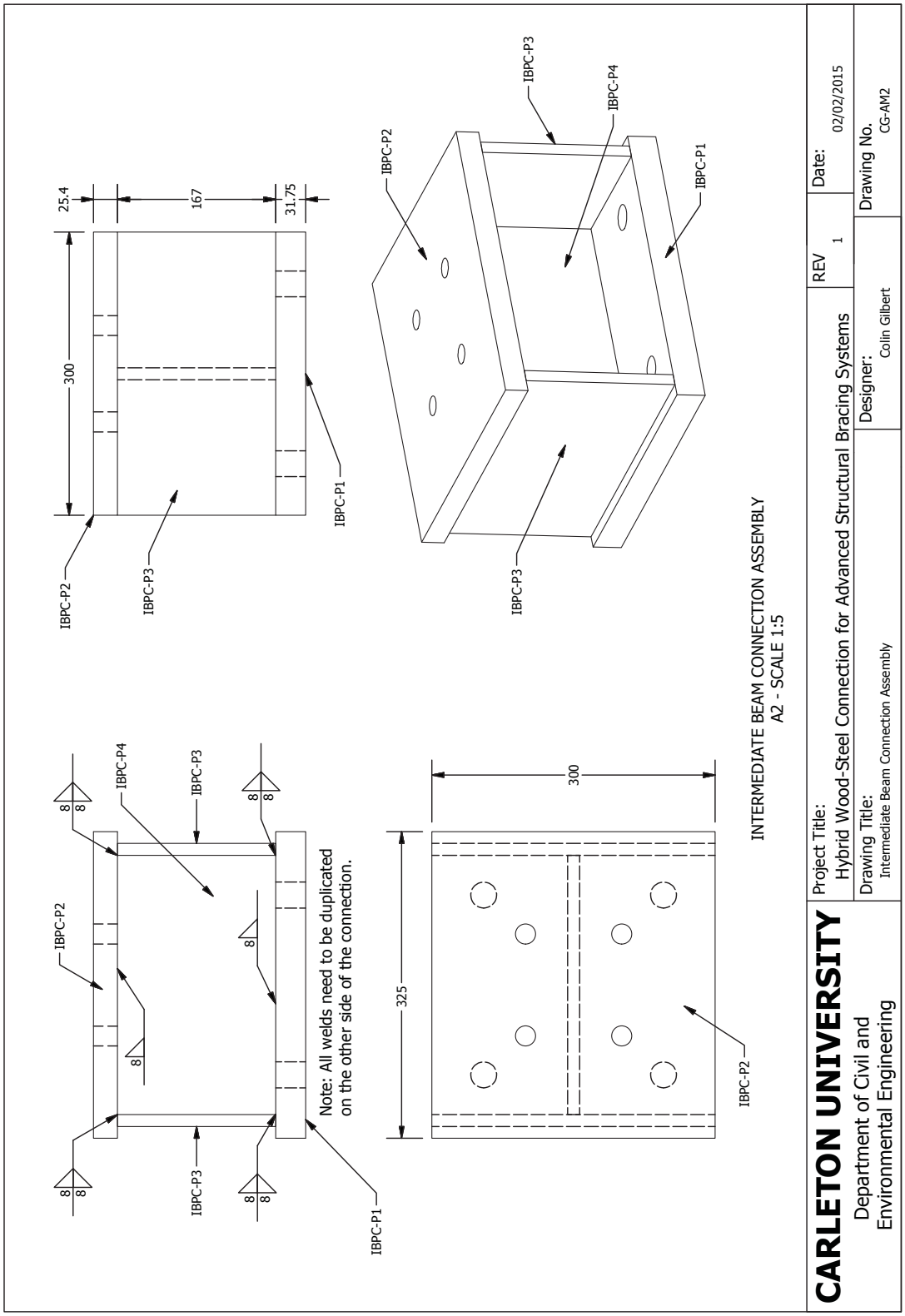
25.4
167
31.75
300
IBPC-P2
IBPC-P3
IBPC-P1
IBPC-P2
IBPC-P3
IBPC-P4
IBPC-P1
IBPC-P3
IBPC-P4
IBPC-P3
IBPC-P2
8
IBPC-P3
IBPC-P1
Note: All welds need to be duplicated on the other side of the connection.
300
325
IBPC-P2
INTERMEDIATE BEAM CONNECTION ASSEMBLY
A2 - SCALE 1:5
CARLETON UNIVERSITY
Department of Civil and Environmental Engineering
Project Title:
Hybrid Wood-Steel Connection for Advanced Structural Bracing Systems
Drawing Title:
Intermediate Beam Connection Assembly
Designer:
Colin Gilbert
REV
1
Date:
02/02/2015
Drawing No.
CG-AM2

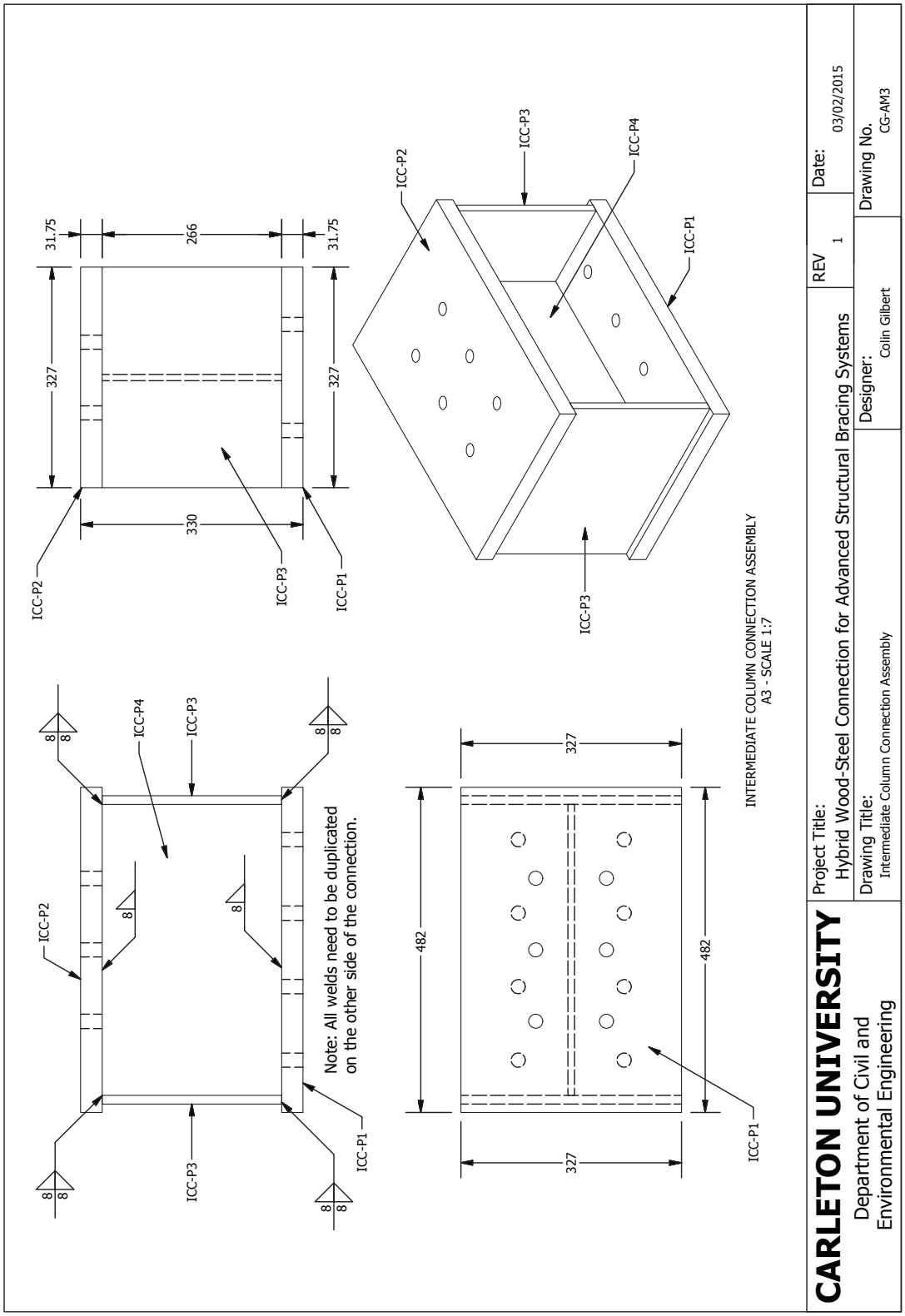
31.75
266
31.75
327
327
330
ICC-P2
ICC-P3
ICC-P1
ICC-P2
ICC-P3
ICC-P4
ICC-P1
ICC-P3
8
8
ICC-P4
ICC-P3
ICC-P2
8
8
Note: All welds need to be duplicated on the other side of the connection.
ICC-P1
ICC-P3
327
482
482
327
ICC-P1
INTERMEDIATE COLUMN CONNECTION ASSEMBLY
A3 - SCALE 1:7
CARLETON UNIVERSITY
Department of Civil and Environmental Engineering
Project Title:
Hybrid Wood-Steel Connection for Advanced Structural Bracing Systems
Drawing Title:
Intermediate Column Connection Assembly
Designer:
Colin Gilbert
REV
1
Date:
03/02/2015
Drawing No.
CG-AM3

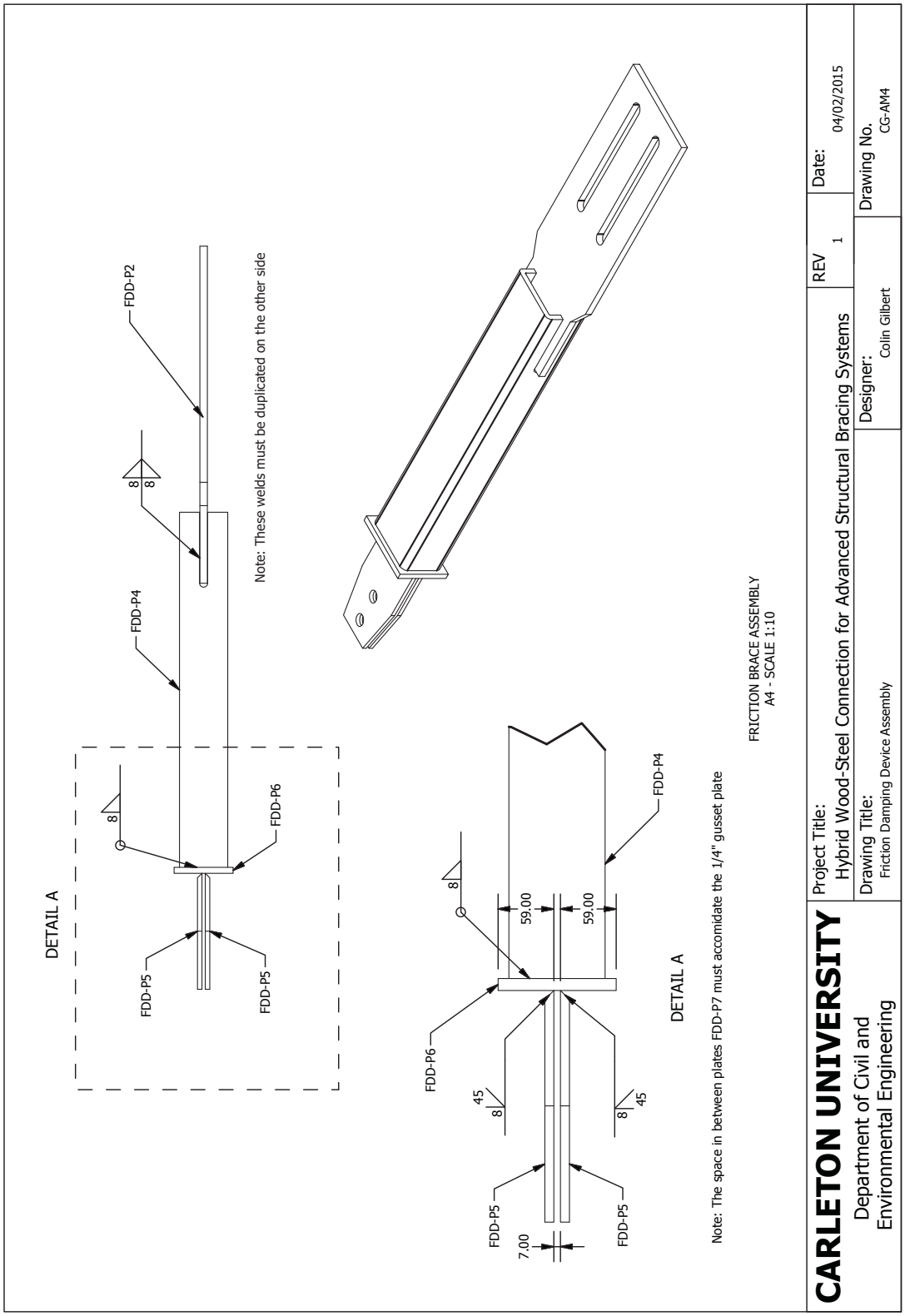
FDD-P2
8
8
Note: These welds must be duplicated on the other side
FDD-P4
DETAIL A
8
FDD-P6
FDD-P5
FDD-P5
FDD-P4
8
59.00
59.00
FDD-P6
45
8
8
45
FDD-P5
7.00
FDD-P5
DETAIL A
Note: The space in between plates FDD-P7 must accomidate the 1/4" gusset plate
FRICTION BRACE ASSEMBLY
A4 - SCALE 1:10
CARLETON UNIVERSITY
Department of Civil and
Environmental Engineering
Project Title:
Hybrid Wood-Steel Connection for Advanced Structural Bracing Systems
REV
1
Date:
04/02/2015
Drawing Title:
Friction Damping Device Assembly
Designer:
Colin Gilbert
Drawing No.
CG-AM4

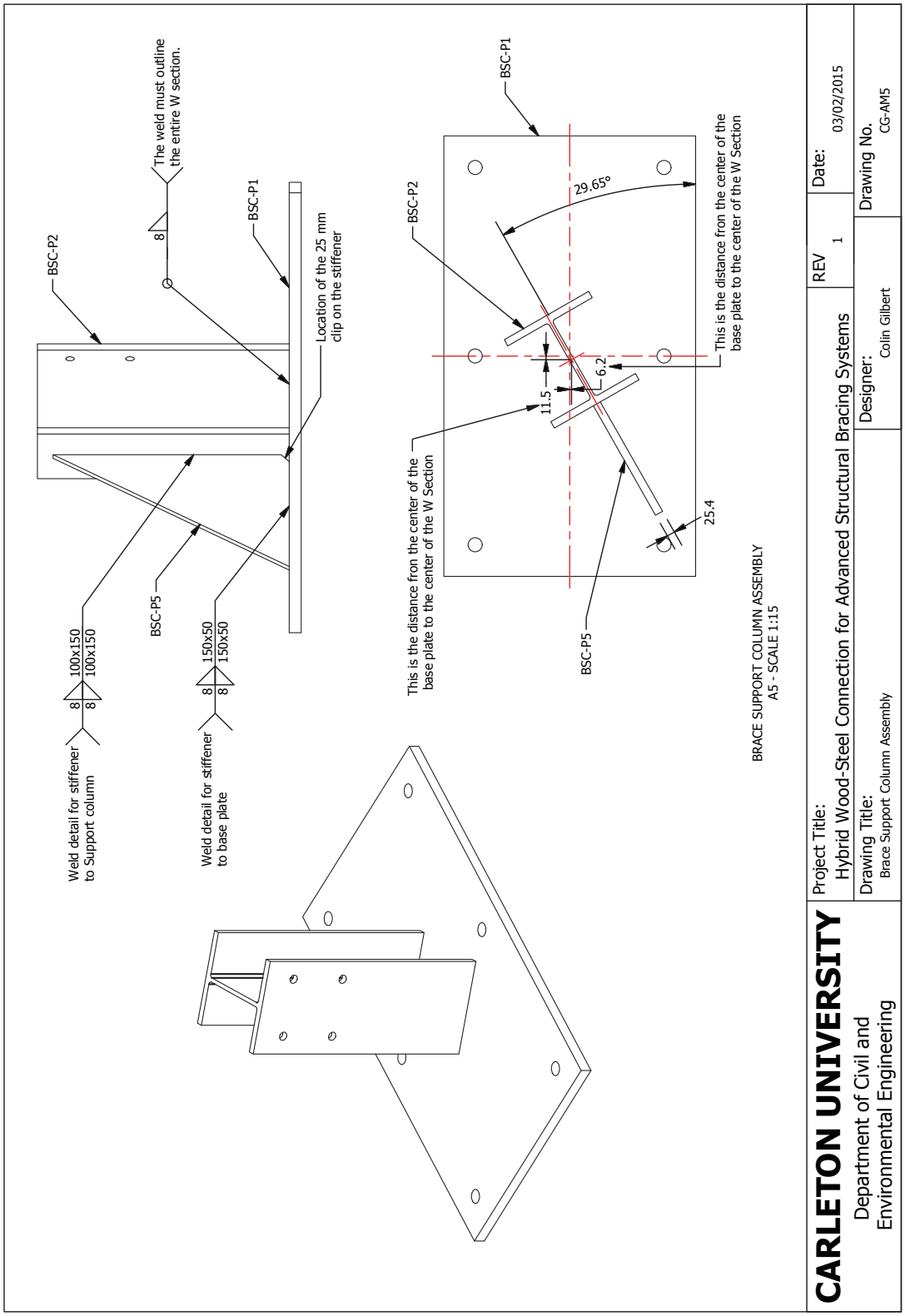
BSC-P2
The weld must outline the entire W section.
8
BSC-P1
Location of the 25 mm clip on the stiffener
BSC-P5
100x150
100x150
8
8
Weld detail for stiffener to Support column
150x50
150x50
8
8
Weld detail for stiffener to base plate
BSC-P1
BSC-P2
29.65°
This is the distance fron the center of the base plate to the center of the W Section
6.2
11.5
This is the distance fron the center of the base plate to the center of the W Section
25.4
BSC-P5
BRACE SUPPORT COLUMN ASSEMBLY
A5 - SCALE 1:15
CARLETON UNIVERSITY
Department of Civil and Environmental Engineering
Project Title:
Hybrid Wood-Steel Connection for Advanced Structural Bracing Systems
REV
1
Date:
03/02/2015
Drawing Title:
Brace Support Column Assembly
Designer:
Colin Gilbert
Drawing No.
CG-AM5

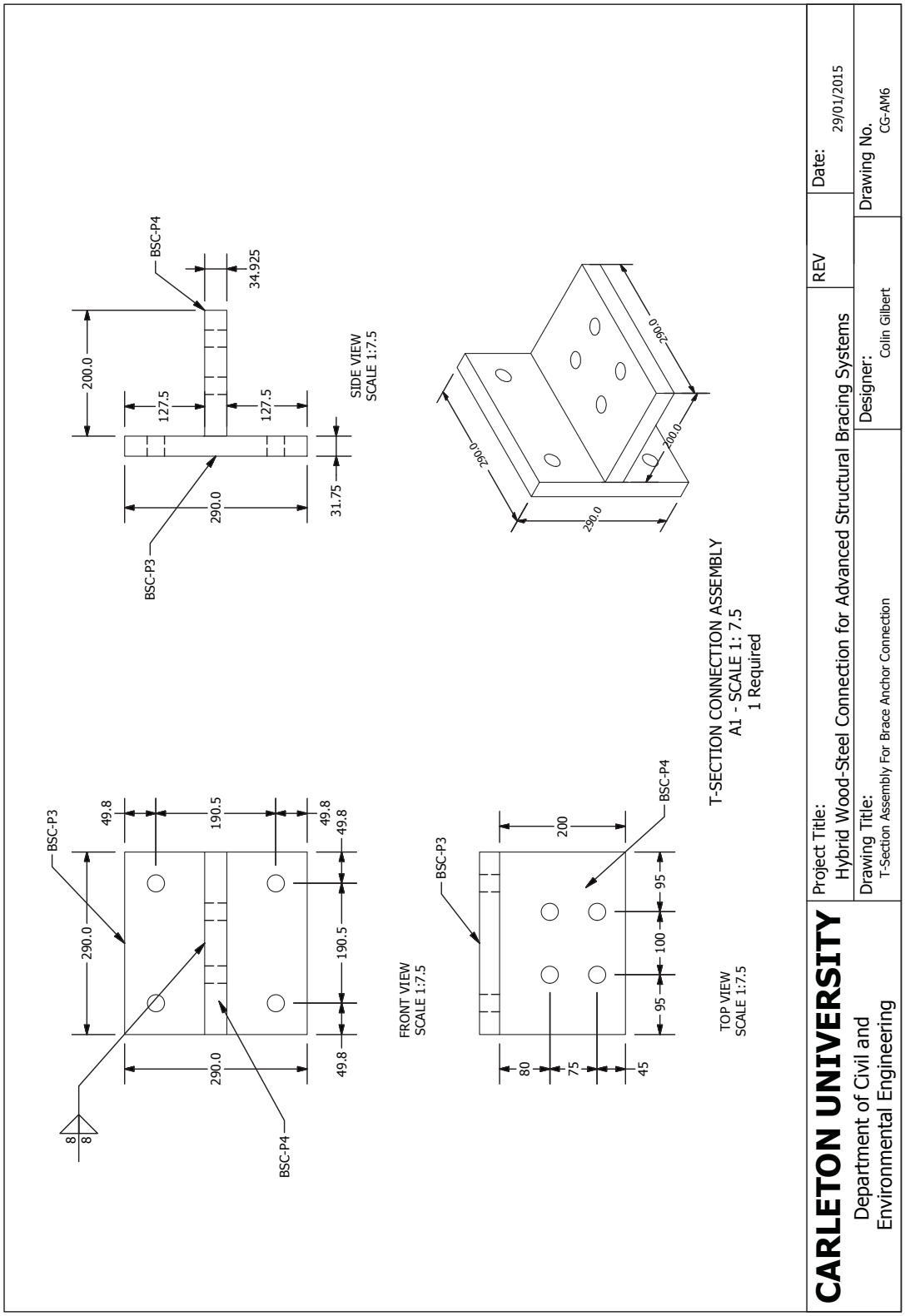
BSC-P4
34.925
200.0
127.5
127.5
290.0
31.75
BSC-P3
SIDE VIEW
SCALE 1:7.5
290.0
290.0
200.0
290.0
BSC-P3
49.8
190.5
49.8
290.0
190.5
49.8
49.8
8
8
BSC-P4
FRONT VIEW
SCALE 1:7.5
BSC-P3
200
BSC-P4
95
100
95
80
75
45
TOP VIEW
SCALE 1:7.5
T-SECTION CONNECTION ASSEMBLY
A1 - SCALE 1: 7.5
1 Required
CARLETON UNIVERSITY
Department of Civil and
Environmental Engineering
Project Title:
Hybrid Wood-Steel Connection for Advanced Structural Bracing Systems
Drawing Title:
T-Section Assembly For Brace Anchor Connection
Designer:
Colin Gilbert
REV
Date:
29/01/2015
Drawing No.
CG-AM6

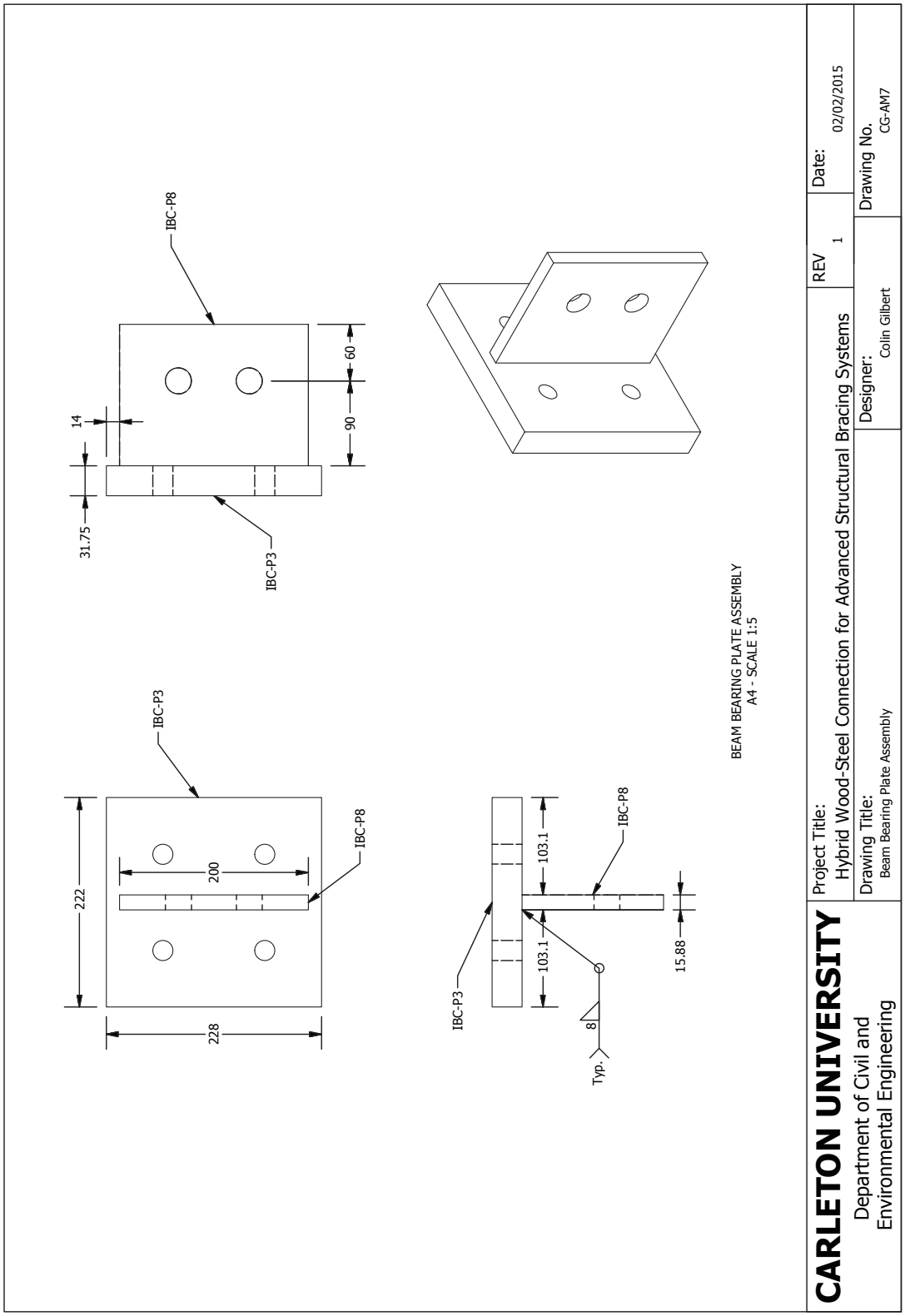
IBC-P8
14
31.75
60
90
IBC-P3
IBC-P3
222
200
IBC-P8
228
IBC-P3
103.1
103.1
IBC-P8
8
Typ.
15.88
BEAM BEARING PLATE ASSEMBLY
A4 - SCALE 1:5
CARLETON UNIVERSITY
Department of Civil and
Environmental Engineering
Project Title:
Hybrid Wood-Steel Connection for Advanced Structural Bracing Systems
Drawing Title:
Beam Bearing Plate Assembly
Designer:
Colin Gilbert
REV
1
Date:
02/02/2015
Drawing No.
CG-AM7

Appendix B: Design of Prototype Structures

The design methods and calculations described in this appendix outline the assumptions and procedures used in the structural analysis and design of a hybrid timber-steel and steel-only structures in Victoria BC, containing buckling restrained brace frame (BRBF). Current capacity design procedures were adapted for use in the design of the hybrid frame that would allow for the force reduction factors of the BRB system to be used in the seismic design. Both structures were analysed using the 3-dimensional structural analysis software ETABS (Computers & Structures Inc., 2013) to accurately determine the seismic design forces and storey drift responses. The buildings were designed in accordance with the structural requirements of the National Building Code of Canada (NBCC, 2010). The BRBs and structural steel components were designed using the Canadian Handbook of Steel Construction CSA S16-09 (2009), while structural members of the hybrid structure were designed using the Canadian Wood Design Manual CSA O89-09 (2009). Lastly, the glued-in rod connections used in the hybrid structure was designed using the procedures outlined in the GIROD Report (2002), LICONS Report (2003) and German design code DIN 1052 (2004).

The six-storey buildings contained two identical moment-resisting frames in the east-west direction, and symmetrical BRBFs in the north-south direction, as shown in Figure B.1. Diagonal bracing geometry was selected to reduce the complexity of the hybrid connections and utilize the high axial resistance of the timber and steel members. The BRBs were positioned in the outer bays of the seismic force resisting systems (SFRSs) of both structures to minimize foundation forces. The first building was designed using hybrid steel-timber systems, and the second was designed as a steel-only structure. Both buildings had identical geometry with a consistent storey height of 3.7 m and bay widths of 6.5 m in both directions. The geometric similarity was used

to facilitate the seismic performance comparisons of the two structures. However, the building materials and construction methods of the two buildings types resulted in different floor systems and structural components. The steel structure was assumed to have concrete composite floor slabs on all levels, while the hybrid structure used a 131-5s cross-laminated timber (CLT) one-way slab floor system. The steel building was designed with beams running east to west and transfer girders in the north-south direction. Where as the high flexural resistance of the CLT floor slab systems in the hybrid structure limited the beam elements to a spacing of 6.5 m, running in the north-south direction. The structural layout of the two building types are shown in Figure B.1.

The gravity load design was completed for the gravity frame and initial design of the SFRS based on the NBCC (2010) requirements. Both structures were designed as typical office buildings of normal importance. The live loads were the same in both cases, however the floor systems of the two structures resulted in different dead loads. The self-weight of the CLT system was determined from the technical documents for 131-5s CLT panels provided by Nordic Structures Inc (Nordic Engineered Wood, 2013a). Additionally, the 93 mm thick concrete slab was assumed to have a self-weight of 2.2 kPa based on a similar building design presented in literature by Choi et al. (2008). The corresponding live and dead loads of the two structures are presented in Tables B.1 and B.2.

The snow load analysis was determined from the NBCC design requirements for Victoria, BC. The roof geometry and 0.5 m parapet resulted in a maximum snow load of 1.142 kPa around the outer perimeter that gradually reduced to 1.08 kPa at a distance of 3 m from the roof's edge. Figure B.2 shows the final snow load distribution that was identical for both buildings.

Lastly, a preliminary wind load analysis was conducted on the structure based on the NBCC (2010) requirements and was determined to not govern the equivalent static design of the lateral force resisting system. The ULS wind pressure of 0.57 kPa was selected for the Victoria location (NBCC, 2010), while the confined urban layout ensure a rough terrain that provided an exposure factor, C_e, determined from equation B.1 (NBCC, 2010):

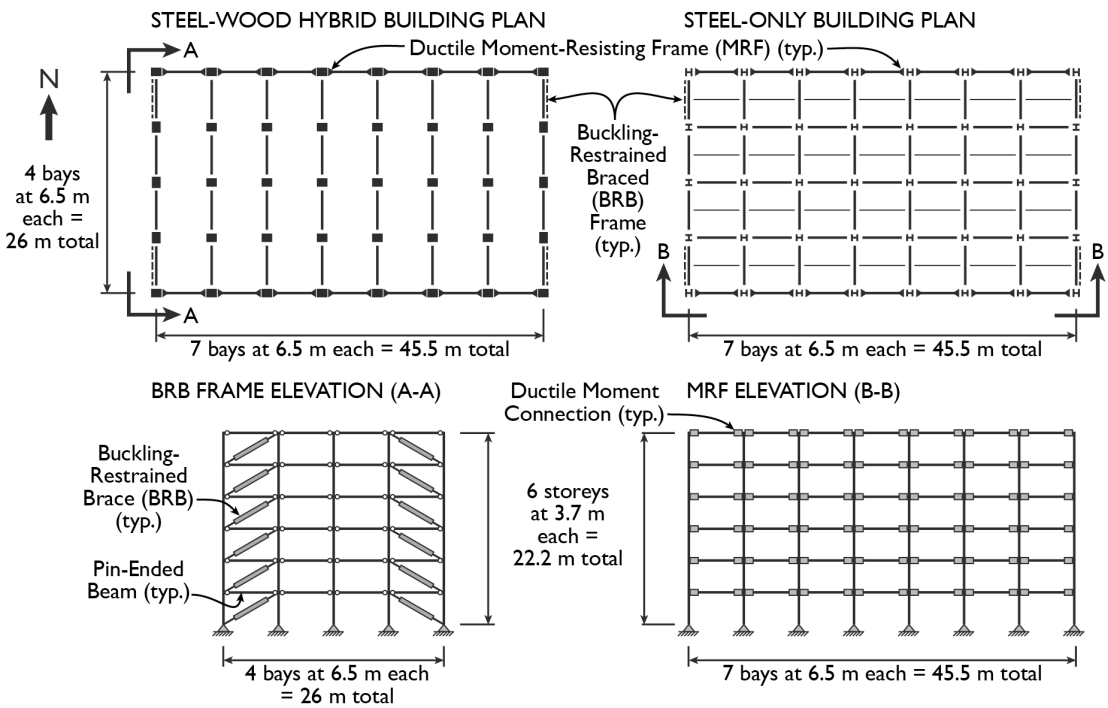

Figure B.1: Hybrid Timber-Steel and Steel-Only Building Details

Table B.1: Summary of Gravity Load for the Hybrid Building

Non-structural Components	Roof Loads (kPa)	Floor Loads (kPa)
Live Load	1.0	2.4
Dead Loads		
Roofing	0.24	-
Partitions	-	1.0
Insulation	0.1	-
Fire proofing	0.1	0.1
Ceiling	0.24	0.24
Floor Covering	-	0.1
CLT Slab	0.62	0.63
Timber Frame	0.3	0.3
Mech/Elec	0.48	0.48
Total	2.08	2.84

Table B.2: Summary of Gravity Load for the Steel-Only Building

Non-structural Components	Roof Loads (kPa)	Floor Loads (kPa)
Live Load	1.0	2.4
Dead Loads		
Roofing	0.24	-
Partitions	-	1.0
Insulation	0.1	-
Fire proofing	0.1	0.1
Ceiling	0.24	0.24
Floor Covering	-	0.1
Concrete Decking	2.2	2.2
Steel Frame	0.72	0.72
Mech/Elec	0.48	0.48
Total	4.08	4.84

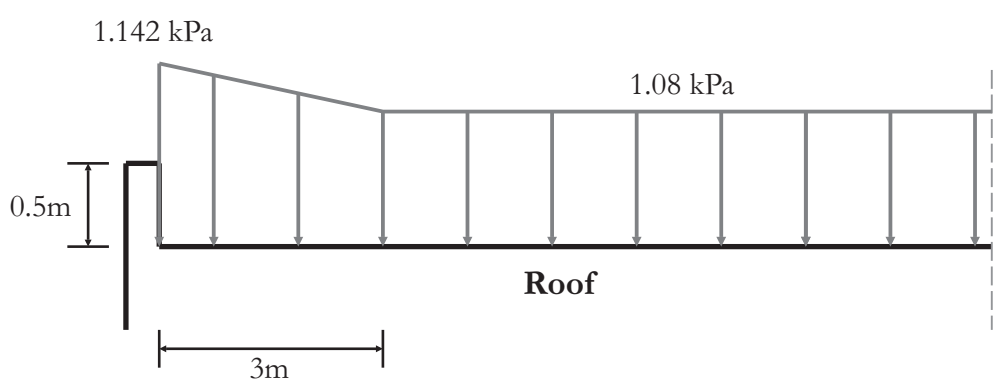

Figure B.2: Snow Load for Victoria, BC

$$C_e = 0.7 * (h/12)^{0.3} \tag{B.1}$$

where h is the total building height of 22.2 m. Since the building height was greater than the low-rise limit of 20 m, the mid-rise wind loading analysis was conducted. The external pressure factor C_p varied depending on the locations of interest on the structure and wind direction, while a gust effect factor, C_g, of 2.0 was used to analysis the structural members. The wind loading analysis was conducted using ULS and SLS importance factors of 1.0 and 0.75, respectively.

B.1 ETABS Modeling

Seismic analysis parameters and design forces were obtained from the ETABS structural analysis models of the two buildings. The timber and steel structural members were modelled using different material types. The glue-laminated Douglas Fir-Larch 24f-EX members were modelled using an orthotropic material type with a specific weight density of 4.8 kN/m^3 and young's modulus of 12800 MPa (CSA O86, 2009). The orthotropic strength and stiffness parameters of the timber sections were taken for Table 6.3 of CSA O86 (2009). The steel members were modelled using the CSA S16 W-section member sizes provided by the software. The braces were modelled using fully supported slender steel plates with an assumed yield strength of 370 MPa taken from Tremblay et al. (2004). Increased strength in the compressive direction due to friction effects was not considered. The self-weight of the BRBs was increased to account for the HSS sections and concrete infill of the restraint mechanisms. Both one-way floor slab systems were modelled using shell elements that were assigned the corresponding material properties.

B.2 Seismic Design Analyses

B.2.1 Equivalent Static Design Method

Prior to completing the response spectrum analysis, the equivalent static seismic design procedure was conducted to establish the preliminary design of the SFRS. This method established the upper limit of the seismic design forces of the structures based on the NBCC fundamental period for braced frames. The steps required for the elastic seismic design of the hybrid timber-steel and steel-only structures are as follows (NBCC, 2010; Filiatrault et al., 2013):

1. Select the location specific 5% damping seismic design spectrum factored for acceleration and velocity amplification soil characteristics.
2. Establish the initial seismic properties of the building type that include, importance factor, design period from the code specified empirical formula (NBCC, 2010), and ductility and overstrength factors of SFRS (NBCC 2010).
3. Compute the structure's seismic weight accounting for self-weight, superimposed dead loads, and 25% of the snow load.
4. Calculate and vertically distribute the static design base shear and the higher mode effect force based on code requirements.
5. Assess torsional sensitivity of the structure and implement the appropriate procedure to account for the forces associated with torsional effects.
6. Factor the distributed seismic forces to account for structural irregularities, notional loads and P-Delta effects.
7. Compile complete seismic design forces accounting for geometric and amplification effects, distribute vertically and apply lateral loads to the SFRS.
8. Preform a complete structural analysis of the SFRS to determine the seismic design forces of the individual members. Re-design the structural elements to establish the most economical design.
9. Reiterate the elastic seismic design procedure until the seismic weight and member sizes converge.

B.2.1.1 Design Parameters and Seismic weight

Given the soil conditions of downtown Victoria, a site class of C was assumed for the hybrid and steel-only structure locations. Therefore, the acceleration and velocity factors F_a and F_v for the assumed soil conditions taken from Tables 4.1.8.4B and 4.1.8.4C of the NBCC (2010) were 1.0 and 1.0, respectively. The 5% supplemental damped design spectrum and factored spectral ordinates presented in Appendix C of the NBCC (2010) for Victoria, BC are presented in Table B.3 and Figure B.3. These accelerations are define at the fundamental periods of 0.2, 0.5, 1.0, 2.0 and 4.0.

The equivalent static base shear and response spectrum analysis were conducted to evaluate the structural seismic performance for drift and strength. The concentrically braced BRBF design period, T_a, of 0.56 sec was determined from equation B.2 (NBCC 2010):

$$T_a = 0.025h_n = 0.025(22.2) = 0.555 \text{ sec} \tag{B.2}$$

where h_n is the total structure height of 22.2 m for both buildings. This period was then used to calculate the design elastic base shear, V_{ed}, at the maximum spectral acceleration. The corresponding spectral acceleration was used to assess the drift performance. However, due to the high lateral stiffness of braced frames drift requirements do not typically govern the BRBF design. The upper limit of the design period required for the strength design of BRBF was calculated as two times the design period limit T_a. Therefore, the upper limit determined for the strength analysis

Table B.3: Design Spectrum for Victoria, British Columbia

T (s)	$S(T)$	$S_a(T)$
0.2	1.2g	1.2g
0.5	0.82g	0.82g
1.0	0.38g	0.38g
2.0	0.18g	0.18g
4.0	-	0.09g

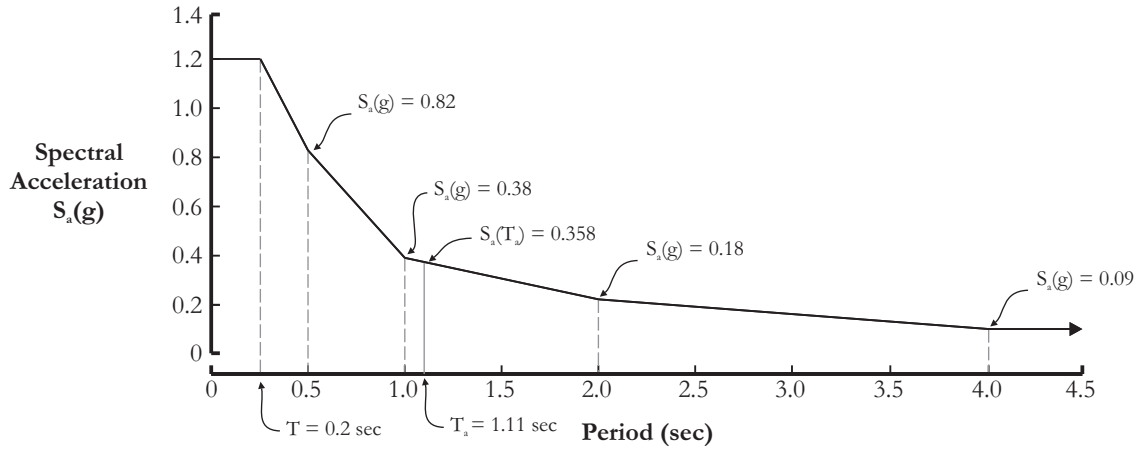

Figure B.3: Response Spectrum for Victoria, BC

of both structures was 1.11 sec, resulting in a spectral acceleration of 0.385 g that was interpolated from the values presented in Table B.3.

Seismic design requirements of the NBCC (2010) defined the load case used to compute the seismic weight of a structure. The seismic weight of the hybrid and steel-only structures was determined from the total dead load and 25% of the anticipated snow load distributed over the floor areas of 1183 m^2. The relevant gravity loads and seismic weights for the hybrid and steel-only structure are presented in Tables B.4 and B.5, receptively. The seismic weight of the steel-only structure is approximately 40% greater than the hybrid structure because of the concrete floor slab system.

B.2.1.2 Design Base Shear Forces

Since the ductile mechanisms in both the hybrid and steel-only structures are steel, identical R_d and R_o factors were assigned to both. This reflects the fact that all of the plastic behaviour will occur in the ductile BRBs. The force modification factors accounting for ductility and over-strength characteristics of BRBs were 4.0 and 1.2, respectively. The higher mode factor, M_v, is equal to 1.0 for a design period, T_a, $\leq$ 1.0 seconds. As previously stated, an importance factor of 1.0 was assigned to both structures. After establishing the seismic properties of each structure the design base shears were calculated using equation (B.3).

Table B.4: Summary of Hybrid Structure Seismic Weight

Storey	Dead Load (kN)	Snow Load (kN)	Total Weight (kN)
Roof	1.78	0.285	2608
5	2.54	0	3216
4	2.54	0	3236
3	2.54	0	3250
2	2.54	0	3284
1	2.54	0	3339
		Total	18933

Table B.5: Summary of Steel Structure Seismic Weight

Storey	Dead Load (kN)	Snow Load (kN)	Total Weight (kN)
Roof	3.36	0.285	4730
5	4.12	0	5297
4	4.12	0	5299
3	4.12	0	5307
2	4.12	0	5320
1	4.12	0	5324
		Total	31277

$$V = \frac{S(T_a)M_v I_E W}{R_d R_o} \tag{B.3}$$

A summary of the site specific seismic design properties and design base shears used in the static analysis for the strength design of the two structures are presented in Table B.6.

B.2.1.3 Vertical Distribution of Seismic Forces

The NBCC method for the seismic design force distribution, based on the relative seismic weight and hight of each storey, was implemented to establish the storey forces using equation (B.4).

$$F_x = \frac{(V - F_t)W_x h_x}{\left(\sum_{i=1}^{n} W_i h_i\right)} \tag{B.4}$$

The additional force F_t that accounts for higher mode effects applied at the roof level of the structure was calculated by equation (B.5).

$$F_t = 0.07 T_a V \leq 0.25V \tag{B.5}$$

A summary of the seismic weight and vertical seismic force distribution for the hybrid and steel-only structures are presented in Tables B.7 and B.8, respectively.

Table B.6: Summary of the Seismic Design Values

Design Parameter	Hybrid Structure	Steel Structure
$S(T_a)$	0.385	0.358
R_d	4.0	4.0
R_0	1.2	1.2
M_v	1.0	1.0
I_E	1.0	1.0
V	1419	2333

Table B.7: Summary of the Initial Seismic Force Distribution of Hybrid Structure

Storey	h_i (m)	Weight (kN)	h_iW_i (m·kN)	F_x/V	F_x (kN)	(kN)
Roof	22.2	2608.1	57900.8	0.302	428.7	4298.7
5	18.5	3216.4	59503.1	0.231	327.2	755.9
4	14.8	3235.6	47886.5	0.186	263.3	1019.3
3	11.1	3249.9	36074.2	0.140	198.4	1217.7
2	7.4	3284.3	24304.0	0.094	133.7	1351.3
1	3.7	3338.9	12354.0	0.048	67.9	1419.3
	Total	18933.3	238022.5	1.000	1419.3	

Table B.8: Summary of Initial Seismic Force Distribution of Steel Structure

Storey	h_i (m)	Weight (kN)	h_iW_i (m·kN)	F_x/V	F_x (kN)	(kN)
Roof	22.2	4730.3	105013.6	0.320	746.9	746.9
5	18.5	5296.7	97988.5	0.226	527.8	1274.8
4	14.8	5298.6	78418.8	0.181	422.4	1697.2
3	11.1	5306.6	58903.8	0.136	317.3	2014.5
2	7.4	5320.3	39370.5	0.091	212.1	2226.6
1	3.7	5323.6	19697.1	0.045	106.1	2332.7
	Total	31276.1	399392.3	1.000	2332.7	

B.2.1.4 Notional loads

Accidental eccentricity of the building due to construction variability and partial inelastic deformation development at the factored loads are accounted for through the notional load calculations. The notional load contribution at each storey was assumed to be equal to 5% of the gravity loads for each structure. These additional forces were applied to the hybrid and steel-only structures in the lateral direction. Tables B.9 and B.10 show the notional load contributions to the seismic design forces for the hybrid timber-steel and steel-only structures, respectively.

B.2.1.5 P-Delta Effect

An increase in the lateral building displacements due to gravitational load contribution is known as the P-Delta effect. The phenomenon is most severe in the lower storeys of mid- to high-rise buildings due to the concentrated gravity loads in these storeys (Erochko et al., 2013). To account for this behaviour the lateral loads were magnified using the factor U_2, determine from equation (B.6):

$$U_2 = (1 + \theta_x) \tag{B.6}$$

where θ_x is the stability coefficient is determined from Equation (B.7).

$$\theta_x = \frac{P_x \Delta_x}{R_o F_x h_{sx}} \tag{B.7}$$

Where, The stability coefficient for each storey was calculated from the total axial gravity loads in the columns, P_x, Δ_x is the anticipated storey drift that includes nonlinear effects, R_o is the overstrength factor, V_x is the seismically induced shear force, and h_{sx} is the storey height. The lateral force contributions of P-Delta effect for the hybrid and steel-only structures are presented in Tables B.11 and B.12.

Table B.9: Summary of the Hybrid Structure Notional Loads

Storey	Dead Load (kN)	Live Load (kN)	Snow Load (kN)	Gravity Loads (kN)	Notional Loads N_t (kN)
Roof	2109.3	1183.0	1351.0	3038.5	15.2
5	3008.4	2839.2	0	4428.0	22.1
4	3008.4	2839.2	0	4428.0	22.1
3	3008.4	2839.2	0	4428.0	22.1
2	3008.4	2839.2	0	4428.0	22.1
1	3008.4	2839.2	0	4428.0	22.1

Table B.10: Summary of the Steel Structure Notional Loads

Storey	Dead Load (kN)	Live Load (kN)	Snow Load (kN)	Gravity Loads (kN)	Notional Loads N_t (kN)
Roof	4348.2	1183.0	337.155	4432.5	22.2
5	5251.74	2839.2	0	5251.7	26.3
4	5253.64	2839.2	0	5253.6	26.3
3	5261.64	2839.2	0	5261.6	26.3
2	5275.34	2839.2	0	5275.3	26.4
1	5278.64	2839.2	0	5278.6	26.4

Table B.11: Summary of the Hybrid Structure P-Delta Loads

Storey	P_x (kN)	θ_x	U_2
Roof	3038.5	0.06	1.06
5	7466.5	0.08	1.08
4	11894.5	0.10	1.10
3	16322.4	0.11	1.11
2	20750.4	0.13	1.13
1	25178.4	0.15	1.15

Table B.12: Summary of the Steel Structure P-Delta Loads

Storey	P_x (kN)	θ_x	U_2
Roof	4432.5	0.049	1.049
5	9684.2	0.063	1.063
4	14937.7	0.073	1.073
3	20199.4	0.084	1.084
2	25474.7	0.095	1.095
1	30753.3	0.110	1.110

B.2.1.6 Structural Irregularities

The symmetric building layout of both structures ensured the center of rigidity and the center of mass were essentially equal. Even though there were no irregularities that would result in additional lateral load amplification, the NBCC (2010) required that torsional sensitivity factor B_x be calculated for each storey to assess the lateral sensitivity of both buildings using equation (B.8):

$$B_x = \frac{\delta_{max}}{\delta_{ave}} \tag{B.8}$$

where, δ_{max} represents "the maximum storey displacement induced by the equivalent static forces acting at a distance of $\pm$ 0.10D_{nx} from the centre of mass of each floor" (NBCC, 2010). Furthermore, the average displacements that occur as a result of the equivalent static force are accounted for by δ_{ave} (NBCC, 2010). The calculated sensitivity factors of each storey for both structures were below the allowable limit of 1.7, justifying that torsional sensitivity could be exempt from the seismic analysis. However accidental eccentricities in the building were considered through the application of a 10% offset between the center of rigidity and center of mass. This consideration would account for additional torsionally induced lateral loads due to construction and fabrication errors, to satisfy NBCC (2010) requirements. To simplify these considerations in the equivalent static analysis the lateral loads were increased by a factor of 1.1. However, the affect of the induced torsional effects on the seismic design forces were considered in the ETABS

model used for the response spectrum analysis.

B.2.1.7 Final Equivalent Static Seismic Design Forces

After establishing the lateral stability and torsional sensitivity effects, the final equivalent static seismic design forces were computed. A summary of the total seismic design forces for both the hybrid timber-steel and steel-only structures are presented in Tables B.13 and B.14. These seismic forces were distributed evenly between the two BRBFs, represented by column $F_{\frac{x,Total}{2}}$, because of the symmetrical building layout which did not require torsional sensitivity considerations.

B.2.2 Response Spectrum Analysis

After completing the equivalent static seismic design procedure, the iterative response spectrum analysis process was conducted to improve the seismic design of the BRBFs in both the hybrid timber-steel and steel-only structures. The response spectrum analysis of both buildings was conducted using the following procedure (NBCC, 2010; Filiatrault et al., 2013):

1. The out-of-plane displacements and rotations of each storey perpendicular to the braced frame were restrained in the model to isolate the BRBF response. Additionally, an eccentricity of 5% was specified in the model to account for accidental torsion.
2. The fundamental period (T_a), seismic weight (W) and elastic base shear (V_e) of the restrained structural model was obtained from the NBCC spectral analysis.
3. The spectral acceleration, $S(T_a)$, corresponding to the fundamental period of the restrained model was interpolated from the response spectrum ordinates.
4. The elastic base shear was factored by the coefficient for short period structures with a ductility factor (R_d) > 1.5 that are located on soil conditions less than class F, calculated using equations (B.9) (NBCC, 2010).

$$\frac{2}{3}\frac{S(0.2)}{S(T_a)} \leq 1.0 \tag{B.9}$$

Table B.13: Summary of the Hybrid Structure Final Seismic Loads

Storey	F_x (kN)	$1.1F_x$ (kN)	N_x (kN)	U_2	$F_{x,Total}$ (kN)	$F_{\frac{x,Total}{2}}$ (kN)
Roof	428.7	471.6	15.2	1.06	515.5	257.8
5	327.2	360.0	22.1	1.08	413.5	206.8
4	263.3	289.7	22.1	1.10	342.1	171.1
3	198.4	218.2	22.1	1.11	267.2	133.6
2	133.7	147.0	22.1	1.13	190.8	95.4
1	67.9	74.7	22.1	1.15	111.2	55.6
				Total	1840.4	

Table B.14: Summary of the Steel Structure Final Seismic Loads

Storey	F_x (kN)	$1.1F_x$ (kN)	N_x (kN)	U_2	$F_{x,Total}$ (kN)	$F_{\frac{x,Total}{2}}$ (kN)
Roof	746.9	821.6	22.2	1.049	885.5	442.8
5	527.8	580.6	26.3	1.063	645.3	322.7
4	422.4	464.7	26.3	1.073	526.9	263.5
3	317.3	349.0	26.3	1.084	406.7	203.4
2	212.1	233.3	26.4	1.095	284.4	142.2
1	106.1	116.7	26.4	1.110	158.8	79.4
				Total	2907.7	

5. The design elastic base shear, V_{ed}, was calculated by factoring the elastic base shear, V_e, by the coefficient determined in the previous step.
6. The minimum earthquake design base shear, V, was determined using equation (B.10) from the equivalent static method.

$$V = \frac{S(T_a)M_v I_E W}{R_d R_o} \tag{B.10}$$

The fundamental period, T_a, was the lesser of the model period or the upper period limit of 1.11 sec from the NBCC (2010) for the strength design of both structures. For drift, the period T_a was taken as the lower code specified limit of 0.56 sec.

7. The design base shear, V_d, had to be calculated using equation (B.11) and shall not exceed 80% of the minimum base shear, V.

$$V_d = (\frac{I_E}{R_d R_o})V_{ed} \geq 0.8V \tag{B.11}$$

8. The strength required the unrestrained response spectrum analysis model results were scaled by the factor V_d/V_e, to establish the response spectrum analysis values. However, for drift design the factored lateral displacements were then amplified to account for inelastic effects by multiplying by R_dR_o.

B.3 Design of Seismic Force Resisting System

Multiple response spectrum analysis iterations were completed for both the hybrid timber-steel and steel-only structures before the seismic weight and design base shears converged. After the analysis was complete, the BRBFs of each structure were designed to resist the seismic design forces taken from the three dimensional unrestrained model. The area of the BRB yielding core was determined from the anticipated seismic brace forces from the response spectrum analysis and equation (B.12).

$$T_r = C_r = \phi A_{sc} F_{ysc} \tag{B.12}$$

The yield strength of the steel core was assumed to be 370 MPa determined in the BRB investigation conducted by Tremblay et al. (2004). The seismic brace forces and core areas of the two structures are presented in Table B.15.

After finalizing the brace core design, the probabilistic tension and compression brace forces were then determined from equations (B.13) and (B.14), respectively.

$$T_{pr} = \omega A_{sc} R_y F_{ysc} \tag{B.13}$$

$$C_{pr} = \beta \omega A_{sc} R_y F_{ysc} \tag{B.14}$$

where, the strain-hardening factor, ω, and compression behaviour factor, β, of 1.2 and 1.1, respectively, were taken from Tremblay et al. (2004) for the force calculations. Through the application of the capacity design procedure, a force multiplication (overstrength) factor of 1.1 was applied to the probabilistic forces used for the design of the gusset plate. This element was to be detailed as the secondary fuse element to provide additional energy dissipation if the brace forces exceed the probabilistic forces previous determined. Lastly, the brace and beam connection and timber fastener forces were capacity protected by additional minimum amplified factors of 1.1.

Once the probabilistic forces were calculated, a detailed structural analysis of the frame was conducted by replacing the anticipated seismic brace forces, previously determined, with the probabilistic brace forces of the BRBs. Various gravity loading patterns were considered in the structural frame analysis to provide the worst case loading scenario to design the structural components of the seismic force resisting system. The lateral force transfer and complex structural analysis methods are presented in Figure B.4. The lateral shear force distributed along the beams of each storey, V_{lat}, was determined by equation (B.15).

$$V_{lat} = \frac{2(((F_{b1,TP} + F_{b1,CP})\cos(\theta_b)) - ((F_{b2,TP} + F_{b2,CP})\cos(\theta_b))}{26} \tag{B.15}$$

Table B.15: Final BRB Design Forces and Brace Core Areas

Storey	Tension Forces (kN)	Compression Forces (kN)	Core Area (mm^2)
Hybrid Timber-Steel Building			
Roof	90	170	510
5	125	240	720
4	155	265	795
3	185	305	920
2	225	345	1040
1	380	380	1140
Steel-only Building			
Roof	415	455	796
5	580	640	1111
4	700	770	1306
3	795	875	1487
2	895	985	1682
1	1055	1160	2042

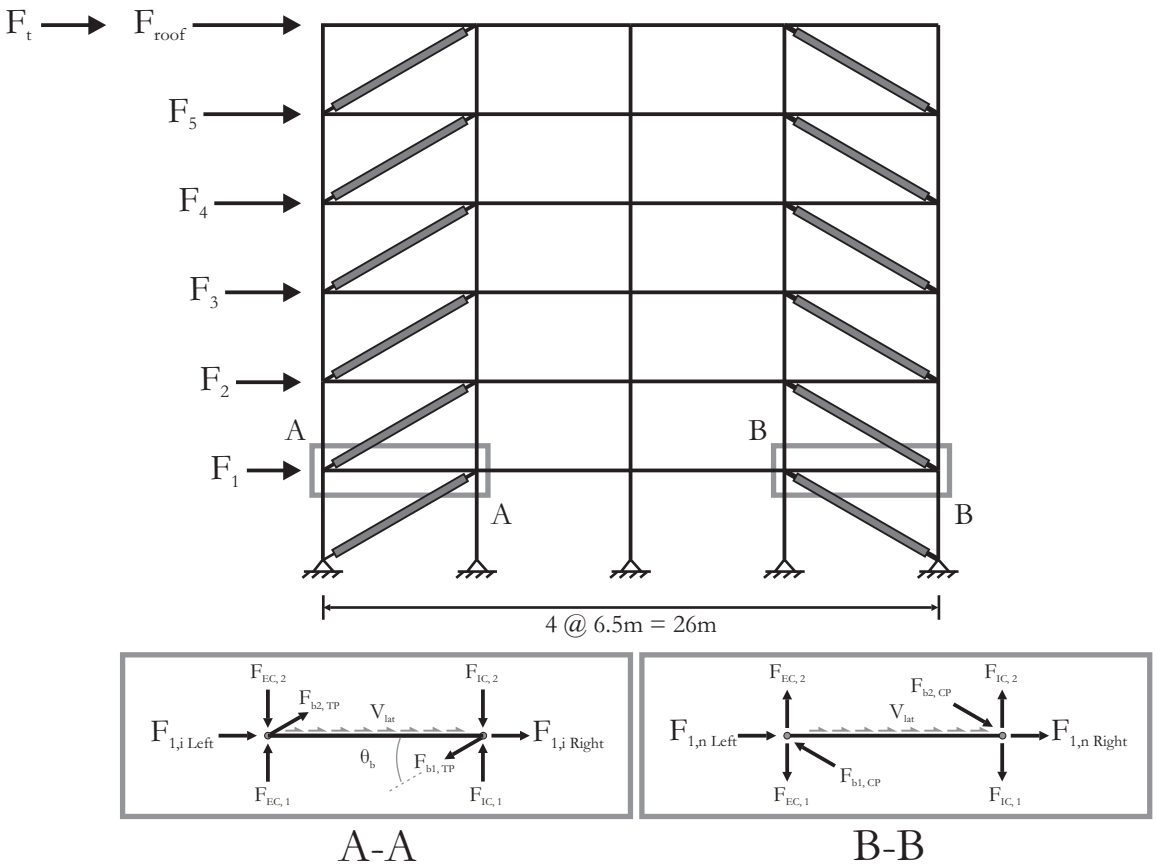

Figure B.4: Structural Analysis of Beam Forces

B.3.1 Capacity Design Procedure

The application of capacity design methodology ensures the integrity of the lateral load resisting system by systematically increasing the seismic forces as they are transfer throughout the structural hierarchy. This procedure was applied in the design of both the hybrid timber-steel and steel-only structures to ensure that the ductility demand of the MCE hazard level earthquake was satisfied in its entirety by the inelastic behaviour of the bracing element. For the capacity design of the BRBFs, an overcapacity of 10% was assigned to the probable tensile and compressive brace forces, as dictated by CSA S16-09 (2009). Furthermore, an additional force amplification factor of 1.1 was applied to the capacity design forces, determined from the structural analysis of the BRBFs, at every stage of the structural hierarchy. The gusset plates of the braced connections were detailed as a secondary failure mechanism to provide supplemental damping through ductile fastener yielding if the seismic brace design forces exceed the probabilistic braced forces of the BRBs.

B.3.2 Final Design and Building Performance

The final member dimensions were governed by the spacing requirements of the glued-in rod connections of the hybrid timber-steel building. However, the members selected for the seismic design of the steel-only building were the result of the dynamic seismic force requirements of the response spectrum analysis. The final member sizes of the two building designs are presented in Table B.16.

After the member sizes were finalized, the story drift responses of the hybrid timber-steel and steel-only structures were conducted to ensure the buildings did not surpass the 2.5% limit outlined in the NBCC (2010). A summary of the peak interstorey drifts of the two buildings are presented in Table B.17.

Table B.16: Final Structural Member Dimensions of the Hybrid and Steel-only BRBFs

Storey	Beam (mm x mm)	Exterior Column (mm x mm)	Interior Column (mm x mm)	Center Column (mm x mm)
Hybrid Timber-Steel Building				
Roof	342 x 215	228 x 215	228 x 215	175 x 152
5				
4	418 x 215	342 x 315	342 x 315	190 x 175
3		465 x 380	465 x 380	215 x 190
2	532 x 215	465 x 456	465 x 456	228 x 215
1				266 x 215
Steel-only Building				
Roof	W 310x21	W 360x51	W 200x52	
5				
4	W 410x46	W 360x64	W 200x100	W 200x42
3				
2		W 360x131	W 250x131	
1				

Table B.17: Storey Drift Responses of the BRBFs

Storey	Inter-storey Drift (%)
Hybrid Timber-Steel Building	
Roof	1.70
5	1.70
4	1.61
3	1.48
2	1.35
1	1.28
Steel-only Building	
Roof	1.69
5	1.67
4	1.65
3	1.50
2	1.40
1	1.33